THE EFFECTS OF AMORPHOUS PHASE SEPARATION ON CRYSTAL NUCLEATION IN BARIA-SILICA AND LITHIA-SILICA GLASSES

Edgar Dutra Zanotto, M.Sc.

Thesis Presented for the Degree of
Doctor of Philosophy of
The University of Sheffield

Department of Ceramics, Glasses and Polymers
The University of Sheffield

March, 1982

ACKNOWLEDGEMENTS

I am indebted to Dr P.F. James for very helpful suggestions, critical appraisal of the manuscript and encouragement given during the course of this work. Thanks are due to Dr A.F. Craievich of Universidade de Sao Paulo (Brazil) for his interest, for performing the SAXS measurements and for many helpful discussions. I would also like to thank Professor H. Rawson for providing the research facilities in the Department.

I am immensely grateful to Luciana for constant encouragement, patience and for valuable help with the photographic printing.

Many thanks are due to Mrs M. Hodgins for typing this thesis. I wish also to thank Ernest Crossland, Jim Smedley, Sonya Saxby, Roy Bacon, Mike Wilson, David Priestley, Lawrence Toothill, Robin Cooper and many others for their friendship and assistance during my years in the Department.

The author acknowledges the help of Dr J.R. Gonçalves da Silva and Mr Ubirajara Raymundo in taking care of his personal interests in Brazil during his absence. Acknowledgements are also due to Universidade Federal de Sao Carlos and CAPES (Brazil) for financial support.

TO

LUCIANA, DIVA AND JOVIANO

SUMMARY

The kinetics and morphology of amorphous phase separation in $BaO-SiO_2$ glasses with well characterized impurity contents were studied by small angle X-ray scattering (SAXS) and transmission electron microscopy (TEM). The kinetics and morphology of crystal nucleation and growth in phase-separated and non phase-separated glasses were determined by quantitative optical microscopy and TEM.

Amorphous phase separation caused a marked increase in crystal nucleation and growth rates due to compositional changes in the baria-rich matrix. However, the highest nucleation rates were observed in the stoichiometric $BaO.2SiO_2$ glass, which did not phase separate.

The compositional effect of phase separation on crystal nucleation rates was also found in the Li_2O-SiO_2 system. The nucleation rates in phase separated Li_2O-SiO_2 glasses with widely differing Li_2O contents were equal, but higher than in the stoichiometric $Li_2O.2SiO_2$ glass. This was attributed to the crystallization of a solid solution phase in the phase separated glasses.

No correlation was found between crystal nucleation and phase separation morphology in these systems. However, there was some evidence of a small additional nucleation, possibly in the diffusion zones around the droplets.

A quantitative test of classical nucleation theory was performed for $Li_2O.2SiO_2$ and $BaO.2SiO_2$ glasses using measured crystal nucleation rates (I) and viscosities, and available thermodynamic data. The temperature dependence of I was well described by theory but the experimental rates were 20-30 orders of magnitude higher than expected. Reasons for this discrepancy are discussed.

A theoretical analysis of errors using quantitative microscopy is given.

Typically, underestimates of 3-14% are expected in the determination of nucleation rates. These predictions were confirmed experimentally.

Experimental crystallinity versus time curves for the $BaO.2SiO_2$ glass did not agree with those calculated from the Johnson-Mehl-Avrami equation. Explanations are given for the discrepancy.

CONTENTS

CHAPTER 1

THEORY

1.1 Introduction

Glass-ceramics are polycrystalline solids prepared by the controlled crystallization of glasses. About 200 years after the work of Réaumur, who converted glass bottles into opaque porcelain-like objects, research carried out by S.D. Stookey [1.1] at Corning Glass Works (USA) led to the development of glass-ceramics. Glass-ceramics can be regarded as a most valuable addition to the materials available to the design engineer. Their unique combination of properties is likely to make them attractive for a number of specialized engineering applications, e.g. machinable glass-ceramics, fibrous and bulk glass-ceramics having oriented microstructures, vacuum tube envelopes, telescope mirror blanks, radomes for the aerospace industry, protective coatings for metals, etc. Also a wide range of consumer goods is becoming available [1.2].

The development of practical glass-ceramics is closely related to studies of nucleation and crystal growth in supercooled liquids which are of great scientific interest. Glass is a very convenient medium for fundamental studies of this type because glass-like liquids have high viscosities so that the diffusion processes and atomic rearrangements which control nucleation and crystal growth occur relatively slowly. Because of the rapid increase of viscosity which occurs when the temperature falls, it is possible to arrest the crystallization process by rapid cooling. Thus various stages of development can be "frozen in" permitting the use of convenient methods of examination.

Closely related to crystal nucleation and growth studies are investigations of amorphous phase separation. This subject is also of fundamental interest. Furthermore, the influence of prior phase separation upon crystallization processes is of prime importance both with regard to

glass-ceramic formation and in relation to the stability of glasses.

The main objectives of this work were to study quantitatively the kinetics of crystal nucleation and its correlation with amorphous phase separation (APS) kinetics in silicate glasses. An experimental test of the classical nucleation theory and of the validity of the Johnson-Mehl-Avrami (JMA) theory of phase transformations, were also attempted for glasses having compositions close to the stoichiometric crystalline phases. The glasses chosen for this study were from the Li_2O-SiO_2 and BaO-SiO_2 systems, because in both systems amorphous phase separation and internal crystal nucleation occur without deliberate addition of nucleating agents.

1.2 Kinetics of Liquid-Liquid Immiscibility in Glass

Glass-in-glass phase separation has been known for 40 years. The inventors of Vycor glass [1.3] observed a phenomenon that could only be explained in terms of a heterogeneous glass structure. The heterogeneous glass structure had also been suggested [1.4,1.5] from various property investigations of glasses. Yet, only after the application of suitable experimental techniques, such as electron microscopy or small angle X-ray scattering, and the realization that phase separation is related to the metastable immiscibility boundary did clear understanding of the phenomenon emerge. Thus, since the early 1960's, there was an intense activity in this field and over 500 papers were published on phase separation.

Several review articles and textbooks on the subject have appeared in the past few years. These include articles by Rawson [1.6], Zarzycki [2.26], Porai-Koshits [1.7], Charles [1.8], Doremus [1.9], James [1.10], Uhlmann and Kolbeck [1.11], Pye [1.12], Vogel [1.13], Craievich [1.14] and Tomozawa [1.15]. The origin of immiscibility, kinetics

of phase separation, influence on the properties, etc., have been discussed in detail in these reviews. Therefore, only a short development of the theories of nucleation, growth, coarsening and spinodal decomposition, which are important for the understanding of this thesis, will be given.

When a homogeneous glass is held at a temperature inside the immiscibility boundary, the glass gradually transforms into a two-phase structure. Theoretically there are two types of transformation mechanisms by which the final structure is attained. One is the nucleation and growth mechanism, and the other is the spinodal decomposition. The mechanisms are closely related to the curvature of the free energy of mixing and, consequently, to the position of the spinodal line, which in a two-component system is defined by the condition that the second derivative of the free energy of mixing (ΔG_m) with respect to composition (mole fraction c of one of the components) is zero: $\partial^2 \Delta G_m / \partial c^2 = 0$. The region between the immiscibility boundary and the spinodal line is called the metastable region and corresponds to a positive value of the second derivative $\partial^2 \Delta G_m / \partial c^2$; while the region inside the spinodal is called the unstable region and corresponds to a negative value of the second derivative. In the metastable region, the nucleation and growth mechanism is expected to be operating while in the unstable region spinodal decomposition is expected (see section 1.3.1.3b). A brief review of these mechanisms is given below.

1.2.1 Nucleation and growth

After a particle is formed by nucleation (the nucleation theory will be discussed in section 1.3) it begins to grow. The case of diffusion controlled growth for isolated spherical particles in an infinite matrix has been treated rigorously by Zener [1.16], Frank [1.17] and Carslaw and Jaeger [1.18] and exact solutions are available. The theory of diffusion

controlled growth leads to a parabolic growth of the particles radius, r, with time

$$r = \gamma(Dt)^{1/2} \qquad (1.1)$$

where γ is a function of particle composition and mean composition of the material. If the diffusion coefficient, D, is constant for a given temperature and composition, $r \alpha t^{1/2}$.

In a polydisperse assembly, the growth law can still be written in terms of an average particle size as $\bar{r} \alpha t^{1/2}$. If, however, the growth is interface controlled (where the rate of transfer of the diffusing species across the interface is slower than the rate of their arrival at the interface), the growth law is linear with time. Wert and Zener [1.19] and Ham [1.20] have carried out these calculations for non-spherical geometry, and their results show that with particles shaped as thin rods, the length of the rod varies linearly with time. Ham also shows that non-spherical particles will have a shape eccentricity which does not change with time.

Spinodal decomposition, on the other hand, predicts that, in the initial stages at least, a selective amplification of a narrow band of wavelengths in the Fourier components of the composition fluctuation occurs, and these wavelengths predominate in the microstructure. Thus, the characteristic microstructure size is *independent* of time in the early stages. This fact has been demonstrated by Zarzycki and Naudin for a lead borate system [1.21].

1.2.2 Coarsening

At the end of the primary growth stage, the reaction proceeds to reduce the total interfacial energy in the assembly, the larger particles growing at the expense of the smaller ones which redissolve.

Following an earlier treatment by Greenwood [1.22] the theory developed by Lifshits, Slyozov and Wagner [1.23,1.24] (LSW theory) describes the kinetics of diffusion controlled particle coarsening when the volume fraction of the minor phase is *small* (< 0.1), so that the mean distance between particle centres is large compared with particle dimensions. Using the Gibbs-Thomson relation for the increase in solubility of a particle as its radius decreases, the time dependence of the average particle radius, $\bar{r}$, may be expressed as

$$\bar{r}^3 - \bar{r}_0^3 = \frac{8\sigma D C_0 V_m^2}{9RT} \cdot t \qquad (1.2)$$

where $\beta = 8\sigma D C_0 V_m^2/9RT$ is the rate constant, $\bar{r}_0$ is the average particle size at the beginning of the coarsening stage, σ is the interfacial energy, D is the diffusion coefficient of solute in the matrix, C_0 is the concentration of solute in the matrix ($mol.m^{-3}$) and V_m is the molar volume of the dispersed phase.

The activation energy for the process can be obtained by determining β for various temperatures. If studied within the temperature range where the equilibrium solubility does not vary significantly, one can obtain the activation energy for interdiffusion from growth studies at different temperatures.

Although the above theory has been verified in various systems, its formulation is valid only for *small* volume fractions of the minor phase. If the volume fraction is constant and the amorphous phase separation (APS) is in the coarsening stage, the number of particles is inversely proportional to the time of isothermal treatment, i.e. $N \alpha t^{-1}$. If the growth of the particles is limited by a surface reaction rate, $\bar{r}^2 \alpha t$ and $N \alpha t^{-3/2}$ [1.24]. Such a process can occur, for example, when an impurity layer exists at the interface between the two phases.

Haller [1.25] has considered the coarsening kinetics for microstructures which show extensive interconnectivity. His treatment does not consider the solubility changes to be due to dispersion in the size of the particles but rather to local changes in curvature of the interface when intersecting growth occurs. He found that if the mechanism of transport is volume diffusion, the decrease in interfacial area varies as $t^{-1/3}$ for diffusion controlled growth, and $t^{-1/2}$ for interface controlled growth. However, his growth equation contains several temperature dependent terms which need not necessarily be Arrhenian, and it is not feasible to identify the mass transfer steps on the basis of an Arrhenian plot of growth rate versus temperature.

Most investigators have observed a diffusion controlled mechanism in the coarsening process. References will be given in Chapter 4 where the SAXS results for phase separation in $BaO-SiO_2$ glasses are shown. A recent review of coarsening in solids was published by Jain and Hughes [1.26].

1.2.3 Spinodal decomposition theory

The spinodal decomposition mechanism differs from the nucleation and growth mechanism in that there is no nucleation of the second-phase composition. Instead, fluctuations with a small extent of composition variation appear. The dimensions of fluctuations are determined by the interfacial energy and transport process. The interfacial energy between two phases is smaller the more diffuse the interface. Therefore, the extremely large dimension is energetically favoured for a given extent of composition variation. The sharp interface would increase the interfacial energy and this type of fluctuation would be unfavourable. Among those fluctuations that are energetically favourable, the transport process would be easier for small-scale fluctuations. Because of these two opposing tendencies, there is an optimum scale (wavelength) of the composition fluctuation.

Hillert [1.27] and Cahn [1.28] developed the quantitative theory of spinodal decomposition in 1961. Cahn's theory will be described briefly assuming *zero strain energy*. The free energy of the inhomogeneous system is given by

$$G = \int_{\bar{V}} [g(c) + K(\nabla c)^2] dv \tag{1.3}$$

where g(c) is the free energy of a unit volume of homogeneous material of composition c and $K(\nabla c)^2$ is the first term of an expansion representing the increase in free energy due to a gradient of composition. K(>O) is called the gradient energy coefficient and the integral is performed over volume v. The composition fluctuation is given by the summation of sinusoidal waves

$$c - c_0 = A \cos \beta X \tag{1.4}$$

with various values of β, where c_0 is the average composition, A an amplitude, $\beta = 2\pi/\lambda$ the wavenumber, λ the wavelength, and X the distance. The free energy difference per unit volume between the solution with a small extent of composition variation and the homogeneous solution is given by

$$\Delta G/V = (A^2/4)[\partial^2 g/\partial c^2 + 2K\beta^2] \tag{1.5}$$

If this is negative, then the solution is unstable with respect to sinusoidal fluctuations of wavelength $2\pi/\beta$. With $\partial^2 g/\partial c^2 > 0$, the solution is stable with respect to infinitesimal sinusoidal fluctuations of all wavelengths. With $\partial^2 g/\partial c^2 < 0$, the solution is unstable with respect to infinitesimal sinusoidal fluctuations of wavelengths greater than $2\pi/\beta_c$ which is given by

$$\frac{2\pi}{\beta_c} = \left[- \frac{8\pi^2 K}{\partial^2 g/\partial c^2} \right]^{1/2} \tag{1.6}$$

A kinetic expression for spinodal decomposition is obtained by solving a diffusion equation in which the thermodynamic factors are included. By using the approximation that is valid only for *initial stages* of spinodal decomposition, the time dependence of the amplitude $A(\beta,t)$ of composition fluctuation with wavenumber β is given by

$$\partial A(\beta,t)/\partial t = R(\beta)A(\beta,t) \tag{1.7}$$

then

$$A(\beta,t) = A(\beta,0)\ \exp[R(\beta)t] \tag{1.8}$$

where

$$R(\beta) = M\beta^2[\partial^2 g/\partial c^2 + 2\beta^2 K] \tag{1.9}$$

M is a mobility related to the interdiffusion coefficient $\tilde{D}$ by

$$\tilde{D} = M\ \partial^2 g/\partial c^2 \tag{1.10}$$

and $A(\beta,0)$ is the amplitude of the initial (t=o) composition fluctuation. Equation (1.8) states that an amplitude of composition fluctuation with wavenumber β changes exponentially with time, the rate of change being determined by the factor $R(\beta)$. The kinetic amplification factor $R(\beta)$ is negative when the solution is stable to that fluctuation, and is shown in Figure 1.1 for inside the spinodal, $\partial^2 g/\partial c^2 < 0$, as a function of β. $R(\beta)$ is zero for $\beta = \beta_c$, positive for longer wavelengths and has a maximum at $\sqrt{2}$ times the critical wavelength.

Cook [1.29] later suggested a modification to Equation (1.7) by adding a thermal fluctuation term due to Brownian motion. Thus

Fig. 1.1 Theoretical amplification factor for early stage of spinodal decomposition (upper left)

Fig. 1.2 Free energy of formation of a spherical crystal nucleus with σ = 200 $mJ.m^{-2}$ for a $Li_2O.2SiO_2$ glass (bottom)

Fig. 1.3 Distribution function for embryos of different sizes according to Volmer and Becker-Döring theories of nucleation (upper right)

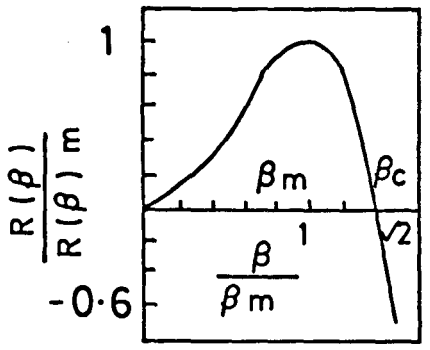
1
R(β)/R(β)m
βm
βc
β/βm
1
√2
-0·6

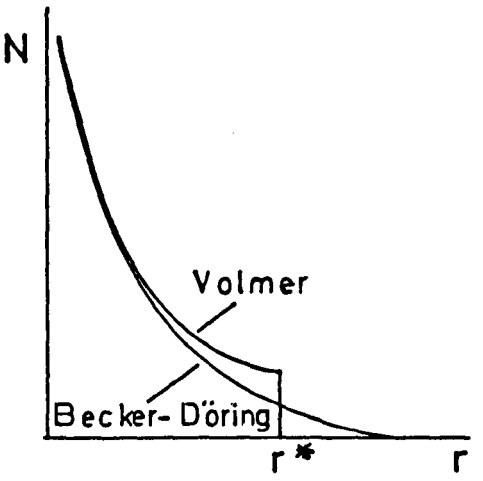
N
Volmer
Becker-Döring
r*
r

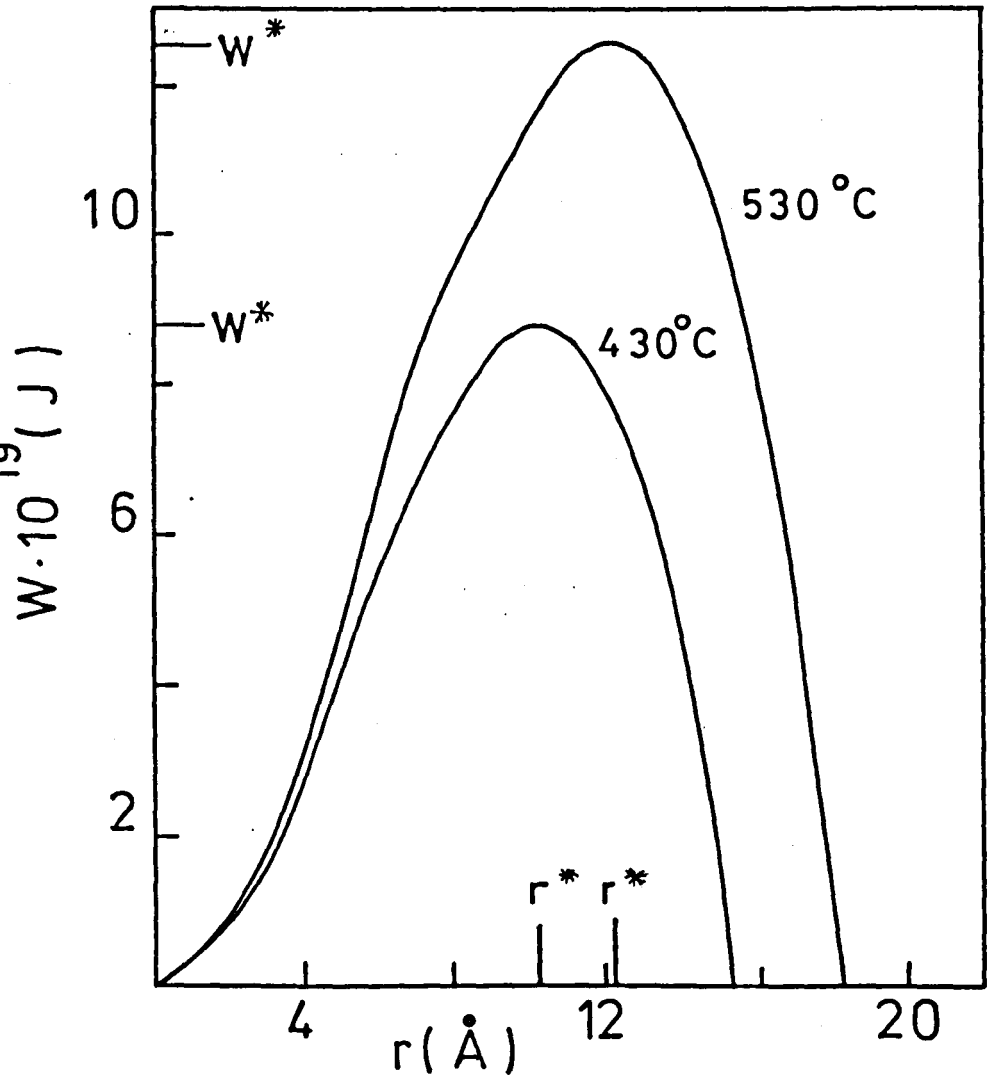
W*
10
W*
6
2
W·10^19(J)
530 °C
430°C
r*
r*
4
12
20
r(Å)

$$\partial A(\beta,t)/\partial t = R(\beta)A(\beta,t) - \beta^2 B(\beta,t) \qquad (1.11)$$

where $B(\beta,t)$ is the Fourier transform of the fluctuating field. With the addition of this term, the ratio of the wavelength with maximum amplification factor to the critical wavelength becomes larger than $\sqrt{2}$.

One important feature of spinodal decomposition is that there is a particular wavelength that grows at the fastest rate. This leads to the unique microstructural morphology.

Although the theory of Hillert and Cahn is often identified with the spinodal decomposition, their theory is actually applicable to both spinodal decomposition and nucleation and growth. According to their theory, nucleation and growth is the special case observable only at the immiscibility boundary. As the original composition approaches the spinodal boundary the interface between the critical nuclei and the matrix gradually becomes more diffuse, and finally at the spinodal line it disappears.

1.2.3.1 Experimental observations of spinodal decomposition

Since the development of Cahn's theory numerous attempts were made to confirm it experimentally in glass systems. The earliest attempts were centred around the morphological studies of phase-separated microstructures. The morphological similarity between the theoretical predictions (computer simulations predicted an interconnected morphology) and the experimental observations was considered as the evidence for spinodal decomposition by Cahn [1.30] and Hammel [1.31]. However, several investigators postulated processes by which independent particles can join together, e.g. Haller and Macedo [1.32] and Hopper and Uhlmann [1.33].

The kinetics of phase separation were studied by small angle X-ray scattering by Rundman and Hilliard [1.34] on metals, followed by Zarzycki

and Naudin [1.21,1.35], Tomozawa [1.36,1.37], Neilson [1.38] and others. However, careful investigation shows a clear discrepancy between the early stage theory of spinodal decomposition and the SAXS data.

Several attempts were made to explain the discrepancy; e.g. using the later stage theory developed by De Fontaine [1.39]; using the modified equation by Cook or taking into account the fact that the diffusion coefficient itself is a function of time at a constant heat-treatment temperature, similar to the case of viscosity of a glass at temperatures in the transformation range.

Srinivasan et al. [1.40] suggested that measurements of the evolution of the volume fraction of the minor phase can be used to distinguish between spinodal decomposition and nucleation and growth.

Tomozawa [1.41] demonstrated that both the viscosity and chemical durability of a commercial borosilicate glass changed gradually with heat treatment time, at low temperatures, indicating the simultaneous gradual composition variation of both phases. This was taken as an indication that phase separation was occurring by spinodal decomposition.

1.3 Nucleation in Glass-forming Systems

Depending on thermodynamic conditions, if concentration fluctations small in amplitude but large in extent occur spontaneously, the reaction may proceed by spinodal decomposition with a continuous fall in free energy. If, however, small fluctuations tend to decay, there is a *nucleation barrier*. Although unstable, such fluctuations exist and occasionally one becomes so large that it is stable and grows to microscopic dimensions. It is the purpose of this section to discuss the kinetics of this latter process of nucleation.

The derivations given below have been summarized from several references where a more complete coverage on the subject can be found, e.g. Fine [1.42], Burke [1.43], Christian [1.44], Zettlemoyer [1.45] and Russell [1.46].

1.3.1 Homogeneous nucleation at constant composition

The problem to be considered is the "birth" of a clump of phase β in a matrix of phase α of identical composition to β. If the process is carried out at constant temperature and external pressure and the difference in Gibb's free energies per mole between phases α and β, ΔG ($= G_\beta - G_\alpha$), is negative, then the process would proceed spontaneously except that a surface between α and β must be created. There are also strain energy considerations, but it will be assumed that viscous flow of the glass matrix removes elastic strains induced during the transformation. If the surface energy per unit area σ is *isotropic* and *no stresses* are exerted on the clump from the matrix, the clump will be spherical. The energy change on forming a spherical clump of radius r, W, is

$$W = \frac{4}{3}\pi r^3 \Delta G_v + 4\pi r^2 \sigma \qquad (1.12)$$

where $\Delta G_v = \Delta G/V_m$ is the free energy difference between phases β and α per unit volume of nucleating phase or *thermodynamic driving force*.

Figure 1.2 is a plot of W vs. r calculated for the lithium disilicate (LS_2) glass, with ΔG given by [1.51] and assuming $\sigma = 200\ mJ.m^{-2}$. For r-small the surface term predominates. For r-large the volume term predominates. The coordinates of the maximum, r* and W*, may be determined by setting $dW/dr = 0$, solving for r* and substituting into equation (1.12):

$$W^* = \frac{16\pi\sigma^3}{3\Delta G_v^2} \qquad (1.13)$$

$$r^* = \frac{-2\sigma}{\Delta G_v} \tag{1.14}$$

Particles of radius smaller than the critical radius r* (embryos) tend to dissolve since an increase in size leads to an increase in W, whilst particles of r > r* (nuclei) will tend to grow since an increase in radius decreases W. W* is often called the thermodynamic barrier. W* and r* increase with temperature.

More generally for non-spherical nuclei it can be shown that [1.47]

$$\begin{aligned} X^* &= - K_4\bar{\sigma}/\Delta G_v \\ W^* &= K_5\sigma^3/\Delta G_v{}^2 \end{aligned} \tag{1.15}$$

where X* is a dimension of the critical nucleus, $\bar{\sigma}$ an average interfacial energy and K_4 and K_5 are shape factors. These equations were fully discussed by Rowlands [1.47].

The process of nucleation can therefore be considered in terms of the rate at which critical nuclei are able to form and how quickly they subsequently grow. Embryos are assumed to grow by unimolecular steps.

1.3.1.1 The Volmer and Weber theory of nucleation

This theory was developed in 1926 for the condensation of a vapour [1.48]. The formation of a nucleus was envisaged as a step process where individual molecules or "formula units" can add on to the embryo,

$$i^*\beta \rightarrow \beta i^*$$

$$\beta_{i^*} + \beta_1 \rightarrow \beta_{i^*+1}$$

$$\beta_n + \beta_1 \rightarrow \beta_{n+1}$$

where i* is the smallest entity that can be recognised as a new phase.

There is a certain probability per unit time that a "formula unity" or molecule will add onto the surface of the embryo β_n converting it into a β_{n+1} embryo. The number of molecules crossing the barrier per second is given by:

$$di/dt = s\nu \exp\left[-\frac{\Delta G_D}{kT}\right] \tag{1.16}$$

where ν is the atomic vibration frequency, ΔG_D is the activation energy per "molecule" or formula unit to cross the surface between α and β, that is, to disconnect itself from α and attach itself to β, and s the number of formula units facing the embryos of β across the interface.

Volmer and Weber neglected the *reverse reaction*, that is, once over the hump an atom does not return to α and assumed that the *growth process is sufficiently slow* so that the number of clumps of critical size is the equilibrium number. A steady state is set up in which the number of critical nuclei forming per unit time equals the number disappearing through growth. Volmer and Weber also assumed the steady-state number to be the *equilibrium* number and the rate of growth to be given by Equation (1.16). Accordingly, the number of clumps of critical size, i.e. nuclei per unit volume is given by the well-known equation:

$$N^* = n \exp(-W^*/kT) \tag{1.17}$$

where n is the total number of "molecules" of nucleating phase per unit volume of the liquid.

The rate of nucleation, I, is given by multiplying the number of critical nuclei by the rate of growth of a clump of critical size.

$$I = ns^*\nu \exp[-(\Delta G_D + W^*)/kT] \tag{1.18}$$

where s^* is the value of s if the clump is of critical size.

1.3.1.2 The Becker and Döring theory

The Volmer and Weber theory was improved in 1935 by Becker and Döring [1.49]. First the reverse reaction was allowed, that is, $\beta i^* - \beta_1 \rightarrow \beta_{i^*-1}$. The top of the W vs. r (Figure 1.2) curve is almost symmetrical and the probability of adding or subtracting a molecule is about equal. Thus the rate given by Equation (1.18) should approximately be divided by two. Second, the steady state number of nuclei per unit volume N* may not be equal to the equilibrium number given by Equation (1.17). The net nucleation rate is given by

$$I = \frac{nkTA^*V_m}{4\pi r^{*3}} \left(\frac{3W^*}{\pi kT}\right)^{1/2} \exp\left[-\left(W^* + \Delta G_D\right)/kT\right] \qquad (1.19)$$

where A* is the surface area of the critically sized embryo.

The distribution function does not fall to zero at the critical radius but approaches zero when r is very large (Figure 1.3). The main effect is to modify the term in the pre-exponential factor by about a hundred. This is not a large factor because values of W* in the exponential term are extremely sensitive to small changes in temperature.

Turnbull and Fischer in 1949 [1.50] used the formalism of absolute rate theory to derive a complete expression for homogeneous steady-state nucleation in solids. The final equation is given by

$$I = A \exp\left[-\left(W^* + \Delta G_D\right)/kT\right] \qquad (1.20)$$

The pre-exponential factor A can be expressed as

$$A = 2n\, V^{1/3}\, (kT/h)\, (\sigma/kT)^{1/2} \qquad (1.21)$$

where V is the volume per formula unit. To a good approximation (one or

two orders of magnitude)

$$A = n(kT/h) \tag{1.22}$$

where $n \approx 10^{28} - 10^{29}$ m^{-3} and $kT/h \approx 10^{13}$ sec^{-1} at ordinary temperatures. Usually A may be treated as a constant in the temperature range used for nucleation measurements.

Equation (1.20) was derived for nucleation in a *one* component liquid. A similar approach can also be used for nucleation in multicomponent liquids. However, the probability of finding a critical sized nucleus will be reduced in proportion to the mole fraction of the nucleating component. Thus in general Equation (1.20) is multiplied by the mole fraction of the crystallizing component. σ, the energy associated with unit area of the interface, now depends not only on the change in molecular order which occurs in the region of the interface, but also on the chemical composition gradient which must be present at the crystal-liquid interface. The kinetic barrier to nucleation, ΔG_D, is also more complex. In addition to the molecular reorientations required to form an ordered crystal, "unmixing" also has to occur whereby the remaining crystallized liquid becomes slightly depleted in the nucleating component. Thus the kinetic barrier is now determined by relatively long range diffusion processes, in which ΔG_D may probably be identified with the activation energy for diffusion of the most slowly moving component.

The Analysis of Experimental Nucleation Data

1.3.1.3a The thermodynamic driving force ΔG - One component system

In order to analyse the nucleation data the values of ΔG, σ and ΔG_D are required. The thermodynamic driving force ΔG, depends not only on

the temperature of the supercooled liquid, but also on its composition if more than one component is present. Consider first a *one component* system. ΔG can be expressed as

$$\Delta G = \Delta H - T\,\Delta S \tag{1.23}$$

where ΔH and ΔS refer to the enthalpy difference and entropy difference respectively between the solid and liquid phases per mole of solid phase at temperature T. Thus below the melting point, T_m, ΔG is given by

$$\Delta G = -\Delta H_f + T\,\Delta S_f - \int_T^{T_m} \Delta C_p\, dT + T \int_T^{T_m} \frac{\Delta C_p}{T}\, dT \tag{1.24}$$

where ΔC_p (< 0) is the difference in specific heats between the crystalline and liquid phases at constant pressure. In general ΔC_p can be expressed in terms of an interpolation formula; $\Delta C_p = A + BT + CT^2$. However it is often found that ΔG vs. T is linear over temperatures ranges as large as 200°C. This occurs when ΔC_p is small. Thus over a specified temperature range ΔG is given by

$$\Delta G = -\Delta H_x + T\,\Delta S_x \tag{1.25}$$

where ΔH_x and ΔS_x are two numerically derived factors. A further approximation can be made if $\Delta C_p \approx 0$. ΔG is then given by the well known expression: $\Delta G = -\Delta H_f + T\,\Delta S_f$. Since at T_m, $\Delta G = 0$, $\Delta S_f = \Delta H_f/T_m$

$$\therefore \Delta G = -\Delta H_f (T_m - T)/T_m \tag{1.26}$$

A similar expression can be obtained from Equation (1.25) viz.,

$$\Delta G = -\Delta H_x \ (Tx - T)/Tx \qquad (1.27)$$

The error in neglecting ΔC_p can be estimated for the $Li_2Si_2O_5$ compound. Table 1.1 compares the values of ΔG calculated from the JANAF Thermochemical Tables [1.51] with those calculated from Equation (1.26). At a supercooling of 600°C, the error in ΔG is only about 6%. Obviously the magnitude of the error depends on the value of ΔC_p.

If ΔC_p is a *constant* from T_m to the temperature of interest, equation (1.24) can be integrated to give:

$$\Delta G = -\Delta H_f \frac{(T_m - T)}{T_m} - \Delta C_p \ (T_m - T) + \Delta C_p \ T \ \ln\left(\frac{T_m}{T}\right) \qquad (1.28)$$

neglecting terms of the order $(T_m - T/T_m + T)^3$ and higher in $\ln(T_m/T)$

$$\Delta G = -\Delta H_f \frac{(T_m - T)}{T_m} \left[1 + \frac{\Delta C_p}{\Delta H_f} \frac{(T_m - T)T_m}{(T_m + T)}\right] \qquad (1.29)$$

For those cases where ΔC_p is an unknown constant, Hoffman [1.52] found:

$$\Delta G \simeq \frac{\Delta H_f \ T(T_m - T)}{T_m^2} \qquad (1.30)$$

Equations (1.26), (1.28) and (1.30) were used to plot curves a, b, c and d in Figure 1.4. It can be seen that all expressions give similar values for ΔG at high temperatures (low undercoolings) irrespective of whether ΔC_p is zero or not. At much lower temperatures the differences between the cases $\Delta C_p = 0$ and $\Delta C_p = -10$ or -20 J.mol^{-1} K^{-1} is significant. It can also be seen that the Hoffman expression (Equation 1.30) gives values which are far away from the measured ΔG (curve d).

Table 1.1

ΔG FOR LS_2 (GLASS → CRYSTAL)

T(K)	ΔT(K)	ΔG (kJ mol^{-1})	
		Eq. (1.26)	Eq. (1.27)
800	507	-20.04	-20.88
700	607	-23.51	-24.98
600	707	-26.99	-29.12

$T_m = 1307K$, $\Delta H_f = 53.97$ kJ mol^{-1}, $\Delta C_p = 0$

$T_x = 1377K$, $\Delta H_x = 47.82$ kJ mol^{-1}, $\Delta C_p \neq 0$ (JANAF)

Fig. 1.4 Thermodynamic driving force for glass → crystal transformation in LS_2 glass. Curves a, b and c were calculated from Eq. (1.28) with ΔC_p = 0, -10 and -20 $J.mol^{-1}.K^{-1}$ respectively. Curve d was calculated from Eq. (1.30). The other curves represent the measured values of ΔG from JANAF tables [1.51] and Takahashi and Yoshio [1.73]. The temperature range of observable internal nucleation in LS_2 glass is also shown.

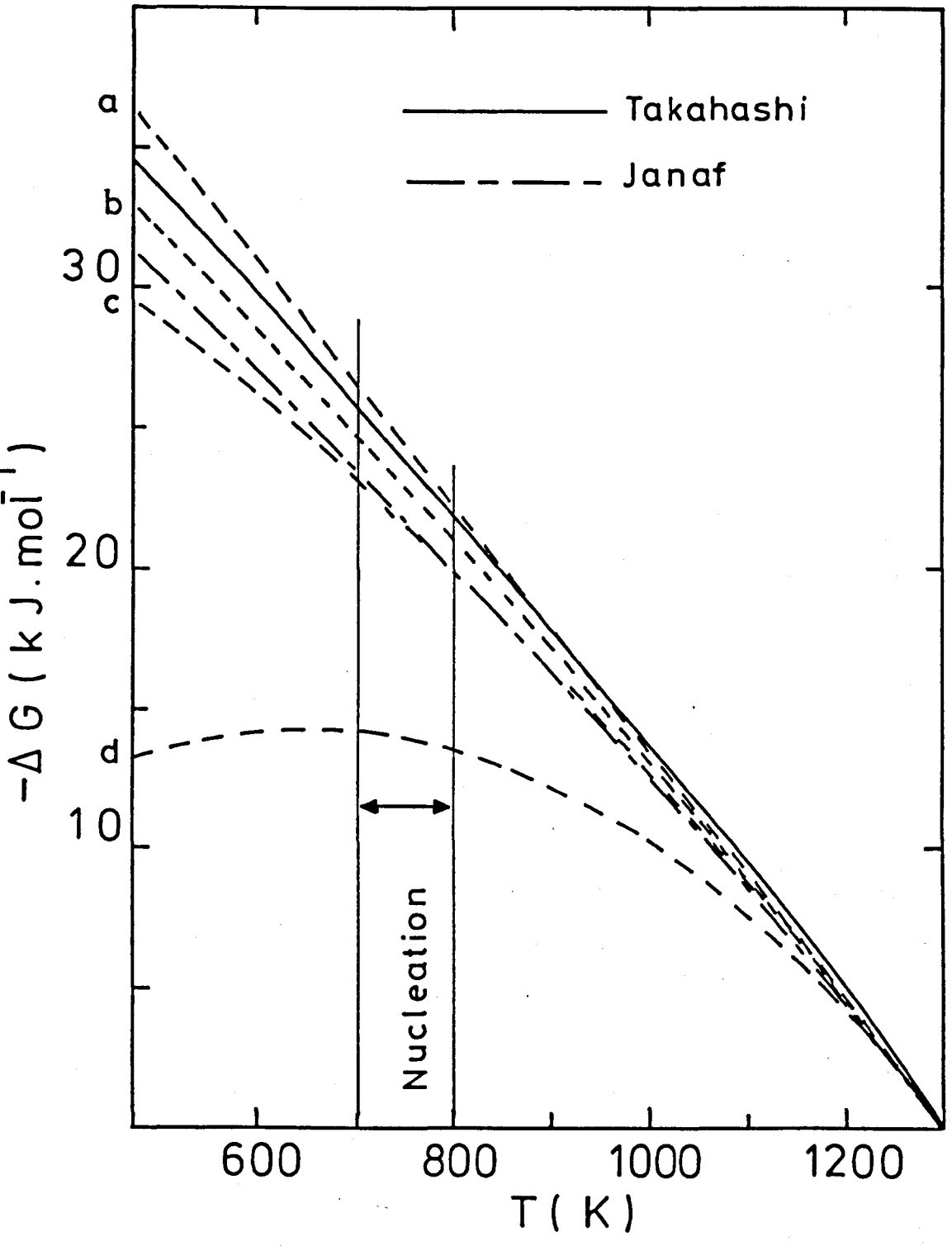
a
b
30
c
20
d
10
Takahashi
Janaf
Nucleation
600
800
1000
1200
T (K)
-Δ G (k J . mol⁻¹)

1.3.1.1b Two component systems

The thermodynamic driving force for binary or higher order systems have been discussed in [1.47, 1.53, 1.63, 2.54] and other references. Consider a schematic free energy-composition diagram for a two-phase system, e.g. a phase separating system, at a temperature where the equilibrium compositions of the phases are a and b (Figure 1.5 a). First consider the case where the initial composition is at x and a small region of the equilibrium composition b separates out. It can be shown [1.44] that, neglecting interfacial effects, the free energy decrease per mole of precipitating phase is given graphically by the distance DE, which is the height above the free energy curve at composition b of the tangent drawn to the curve at the initial composition x. This is the overall driving force for separation of the equilibrium phase. For a small region (or fluctuation) of composition d to separate, the driving force is again the difference between the tangent and the free energy curve at d. However, now there is an increase in free energy (ΔG). Clearly a fluctuation must exceed the composition e before the free energy will decrease and the driving force is favourable. There is thus a thermodynamic barrier to overcome before precipitation (or phase separation) will occur. If x lies between a and the point of inflexion on the curve the system is *metastable* to infinitesimal compositional fluctuations. This corresponds to the region between the binodal and spinodal curves (Figure 1.5b) often referred to as the region of nucleation and growth. If x lies just to the right of the inflexion point (at d for example) for a small fluctuation, ΔG is negative and there is no barrier for separation other than that of diffusion. This process is spinodal decomposition (see section 1.2.3). Although the above discussion refers to phase separation, the same principle applies for crystallization and will be shown below.

Fig. 1.5a Schematic free energy-composition diagram for $T < T_c$ showing graphical method of determining the thermodynamic driving force for amorphous phase separation.

Fig. 1.5b Schematic miscibility gap with the nucleation and growth (shaded area) and spinodal regions.

Fig. 1.6 Schematic free energy-composition diagram for a simple binary system at a temperature below the melting points of the crystalline phases α and β, showing graphical determination of the thermodynamic driving force $\Delta G(=DE)$ for crystallization of the equilibrium phase α from the liquid (L) composition at X.

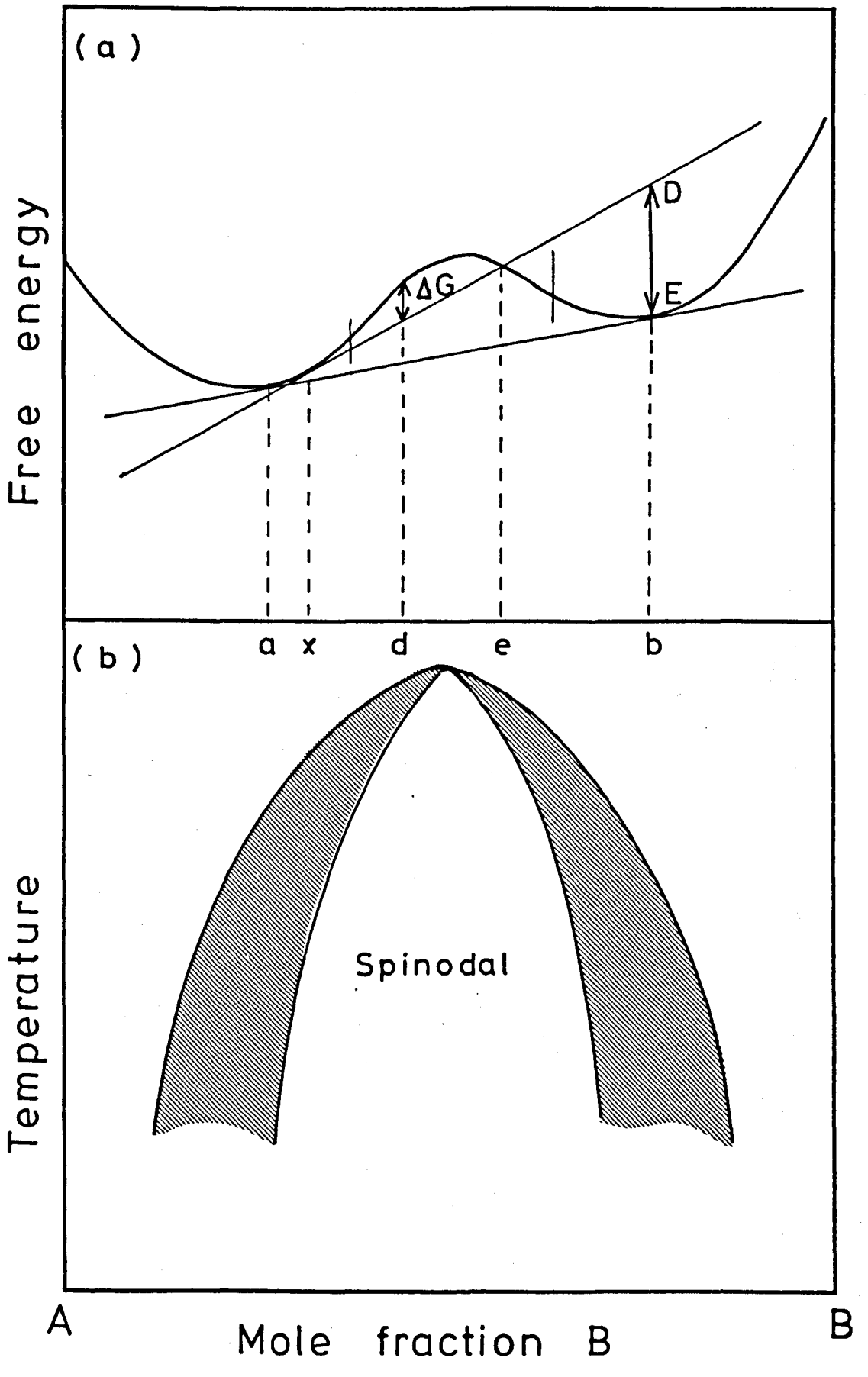
(a)
Free energy
ΔG
D
E
a
x
d
e
b
(b)
Temperature
Spinodal
A
B
Mole fraction B

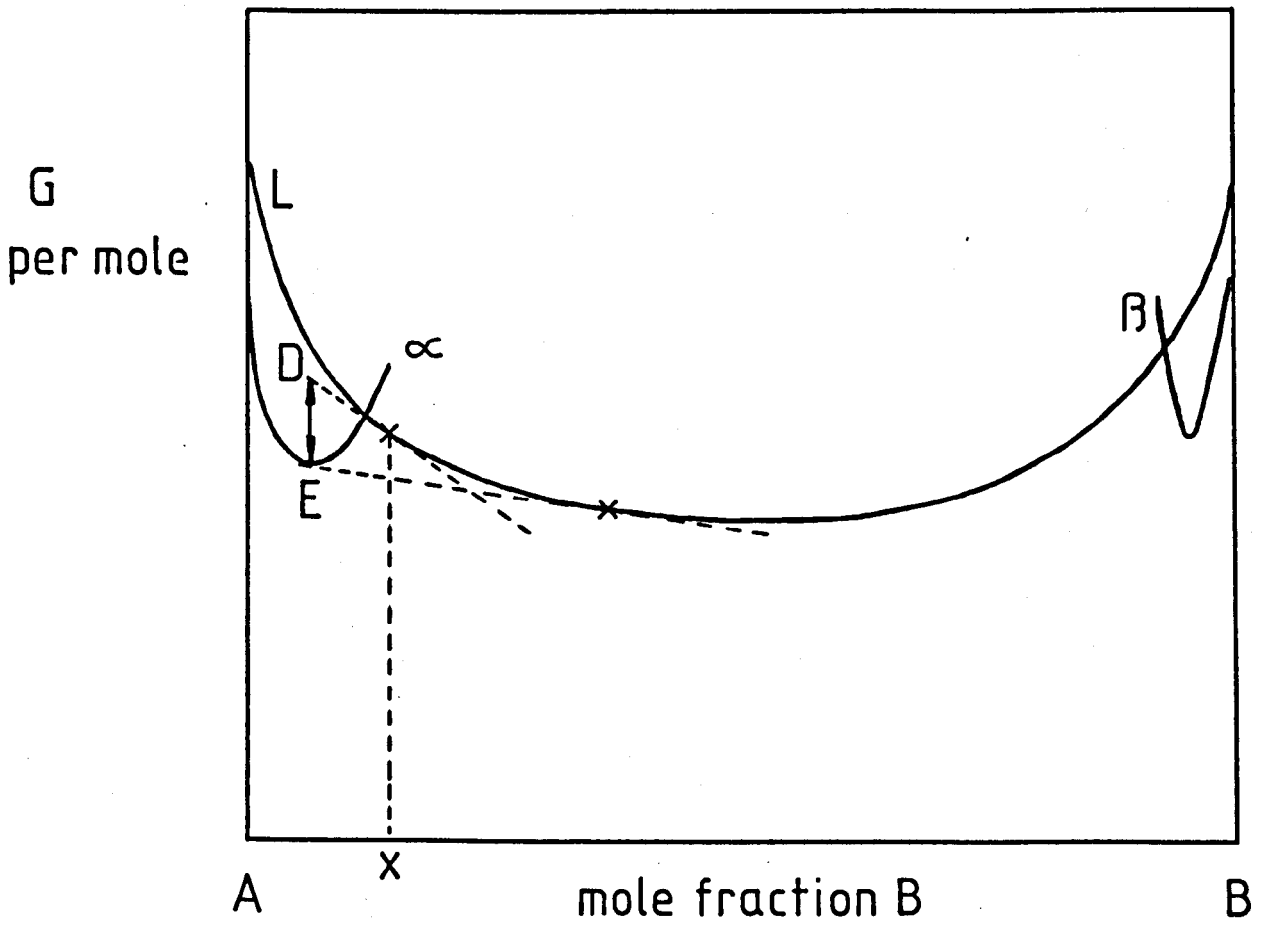
G
per mole
L
D
E
∝
β
A
X
mole fraction B
B

Figure 1.6 shows a schematic free energy composition diagram for a simple system A-B at a temperature below the melting points of the crystalline phases α and β. Suppose the initial composition of the liquid is at x and a small region of the equilibrium phase α is formed. As for phase separation, the free energy decrease per mole of the precipitating phase is given graphically by the distance DE. A tangent is drawn to the liquid-free energy curve at the initial composition x and DE is the height of this tangent above the free energy curve for the crystal phase α at the equilibrium composition of α. Clearly this driving force ΔG (=DE) will have a *maximum* value for an initial liquid composition at or near the equilibrium composition of the phase α, for the simple case shown in Figure 1.6. The situation will be more complex when the solubility of component B in the solid phase α is much greater than shown in the diagram. Then, depending on the shapes of the liquid and crystalline free energy curves it is possible in principle to find situations when the driving force would be greater for the precipitation of a small region of a somewhat different composition from that of the final equilibrium phase. However, the composition of the phase that first precipitates in practice will probably also be governed by other factors including the interfacial energy σ (W^* depends on both ΔG and σ), and the kinetic barrier ΔG_D.

Probably σ will tend to be lower the closer are the compositions of the initial liquid and of the precipitating phase (although this may not be always the case). If in this situation ΔG is also a maximum as in Figure 1.6, then W^* will be a minimum and the nucleation rate I for a given temperature, will tend to have a maximum value. On the other hand, the variation of ΔG_D (or ΔH_D) with composition must be considered and this may also influence the composition of the liquid giving the highest

nucleation rates. The driving force for a crystal phase precipitating out of a phase-separated system is discussed in Chapter 2.

1.3.1.4 The interfacial energy σ

The classical nucleation theory assumes the presence of homogeneous phases, the existence of a sharp interface between the phases and a constant value of σ that is identified as σ_∞, the macroscopic surface energy. The latter assumption may not be justified since σ may vary with the size of the droplet. The theory of Benson and Shuttleworth [1.54] indicates that in the extreme case of a close packed cluster of 13 atoms, σ is 15% less than σ_∞.

A more rigorous treatment of diffuse interfaces by Cahn and Hilliard [1.55,1.56] for nucleation in a two-component system leads to results that are comparable with the classical theory if the supersaturation is small.

It is reasonable to assume that during the crystallization of a glass, surface energy will depend on the crystal plane in contact with the liquid. The faceting of a crystal will be controlled to a large extent by the surface energies of the various planes in contact with the liquid and as a result the shape of the crystal will deviate from a sphere to favour facets of low surface energy. Also, there is no consensus yet about the temperature dependence of σ, although a decrease with temperature was postulated by some authors. This will be fully discussed in Chapter 5.

Up to now, no measurements independent of nucleation studies have been reported for σ, for glass-like liquid/crystal transformations, and one has to accept the existing semi-empirical equations in order to estimate σ. Values of σ were inferred from nucleation experiments with non-ionic liquids and correlated with the heat of fusion by Turnbull [1.57]

$$\sigma = \alpha \Delta H_f / N_0^{1/3} V^{2/3} \qquad (1.31)$$

where N_0 is Avogadro's number, V_m is the molar volume of the crystal and α is a constant being equal to about $\frac{1}{2}$ for metals and $\frac{1}{3}$ for semi-conductors, water and organic substances. On the other hand, Skapski [1.58] has proposed a method for calculating α which is based on the nearest neighbour model of intermolecular forces. This model gives $\alpha \simeq 0.4$ to 0.5 for simple liquids.

1.3.1.5 The kinetic barrier ΔG_D

ΔG_D can be expressed in terms of an effective diffusion coefficient in the liquid given by $D = D_0 \exp(-\Delta G_D/kT)$ where $D_0 = kT\lambda^2/h$, λ being a quantity of the order of the atomic dimensions (jump distance). A number of authors have related D to the viscosity η of the liquid by the Stokes-Einstein relation $D = kT/3\pi\lambda\eta$, obtaining

$$I = \frac{nkT}{3\pi\lambda^3\eta} \exp(-W^*/kt) \qquad (1.32)$$

The uncertainty of the Stokes-Einstein relation is estimated to be, at least, an order of magnitude in absolute terms.

It might be supposed that ΔG_D for nucleation and for growth ($\Delta G_D'$) would be equivalent. However this need not be so, and Turnbull and Cohen [1.59] have pointed out conditions under which D for nucleation should be much *smaller* than that for growth (D'). In particular this should be so for reconstructive crystallization processes in which nuclei must form by changes in first coordination effected by the breaking of covalent bonds. In this case bonds would have to be broken during crystallization, but there are possibilities for catalysis of growth [1.59]

which do not exist for nucleation, so that $D' >> D$. When D' greatly exceeds D, the period during which the nucleation frequency is below its steady-state value can be a substantial part of the transformation time. On the other hand, it is reasonable to suppose that in non-reconstructive crystallization processes both D and D' are near the self-diffusion constant of the undercooled liquid.

1.3.2 Non steady-state nucleation

According to later developments in the theory, the steady-state crystal nucleation rate in a supercooled liquid is not achieved immediately at a constant temperature but only after the elapse of a certain period of time. This period is required to create a equilibrium size distribution of embryos. Most theoretical treatments involve solving the so-called Zeldovich-Frenkel equation. References are given by Gutzow [1.60]. An approximate solution for the transient nucleation rate I' valid for small time t only is

$$I' = I \exp(- \tau/t) \tag{1.33}$$

where τ is an induction time and I the steady-state nucleation rate. Another approximate, but more accurate analytical solution to the problem has been given by Kashchiev [1.61] in the form of an infinite series

$$I' = I\left[1 + 2 \sum_{n=1}^{\infty} (- 1)^n \exp(- n^2 t/\tau) \right] \tag{1.34}$$

where n is an integer. An often more convenient form for comparison with experiment is

$$\frac{N(t)}{I\tau} = \frac{t}{\tau} - \frac{\pi^2}{6} - 2 \sum_{n=1}^{\infty} \frac{(-1)^n}{n^2} \exp(- n^2 t/\tau) \qquad (1.35)$$

where N(t) is the number of nuclei at time t. For $t > 5\tau$ this reduces to the simple equation

$$N(t) = I(t - \pi^2\tau/6) \qquad (1.36)$$

According to Kashchiev [1.61] the induction time for homogeneous nucleation τ is given by

$$\tau = \frac{8kT}{\pi^2 S^* Z \beta^*} \qquad (1.37)$$

where $\beta^* = (\partial^2 \Delta G_n / \partial_n{}^2)_{n=n^*}$, ΔG_n being the Gibbs free energy required to form a cluster of n formula units (* refers to the critical nucleus); S^* is the surface area of the critical nucleus, and Z is the number of formula units that join the critical nucleus per unit time per unit area and can be obtained from

$$Z = \frac{kT}{h\lambda^2} \exp(- \Delta G_D/kt) \qquad (1.38)$$

Here ΔG_D is the activation energy for self-diffusion in the liquid and, for simplicity, is assumed to be the same as the kinetic barrier defined before. It can be shown that [1.62]

$$\tau = \frac{16}{\pi^2} \frac{h\lambda^2\sigma}{V_m{}^2 \Delta G_v{}^2} \exp(+ \Delta G_D/kT) \qquad (1.39)$$

Furthermore, assuming the Stokes-Einstein relation

$$\tau \simeq \frac{48}{\pi} \frac{\sigma\lambda^5\eta}{V_m{}^2 \Delta G_v{}^2} \qquad (1.40)$$

1.3.3 Heterogeneous nucleation

In the case of heterogeneous nucleation the probability of nucleation at certain preferred sites in the assembly is much greater than at other sites. Nucleation can occur on inclusions or solid impurity particles, on the surface of the supercooled liquid, etc. Assuming the existence of p flat rigid substrates per unit volume in the supercooled liquid, let us consider the formation of a spherical cap of radius r of the solid (s) on the substrate (f). At equilibrium the contact angle satisfies; $\cos\theta = (\sigma_{\ell f} - \sigma_{sf})/\sigma_{\ell s}$, where $\sigma_{\ell f}$, σ_{sf} and $\sigma_{\ell s}$ are the interfacial free energies per unit area between liquid-substrate, solid-substrate and liquid-solid respectively. The free energy involved in forming such a cap can be written as

$$W_f = V_{\ell s}\,\Delta G_v + A_{\ell s}\,\sigma_{\ell s} + A_{sf}\,\sigma_{sf} - A_{sf}\,\sigma_{\ell f} \qquad (1.41)$$

where $V_{\ell s} = \pi r^3 \left[\frac{2-3\cos\theta+\cos^3\theta}{3}\right]$; $A_{\ell s} = 2\pi r^2(1-\cos\theta)$ and $A_{sf} = \pi r^2(1-\cos^2\theta)$. The free energy of formation of the critical size nucleus can be calculated by solving $(dW_f/dr)_{r=r^*} \equiv 0$. The critical radius obtained is

$$r^* = -\,2\,\sigma_{\ell s}/\Delta G_v \qquad (1.42)$$

and the work of formation is

$$W_h^* = \frac{16\pi}{3}\,\frac{\sigma_{\ell s}^3}{\Delta G_v^2}\left[\frac{2-3\cos\theta+\cos^3\theta}{4}\right] \qquad (1.43)$$

The function of θ varies from 0 to 1 when θ varies from 0 to π. Therefore, the thermodynamic barrier for nucleation can be much smaller

in the heterogeneous nucleation case. The critical radius remains the same. For $\theta = 0$ there is no thermodynamic barrier to nucleation.

The interfacial energy between s and f can be approximately described as $\sigma_{sf} = \sigma_{sf}^{q} + \sigma_{sf}^{st}$ [1.42]; where σ_{sf}^{q} arises from the chemical interaction between s and f molecules across the interface, and σ_{sf}^{st} corresponds to the elastic strains in s and f and the dislocations at the interface necessary to accommodate the mismatch δ_i between them. The "ideal disregistry" is defined as $\delta_i = \frac{a_f^\circ - a_s^\circ}{a_s^\circ}$ where a_f° and a_s° are the equilibrium atomic spacings of the free substrate (f) and free solid (s) respectively.

The equilibrium number of embryos of radius r is given by

$$N_r = N^h \exp(- W_h(r)/kT) \qquad (1.44)$$

where N^h is the total number of "molecules" of liquid in contact with substrate particles. The number of nuclei produced per unit time is [1.44] $\frac{N^h kT}{h} \exp[- (W_h^* + \Delta G_D)/kT]$. The nucleation rate per unit volume of liquid is obtained if we replace N^h by n_h, where n_h is the total number of "formula units" of liquid in contact with the substrate particles per unit volume of liquid. This number is given by

$$n_h = p\, n^f$$

where n^f is the number of "formula units" of liquid in contact with *one* substrate particle.

1.3.4 Experimental observations of nucleation in glasses

Since the late 1950s hundreds of papers have been published on crystal nucleation in glasses. The predictions of the nucleation theory have been verified, at least in qualitative terms, e.g. the nucleation rate curves are hump shaped and induction periods are observed. A few authors attempted to test in a quantitative way the classical theory and their work will be briefly summarized below. References and information concerning several different aspects of crystal nucleation in glasses can be found in the review papers of Tashiro [2.22], Hammel [2.23,1.64], Hinz [1.65] and James [2.27].

Evidence supporting the view that volume nucleation in lithium disilicate glasses is predominantly *homogeneous* has been obtained by James et al. [1.66]. No major differences in nucleation kinetics were observed in glasses melted under platinum-free conditions and glasses melted in normal conditions. Glasses prepared from ordinary purity batch materials and from very high purity materials also yielded similar results. Burnett and Douglas [1.67] found similar behaviour when studying the nucleation of $BaO.2SiO_2$ crystals in $BaO\text{-}Na_2O\text{-}SiO_2$ glasses melted in different conditions.

The methods of analysing the experimental steady-state nucleation rates were first applied in glass systems by Filipovich and Kalinina [1.68] and Matusita and Tashiro [1.69]. The last authors measured nucleation rates in a $Li_2O.2SiO_2$ glass employing the two stage treatment method. Using equation (1.32), a plot of $\mathrm{Log}(I\eta)$ vs. $1/\Delta G^2T$ was linear. From the slope the crystal liquid interfacial energy σ was found to be 196 $mJ.m^{-2}$. These authors, however, took no account of non-steady state effects. Also they used a rather high development temperature (700°C) which might account for the low values of I obtained when compared with other workers [1.62,1.66,1.70].

Klein et al [1.71] studied the kinetics of crystal nucleation in a $Na_2O.2SiO_2$ glass. Assuming the Johnson-Mehl-Avrami equation, from the times required to reach a volume fraction of 10^{-4} and knowing the crystal growth rates, they deduced the nucleationrates. From a plot based essentially on equation (1.32) they found a σ value of 55 $mJ.m^{-2}$ and a pre-exponential factor of 10^{31} $m^{-3}.Pa$. According to the authors this is in good agreement with that predicted by the classical theory. In their analysis the Hoffman expression (Equation 1.30) was used since ΔC_p data were not available. However, Matusita and Tashiro [1.69] were only able to observe *surface* crystallization in their $Na_2O.2SiO_2$ glass over a wide range of temperatures. Also in this study, two Na_2O-SiO_2 glasses, close to the NS_2 composition, have been melted and given several different double-stage heat treatments. Again, only *surface* nucleation was observed indicating that the results of Klein et al. are probably fortuitous and do not serve as a test of the classical theory.

Rowlands and James [1.72] have discussed various ways of determining the parameters A, ΔG_D and σ in the theory from experimental data. Expressing ΔG_D as $\Delta G_D = \Delta H_D - T\Delta S_D$, where ΔH_D and ΔS_D are the activation enthalpy and activation entropy respectively, Equation (1.20) can be written

$$I = A \exp(\Delta S_D/kT) \exp[-(W^* + \Delta H_D)/kT] \qquad (1.45)$$

Assuming that ΔH_D, ΔS_D and σ were constants over the temperature range studied, Equation (1.45) was fitted to the nucleation data of James [1.62] for a LS_2 glass, using published thermodynamic data for ΔG [1.51,1.73]. For one method of analysis the values for ΔH_D and σ were 900 $kJ.mol^{-1}$ and 222 $mJ.m^{-2}$. The pre-exponential factor A cannot be determined using

Equation (1.45) since ΔS_D is unknown. However, A may be estimated by another method in which ΔG_D is derived from viscosity data through Equation (1.32). Using the viscosity data of Matusita and Tashiro [1.69], a plot of $\ln(I\eta/T)$ vs. $1/T\Delta T_x^2$, where ΔT_x is related to ΔG (see Equation (1.27)), gave a straight line for higher temperatures (above the nucleation maximum T_{max}). The slope yielded σ = 190 $mJ.m^{-2}$ in good agreement with a value of 220 $mJ.m^{-2}$ calculated from a model of the solid liquid interface developed by Skapski (Equation (1.31)). The temperature variation of I is well described by Equation (1.32) above T_{max} but not as well at lower temperatures. Furthermore, the experimental value of A, determined from the intercept of the above plot was about 20 orders of magnitude *higher* than the theoretical value of $6.3 \times 10^{41} m^{-3} s^{-1}$ for the $Li_2O.2SiO_2$ glass.

Rowlands and James [1.72] discussed various possible reasons for the above discrepancy, but show that the possibility of heterogeneous nucleation could not explain it. However, the discrepancy could be explained by postulating a temperature dependent interfacial free energy with a small negative interfacial entropy. In this case, it was necessary to express σ in the form $\sigma = 64.0 + 0.109T$ $(mJ.m^{-2})$.

Neilson and Weinberg [1.74] have independently carried out a very similar analysis for LS_2 (using the same experimental data as Rowlands and James) and have reached almost identical conclusions. It should be stressed, however, that the viscosity data and the nucleation data used were obtained from different melts (of same nominal composition, LS_2) and differences in "water" levels or other impurities could have a marked effect in these data.

Nucleation rates for the barium disilicate crystal phase in a glass of the same composition have been measured by Rowlands and James [1.47,1.75].

Analysis of the I vs. T curve using Equation (1.45) gave a σ of 132 $mJ.m^{-2}$, assuming a spherical nucleus. Unlike LS_2, detailed thermodynamic data were not available and ΔG was estimated from the approximate Equation (1.26), using the heat of fusion measured by DTA [1.47]. No viscosity data were available to allow an estimate of A to be made.

Steady-state nucleation rates have been analysed in the $Na_2O.2CaO.3SiO_2$ (NC_2S_3) composition by Gonzalez-Oliver and James [1.53,1.76], using measured viscosity and thermodynamic data (ΔH_f and $\overline{\Delta C_p}$). A plot of $\log(I\eta/T)$ vs. $1/T\Delta G^2$ gave a straight line, the slope indicating a σ of 180 $mJ.m^{-2}$ in good agreement with a value of 193 $mJ.m^{-2}$ obtained from the empirical formula given by Matusita and Tashiro [1.69]. In the analysis, ΔG was calculated from the more accurate Equation (1.28) using the measured values of ΔH_f and $\overline{\Delta C_p}$. From the intercept of the plot the pre-exponential factor A was 49 orders of magnitude *higher* than the theoretical value. The authors observed that this discrepancy should be viewed as tentative since the ΔG for NC_2S_3 was obtained using an average ΔC_p over the temperature range studied. Even a small error in ΔG could produce a large change in A, although the value of σ would be altered only slightly.

Recently, Cranmer et al. [1.77] determined the nucleation frequency of anorthite from the JMA equation (in the same way as Klein et al. [1.71]). The times required to reach a volume fraction of crystallized material of 0.001 were used together with previously measured crystal growth rates in order to obtain I. From the measured viscosity values and by employing the Hoffman expression (Equation 1.30) for ΔG, a test of the classical theory could be made. A plot of $\ln(I\eta)$ vs. $(\Delta T_r^2 T_r^3)^{-1}$ gave a straight line indicating a value of 190 $mJ.m^{-2}$ for σ. The intercept gave an A value of 2×10^{33} $m^{-3}.Pa$, which was considered by the authors to be in good agreement with the value of 10^{30} $m^{-3}.Pa$ expected from classical

nucleation theory. It was concluded that classical theory can be used to describe nucleation in glass-forming silicate systems, and suggested that the nucleation data of James [1.62] on $Li_2O.2SiO_2$ be re-examined. Although the authors mentioned that the presence of many small crystals distributed randomly throughout the bulk of the material was revealed by optical examination (the same statement was given in Klein's paper [1.71]) no experimental evidence was given.

Hammel [1.108] selected a $76SiO_2.13Na_2O.11CaO$ glass composition near the edge of the miscibility gap. Particle size distributions of amorphous droplets were obtained from electron micrographs of heat-treated glass samples. Knowing the number and size of particles in a given size interval and their growth rate, he was able to determine the steady-state nucleation rates between 601°C and 640°C. ΔG_v was estimated at various undercoolings by fitting the Lumsden solution model [1.78] to experimental miscibility gap data. A value of 4.6 $mJ.m^{-2}$ was obtained for σ by measuring the variation of solubility temperature with particle radius. ΔG_D was found from measured particle growth and miscibility gap data, assuming that the diffusion mechanisms involved in nucleation and growth are the same. Fitting these values into Equation (1.20), the calculated nucleation rates were within an order of magnitude of the experimental results. This is a remarkably good agreement but, as pointed out by Hammel, it depends strongly on the assumptions made in calculating ΔG, and does not constitute a definitive test of nucleation theory.

1.3.4.1 Experimental observations in organic liquids and metals

Heady and Cahn [1.79] made a thorough experimental test of classical theory in the C_7H_{14}-C_7F_4 liquid-liquid miscibility gap system. The observed undercoolings for detectable nucleation were much greater than

predicted by theory (~ 4 times) confirming earlier work of Sundquist and Oriani [1.80]. They were unable to explain the discrepancy by simple modifications of the theory or by considering the diffuse nucleus theory of Cahn and Hilliard [1.56] and concluded that their result challenged the basis of the classical theory.

Huang et al. [1.81] studied the homogeneous nucleation in a binary fluid mixture of cyclohexane-methanol. The measured critical supercoolings were in good agreement with the predictions of the Cahn and Hilliard theory, as modified by Sarkies and Frankel [1.82].

Nucleation in metals has also been analyzed in terms of the critical nucleation temperature, e.g. Turnbull [1.57,1.83], by the droplet technique. This is one successful technique used in studying the homogeneous nucleation in a liquid/solid transformation and consists in separating the liquid into small droplets until the number of droplets is greater than the number of impurities present in the total liquid volume. In this way, some of the droplets can nucleate homogeneously.

Turnbull [1.83] studied the solidification of mercury droplets coated with various mercuric salts. Once nucleation had occurred, the droplet solidified almost instantaneously and volume change measurements followed the nucleation process quite accurately. Mercury acetate acted as a substrate for heterogeneous nucleation and droplets given this coating solidified at rates proportional to their surface area, and in good agreement with heterogeneous nucleation theory. However droplets coated with mercuric laurate nucleated homogeneously at rates proportional to the droplet volume. The data obtained gave a value of 10^{48} m^{-3} s^{-1} for A (10^{7} *larger* than predicted). Explanations for this discrepancy included the possibility that the surface energy is temperature dependent and that

the nucleus has a structure which is distorted from the equilibrium structure. Lothe and Pound [1.86] have attributed the 10^7 factor to the free rotation of the crystal nuclei in the liquid. Such rotation would be impossible when the nuclei are attached to a substrate and so the heterogeneous nucleation results of the droplets should give good agreement with theory.

Earlier experiments by Turnbull [1.57] had given good agreement with homogeneous nucleation theory. The results for σ for several metals were of the right magnitude when compared with the few independent values of σ available [1.84].

An quantitative test of solid-solid nucleation theory was performed by Servi and Turnbull [1.85] on a series of Cu-based alloys containing from 1.0-2.7 wt% Co. The temperature dependence of the experimental results were well described by the theory. The surface energy calculated from the slope was 200 $mJ.m^{-2}$ and agreed well with the value calculated by a semi-empirical equation. The 10^{38} intercept was in good agreement with the theoretical estimate of 10^{41}. These results constitute impressive quantitative agreement between theory and experiment. However, the crystal nucleation densities were calculated from a JMA equation and not obtained directly by experiment.

Kirkwood [1.87] conducted an electron microscopic investigation of the homogeneous nucleation of a coherent ordered phase (γ^1 = Ni_3Al) from a disordered Ni-6.55 wt% Al alloy. A minimum supercooling of 65°C was needed for copious homogeneous nucleation. ΔG was calculated from a regular solution model and measured heats of solution, ΔG_ε (the strain term) was determined by a method described in [1.46]. A value of σ = 30 $mJ.m^{-2}$ was obtained from particle coarsening experiments. The calculated undercooling was 63°C, in good agreement with the measured value.

Miyazawa and Pound [1.88] found an A factor 10^6 *greater* than the theoretical value for the homogeneous nucleation of supercooled gallium. This was explained in terms of a temperature dependent interfacial energy.

Another interesting study was carried out by West [1.89] who repeated Kirkwood's work using improved techniques. Precipitate number density of the γ phase in two Ni-Al alloys, containing 6.55 wt% Al and 6.05 wt% Al, was measured as a function of time after direct quenching to different transformation temperatures. Precipitate densities were also measured in specimens up-quenched to the transformation temperature and in specimens held at different solution heat-treatment temperatures before down-quenching to the reaction temperature. In all the specimens, the precipitate densities were measured directly using dark field electron microscopy. Measurements of the nucleation rate at the different transformation temperatures were calculated from the experimental results and compared with the predictions of classical nucleation theory. A large discrepancy was found between the experimental values and theory (A was 10^7 *lower* than predicted) which could not be attributed entirely to inaccuracies in the thermodynamic data.

In conclusion, it is clear that direct measurements of nucleation rates are important if quantitative comparison with theory is to be made. These are most easily done in glass systems due to their high viscosities. On the other hand, there is much controversy about the validity of the classical theory and more work is needed to clarify the subject. The assumption in theory that the properties of embryos are the same as those of the bulk phase, however, is extremely unlikely because (a) even in a stable phase the energy of small groups of atoms deviates considerably from the mean, (b) atomic configurations that minimize the interfacial energy probably exist in embryos, whereas in the bulk phase surface effects

are negligible and the surface energy plays no part in determining the atomic configuration, (c) the interfacial energies derived from bulk samples generally refer to interfaces that are plane or nearly so, and in using these values for nucleation calculations it is assumed that σ is independent of the radius of curvature, an assumption that is not expected to hold at small radii.

1.4 Crystal Growth in Supercooled Liquids

Once a stable nucleus has formed the growth of the crystal proceeds by incorporating atomic species from the supercooled liquid. Again the free energy difference between liquid and crystal drives the transformation. Also an activation energy $\Delta G_D'$ (in general different from ΔG_D for nucleation) for an atom or growth unit to cross the liquid/solid interface has to be considered. As no specific experiment to test crystal growth mechanisms and theories has been undertaken in this thesis and excellent reviews are available, e.g. Uhlmann [1.90], Kirkpatrick [1.91] and Gutzow [1.92], only a brief summary of the present theories will be given.

The rate-controlling process may be diffusion in the melt, heat flow, or the reaction at the crystal melt interface. Diffusion or heat flow controlled growth generally leads to a cellular morphology. For most silicates, interface-controlled growth leads to a faceted morphology. If the rate-controlling process is interface reaction, the mechanisms at the interface may be either continuous, with molecular attachment occurring at all points on the crystal surface, or lateral, with attachment occurring only on steps of the surface. The mechanism actually occurring can be determined by the dependence upon undercooling of the growth rate corrected for the viscosity of the melt. The nature of the interface can be

described in terms of the interface roughness, which may be considered to be the topographic relief of the surface. Materials with small latent heats of fusion, such as quartz, should have molecularly rough interfaces and grow with a non-faceted morphology, while materials with large latent heats, such as most other silicates, should have smooth interfaces and grow with a faceted morphology.

1.4.1 Rate-controlling processes for crystal growth

The rate at which crystals grow can be controlled by any of the three factors: diffusion in the melt (either long or short range), flow of latent heat away from the growing crystal surface or reactions at the crystal-melt interface.

If controlled by long-range diffusion, the growth rate U of a flat interface is given by Christian [1.44] as

$$U = K(D/t)^{1/2} \qquad (1.46)$$

where K is a constant involving concentration terms and D the diffusion coefficient of the rate-controlling species in the liquid.

Short-range diffusion can affect growth by causing the crystal to break up into a cellular morphology. In this case U is independent of time [1.94].

The interface generally has a cellular morphology if flow of latent heat is the rate-controlling process. As with diffusion-induced instability, the rates are generally independent of time [1.95].

If the reaction at the crystal-liquid interface is the slowest step in the growth process, U is also independent of time [1.96,1.97].

1.4.1.1 Theory of interface-controlled growth

The general theory for the rate of interface-controlled growth was developed by Volmer and Marder in 1931 [1.98] and Turnbull and Cohen in 1960 [1.99]. The final equation can be written as

$$U = f\, a_0\, \nu \exp(-\Delta G_D'/kT)\,[1 - \exp(-\Delta G/kT)] \qquad (1.47)$$

where the activation energy for diffusion across the boundary $\Delta G_D'$ is generally different from ΔG_D for nucleation, f is the fraction of sites of the crystal surface available for attachment, ν the vibrational frequency and a_0 the thickness per molecular layer.

At small undercoolings, Equation (1.47) may be expanded to give

$$U = f\, a_0\, \nu\, \Delta G/kT \exp(-\Delta G_D'/kT) \qquad (1.48)$$

At greater undercoolings $\Delta G >> kT$, and Equation (1.47) may be approximated by

$$U = f\, a_0\, \nu \exp(-\Delta G_D'/kT) \qquad (1.49)$$

Neglecting pressure effects

$$\Delta G_D' = \Delta H_D' - T\Delta S_D' \qquad (1.50)$$

where $\Delta H_D'$ is the activation enthalpy and $\Delta S_D'$ the activation entropy. Substituting this into Equation (1.49) gives

$$U = f\, a_0\, \nu \exp(\Delta S_D/kT)\,[\exp(-\Delta H_D'/kT)] \qquad (1.51)$$

This formalism appears to describe very well the rates of crystal

growth in most systems. It can be made more predictive by approximating $\Delta G_D'$ by ΔG_η (activation energy for viscous flow) by means of the Stokes-Einstein relation (see section 1.3.1.5). Therefore Equation (1.47) can be written

$$U = f\, kT/3\pi a_0^2 \eta\, [1 - \exp(-\Delta G/kt)] \qquad (1.52)$$

In studying crystal growth it is useful to rewrite Equation (1.52) and to define the reduced growth rate U_r, as

$$U_r = U\eta/[1 - \exp(-\Delta G/kT)] = kT/3\pi a_0^2 f \qquad (1.53)$$

U_r is primarily a measure of the fraction of sites on the crystal surface available for molecular attachment.

This relationship is used to distinguish which mechanism controls the interface reaction, because f has a different temperature dependence for each mechanism.

Mechanisms of interface-controlled growth

The mechanism of growth may be defined as the manner in which atoms or "formula units" attach to the growing crystal surface. Two broad categories can be distinguished according to Jackson et al. [1.100]; lateral and continuous. The continuous mechanism operates when molecules can attach at essentially any site, allowing the interface to advance uniformly. Lateral growth occurs by movement of one-molecule-high step across the crystal surface. Molecules can attach only at that step.

1.4.2 Continuous (or normal) growth

According to [1.101] and [1.102] f is assumed to be temperature independent and large. Therefore plots of U_r vs. ΔT should be straight lines with zero slope, especially at *small undercoolings* where $\Delta G \simeq \Delta H_f \Delta T/T_m$ (Equation (1.26)) and $\Delta H_f \Delta T/T_m << kT$ (valid for many materials). Therefore Equation (1.52) yields

$$U \simeq f\, k/3\pi a_0^2 \eta\, \Delta H_f\, \Delta T/kT_m \qquad (1.54)$$

and

$$U\eta = B\, \Delta T \qquad (1.55)$$

where B is a constant.
Thus, at small undercoolings, plots of $U\eta$ vs. ΔT should be straight lines with positive slopes.

1.4.3 Surface-nucleation mechanism

In the surface-nucleation mechanism (Hillig in 1966 [1.103]; Calvert and Uhlmann in 1972 [1.104]) it is assumed that molecules can attach only at the edges of one-molecule-thick layers on the crystal surface. The growth rate is given by

$$U = B/\eta \exp(-B'/T\Delta T) \qquad (1.56)$$

where B and B' are constants. Thus the reduced growth rate increases approximately exponentially with undercooling. In addition, plots of $\ln(U\eta)$ vs. $1/T\Delta T$ are straight lines with negative slopes.

1.4.4 Screw dislocation mechanism

The screw dislocation model described by Hillig and Turnbull in 1956 [1.105] assumes that screw dislocations emerge from the growing crystal face and cause a perpetual repeating step in the shape of an Archimedean spiral. The fraction of sites available for molecular attachment is given by

$$f \simeq \Delta T/2\pi T_m \tag{1.57}$$

Incorporating Equation (1.57) into the small undercooling approximation for the growth rate, Equation (1.55) yields

$$U\eta = B\ \Delta T^2 \tag{1.58}$$

where B is a constant. Thus near the liquidus, plots of $U\eta$ vs. ΔT^2 should be straight lines with positive slopes.

There are experimental results for various systems confirming all these crystal growth mechanisms. Also, the crystal morphology of all materials so far investigated is that predicted by Jackson's theory [1.106], i.e. materials with small entropies of fusion have a non-faceted morphology, and materials with large entropies of fusion have faceted morphology. Full lists of references are given in the reviews mentioned above [1.90,1.91,1.92].

Of special interest is the fact that the experimental growth rates for SiO_2 and GeO_2 are larger by about an order of magnitude than those predicted by the normal growth model using the Stokes-Einstein relation to evaluate ΔG_D° from ΔG_η [1.90]. The similarity of the temperature dependence for the observed and calculated rates, however, is encouraging and indicates that, at least for these "simpler" systems, the processes controlling viscous flow and crystal growth are similar.

Recently, Shkol'nikov [1.107] carried out an analysis of the published data on the growth kinetics of crystals in $M_2O.2SiO_2$ glasses (M = Li, Na and K) and confirmed the screw dislocation model of growth at a wide range of supercooling. The maximum rate of crystal growth occurs at approximately 0.92 T_m and the experimental values for U were shown to be about two orders of magnitude higher than the theoretical values, which in his view was a result of the approximation involved in using the Stokes-Einstein relation.

CHAPTER 2

LITERATURE REVIEW

2.1 The Phase Diagram of $BaO-SiO_2$

The phase diagram of the baria-silica system is given by Roth and Levin [2.1]. They also discovered the polymorphic transformation of $BaO.2SiO_2$ (BS_2) taking place at 1350°C. The orthorhombic structure of the low temperature form ℓ-BS_2 was deduced by Douglass [2.2]. The high temperature monoclinic form h-BS_2 is described by Katscher et al [2.3]. Full crystal data of all $BaO-SiO_2$ compounds are given by Oehlschlegal [2.4].

Calculations by Charles [2.5] of thermodynamic activities in the $BaO-SiO_2$ system indicated a critical point at 8 mol% BaO and 1600°C. Seward et al. [2.6] determined experimentally the binodal curve with a critical point of 1460°C and 10 mol% BaO, the accuracy being ±1 mol% BaO and 50-100°C. The model of Haller et al. [2.7], assuming regular mixing between $BaO.2SiO_2$ and $(SiO_2)_8$ "multimers", can be fitted to the data of Seward et al. very successfully.

In Figure 2.1 the phase diagram with the metastable miscibility gap is shown together with the experimental points of Ramsden [2.54] who used the "clearing" technique, and the experimental results obtained by SAXS in this work (⊣). The spinodal region calculated by Haller et al. [2.7] is also depicted.

2.2 Crystallization of Baria-Silica Glasses

MacDowell [2.8] has shown that for glasses in the composition range $BaO.2SiO_2$ to $2BaO.3SiO_2$ internal crystal nucleation occurs without deliberate addition of nucleating agents. A spherulite to lath transformation was

Fig. 2.1 Phase diagram of the $BaO-SiO_2$ system showing the metastable miscibility gap. The solid line represents the binodal boundary and the dash-dotted line represents the spinodal calculated by Haller al. [2.7]. The experimental points for the binodal are from: O Seward et al. [2.6]; □ Ramsden [2.54] and — this work. The filled circles indicate the heat treatments used here.

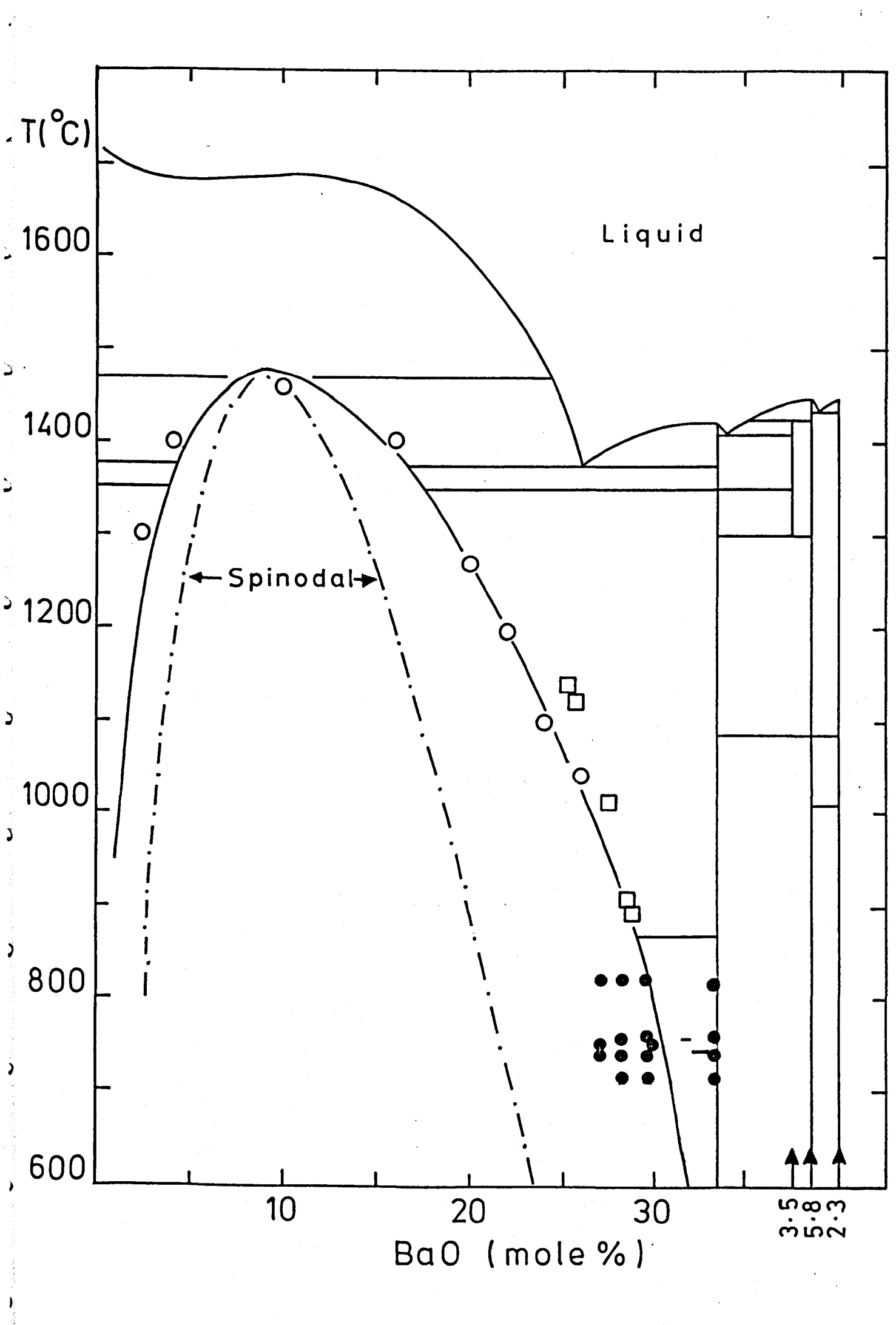
T(°C)
1600
1400
1200
1000
800
600
Liquid
Spinodal
10
20
30
BaO (mole %)
3·5
5·8
2·3

detected at 975°C by DTA, although X-ray diffraction (XRD) did not indicate any change in phase.

Rowlands [1.47] confirmed the observations of MacDowell. Rowlands also measured crystal nucleation rates for a BS_2 composition and showed that internal nucleation of $Li_2O.2SiO_2$(LS_2) or BS_2 occurred in several compositions of the $Li_2O.2SiO_2$-$BaO.2SiO_2$ eutectic subsystem. Crystal growth kinetics (at high undercoolings) in this subsystem were adequately described by Arrhenius plots. Only slight variations of activation enthalpy were found as a function of composition, except near $BaO.2SiO_2$ where a marked increase occurred. This was reflected in a decrease in the growth rates.

Burnett and Douglas [1.67] described the growth of $BaO.2SiO_2$ spherulites in a $70SiO_2.20BaO.10Na_2O$ glass at 600°C. Small spheres of h-BS_2 were first to appear. These nucleated needles of ℓ-BS_2 and the characteristic spherulitic forms began to appear. After a long heating period the spherulite transformed to laths and the remaining h-BS_2 reverted to ℓ-BS_2.

Freiman et al. [2.9] observed similar changes in microstructure from spherulites to laths in a $3BaO.5SiO_2$ glass. The transformation was accompanied by sharp changes in the electrical resistivity and heat evolution. A review of spherulitic crystallization was also given.

Oehlschlegal [2.4] reported a four stage crystallization process consisting of: 1) classical nucleation, 2) spherulitic growth, 3) crystallization of h-BS_2 and 4) $3BaO.5SiO_2$ decomposes to ℓ-BS_2 and ℓ-B_5S_8. For $BaO.2SiO_2$ glass, stage 3 represented the conversion of high to low BS_2.

Lewis and Smith [2.10] studied the spherulitic growth in BaO-SiO_2 glasses in detail by electron microscopy and electron diffraction. They demonstrated that spherulites formed at 700°C (close to T_g) consisted of fibrilar (~ 100 Å in diameter) monoclinic crystals (h-BS_2) in confocal arrangement with preferred crystallographic growth axes. High temperature

(900°) spherulites were composites of radially oriented plate-shaped orthorhombic crystals (ℓ-BS_2) with lateral growth of epitaxially nucleated fibrillar monoclinic crystals. At intermediate temperatures "axialites" consisting of a single orthorhombic crystal with monoclinic fibrillar side-growths, grew in competition with the low temperature morphology.

Ramsden [2.54] reached very similar conclusions in his independent study. Ramsden has also studied the kinetics of crystal nucleation in several glasses inside and outside the miscibility gap of the system. His experiments and conclusions will be thoroughly discussed in sections 2.5.1 and 2.6.

James and Rowlands [1.75] determined the nucleation rates of a $BaO.2SiO_2$ glass from 662 to 780°C. Equation 1.45 was fitted to the experimental data, and assuming a spherical nucleus and the known heat of fusion, σ was found to be 132 m J. m^{-2} and ΔH_D was 741 $kJ.mol^{-1}$

As far as this author is aware these are the only studies on crystallization in $BaO-SiO_2$ glasses made so far. In Table 2.1 several physical properties, collected from the literature, are presented.

2.3 The Phase Diagram of Li_2O-SiO_2

The phase diagram of the lithia-silica system was determined by Kracek [2.11]. The miscibility gap was determined by several authors [2.7,2.12,2.13], and there is a good agreement between the different determinations. Figure 2.2 shows the SiO_2-rich side of the equilibrium phase diagram and the miscibility gap. The model of Haller et al.[2.7] also fits the existing data very well, assuming regular mixing between $Li_2O.2SiO_2$ and $(SiO_2)_6$ "multimers". Crystallographic data for lithium disilicate have been reported by Liebau [2.20] who also described a polymorphic transformation at 936°C.

Fig. 2.2 Phase diagram for the Li_2O-SiO_2 system showing the metastable miscibility gap. The solid line represents the binodal and the dash-dotted line represents the spinodal calculated by Haller et al, [2.7]. The experimental points for the binodal are from: ● Andreev et al. [2.12]; Δ Moriya et al. [2.13] and Haller et al. [2.7]. The smaller filled circles indicate the heat treatments used here. The shaded area represents the range of solid solution formation [2.21].

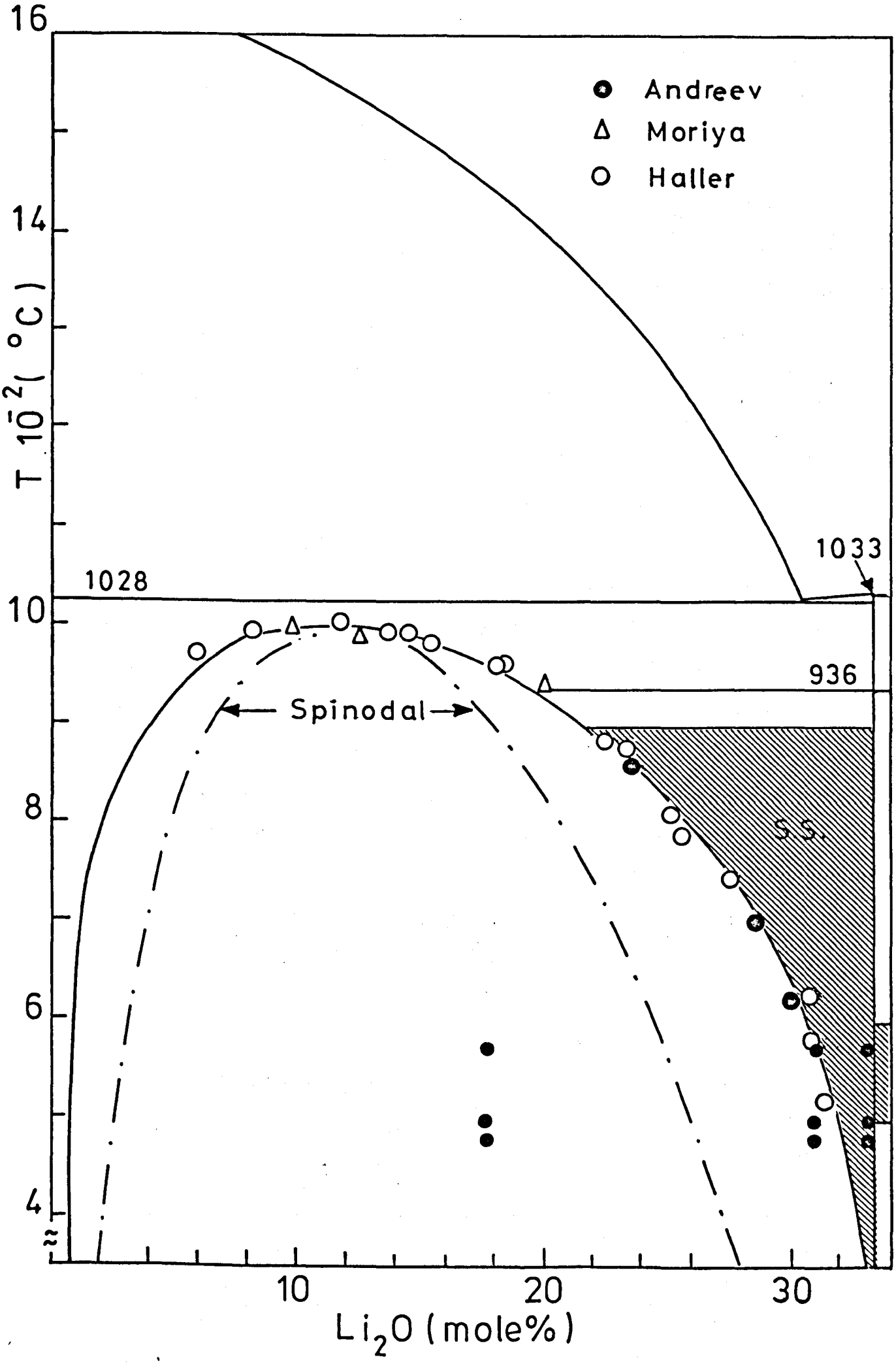
16
14
10
8
6
4
T 10⁻²(°C)
Andreev
Moriya
Haller
1033
1028
936
Spinodal
S.S.
10
20
30
Li₂O (mole%)

2.4 Crystallization of Li_2O-SiO_2 Glasses

In contrast to BaO-SiO_2 glasses, the crystal nucleation and growth of Li_2O-SiO_2 glasses have been extensively studied. Of particular interest to the present work are the quantitative studies of crystal nucleation kinetics, especially the attempts to test the classical nucleation theory and the attempts to correlate the amorphous phase separation with crystal nucleation behaviour. References have already been given in section 1.3.4 and others will be given when discussing the previous work on the relationship between phase separation and crystallization (sections 2.5.1 and 2.6).

The morphological aspects of the growth units have been studied in detail by Tomozawa [2.56], James and Keown [2.1] and Lewis et al. [2.15]. It was conclusively shown that the lithium disilicate (LS_2) crystals consisted of faceted single crystal plates containing a high defect concentration. New branches formed on most of the crystals, probably by a twinning mechanism. The regular nature of the branching explained the morphology of crystallization after prolonged growth (clusters of single crystals). It was also shown [2.16,2.33,2.55] that the liquid droplets did not interfere with the growing crystals, the unchanged droplets remaining embedded within the crystals. Thus evidence for the similarity of the LS_2 clusters to the more complex spherulites in BaO-SiO_2 glasses is lacking.

Kinser and Hench [2.17] studied a $30Li_2O.70SiO_2$ glass during isothermal heat treatment at 500°C with electron microscopy, XRD, and dc and ac electrical measurements and concluded that metastable, crystalline lithium metasilicate (LS) precipitates first and subsequently redissolves ($t > 5$ h) prior to the appearance of the equilibrium LS_2 crystals.

Hench et al. [2.18] also indicated that the LS crystal precedes the equilibrium crystallization in a glass with nominally 33 mol% Li_2O.

Kalinina [2.19] has demonstrated the existence of a enantiotropic

polymorphic transformation of lithium disilicate at about 930°C. The system and unit-cell constants of both low and high-LS_2 were also determined.

West and Glasser [2.21] have made a comprehensive study of crystallization in this system. They demonstrated that the first crystallization product of Li_2O-SiO_2 glasses is a metastable *lithium disilicate solid solution*; its composition ranging from 28 to 38 mol% Li_2O. (Figure 2.2). The solid solution containing 28 to 33.3% Li_2O was formed at temperatures as high as 930°C, although it decomposed rapidly at these temperatures. At lower temperatures, between 500°C and 700°C, the solid solutions persisted indefinitely, but their extent was limited by the binodal boundary. Several structural variants of the silica-rich disilicate solid solutions have been characterized by their X-ray powder diffraction patterns, which exhibit systematic variations in intensities and sharpness of some reflections. Therefore, these results challenged the earlier work of Kinser and Hench [2.17].

Table 2.2 shows several physical properties of LS_2 glass and crystal.

2.5 The Effects of Liquid-Liquid Phase Separation on Crystal Nucleation

It has long been known from phase diagrams that prior liquid-liquid phase separation can have a marked influence on the course of crystallization in a system. Thus liquid unmixing may produce two compositions, one of which has a greater tendency to crystallize than the initial non-separated glass. However, it is also known that liquid phase separation is not always essential to produce internal crystal nucleation in glasses; e.g. $BaO.2SiO_2$, $Li_2O.2SiO_2$, $Na_2O.2CaO.3SiO_2$ and other glass compositions do

Table 2.1

PHYSICAL PROPERTIES OF GLASSY AND CRYSTALLINE BS_2

	Glass	ℓ-BS_2 (ort.)	h-BS_2 (mon.)
ρ ($kg.m^{-1}$)	3740	3770	3730
α ($°C^{-1}$)	91.7×10^{-7}	126.3×10^{-7}	-
V_m ($m^3.mol^{-1}$)	73.14×10^{-6}	72.56×10^{-6}	73.34×10^{-6}
M.W ($kg.mol^{-1}$)	-	273.54×10^{3}	273.54×10^{3}
T_m (°C)	-	-	1420
ΔH_f ($kJ.mol^{-1}$)	-	-	37.0 ±1.0
ΔH_c ($kJ.mol^{-1}$)	-	-	32.0 ±2.0

Table 2.2

PHYSICAL PROPERTIES OF GLASSY AND CRYSTALLINE LS_2

	Glass	ℓ-LS_2 (ort.)	h-LS_2 (ort.)
ρ ($kg.m^{-3}$)	2325	2445	-
α ($°C^{-1}$)	120×10^{-7}	-	-
V_m ($m^3.mol^{-1}$)	64.55×10^{-6}	61.38×10^{-6}	-
M.W ($kg.mol^{-1}$)	-	150.08×10^{3}	150.08×10^{3}
T_m (°C)	-	-	1034
ΔH_f ($kJ.mol^{-1}$)	-	-	57.3
ΔH_c ($kJ.mol^{-1}$)	-	-	61 ±4

not show phase separation and still crystallize internally. Also, several glass compositions in the Na_2O-SiO_2, alkali-B_2O_3 and other systems show extensive liquid unmixing and do not crystallize internally. Theoretically, amorphous phase separation (APS) could influence crystal nucleation in several ways but most of the possibilities fall into two main categories associated either with i) the different *compositions* of the separating liquid phases, or with ii) the *interfaces* between the glassy phase. These points have been fully discussed by several authors, including Tashiro [2.22] and Hammel [2.23]. Extensive arguments were presented at a meeting on "The Vitreous State" in 1970, University of Bristol, by Scholes [2.24] Uhlmann [2.25] and Zarzycki [2.26]. Recently, James [2.27] summarized the present state-of-art on the subject. Thus the *compositional changes* resulting from liquid phase separation may affect W* (through ΔG or σ) and ΔG_D. Figure 2.3 illustrates schematically how the thermodynamic driving force ΔG *for crystallization* may depend on whether prior metastable immiscibility occurs or not. In the example shown, which represents the situation at high undercooling below the melting point of the crystal phase α, the driving force for crystal nucleation is *increased* after the occurrence of liquid phase separation for initial parent compositions between a and b, but it is *lowered* after phase separation for initial compositions between b and c. In the parent non-phase separated glass, ΔG exhibits either a maximum or minimum at the spinodal compositions (e and f). The phase separated glass (compositions a and c) has a constant ΔG. (Refer also to section 1.3.1.3). The situation presented in Figure 2.3 is quite likely to be met in practice for glass ceramic systems at high undercoolings below the liquidus.

Liquid phase separation could also result in one of the liquid phases having a lower ΔG_D, i.e. an appreciably higher atomic mobility at large undercoolings than the parent liquid phase, which also could result in an increase

Fig. 2.3 (a) Schematic diagram for the thermodynamic driving force for crystal nucleation as a function of composition, in a system undergoing metastable phase separation

(b) Variation of thermodynamic driving force ΔG with composition for parent non-phase separated glass (solid curve) and for phase separated glass (dotted line).

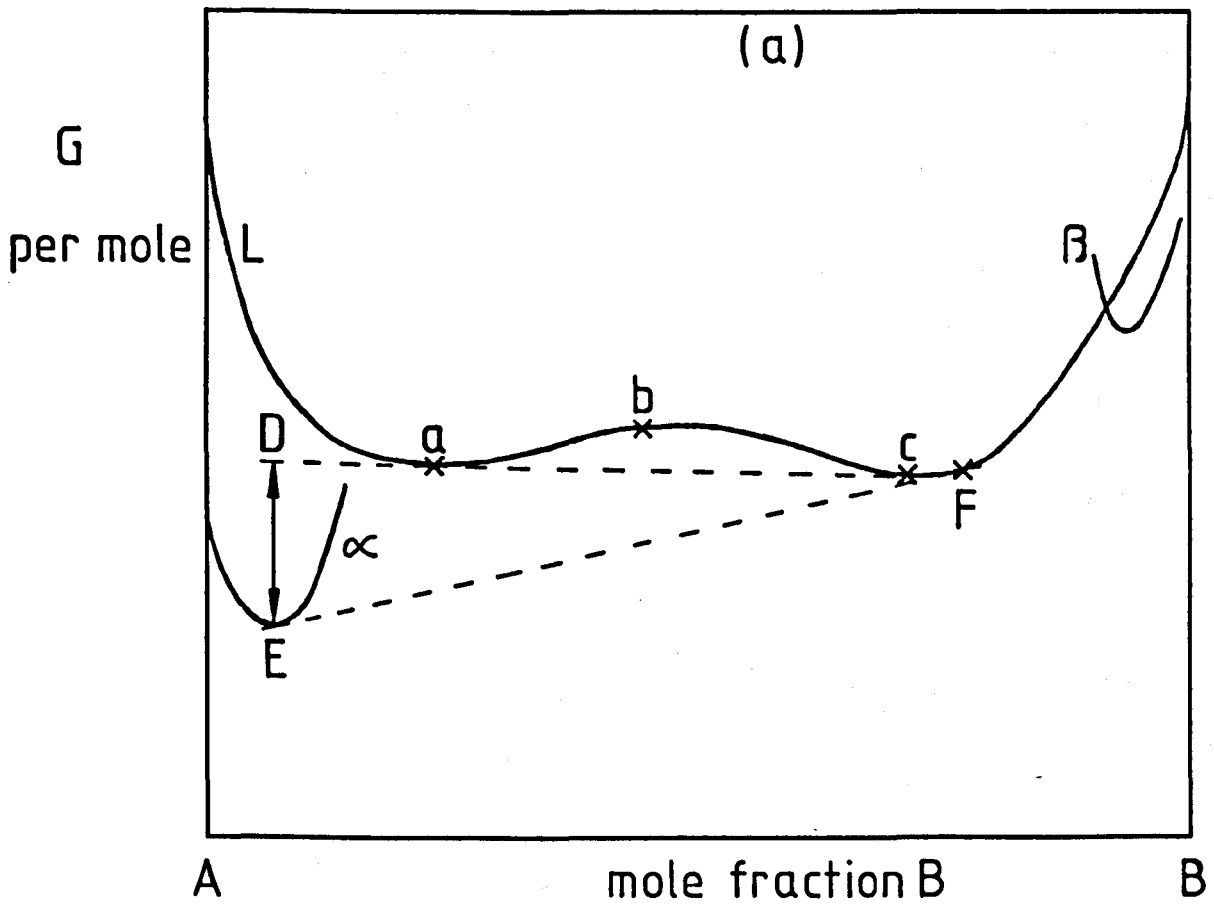
(a)
G
per mole
L
β
b
D
a
c
F
∝
E
A
mole fraction B
B

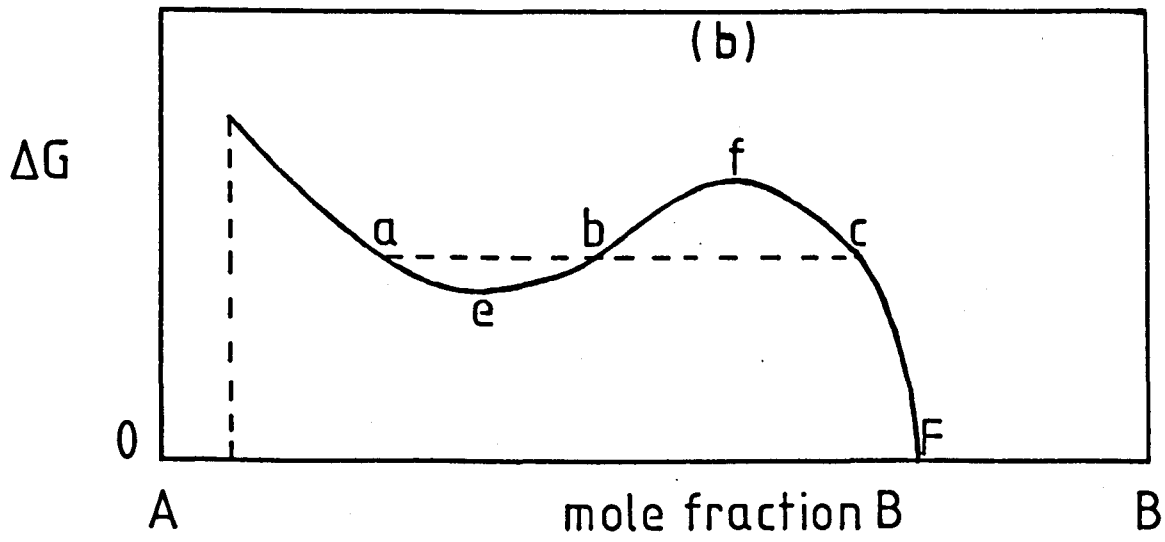
(b)
ΔG
f
a
b
c
e
0
F
A
mole fraction B
B

in the homogeneous crystal nucleation rate. Also,the crystal-liquid interfacial energy σ could be lower for one of the liquid phases than for the parent liquid phase, having an important effect on the nucleation rate of crystals.

The mechanisms for the enhancement of crystal nucleation associated with the *interfaces* between the amorphous phases could be of various types: i) "Direct" heterogeneous crystal nucleation at the interfaces; ii) an enrichment of some component, perhaps a "nucleating agent", at the boundaries between the amorphous phases causing a locally higher ΔG or atomic mobility or even a lower interfacial energy. It has been further suggested that a sparingly soluble component might crystallize out at the interface and promote heterogeneous nucleation in the bulk of the glass [2.24], (iii) Another possible mechanism suggested by Tomozawa [2.28] is preferential nucleation in the diffusion zones around liquid phase droplets. This will be discussed later.

2.5.1 Experimental observations of the effects of amorphous phase separation on crystal nucleation

There is a plethora of experimental studies on the relationships between phase separation and crystallization (especially on nucleation) but only a number of the most important will be discussed.

In earlier studies some authors have suggested that the heat treatment for crystal nucleation was principally a treatment to induce phase separation, and that "nucleating" agents such as TiO_2, ZrO_2 and P_2O_5 were components to enhance the phase separation tendency [1.15].

In a review on catalyzed crystallization of glass in 1959, Stookey [2.29] suggested that liquid phase separation could help subsequent crystal-

lization because homogeneous nucleation could occur in one of the separated amorphous phases.

The work of Vogel and co-authors [2.30,2.31,2.32,2.33] has included qualitative studies of crystallization in phase separating glasses of the following systems: Li_2O-SiO_2, LiF-BeF_2, MgO-P_2O_5 and more complex compositions.

Excellent electron micrographs showed crystals growing in the amorphous matrix *or* within the droplets (Figures 9 and 10 in [2.32] and Figures 182, 183, 184 and 185 in [2.33]). Vogel [2.33] also stated that Figures 110 and 111 in his paper "show clearly that crystallization begins with the granular formations ($Li_2Si_2O_5$ spherulites) at *the periphery* of the larger (amorphous) droplet zones". It should be stressed, however, that in Figures 110 and 111 (TEM micrographs of a $20Li_2O.80SiO_2$ (mol%) glass heated for 1 hour at 580°C and 1 hour at 650°C, respectively) the crystallization front just advances into the two-phase glass by-passing the undisturbed amorphous droplets. Therefore there is no evidence that crystal nucleation *started* on the interfaces of the droplets.

Ohlberg et al. [2.34] studied MgO-Al_2O_3-SiO_2-TiO_2, Li_2O-CaO-SiO_2-TiO_2 and Li_2O-MgO-Al_2O_3-SiO_2 glasses. They concluded that internal crystal nucleation was the result of amorphous phase separation in the three cases. In the first glass, the amorphous droplets formed spontaneously on cooling and, on heating, they reached 500 Å before crystallization occurred. In the second glass droplets having 2000 to 4000 Å in diameter also formed on cooling. During heat treatment, crystal growth in the matrix was apparently initiated at the droplet-matrix interface. In the third system, droplets as large as 60 μm were formed by heat treatment. Again, crystal growth could be detected at the amorphous droplets-matrix interface.

Maurer [2.35,2.36] made light scattering studies on a SiO_2-MgO-Al_2O_3-TiO_2 glass heat treated at different temperatures and found that the scattering centres became increasingly anisotropic. This was interpreted as a crystallization of amorphous droplets.

Kalinina et al. [2.37] studied the crystallization of Li_2O-SiO_2 glasses within the composition range 20.0-30.3 mol% Li_2O by DTA and XRD. A small amount of lithium metasilicate, and lithium disilicate were detected at 480-630°C. At 900-960°C,cristobalite and one strong trydimite line appeared. It was suggested that crystal nucleation started in the amorphous phase, although no specific experiment to test this hypothesis was undertaken.

Buzhinskii et al. [2.38], in a study of physical properties of glasses in the Li_2O-Al_2O_3-SiO_2 (TiO_2,Fe_2O_3) system, suggested that the glasses separated into two amorphous phases with formation of minute droplets having the composition of the crystals which subsequently deposited. Again, no direct experiment was performed to test this hypothesis.

The results of Doherty et al. [2.39], who studied the crystallization of Li_2O-Al_2O_3-SiO_2 glasses with and without TiO_2, indicated that TiO_2 was responsible for internal nucleation of β-eucryptite rather than the liquid-liquid immiscibility.

Burnett and Douglas [2.40] in a TEM study of crystallization in Na_2O-BaO-SiO_2 glasses said "the main effect of the liquid unmixing appears to be that of producing two compositions, one of which is more prone to crystallize. In this system no crystallization was observed to be initiated from the liquid-liquid interface; nucleation of the crystallites occurred within the baria-rich phase and at a much lower nucleation density than that of the liquid separation."

Bayer and Hoffmann [2.41], in their study of Na_2O-TiO_2-SiO_2 glasses,

show replica micrographs of needle-shaped crystals on the borders of droplets (Figure 6 in [2.41]), and concluded that in glasses with an unmixing tendency heterogeneous nucleation takes place at the internal interfaces of the droplets. However, it was also mentioned that the droplets showed single crystal patterns of the same phase as the needle-shaped crystals. Therefore, they were not amorphous.

Other systems for which it has been suggested that droplet interfaces initiate crystallization include: fluor-richterite ($Na_2.Ca.Mg_5.Si_8.O_{22}.F_2$) [2.42]; SiO_2-Al_2O_3-CaO-MgO-TiO_2 [2.43], for which it was said "Tout se passe comme si les interfaces des phases vitreauses séparées agissaient comme nucléateurs de la cristallisation du rutile à partir de la phase vitreuse la plus rich en TiO_2. Ce rutile servirait ensuit de nucléateur hétérogène pour la précipitation des alumino-silicats."; and CaO-MgO-P_2O_5-SiO_2-(F) glasses [2.44]. However, conclusive evidence for the effects of phase separation was not presented.

McMillan and co-workers [2.45,2.46,2.47] have studied glasses of the system Li_2O-SiO_2(P_2O_5). They observed that the finest crystals were produced in glasses which contained both P_2O_5 and a phase separated microstructure.

In a later work McMillan [2.48] studied the crystallization of a $30Li_2O.69SiO_2.1P_2O_5$ glass. Specimens were nucleated at 550°C from 0.1 to 6 hours and "developed" at 750°C for 1 hour. Maximum nucleation efficiency was achieved with a duration of 20 minutes at 550°C. There was no simple correlation between this observation and the phase separated microstructure since the number density of phase separated particles and their interfacial area continued to decrease throughout the heat treatment period. This result did not support the idea that phase separated particles (interfaces) provide nucleation sites for subsequent crystallization. To reconcile

these findings with the fact that APS enhance crystal nucleation rates (from earlier work), McMillan [2.48] proposed that after a initial period at the nucleation temperature the number of crystal nuclei decreases because of a coarsening process. Thus, in his opinion, the occurrence of APS in the glass could hinder the coarsening process through an increase of the activation energy of diffusion. Therefore, the beneficial effect of prior phase separation on nucleation density was seen as an indirect one, rather than the direct provision of nucleation sites.

Studying a $Li_2O,2.5SiO_2$ glass, Nakagawa and Izumitani [2.49] observed that the difference in the number of crystals formed in a previously phase separated specimen and in a quenched sample of the same overall composition was negligible. They also found that the maximum nucleation rate of LS_2 crystals was at 480°C while that of amorphous droplets was at 450°C. It was concluded that amorphous phase separation did not influence crystal nucleation. However, later work [1.62,1.68,1.70] has shown that the maximum in crystal nucleation also occurs at about 450-455°C. For a $68SiO_2$, $22.5TiO_2,9.5Li_2O$ glass, micrographs were published (Figures 16b and c in [2.49]) showing crystals of $Li_2O.TiO_2$ around the liquid droplets. These crystals acted as nucleation sites for the main crystal phase.

A very detailed study was carried out by Tomozawa [2.28] who compared the kinetics of amorphous separation for Li_2O-SiO_2 glasses with the nucleation of crystals as a function of temperature and time. The nucleation rate of crystals, I, in a glass outside the immiscibility gap was constant with time, but for glasses that underwent phase separation simultaneously, a temporary but marked increase in I was observed. This increase was attributed to the presence of a diffusion zone (depleted in silica), surrounding the silica-rich droplets, which acted as a favourable site for crystal nucleation by lowering the effective surface energy. Tomozawa

rightly pointed out that these observations could not be explained in terms of the compositional shift of the matrix phase during phase separation. Also, straightforward heterogeneous nucleation did not provide a complete answer since the period of enhanced crystal nucleation at a given temperature did not correspond to the time for a maximum in the interfacial area of the liquid droplets.

A similar study was made recently by Zanotto and Craievich [2.50] using splat cooled glasses and a more rigorous technique for measuring crystal nucleation densities. Although the general conclusions were in agreement with Tomozawa's work, the observed temporary increase in I was much smaller. It was also shown that the crystal nucleation density (N_v) vs. time curve for glass specimens previously phase separated at 500°C and then nucleated at 475°C was different from that for as-quenched specimens nucleated at 475°C. These results, therefore, did not agree with those of Nakagawa and Izumitani [2.49]. As the crystal nucleation rates in phase separating glasses were about 2 times higher than that in a stoichiometric LS_2 glass, the effect of APS on crystal nucleation could not be explained in terms of compositional shifts and nucleation associated to the amorphous droplet-matrix interfaces was assumed. The increase in crystal nucleation rates, however, was very small if compared with the 5-6 orders of magnitude increase reported for the incorporation of 3 mol% P_2O_5 in a LS_2 glass [2.51].

Matusita and Tashiro [2.51] determined the effect of a series of oxide additives on the crystal nucleation and growth of a Li_2O-$2SiO_2$ glass. They showed that changes (decrease) in nucleation rate caused by the additives (except P_2O_5 and V_2O_5) were due to changes (increase) in viscosity. They also suggested that P_2O_5 and V_2O_5 influenced the nucleation kinetics by inducing liquid phase separation.

Matusita et al. [2.52] have also examined the effect of oxide additions

(RO_n) on the crystal nucleation and growth kinetics of $Li_2O.2SiO_2$ crystals in $Li_2O.3SiO_2.RO_n$ glasses. The ratios of the number of nuclei between glasses $Li_2O.3SiO_2.RO_n$ and $Li_2O.2SiO_2.RO_n$ and also the ratios of the crystal growth rates where shown to increase with T_b, the immiscibility temperatures of $Li_2O.3SiO_2.RO_n$ glasses. The results were partly explainable on the basis that liquid immiscibility in the higher T_b glasses produced a liquid phase closer to the $Li_2O.2SiO_2$ composition. However, the ratios of the growth rates between the two glasses were always less than the nucleation rate ratios. From the classical nucleation and growth theories they showed that nucleation rates were *more* sensitive than the growth rates for composition shifts in the matrix produced by phase separation. Thus, the nucleation ratios should be less than the growth ratios. It was suggested that the nucleation ratios in the phase separated glasses were higher than expected because crystals nucleated at or near the interfaces between the two glassy phases.

Hautojärvi et al. [2.53] studied Li_2O-SiO_2 glasses with positron lifetime, annihilation line-shape and electron microscopy. They showed that phase separation increased the numbers of crystals and the rate of volume crystallization.

Another very extensive study was carried out by Ramsden [2.54]. He studied the nucleation kinetics of the barium disilicate crystal phase (BS_2) for glass compositions in the range 25 to 34 mol% baria. Although he could not readily compare the nucleation kinetics of the several glass compositions because his glasses had different degrees of the main impurities, i.e. Al_2O_3 (0.02 to 0.48 mol%) and up to 1 mol% SrO, an elegant experiment was devised. Three sets of specimens from a glass with 25.3 mol% BaO were prepared as follows: Glass A was rapidly cooled in air. Glass B was heated

at 800°C for 1 hour. Glass C was heated at 900°C for 10 min (the number and size of the SiO_2-rich droplets were completely different in the three glasses). Then, all the glasses were nucleated at 700°C ($T_g \simeq 695$°C for the BS_2 glass) for various times and grown at 840°C, so the crystals could be observed in an optical microscope. The effects of the different heat treatments prior to the crystal nucleation treatments were striking (any nucleation produced in the prior treatments was negligible in comparison to crystal nucleation at 700°C (where the maximum in crystal nucleation rate is observed for the stoichiometric BS_2 glass). Crystal nucleation was higher in glass B when compared with C (and A). This was attributed to the greater degree of phase separation initially present in B, and hence to the significant shift in matrix composition that had already occurred in this glass. Estimations of the interfacial area per unit volume of the phase separated glass using replica electron microscopy showed that this quantity changed only very slowly at 700°C for A, B and C. However, the crystal nucleation rates changed considerably with time at 700°C indicating that the interfacial area was *not* affecting crystal nucleation directly. Also the number of droplets per unit volume in glass A was about ten times greater than in glass C, but initially A had a crystal nucleation rate less than (but similar to) C. It was concluded that the morphology of the phase separation had little or no influence on crystal nucleation and that the effects observed were due predominantly to the progressive shift in composition of the matrix (baria-rich) phase as result of phase separation.

To conclude this section, it seems that the use of complex compositions, especially when "nucleating agents" are present, can lead to great difficulties in interpreting relationships between APS and crystal nucleation. The use of "simpler" systems such as Li_2O-SiO_2 and BaO-SiO_2 allow more

reliable conclusions to be made. At present, there is growing evidence that *enhanced* crystal nucleation can be obtained for glasses undergoing phase separation. In the Li_2O-SiO_2 system the phenomenon can be tentatively explained by nucleation related to the interfaces of the amorphous phases. In the BaO-SiO_2 system it can be explained by compositional shifts.

Therefore, one of the main objectives of this thesis is to study in a quantitative way the kinetics of amorphous phase separation and crystal nucleation in BaO-SiO_2 glasses, with well characterized impurity contents, over a wide range of temperatures. This would complement the only work carried out so far by Ramsden [2.54] at one nucleation temperature (700°C). Also, a limited number of experiments (due to the great number of studies already done in this system) on the nucleation kinetics of very pure Li_2O-SiO_2 glasses with compositions inside and outside the miscibility gap could complement the previous studies, especially those of Tomozawa [2.28], Hautojärvi et al. [2.53] and Zanotto and Craievich [2.50]. This study might explain why interfaces are apparently only important in Li_2O-SiO_2 glasses and compositional shifts are important in BaO-SiO_2 glasses.

One further point should be made. The apparent observation, in some cases, of heterogeneous nucleation of crystals on the surface of droplets could imply that crystals prefer to form there. However, there is a possibility that interfaces may migrate during heat treatment, and any relation between the interface and the crystals they nucleate may be lost. Nevertheless, the dependence of the nucleation rate on the parameters describing phase separation morphology would still be retained, and hence it should be possible to study experimentally the importance of interfaces in nucleating crystals.

2.6 The Effects of Liquid-Liquid Phase Separation on Crystal Growth

Phase separation can also affect crystal growth rates. However, experimental studies on the subject have yielded conflicting results. Some authors suggested that "mechanical interference" could occur between the growing crystals and amorphous droplets resulting in an overall decrease in growth rates [1.67,2.47].

Ogura et al. [2.55] determined the growth rates of surface crystals and activation enthalpies (ΔH_D) of a series of Li_2O-SiO_2 glasses (22-40 mol% Li_2O) between 520-640°C. Within the immiscibility dome (glasses having 22-28 mol% Li_2O) the growth rates and activation enthalpies were essentially identical ($\simeq$ 265 kJ.mol^{-1}), but increased with Li_2O content outside the immiscibility dome ($\Delta H_D \simeq$ 298 kJ.mol^{-1} for a glass with 33.2 mol% Li_2O). It was also shown that DTA crystallization peaks appeared at the same temperature for the phase separating glasses and that crystal growth proceeded in the matrix, independently of the existence of dispersed droplets. These results indicate that the liquid immiscibility effect was mainly compositional rather than morphological.

The results of Tomozawa [2.56] for the Li_2O-SiO_2 system showed that as the LS_2 composition was approached ΔH_D increased. Phase separated glasses had a similar ΔH_D ($\simeq$ 226 kJ.mol^{-1}) which was lower than the value of 345 kJ.mol^{-1} found for a glass with 32.5 mol% Li_2O (outside the gap). It was concluded that the shift in matrix composition due to amorphous phase separation had a significant effect on crystal growth behaviour.

Kommpa [2.57] also measured crystal growth rates in two Li_2O-SiO_2 glasses inside the miscibility gap and in one glass just outside the gap. The crystal growth rates were very similar for the three compositions showing that the compositional shifts caused by phase separation have a

marked influence on the growth behaviour of LS_2 crystals. Otherwise, the growth rates would be different due to differences in initial compositions (and viscosity) of the parent glasses. Therefore, the results of [2.55] [2.56] and [2.57] are in agreement, although the absolute values of U and ΔH_D vary somewhat among the three studies.

Ramsden [2.54] made a detailed study of crystal growth behaviour in phase separated and "homogeneous" $BaO-SiO_2$ glasses. He showed that induction periods were caused by a change in growth morphology and crystal form, from spheres (h-BS_2) to rapidly growing needles (ℓ-BS_2) nucleated at the sphere-glass interfaces. The induction time decreased with rise in temperature. Phase separation increased the growth rates due to accompanying shift in composition of the baria-rich phase during heat treatment. This shift also caused an apparent reduction in the measured activation enthalpies for growth in the phase separated glasses. The morphology of the two liquid phases had no influence on crystal growth rates.

Scherer and Uhlmann [2.58],in a detailed study of the surface crystallization kinetics of the metastable phase crystobalite in Na_2O-SiO_2 glasses with 1.5, 10.0 and 15.0 mol% Na_2O,found no significant effect of phase separation on crystal growth kinetics. They suggested that "In this case, the scale of phase separation was smaller than that of the growing crystals and their associated diffusion fields. Under these conditions, the lack of a significant effect of phase separation is not surprising. In other cases, where the scale of phase separation exceeds that of the crystals, a significant effect might be anticipated". This work was later criticized by Tomozawa [1.15],who replotted the data of Scherrer and Uhlmann for the glass containing 10.0 mol% Na_2O as log U vs. 1/T. A kink at 845°C, approximately the same temperature as the immiscibility temperature for that

glass, was clearly observed. Thus, the phase separation did appear to influence the crystal growth rate.

In conclusion, it seems that liquid-liquid immiscibility affects crystal growth mainly by means of compositional shifts in the amorphous matrix.

CHAPTER 3

EXPERIMENTAL TECHNIQUES

3.1 Preparation of Glasses

A wide range (27.0-34.7 mol% BaO) of $BaO-SiO_2$ glasses were prepared from Silquartz SiO_2, Analar grade $BaCO_3$ (Fisons and BDH) and Ultrapure grade $BaCO_3$. Glass 33.3P was made from Optipur SiO_2 (Merck) and Puratronic $BaCO_3$ (Ventron). Batches of 150-250 g were melted in Pt-Rh crucibles in electric furnaces at 1550°C. The melts were poured into water and remelted from four (33.3 and 34.7 mol% BaO) to eight times (27.0 and 28.3 mol% BaO) to ensure homogeneity. A sintering treatment in Pt dishes at 1300°C for 24 hours was given to the batches before the melting procedure. This was necessary to encourage the chemical reaction and to aid melting. Otherwise these glasses were very difficult to homogenize. The melts were finally cast and pressed between two steel plates. Clear samples of 1-2 mm in thickness were obtained in this way. Most of them contained a few small bubbles.

The Li_2O-SiO_2 glasses ranging from 17.7 to 33.7 mol% Li_2O were prepared from Optipur SiO_2 (Merck) and 99.999% Li_2CO_3 (Aldrich). Batches of 70-200 g were melted in new Pt-Rh crucibles at temperatures ranging from 1550°C (17.7 mol% Li_2O) to 1300°C (33.7 mol% Li_2O). The crushing remelting technique was employed to ensure homogeneity. Clear samples of the 17.7 mol% Li_2O glass, approximately 1 mm thick, were obtained by splat cooling the melt using the spring loaded metal piston arrangement shown in Figure 3.1. Melts of the other compositions were pressed in the same way as the $BaO-SiO_2$ glasses.

Specimens for viscosity determinations were cast in graphite cylinders with diameters of 20-30 mm and subsequently transferred to an annealing furnace maintained at 640°C for the $BaO.2SiO_2$ glass and at 400°C for the

Fig. 3.1 Photograph of the splat-cooling device used in this work. The spring loaded piston was released by the trigger while the melt was being poured between the metal plates.

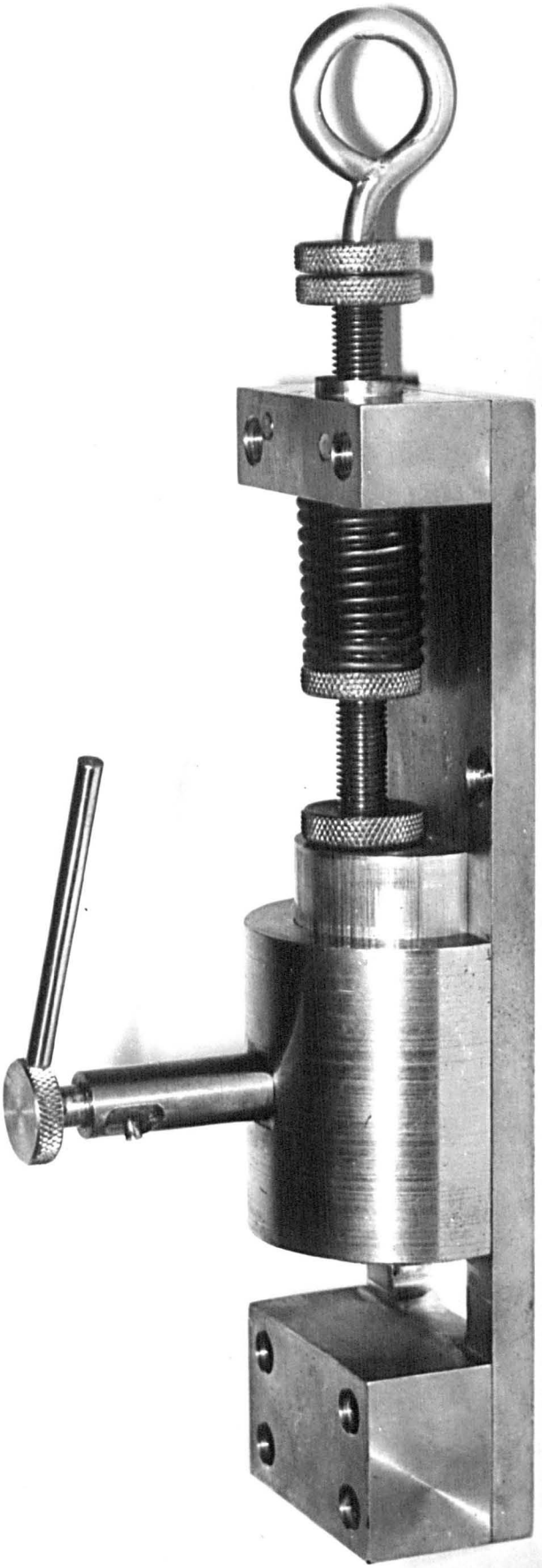

$Li_2O.2SiO_2$ glass. The furnace was then switched off and the specimens allowed to cool overnight. No internal crystallization was observed in these glasses.

The $Na_2O.2SiO_2$ glass was melted at 1350°C for 7 hours, being stirred mechanically with a Pt blade at 50 rev/min during 4 hours. The melt was then pressed between two steel plates.

3.2 Chemical Analysis

3.2.1 $BaO-SiO_2$ glasses

The following elements were analysed in the $BaO-SiO_2$ glasses: Si, Ba, Sr, Ca, Na, K, Li, Fe, Al, Pt and Ti. Different methods were used for each element and some of them were analysed by more than one technique in order to estimate the accuracy of the experimental results. The barium carbonates and silquartz were also analyzed.

Estimates of BaO

Approximately 0.1 g of finely crushed glass was weighed and dissolved in Pt dishes, with 5 ml of 40% HF and 2 ml of 72% $HClO_4$ in a steam bath. After dissolution, the $HClO_4$ was evaporated away on a hot plate and the chemical treatment repeated to remove all traces of Si as SiF_4. The residue (barium perchlorate and impurities) was dissolved in water and transferred to a 250 ml beaker. Barium was precipitated as $BaSO_4$ with 1.5 ml of 2.5% H_2SO_4. The precipitate was digested overnight, filtrated in porcelain filters (grade 4) and ignited at 600°C. The BaO content in the residue was calculated as 0.69659 times the weight of precipitate. The analysis was repeated from four to six times for each glass, and the average and 95% confidence limits calculated. As will be shown later, approximately $^2/_3$ of the Sr, the main impurity present, precipitated together with Ba.

However, this affected the present results hardly at all because the statistical error in most cases was higher than the Sr level. As can be seen in Table 3.1, the agreement of the present results with the nominal content of BaO in the glasses is very good and, in most cases, they also agree with the BaO determinations done at the Federal University of Sao Carlos (UFSCar) and with Electron Probe Micro Analysis (EPMA) results.

Estimates of SiO_2

The percentage of SiO_2 in most glasses was determined gravimetrically at UFSCar and the experimental results are 0-1.5 mol% lower than the nominal contents. The EPMA results for SiO_2 in glasses 33.3A, 28.3A, 33.1U and 29.7H are close to the nominal percentages.

Determination of impurities

The impurity elements were determined by Flame Emission Spectroscopy (FES) and/or Atomic Absorption Spectroscopy (AAS) in dissolved glass solutions which were obtained in the way described above. Some determinations of strontium were made on the filtrate solutions, i.e. after the elimination of the barium ions from the solutions. Glasses 33.3A and 33.1U were also analyzed by EPMA. The Sr and Pt levels in glasses 28.3A and 29.7H were also determined by EPMA.

Estimates of SrO

The SrO level in the glasses and barium carbonates was determined by FES with a digital Pye Unicam SP191 Spectrometer at 460.73 nm, using a nitrous oxide/acetylene flame. An Aldrich 1,006 ppm Sr^{++} standard solution was used as a source for the calibration solutions, which contained from 0.5 to 2 ppm of Sr. In order to eliminate the strong ionization of Sr in the hot flame and inherent instability of the equipment, it was necessary to add to samples and calibration solutions 2,000 ppm of 99.999% CsCl. As Figure 3.2 shows, up to 78% of the Sr atoms can be ionized in the hot flame

Table 3.1

CHEMICAL ANALYSIS OF $BaO-SiO_2$ GLASSES

Glass 27.0 (Fisons $BaCO_3$ - A.R. Grade)

Oxide	Mole % Nominal	Weight % Nominal	Weight % Analyzed
SiO_2	72.308	50.66	-
BaO	27.433	49.04	48.5 ±0.3
SrO	0.237	0.286	0.26
CaO	0.0068	0.0045	0.015
Na_2O	0.0065	0.0047	-
K_2O	0.0070	0.0077	0.027
Al_2O_3	0.0008	0.0010	-
Fe_2O_3	0.0003	0.0006	-

Glass 28.3A (Fisons $BaCO_3$ - A.R. Grade)

Oxide	Mole % Nominal	Weight % Nominal	Weight % Analyzed	
SiO_2	71.407	49.544	48.0 FU	49.25 EP
BaO	28.326	50.144	50.1 ±0.2	49.9 EP
SrO	0.244	0.292	0.27	0.33 EP
CaO	0.007	0.0045	0.034	-
Na_2O	0.0066	0.0047	0.011	-
K_2O	0.0072	0.0078	0.023	-
Al_2O_3	0.0008	0.0009	-	-
Fe_2O_3	0.0003	0.0006	0.0045	-

EP = Electron Probe Microanalysis

FU = Federal University of Sao Carlos

Glass 28.3B (Fisons $BaCO_3$ - A.R. Grade)

Oxide	Mole % Nominal	Weight % Nominal	Analyzed	
SiO_2	71.407	49.544	-	48.5 FU
BaO	28.326	50.144	50.1 ±0.5	50.2 FU
SrO	0.244	0.292	0.27	-
CaO	0.007	0.0045	0.023	-
Na_2O	0.0066	0.0047	0.013	-
K_2O	0.0072	0.0078	0.014	-
Al_2O_3	0.0008	0.0009	-	-
Fe_2O_3	0.0003	0.0006	0.0004	0.068 FU

Glass 29.9 (Fisons $BaCO_3$ - A.R. Grade)

Oxide	Mole % Nominal	Weight % Nominal	Analyzed
SiO_2	69.794	47.603	-
BaO	29.925	52.075	52.1 ±0.3
SrO	0.258	0.303	0.28
CaO	0.0073	0.0046	0.023
Na_2O	0.0067	0.0047	-
K_2O	0.0075	0.0080	0.024
Al_2O_3	0.0008	0.0009	-
Fe_2O_3	0.0003	0.0007	-

Glass 33.3A (Fisons $BaCO_3$ - A.R. Grade)

Oxide	Mole % Nominal	Weight % Nominal	Analyzed		
SiO_2	66.286	43.599	—	44.7-44.1 EP	43.12 FU
BaO	33.402	56.054	56.0 ±0.3	56.15 EP	56.07 FU
SrO	0.288	0.327	0.29	0.33 EP	
CaO	0.0079	0.0048	0.038	0.034 EP	
Na_2O	0.0069	0.0047	0.007	0.12 EP	
K_2O	0.0083	0.0085	0.026	0.021 EP	
Al_2O_3	0.0007	0.0008	-	0.056 EP	
Fe_2O_3	0.0004	0.0007	0.0007	<0.035 EP	

Glass 33.2B (Fisons $BaCO_3$ - A.R. Grade)

Oxide	Mole % Nominal	Weight % Nominal	Analyzed	
SiO_2	66.286	43.599	-	43.51 FU
BaO	33.402	56.054	55.8 ±0.2	56.07 FU
SrO	0.288	0.327	0.30	-
CaO	0.0079	0.0048	0.038	-
Na_2O	0.0069	0.0047	-	-
K_2O	0.0083	0.0085	0.025	-
Al_2O_3	0.0007	0.0008	-	-
Fe_2O_3	0.0004	0.0007	-	0.05 FU

Glass 33.2C (Fisons $BaCO_3$ - A.R. Grade

Oxide	Mole % Nominal	Weight % Nominal	Analyzed
SiO_2	66.286	43.599	-
BaO	33.402	56.054	55.8 ±0.4
SrO	0.288	0.3	-

Glass 33.3P (Ventron $BaCO_3$ - Puratronic Grade)

Oxide	Mole % Nominal	Nominal	Analyzed
BaO	33.33	56.06	56.02 ±0.2
SrO	-	0.0050	0.0043

Glass 33.1U (Ventron $BaCO_3$ - Ultrapure Grade)

Oxide	Mole % Nominal	Weight % Nominal	Analyzed	
SiO_2	66.454	43.755	-	43.87 EP
BaO	33.385	56.085	55.8 ±0.2	55.2 ±0.8 EP
SrO	0.112	0.127	0.13	0.20 EP
CaO	0.0326	0.020	0.022	0.028 EP
Na_2O	0.0110	0.0074	0.012	0.142 EP
K_2O	0.0037	0.0038	0.0094	<0.019 EP
Al_2O_3	0.0007	0.0008	-	<0.018 EP
Fe_2O_3	0.0004	0.0007	0.010	<0.021 EP

Glass 29.7H (BDH $BaCO_3$ - A.R. Grade)

Oxide	Mole % Nominal	Weight % Nominal	Analyzed		
SiO_2	69.762	47.607	-	47.54 EP	47.0 FU
BaO	29.806	51.897	51.8 ±0.2	51.43 EP	51.40 FU
SrO	0.409	0.481	0.54	0.61 EP	0.45 FU
CaO	0.0103	0.0066	0.014	-	-
Na_2O	0.0079	0.0056	0.013	-	-
K_2O	0.003	0.0033	0.012	-	-
Al_2O_3	0.0008	0.0009	-	-	-
Fe_2O_3	0.0004	0.0007	0.0094	-	0.068 FU

Glass 34.7H (BDH $BaCO_3$ - A.R. Grade)

Oxide	Mole % Nominal	Weight % Nominal	Analyzed		
SiO_2	64.895	42.132	-		
BaO	34.605	57.322	57.4 ±0.2	58.9	FU
SrO	0.474	0.531	0.62	-	
CaO	0.0127	0.007	0.030	-	
Na_2O	0.0084	0.0056	-	-	
K_2O	0.0033	0.0034	0.013	-	
Al_2O_3	0.0007	0.0008	-	-	
Fe_2O_3	0.004	0.007	-	0.055	FU

if no CsCl is added. The same figure also shows some results for the ionization of Ca and Ba atoms.

It was rather surprising that all the barium carbonates except one contained more Sr than advertised by the suppliers (Table 3.3b). This could imply that the technique used (FES) overestimated the Sr levels. However, the good agreement with the EPMA determinations for the glasses eliminates this hypothesis. Reproducibility experiments show that the accuracy of the Sr determinations was approximately 10%. The analysis of the filtrate solutions gave much lower percentages of strontium in the glasses (Table 3.2), implying that most of the strontium precipitates together with barium.

Estimates of CaO

The calcium content in the glasses and barium carbonates was determined by FES and AAS, both at 422.67 nm with a N_2O/acetylene flame. The standard 1,000 ppm Ca^{++} solution was supplied by Aldrich Chemical Company. As Figure 3.2 shows, there could be up to 42% ionization in the flame, but 2,000 ppm of CsCl was added to all samples and calibration solutions to eliminate this possibility. According to [3.2] HCl could have some influence on the CaO determination but no effect was found.

The differences between the FES and AAS determinations varied from 60 to 20% and the average of the two determinations is quoted in Table 3.1. The experimental weight percentages of CaO in the glasses are about five times higher than the nominal values.

Estimates of Na_2O

The sodium content of the glasses and carbonates was determined by AAS at 589.0 nm using an air/acetylene flame. The standard 1,000 ppm Na^+ was supplied by Aldrich Chemical Company. The nominal percentages of Na_2O in the glasses are about three times smaller than the AAS results which, in

Table 3.2

STRONTIUM OXIDE LEVELS IN $BaO-SiO_2$ GLASSES (wt%)

Specimen	AAS	EPMA	Filtrate Solution
27.0	0.26	-	0.09
28.3A	0.27	0.33	0.08
29.9	0.28	-	0.10
33.1U	0.13	0.20	0.03
33.3P	0.004	-	0.000
G26*	0.86	1.00	0.30
G30*	0.89	1.03	0.21

* G26and G30 were used by Ramsden [2.54]

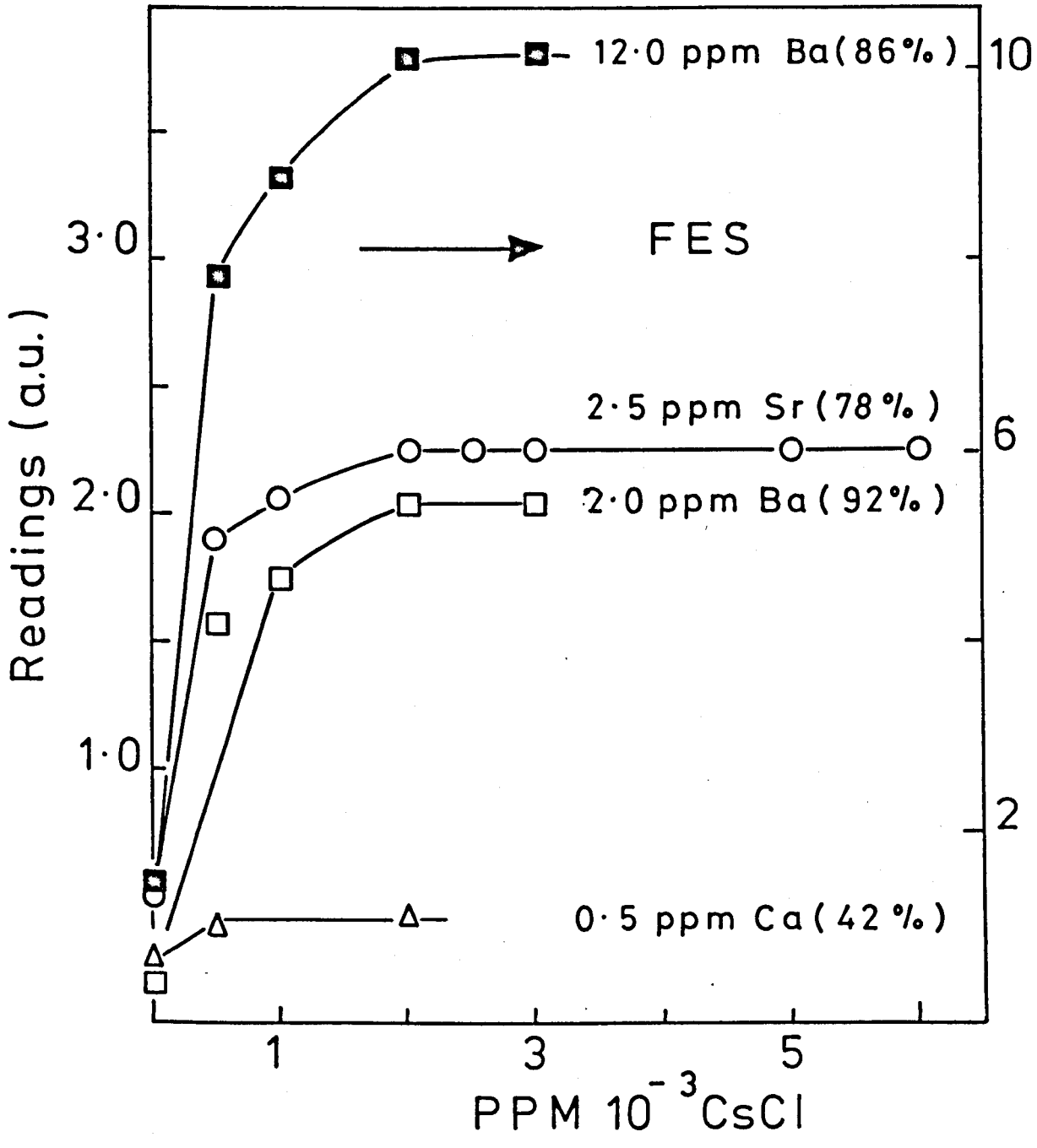

Fig. 3.2 Flame Emission Spectroscopy readings as a function of the amount of CsCl added to some solutions of Calcium, Strontium and Barium.

turn, are about ten times smaller than the EPMA results. The determined percentages of Na_2O in the analar grade barium carbonates (Fisons and BDH) are close to the nominal percentages. They are, however, five to ten times higher than the nominal contents of Na_2O in the Ventron barium carbonates.

Estimates of K_2O

Potassium was determined by AAS at 766.49 nm using an air/acetylene flame. Calibration solutions prepared from an Aldrich 1,000 ppm K^+ standard solution were used to set the equipment. 2,000 ppm of CsCl was added to the solution as an ionization supressor. The experimental results of Table 3.1 show that the calculated (nominal) contents of K_2O in the glasses are two to three times less than the real percentages. The agreement between the AAS and EPMA results is good.

Estimates of Fe_2O_3

Iron oxide was determined by AAS at 248.33 nm using an air/acetylene flame. The standard solution was prepared by dissolving 1.0000 g of iron granules in a solution of 20 cm^3 of 5 M HCl and 5 cm^3 of HNO_3 (s.g. 1.42) and diluting to 1 litre. The experimental results agree well with the nominal Fe_2O_3 content in the barium carbonates (Table 3.3b). The Fe_2O_3 percentage in the glasses is zero to fifteen times higher than the calculated percentages; however, the AAS results agree with the EPMA results. The UFSCar determinations of Fe_2O_3 are systematically higher than the AAS and EPMA results.

Other Elements

The Al_2O_3 and Li_2O contents in the glasses were below the AAS detection limits, i.e. 0.05 and 0.002 wt% respectively. Platinum and TiO_2 were also found to be below the EPMA limits, i.e. approximately 0.05 and 0.07 wt% respectively.

Chemical analysis of batch materials

The level of impurities in the silquartz was determined by X-ray Fluorescence Analysis at the British Ceramic Research Association (BCRA). The results are in excellent agreement with the suppliers analysis (Table 3.3a).

The four different barium carbonates used were dissolved in HCl and analysed by AAS and/or FES. The experimental results are compared with the suppliers analysis in Table 3.3b. The analysed impurity content of the Analar grade barium carbonates (Fisons and BDH) is very close to the suppliers quotation; however the Ventron barium carbonates (Ultrapure and Puratronic grades) are more impure than expected from the suppliers certificate of analysis. The highest quotation for each oxide was used for the calculation of the nominal composition of the glasses.

Conclusions

The main impurity in the $BaO-SiO_2$ glasses is strontium. It comes from the barium carbonates and its content is very low in the Ventron Puratronic grade barium carbonate (0.0072 wt%), and very high in the Analar BDH barium carbonate (0.71 wt%). The levels of Ca, Na, K and Fe in the glasses are low, although they are generally two to fifteen times higher than expected from the chemical analysis of the batch materials. This implies that contamination of the glasses occurs probably during the melting procedure. The Na_2O and Fe_2O_3 contents in the glasses, determined by AAS, are lower than the results of EPMA and UFSCar respectively, but the AAS determinations are closer to the nominal contents. The experimental BaO and SiO_2 contents are very close to the nominal values.

Table 3.3a

CHEMICAL ANALYSIS OF SILQUARTZ

wt% ON IGNITED BASIS

	Suppliers	BCRA
SiO_2	-	99.99
Al_2O_3	0.0015	0.002
Fe_2O_3	0.0001	<0.001
CaO	0.002	<0.001
MgO	0.001	<0.002
K_2O	0.002	0.001
Na_2O	0.005	0.005
Ignition (1025°C)	-	0.12

Table 3.3b

CHEMICAL ANALYSIS OF BARIUM CARBONATES (wt%)

Oxide	AR Fisons		AR BDH	
	Analyzed	Nominal	Analyzed	Nominal
SrO	0.450	-	0.713	<1.8
CaO	0.055	-	0.0084	<0.14
Na_2O	0.0035	<0.014	0.0048	<0.007
K_2O	0.0106	<0.005	0.0035	<0.005
Fe_2O_3	0.0008	<0.0014	0.0008	<0.0014
$BaCO_3$*	99.480	>99.5	99.269	>99.5
	Untrapure	Ventron	Puratronic	Ventron
	Analyzed	Nominal	Analyzed	Nominal
SrO	0.175	<0.006	72 ppm	6 ppm
CaO	0.027	<0.003	77	7
Na_2O	0.011	<0.001	57	1.3
K_2O	0.004	<0.001	62	-
Fe_2O_3	<0.0014	<0.001	<4	1.4
$BaCO_3$*	99.782	>99.988	99.972	>99.998

* $BaCO_3$ by difference

3.2.2 Li_2O-SiO_2 glasses

The Li_2O-SiO_2 glasses were dissolved in the same way as described for BaO-SiO_2 glasses. The residue (lithium perchlorate and impurities) was dissolved in distilled water and stored in polyethylene flasks.

Estimates of Li_2O and Na_2O

The Li_2O content in the glasses was determined by Flame Photometry (FP) in an Evans EEL instrument. FES was also employed, using a Na_2O/acetylene flame at 670.8 nm. The calibration solutions were prepared from an Aldrich 1,000 ppm Li^+ standard solution. The Na_2O content was analyzed as described in section 3.2.1. The experimental results including EPMA determinations are shown in Table 3.4. The results quoted for Li_2O are the average of two determinations. The agreement among the three methods is good, but the FP results are somewhat higher than the FES and EPMA results. There was little loss of Li during the melting procedure. The Fe_2O_3 and Al_2O_3 contents were below the detection limits, i.e. 0.0004 and 0.05 wt% respectively.

Conclusions

The Li_2O-SiO_2 glasses are quite pure. The main impurity is Na_2O (0.01 ~ 0.02) and the levels of Fe_2O_3 and Al_2O_3 are very low.

3.2.3 Electron Probe Microanalysis (EPMA): BaO-SiO_2 glasses

Apart from the analysis of the main constituents and impurities in the glasses, it was of interest to analyse the crystals growing in the BaO-SiO_2 glasses in order to detect whether the impurities were being rejected by, or incorporated in, the crystalline phase. The behaviour of strontium was of particular interest because its content was relatively high in all glasses, except in glass 33.3P (obtained from a Ventron Puratronic Grade $BaCO_3$).

Table 3.4

CHEMICAL ANALYSIS OF Li_2O-SiO_2 GLASSES

Glass	Mole % Li_2O	Wt% Li_2O				Wt% Na_2O
	Nominal	Nominal	FES	FP	EPMA	AAS
17.7	18.0	9.84	9.67	9.69	9.67	0.012
31.0	31.0	18.28	18.30	18.49	18.00	0.017
33.2A	33.3	19.91	-	19.85	19.63	0.011
33.2B	33.3	19.91	-	-	19.82	-
33.7	33.7	20.17	20.16	20.34	-	0.025

The following glasses were heat treated, polished and etched in the usual way and analyzed: Glass 28.3A heated for 24 h at 743°C, Glass 29.7H heated for 15h at 760°C and Glass 33.3B heated at 760°C for 4.25 h. These heat treatments were chosen in order to produce a relatively low density of crystals having a reasonable size (5-10 μm). The approximate 'size' of the electron beam was dependent on the accelerating potential, i.e. 3.5 μm for Sr, 2.5 μm for Ba and 1-2 μm for Si.

The equipment used was an AEI-SEM 2 and the polished specimens were coated with a 300 Å layer of carbon. The analysis was carried out using standards of Al_2O_3, Fe, KCl, Pt, $CaCO_3$, NaF, Ti, $SrCO_3$, SiO_2 and $BaCO_3$. Si, Al and Na were determined at an electron accelerating potential of 15 KV; K, Ca, Ti and Ba at 20 KV; Fe at 25 KV and Sr at 35 KV using SrKα as the analysis line, since at low concentrations the Si signal interfered with the SrLα line. X-ray intensity ratios (equal to approximate weight concentrations) were corrected for X-ray absorption, electron scattering effects and secondary X-ray fluorescence to give the final concentration figures. Counts were recorded at 8-10 points for each element in the samples. A detailed account of EPMA theory is given in reference 3.4.

Table 3.5 shows the average of two EPMA determinations for Si, Ba and Sr in the glassy and crystalline phases in the heat treated glasses already mentioned. It can be seen that there is no appreciable difference in the composition of the glassy and crystalline phases and, at first sight, one could conclude that the crystals are solid solutions with compositions close to the parent glass. On the other hand, taking into account the fact that the "crystalline phase" is composed of spherulites which are only 64% crystalline (see volume fraction of crystallinity versus time curves in Chapter 4), one realizes that, if the crystalline domains of the

Table 3.5

EPMA RESULTS FOR SiO_2, BaO AND SrO IN SOME HEAT TREATED GLASSES. GLASSY AND 'CRYSTALLINE PHASES' (wt%)

Glass 28.3A - 24 h at 743°C

Oxide	Nominal	Glass	Crystal
SiO_2	49.55	49.15	49.35
BaO	50.14	50.13	49.59
SrO	0.29	0.31	0.32
	99.98	99.59	99.26

Glass 29.7H - 15 h at 760°C

Oxide	Nominal	Glass	Crystal
SiO_2	47.61	47.51	47.56
BaO	51.90	51.70	51.15
SrO	0.48	0.47	0.43
	99.99	99.68	99.14

Glass 33.3A - 4.25 h at 760°C

Oxide	Nominal	Glass	Crystal
SiO_2	43.60	43.93	44.24
BaO	56.05	56.18	56.12
SrO	0.33	0.50	0.46
	99.98	100.61	100.82

spherulites have stoichiometric composition (56.06BaO-43.94SiO_2 by weight) and the glassy part is depleted in barium and has all the strontium, the EPMA still would give the same results as above.

3.2.4 EPMA: Li_2O-SiO_2 glasses

In the case of Li_2O-SiO_2 glasses the crystalline clusters are not as complex as the BaO-SiO_2 spherulites. They are formed by branching of single crystals [2.14] and the degree of crystallinity is expected to be much higher. Therefore, it is possible, in principle, to analyse the chemical composition of the crystal clusters in the glassy matrix. This was attempted for glasses 17.7, 31.0, 33.2A and 33.2B nucleated at 481°C for 1 h and developed at 570°C. Large crystals (~ 30 μm in diameter) were grown in the glassy matrix.

Analysis for SiO_2 was carried out at an electron accelerating potential of 15 kV using pure SiO_2 as standard. Li is outside the element range of the instrument, but the presence of Li_2O in the samples was taken into account when performing matrix corrections. The crystals were large enough to allow X-ray intensities to be measured using a defocused probe, but only relatively short count-times could be employed before surface damage and composition changes occurred.

Measurements were made in 10 different crystals and the surrounding glass in each sample, but *no* significant differences in the compositions of crystals and glass were detected in any of the four samples. The results obtained and estimates of precision are given in Table 3.6.

Table 3.6

SiO_2 CONCENTRATIONS (WEIGHT %)

Glass	Crystals		Matrix	
	SiO_2	95% confidence range	SiO_2	95% confidence range
17.7	90.12	±0.50	90.54	±0.39
31.0	82.03	0.25	81.95	0.15
33.2A	80.23	0.33	80.51	0.51
33.2B	80.11	0.40	80.26	0.22

It should be realized, however, that for glasses 17.7 and 31.0 the presence of amorphous SiO_2-rich droplets within the crystal clusters does not allow an unbiased determination of this component by EPMA. On the other hand, West and Glasser [2.21] showed by XRD that crystalline lithium disilicate metastable *solid solutions*, with compositions ranging from ~ 28 to 38mol% Li_2O are formed and persist indefinitely between ~ 500°C and 700°C. Russian authors [3.5] also demonstrated the existence of solid solutions in Li_2O-SiO_2 glasses by refractive index measurements.

All the analytical methods employed in this work can be found in Vogel [3.1], Price [3.2], Wise et al. [3.3] and Sweatman and Long [3.4].

3.3 Infra-red Spectroscopy (IR)

It is well established that trace amounts of "water" can affect several properties of glasses [3.6,3.7,3.8] including the viscosity and the nucleation and growth of second phases [3.9]. Therefore, it is necessary to know the level of water if comparison of any kind of phase transformation is to be made among glasses of different compositions.

The glass specimens for IR (transmission) spectroscopy were ground to about 20 x 7 x 0.6 mm and polished with cerirouge. Then they were "dried" at 400°C for several hours, transferred to a desiccator and analyzed in a Perkin-Elmer 683 spectrometer.

The IR traces of several BaO-SiO_2 glasses electrically melted for this study are shown in Figure 3.3a. The extinction coefficients are not available for the quantitative determination of water in these glasses, but it can be seen that the amount of water (proportional to the area under the peaks) is much lower than in the BaO-SiO_2 glass melted in a gas furnace by Ramsden [2.54]. This behaviour was also verified for other glasses melted in gas furnaces by Ramsden [2.54] and Rowlands [1.47].

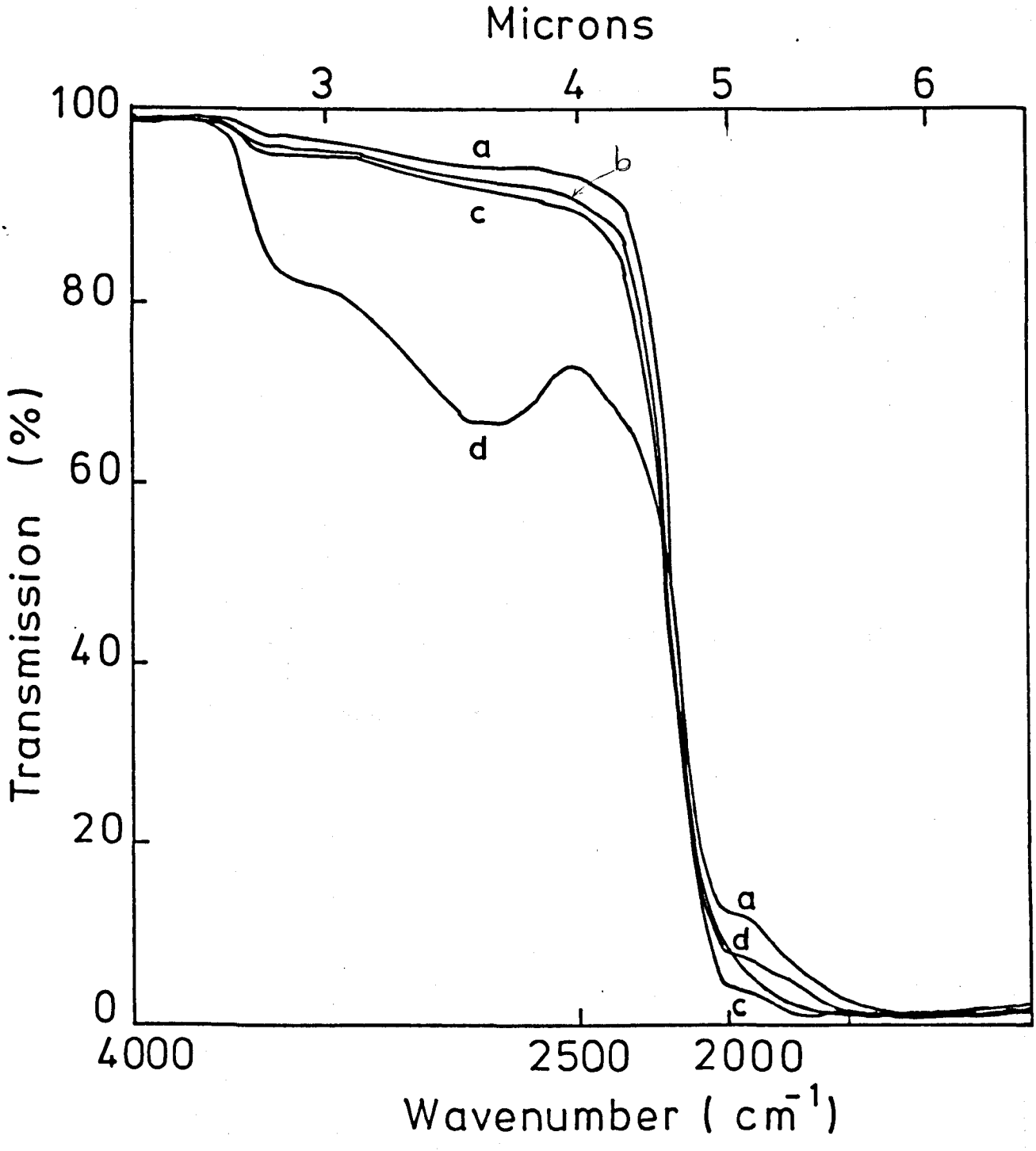

Fig. 3.3a I.R. transmission curves for $BaO-SiO_2$ glasses:

a) glass 33.3P - 0.57 mm thick

b) glass 28.3B - 0.65 mm thick

c) glass 27.0 - 0.67 mm thick

d) glass 37 - 0.63 mm thick (melted in [2.54])

Fig. 3.3b I.R. transmission curves for Li_2O-SiO_2 glasses:

a) glass 17.7 - 0.68 mm thick

b) glass 31.0 - 0.64 mm thick

c) glass 33.2A - 0.66 mm thick

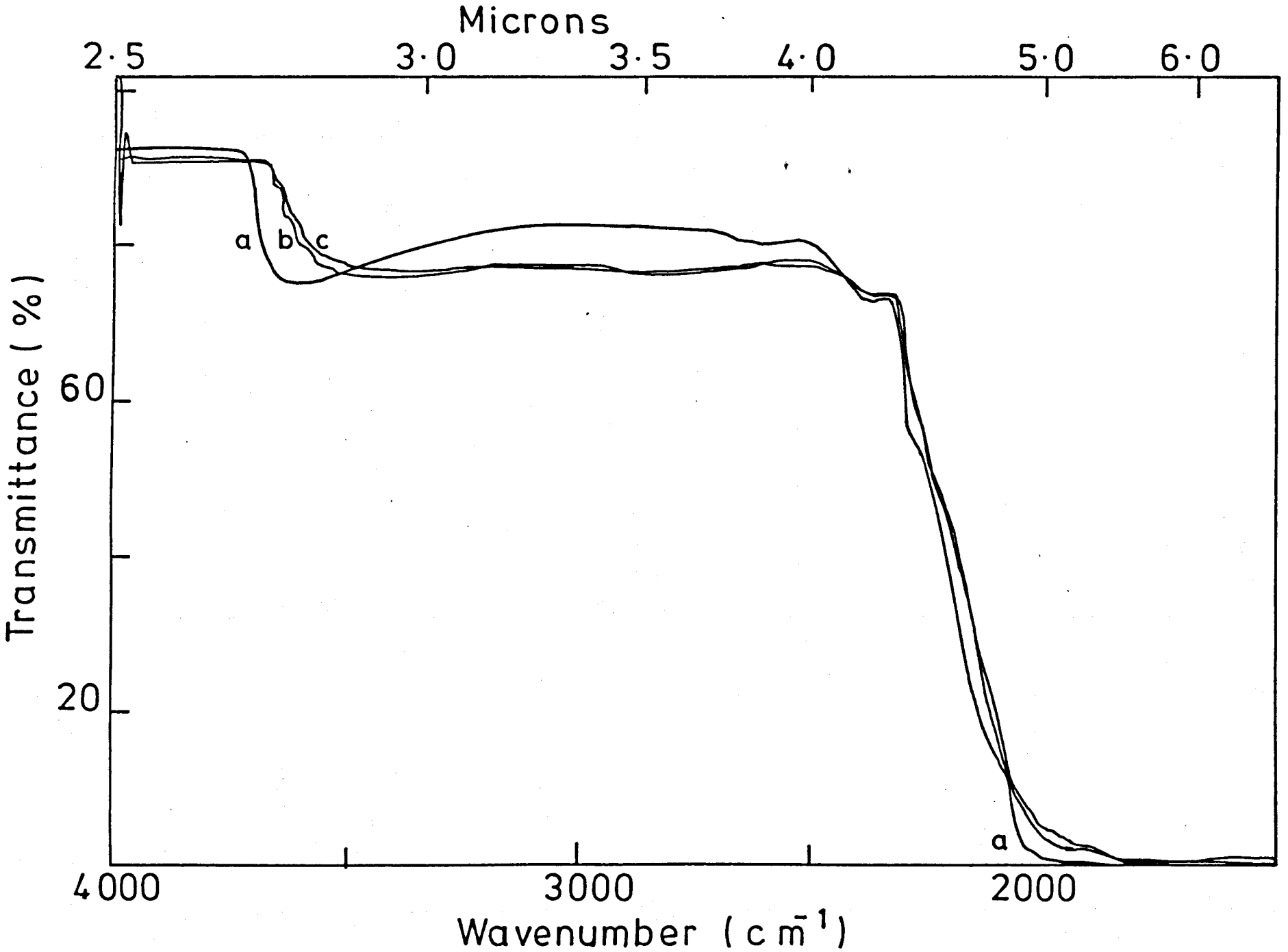
Microns
2·5
3·0
3·5
4·0
5·0
6·0
Transmittance (%)
60
20
a
b
c
a
4000
3000
2000
Wavenumber (c m⁻¹)

Fig. 3.4 Part of the phase diagram for the $BaO-SiO_2$ system showing the crystallization and melting peaks obtained by DTA.
(X) beginning and (●) peak of melting endotherms.

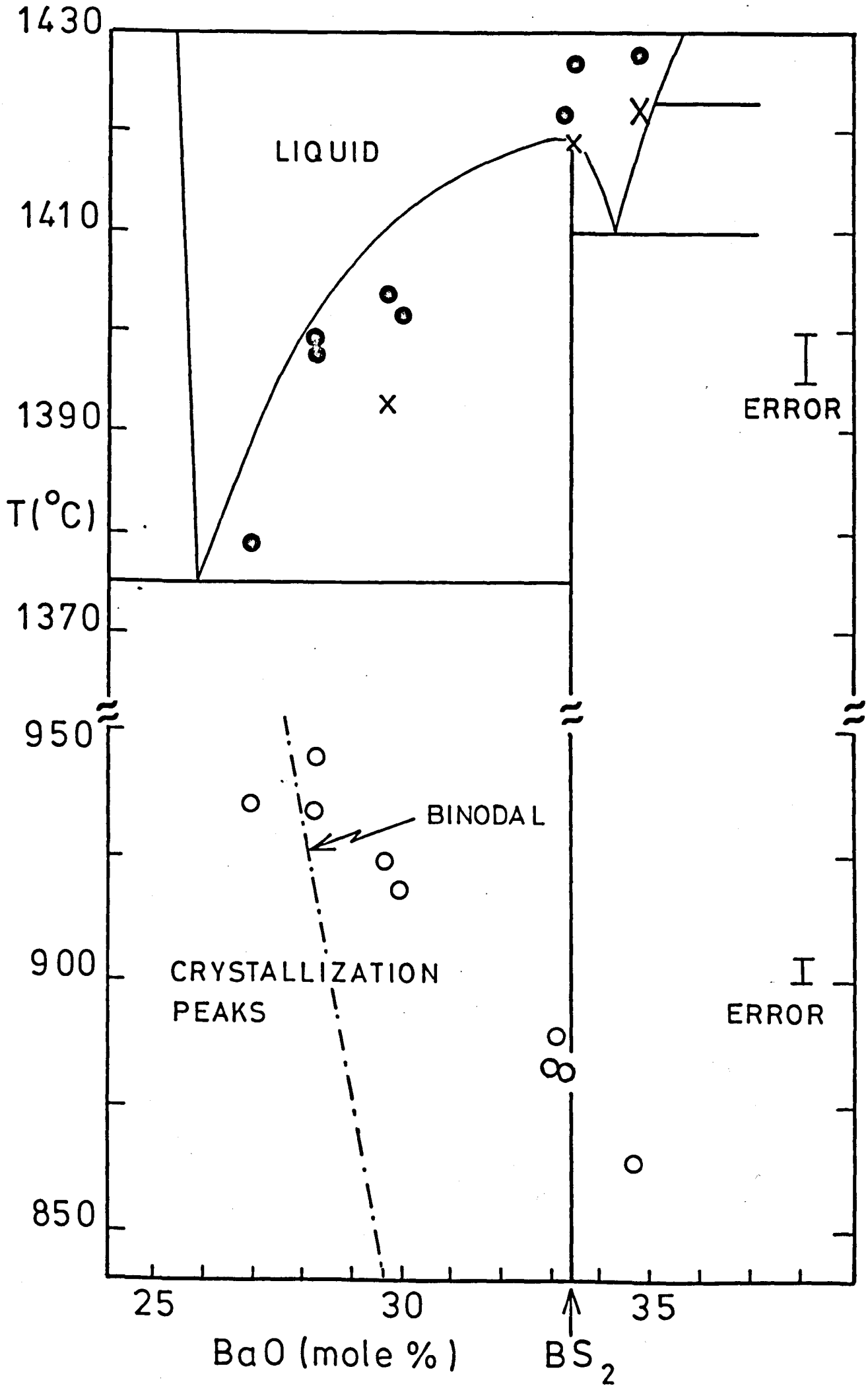
1430
1410
1390
T(°C)
1370
950
900
850
LIQUID
ERROR
BINODAL
CRYSTALLIZATION
PEAKS
ERROR
25
30
35
BaO (mole %)
BS2

However, more important, is the fact that all glasses used in the present work have very *similar* water contents.

Figure 3.3b shows the IR spectra for Li_2O-SiO_2 glasses 17.7, 31.0 and 33.2A. The characteristic curves for the last two glasses are very similar. The IR trace for glass 17.7 has a different shape (probably due to its highly interconnected phase separated structure), but the overall area under the curve, and total amount of water are also very *similar* for the three glasses.

3.4 Differential Thermal Analysis (DTA)

Small *monolithic* pieces (about 100 mg) of all glass compositions were analyzed in a Standata 6-25 DTA apparatus with 10°C/min as heating rate. The glass transition temperatures (T_g) determined for all BaO-SiO_2 glasses were between 690 and 700°C showing no systematic variation with composition. These values are in good agreement with the dilatometric determinations of Shelby [3.10], i.e. 695°C for compositions between 27.0 and 34.7 mol% BaO. A viscosity of 10^{12} Pa.s corresponds to 689°C for the 33.2C glass (section 4.5). The crystallization peaks (T_c) show a strong dependence on the chemical composition of the base glass, increasing as the SiO_2 content increases (Figure 3.4). Ramsden [2.54] has not observed systematic variations in T_c with composition, but he used finely powdered samples in which the surface crystallization probably had a predominant effect.

In principle, the liquidus curve could be determined by DTA if a very slow heating rate was employed allowing equilibrium to be attained. In this condition, the *beginning* of the melting endotherm would correspond to the melting temperature for a stoichiometric compound (e.g. $BaO.2SiO_2$) or a eutectic composition, and the *peak* of the endotherm should be near the liquidus temperature (T_L) for a non-stoichiometric composition because,

in this case, the beginning of the endotherm should be near the solidus line. Figure 3.4 shows that the beginning of the melting endotherm of glass 33.3A is, indeed, very near to the published melting point of the BS_2 compound, demonstrating the accuracy of the chemical analysis (33.3 mol% BaO) and the validity of the DTA test. For the other compositions, except for glass 34.7H, the peak temperatures are systematically 0-10°C lower than the published liquidus temperatures (although they are within the 95% confidence limits). There is also a second peak at lower temperatures probably due to the transformation of the low-temperature form of BS_2. This phase should tranform to h-BS_2 at 1350°C under equilibrium conditions. In conclusion, we suggest that DTA can be used as a mean of estimating liquidus temperatures, at least for comparative purposes, among different glass compositions.

3.5 Optical Microscopy

To study the nucleation behaviour of crystals in glasses the most "direct" and quantitative method is to subject the specimens first to a nucleation heat treatment and then to a development (growth) heat treatment at a higher temperature. The nuclei then grow to dimensions resolvable in the optical microscope. The development temperature must be chosen with the requirements that: i) the nucleation of new crystals is negligible, ii) there is no appreciable dissolution of the existing nuclei. Both conditions can be tested experimentally and, in practice, they are met it careful precautions are taken [3.11]. After the heat treatment the specimens must be polished and etched to improve the contrast between crystal and glass. Micrographs are then taken and the size distribution of crystals, shape and number per unit area of crystals are obtained. A precise

stereological equation is applied to give the number of crystals per unit volume.

In this study, glass specimens of about 3 x 3 x 1 mm were nucleated at 680-770°C ($BaO-SiO_2$) and at 440-500°C (Li_2O-SiO_2) for different periods, air quenched and subsequently developed at 800-830°C for 10-30 min ($BaO-SiO_2$) and 570-600°C for 30-70 min (Li_2O-SiO_2) respectively. The electric tubular furnaces employed were maintained within ½°C with proportional controllers. The furnaces were found to have a "plateau" around the hot spot, in which the temperature varied by less than 1°C over 2 cm. The glass specimens were kept inside a small mullite boat being touched by the tip of a Pt/13Rh thermocouple during the treatment. The thermocouple readings were found to be within 1°C of a standard thermocouple. The furnaces usually attained the equilibrium temperatures 10-20 min after the insertion of the specimens, the maximum variation being 7°C in the first minutes (depending on how fast and careful the operation was performed). Therefore, some uncertainty in the heat treatments is expected for samples treated for short periods ($t < 30$ min).

The heat treated specimens were mounted in glass plates with Canada balsam, ground with SiC (400 and 600 grit) and polished with colloidal Ce_2O_3. An etching of 10-15 sec in a 0.6% HF 0.2% HCl solution was enough to reveal the microstructure of $BaO-SiO_2$ glasses. Li_2O-SiO_2 glasses required from 2 min (33.2 mol% Li_2O and 17.7 mol% Li_2O) to 4 min (31.0 mol% Li_2O) to reveal the microstructure. Photographs were taken with a Zeiss Ultraphot 2 microscope with 16x or 40x objectives, depending on the size of the crystals. The total magnification on the final prints was obtained by means of a calibrated graticule which was photographed in the same microscope.

3.5.1 Stereological Analysis

De Hoff and Rhines [3.12] developed an exact theory which allows the number of particles per unit volume, N_V, to be related to the number of such particles intersecting a planar section per unit area, N_S, i.e.

$$N_V = \frac{2}{\pi K(q)} N_S \bar{z} \tag{3.1}$$

where $\bar{z}$ is the average of the reciprocal of minor axis of the planar intersections on the micrograph and K(q) is a function of the shape of the particles. For spherical particles K(q) = 1, whereas for prolate ellipsoidal particles [3.12]

$$K(q) = \frac{1}{q} + \frac{q \ln\left[\frac{1 + \sqrt{1-q^2}}{q}\right]}{\sqrt{1-q^2}} \tag{3.2}$$

where q is the ratio minimum/maximum diameter. These equations allow the number of particles (crystals) per unit volume to be determined from reflection optical micrographs.

These equations are rigorous, and if the shape of the particles is known the accuracy of the determination depends on the statistics, i.e. on the number of crystals measured and counted for the calculation of N_S and $\bar{z}$. In this study, from 200 to 800 crystalline particles were counted and from 100 to 400 particles were measured in each sample. The determination of the ratio q (minimum/maximum diamter of the ellipsoidal crystals) was performed by searching out the planar intersection on the micrographs that had the greatest deviation from an equiaxial shape and measuring their axial ratios. Only the particles with the largest two-dimensional intersections were considered in this determination. Typical values of q for glasses 17.7, 31.0 and 33.2B, nucleated at 481°C for different periods and

developed at 570°C, were 0.86, 0.82 and 0.74 respectively. The statistical error in N_V was ±10-20% (95% confidence limits), depending on the size distribution of crystals and number of crystals counted and measured.

There is however another source of error, which has not been considered in the past but can be quite appreciable. The resolution of optical microscopes are usually around 1-3 μm, the sectioning of the particles always producing a certain percentage of intersections below the resolution limit, which will not be taken into account in the calculation of N_S and $\bar{z}$. This will cause N_V to be underestimated by a value which depends on the resolution of the microscope, the size distribution of particles and the maximum size and shape of particles. A complete mathematical derivation of these errors for several size distributions and resolutions is given in Appendix 1. For usual cases, i.e. a size distribution due to a double stage heat treatment, I and U being constant, an underestimation of 3 to 14% can be expected for the measured values of N_V and nucleation rates I. If the crystals are too small on the prints (< 2-3 mm) measurement errors can be significant also and increase the uncertainty in N_V and I. Hence only print magnifications giving a large majority of crystals greater than 3 mm in size were used in the analysis. It was found experimentally that nucleation densities up to 10^6 mm^{-3} can be measured quite well in optical micrographs, electron microscope techniques being required for larger densities. Other complications arise in this case.

All the above arguments are valid if the glass specimen under study is chemically homogeneous, variations in chemical compositions causing variations in N_S and N_V. Figure 3.5 shows the number of crystals per unit area in a glass with 32 mol% BaO, heat treated at 718°C and 820°C, as a function of the size of field of view under the optical microscope. About 400 crystals were measured in each case and both N_S and the variance, S^2,

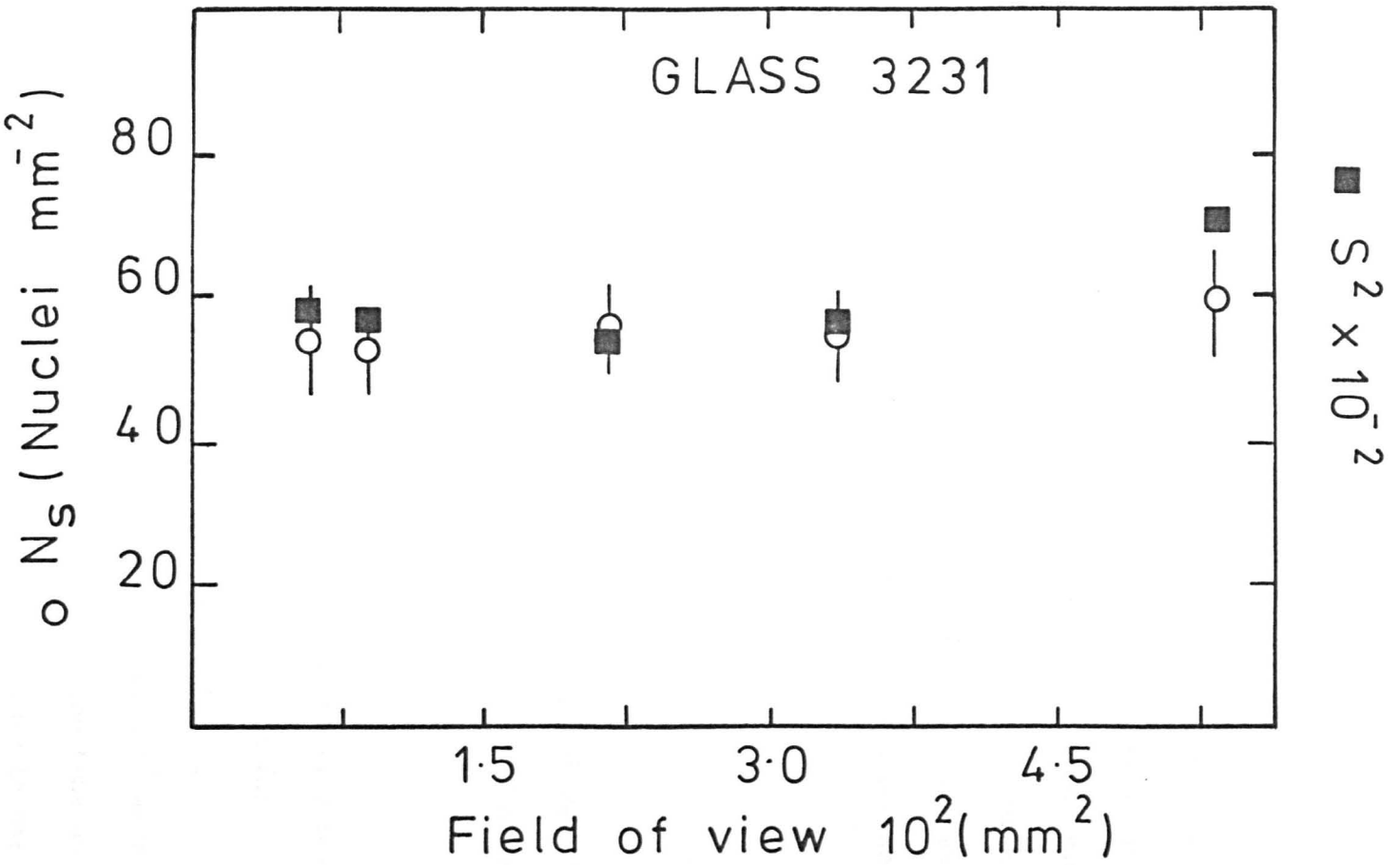

Fig. 3.5 Number of crystals per unit area and its variance as a function of size of field of view in the microscope.

are constants showing that the crushing/remelting technique gives homogeneous glasses, at least within the size domain studied. The "smoothness" of the N_v vs. time curves (see Results) also support this suggestion.

3.6 Viscosity Measurements

Viscosity data are useful in interpreting the kinetics of phase transformations in glasses. For the $BaO-SiO_2$ and Li_2O-SiO_2 glasses, which crystallize easily, it is difficult to obtain viscosities in the range 10^2-10^7 Pa.s. However, it is often possible to obtain data at high temperatures (10^8 -10^{12} Pa.s) by the penetration, parallel plate, fibre extension or beam bending methods. In this section the theory, operation and results obtained with penetration viscometers are described.

3.6.1 Penetration viscometer

Apparatus

The technique consists in measuring, at a given temperature, the penetration into the glass of a rigid indentor under the action of a load as described in [1.53].

Briefly the apparatus used consisted of:

(i) A tube furnace (Kanthal wound) which could be vertically moved.

(ii) A silica column on which the sample was placed. It was separated from the column by a platinum (or mica) foil.

(iii) A silica tube clamped to a saddle on which the weights were placed. The indentor was inserted into the lower end of the tube as shown in Figure 3.6. After several trials it was decided to use a total load of 2.256 Kg. To obtain deformations corresponding to viscosities in the 10^8-10^{12} Pa.s range, cylindrical indentors with

with diameters of 1, 2 and 3.85 mm,and spherical indentors with diameters of 3.18 mm were used.

(iv) A measuring device - a capacitance sensor with accessories. The calibration was such that a penetration of 1 mm corresponded to 140 mm in the y axis on the recorder.

(v) An hydraulic system allowing the saddle to be released.

The furnace temperature was controlled to ±0.5°C and the measuring thermocouple (Pt/Pt-Rh) was placed touching the sample (Figure 3.6). The glass specimens were cylinders of approximately 20-30 mm diameter and 8.0-10.0 mm thickness. They were ground flat and parallel with several grades of SiC and polished with Cerirouge. The polishing was necessary in order to inspect the samples for visible cracks, cords, etc.

Operation

With the sample and furnace in position, a stabilisation period of 20 - 40 minutes was required. Although 30 minutes stabilisation was usually employed, a time of only 20 minutes was allowed for samples tested at high temperatures where the danger of crystallization was greater. During the holding time the y axis magnification was checked and the x axis pen speed set according to the total deformation expected. Then the saddle was loaded and simultaneously both the recorder and the stop watch started. The sample temperature was measured at regular intervals during the course of the experiment. At the end of the experiment the time on the stop watch was recorded, the saddle lifted and the sample taken out. The specimens were examined for crystals after the viscosity measurements.

The accurate measurement of temperature is an important step and for this reason the Pt/Pt-13 Rh thermocouple was calibrated against a standard thermocouple and positioned in order to touch the glass samples, passing through the perforated indentor.

Indentors

The indentors can be spherical, cylindrical (flat circular base) and conical. In this work two spherical and three cylindrical indentors were used. A Nimonic 105 spherical indentor was machined in our Department. Its closeness to a perfect sphere was tested by measuring the viscosity curve of a low temperature glass (NBS 711) with a perfect ball-bearing steel indentor, and comparing it with the values obtained with the Nimonic indentor. Close agreement was found. The cylindrical Nimonic 105 indentors were made with 1.0, 2.0 and 3.85 mm diameters. In this way a wider range of viscosity could be measured, i.e. 10^{12}-10^{8} Pa.s.

Determination of the viscosity by indentation of a glass plate

3.6.2 Cylindrical indentors

This derivation follows that presented by Nemilov [3.13]. In the framework of Buerger's model (Figure 3.7), which is one among the several rheological models of glass, the viscous (η_1) and elastic (G_1) elements are connected in series with the Kelvin model, which is a parallel combination of the viscous (η_2) and elastic (G_2) elements. This model reflects the delayed elastic properties of glass. The rate of total deformation, with a constant shear stress σ and zero initial deformation, is made up from the rate of Newton's viscous deformation, $d\varepsilon_N/dt = \sigma/\eta_1$, and the rate of deformation of Kelvin's solid $d\varepsilon_K/dt = (\eta_2/G_2)(d^2\varepsilon_K/dt^2)$ [3.14]. Since $\varepsilon_K = (\sigma/G_2)\left[1 - \exp\left(-\frac{G_2}{\eta_2}\, t\right)\right]$ [3.13], for any moment in time (with a constant σ) we obtain

$$\frac{d\varepsilon}{dt} = \frac{\sigma}{\eta_1}\left[1 + \frac{\eta_1}{\eta_2}\exp\left(-\frac{G_2}{\eta_2}\, t\right)\right] \qquad (3.3)$$

where $\varepsilon = \varepsilon_N + \varepsilon_K$.

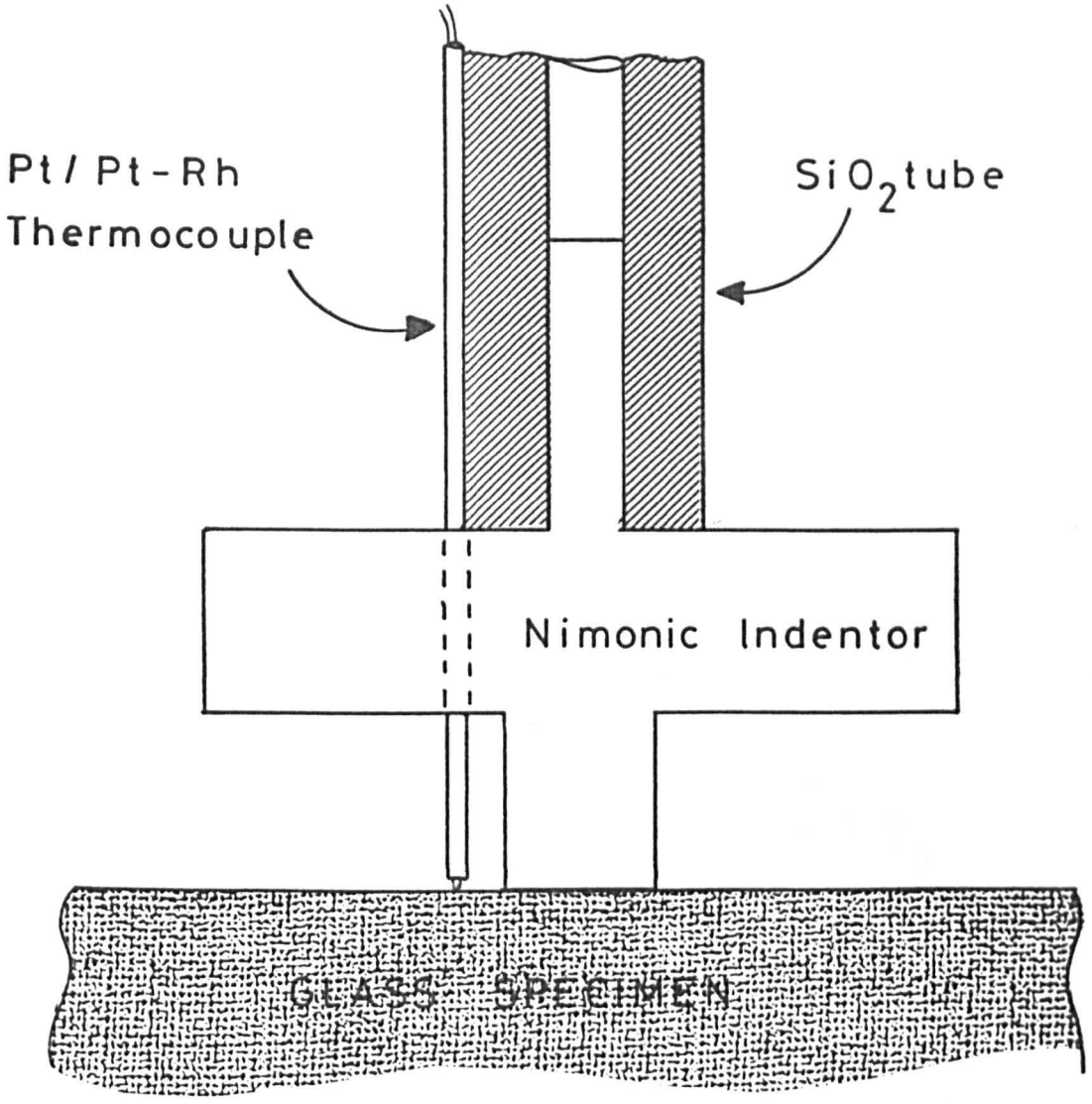

Fig. 3.6 Assembly used in the viscometer (cylindrical indentor)

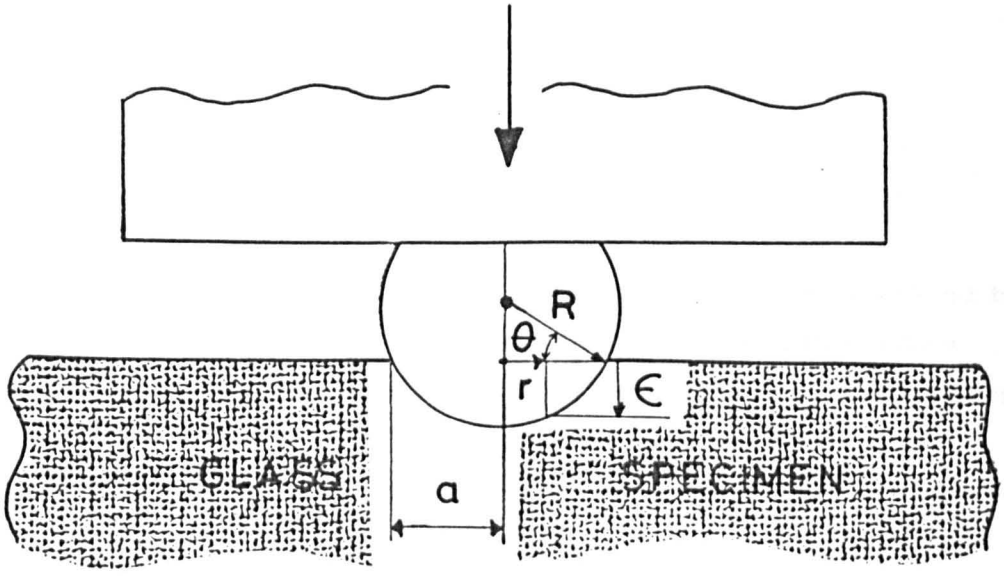

Fig. 3.8 Assembly used in the viscometer (spherical indentor).

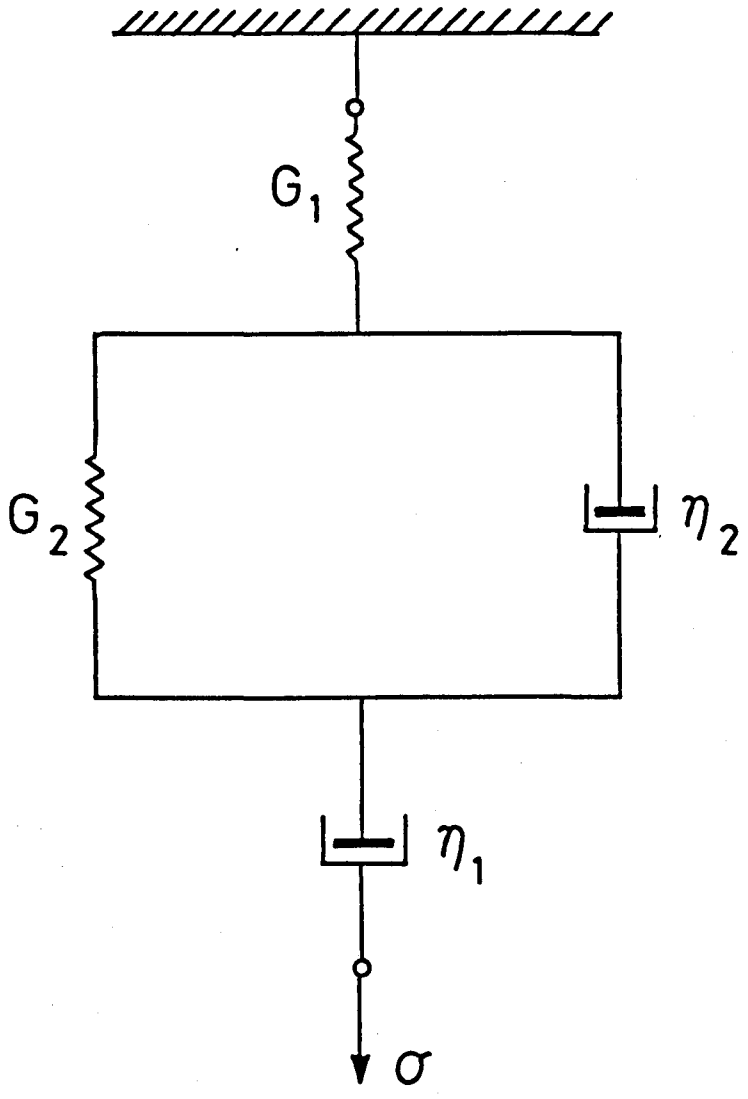

Fig. 3.7 Burger's model for a solid characterized by delayed elastic deformation and viscous flow. The parallel connection of G_2 and η_2 represents the model of Kelvin.

The external stress σ and the established equilibrium elastic deformation of the whole solid ε_{el} are associated by the relationship $\sigma = G\varepsilon_{el}$, where G is the shear modulus of the glass. When $t \to \infty$ (in practice when $t >> \eta_2/G_2$), corresponding to Newtonian flow, Equation (3.3) becomes

$$\frac{d\varepsilon}{dt} = \frac{G\varepsilon_{el}}{\eta} \tag{3.4}$$

The equilibrium elastic deformation ε_{el} produced in a semi-infinite plate by an absolutely rigid flat indentor (cylindrical or parallelepiped) is determined from the equation obtained by Streicher [3.15] on the basis of the solution of the corresponding contact problems in elasticity theory

$$\varepsilon_{el} = m\frac{(1 - \mu^2)Mg}{E\sqrt{S}} \tag{3.5}$$

where S is the area of the base of the indentor, μ the Poisson coefficient, E is the Young's modulus, M the mass of the load, g the acceleration due to gravity and m is a coefficient. For a cylinder, $m = 16/3\ \pi^{3/2} = 0.96$. This factor is the numerical value of the integral which takes into account that stresses equal to infinity arise along the edge of the indentor but, as a result of irreversible deformations (plastic or viscous), are smoothed out under the base in accordance with specific laws. The total deformation is the result of the action of compressive, shear and extensive stresses. The tangential stresses reach a maximum at a depth of the order of the radius of the indentor and then fade away [3.13].

Using Equations (3.4) and (3.5), and $E = 3G(\mu = 0.5)$, we obtain an expression for the viscosity

$$\eta = m\frac{Mg}{4\sqrt{S}\ v} \tag{3.6}$$

in which $v = d\varepsilon/dt$ is the steady state rate of penetration of the indentor and η is the viscosity.

3.6.3 Spherical indentors

If two elastic spheres are pressed into contact, it may be shown [3.16] that the displacement ε at a distance r from the centre of the area of contact (Figure 3.8) is given by

$$\varepsilon(r) = (K_1 + K_2)\frac{g_0\pi^2}{4a}(2a^2 - r^2) \qquad (3.7)$$

where $K_1 = \frac{1 - \mu_1^2}{\pi E_1}$, $K_2 = \frac{1 - \mu_2^2}{\pi E_2}$, E is Young's modulus, μ Poisson's ratio and g_0 = maximum pressure = $3P/2\pi a^2$, P(=Mg) the applied force and a the radius of the circle of contact. If the spheres are incompressible ($\mu = 0.5$) and one has infinite rigidity, $K_1 = 0$ and $K_2 = 3/(4\pi E_2)$. Thus, for $r = 0$, $\varepsilon = 9P/16aE_2$. This equation is true for a viscous body if, based on the analogy between the elastic and viscous deformations [3.17], $d\varepsilon/dt$ is substituted for ε, and the viscosity, η, for $E_2/3$. Thus

$$\frac{d\varepsilon}{dt} = \frac{3P}{16a\eta} \qquad (3.8)$$

If ε is the depth of penetration (at $r = 0$), then $\varepsilon(2R - \varepsilon) = a^2$, where R is the radius of the rigid sphere. The viscosity coefficient can be calculated by using the following change of variables

$$\varepsilon = R - R\sin\theta \quad \text{and} \quad d\varepsilon = -R\cos\theta\, d\theta \;;\; \varepsilon = 0 \;,\; \theta = \pi/2$$

Then $a = R\cos\theta$. Hence Equation (3.8) can be integrated to give

$$\frac{9P}{32\eta(2R)^{1/2}}t = \frac{3}{32}(2R)^{3/2}[\pi - 2\theta - \sin\theta] \qquad (3.9)$$

if the function on the right-hand side of Equation (3.9) is denoted $F(\varepsilon)$, when $\varepsilon \ll 2R$, $F(\varepsilon) \rightarrow \varepsilon^{3/2}$ and

$$\eta = \frac{9P}{32(2R)^{1/2}\,\varepsilon^{3/2}}\,t \qquad (3.10)$$

This equation was used by Douglas et al. [3.18] and Brückner et al. [3.19] for viscosity determinations. In this study the more exact Equation (3.9) was employed.

3.7 X-ray Diffraction (XRD)

For the determination of crystallinity during studies of the kinetics of crystallization of glasses different methods can be used, i.e. density measurements, quantitative DTA, dilatometry, I.R. spectroscopy, quantitative stereology, etc. Quantitative X-ray diffraction (measurements of maxima of peaks from crystals) is also widely used. However, when the crystals are too small or imperfect the broadening of the peaks renders the analysis difficult and also it is always necessary to have a standard sample, usually the pure crystalline species.

Ohlberg and Strickler [3.20] applied an X-ray diffraction method, similar to one used in the determination of the crystallinity of stretched rubber, to partially crystallized glass. The volume fraction crystallinity, α, was equated to

$$\alpha = (I_g - I_x)/(I_g - I_b) \qquad (3.11)$$

where I_g, I_x and I_b are respectively the non-crystalline scattering intensities; measured at a single value of 2θ, for the parent glass (zero crystallinity), the partially crystallized glass, and a mechanical mixture

of crystalline compounds chemically equivalent to the parent glass. The value of 2θ must be selected such that the non-crystalline scattering is high for the parent glass and at the same time is free of crystalline scattering in the case of the partly devitrified glass and of the mechanical mixture.

The assumptions inherent in the method are the following:

(i) no changes in volume take place during crystallization,

(ii) there are no chemical changes inside the different crystalline and/or glassy phases during crystallization,

(iii) a supplementary demand must be added to these assumptions, namely, that a plateau in the $(I_g - I_x)/(I_g - I_b)$ vs. 2θ curve must be found.

These assumptions have been fully discussed by Cervinka and Dusil [3.21] who successfully measured the crystallinity of a glass ceramic from the SiO_2-Al_2O_3-MgO-ZrO_2-TiO_2 system. Ohlberg and Strickler [3.20] also found that the determined percent crystallinities were within 5% of the calculated values (from mechanical mixtures) for both silica and a TiO_2-cordierite glass.

In this thesis, a study was undertaken of the volume fraction of crystallinity versus time of heat treatment for glass 33.2B at 743°C and 760°C. For this purpose, specimens measuring about 20 x 15 x 1.5 mm were heat treated, the crystallized surface layer removed, and subsequently polished with Cerirouge. The intensity diffracted at $2\theta = 18°$ was recorded for 20 min, the average of, at least, four measurements being taken. An as quenched specimen of BS_2 glass (33.2B) was used for the determination of I_g, and a specimen previously heated at 743°C for 12 h and at 1000°C (above the spherulite-lath transformation) for 5 hours, was used for the determination of I_b. At $2\theta = 18°$, the X-rays cross-section was less than

1 cm^2 and a layer of only about 5 μm of glass was responsible for most of the diffracted intensity (Figure 3.9). Under these conditions, the volume of diffracting material was kept constant. Furthermore, assumption (i) was nearly fulfilled because the difference in density between glass and crystal is very small (Table 2.1). Assumption (ii) was satisfied because the chemical composition of the spherulites and parent glass were the same. The third assumption was tested by measuring the diffracted intensities at $2\theta = 36°$ as well. No difference was found in the values of α determined from Equation (3.11).

The same heat treated and polished glass specimens were etched and photographed as explained in section 3.5. The volume fraction of spherulites was also measured in optical micrographs by the point-counting method described by Hilliard and Cahn [3.22] as a check of the X-ray measurements.

3.8 Transmission Electron Microscopy (TEM)

Thin foils and replicas were examined with TEM in a Hitachi HU11A microscope at 75 or 100 KV. The morphology of the internally nucleated crystals in the early stages and of the amorphous droplets in phase separated glasses were studied in this way.

Thin glass sections were prepared by the ion beam thinning technique. The glass sample was first cemented to a glass slide together with six other pieces of glass surrounding the first sample. They were ground flat with 600 grade SiC and polished with Cerirouge. Next the sample was turned over and cemented toa new slide together with 100 μm thick glass pieces as before. Grinding was carried out until the edges of the 100 μm pieces started to disappear. Grinding was then continued with 3 μm diamond until a thickness of about 15 μm was obtained.

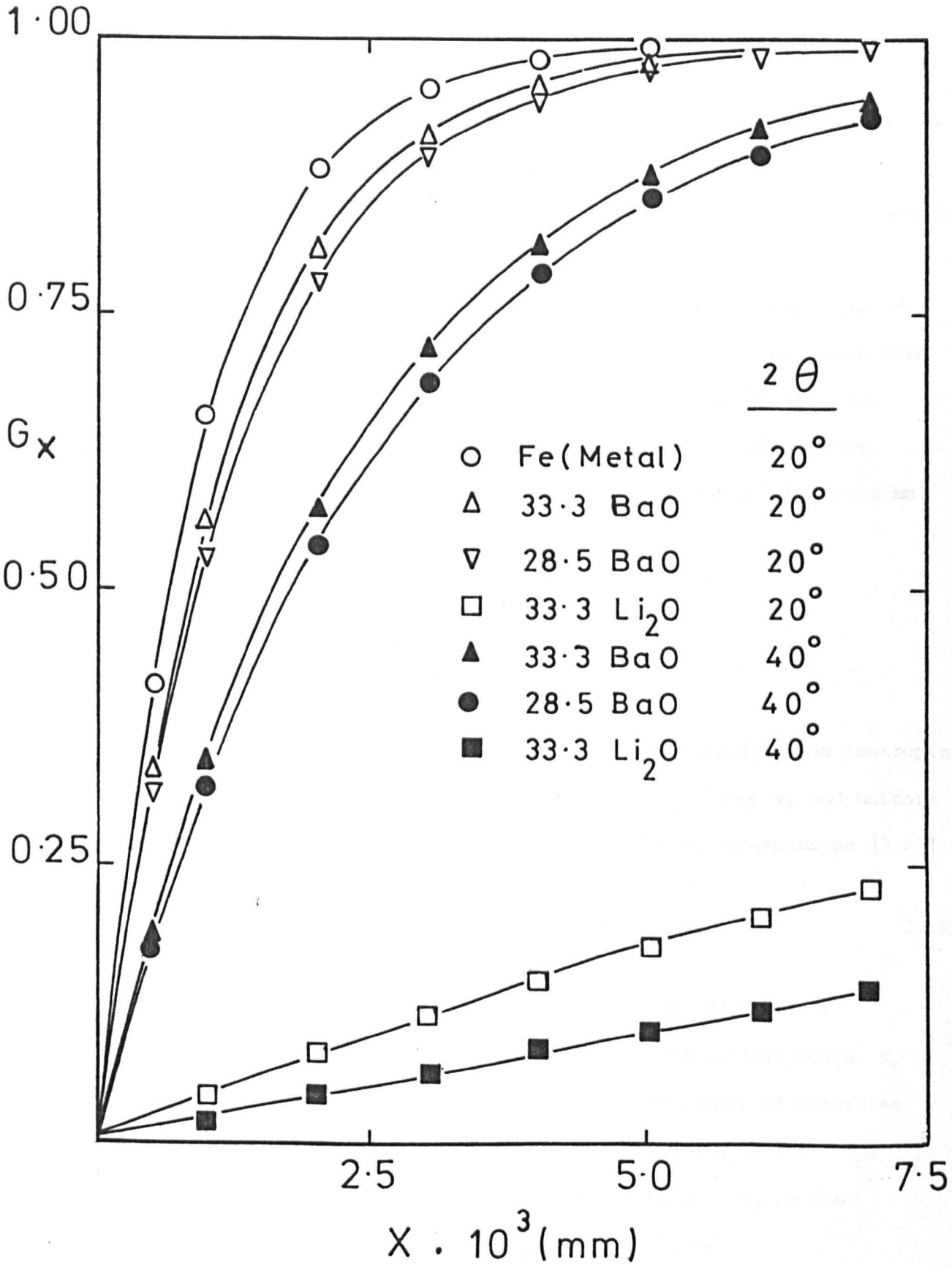

Fig. 3.9 Fraction of intensity (G_X) diffracted by a layer of thickness x for various silicate glasses and metalic iron. (Copper Kα radiation). G_X is given in [3.40].

The foil was removed with methanol and cemented to a copper grid which was placed in a vacuum chamber on a rotating plate in an Edwards IBMA2 machine. After a vacuum of 10^{-4} torr was reached the specimen was bombarded with Ar ions at 12° until a small hole appeared in the glass.

Replicas were prepared by evaporating carbon to previously polished and etched glass samples, at angles of 30-40 degrees. The specimens were then soaked in a 2% HF solution until the replicas became detached and floated on the liquid surface, and could be collected on copper grids.

The microscope magnifications used were checked with a 2160 lines/mm standard diffraction grating replica.

3.9 Small Angle X-ray Scattering (SAXS)

3.9.1 Monodispersed systems

The intensity I(s), of X-rays scattered at small angles by an isotropic system of identical and widely dispersed particles of volume v, and uniform electronic density ρ_0, can be represented by the following expansion [3.23]

$$I(s) = I_e N \Delta\rho^2 v^2 [\, 1 - 1/3\ R_g^2 (2\pi s)^2 + \ldots] \qquad (3.12)$$

where $\Delta\rho = (\rho - \rho_0)$, ρ is the electronic density of the matrix, $s = (2 \sin\theta)/\lambda$ the modulus of the scattering vector in reciprocal space, I_e the intensity scattered by a free electron and N the number of particles in the irradiated volume. At small angles $s \simeq \varepsilon/\lambda$ where $2\theta = \varepsilon$, the scattering angle, and λ is the wavelength of the X-rays. R_g is the 'electronic radius of gyration' of the particle given by

$$R_g^2 = \int r^2 \rho(r)\, dv / \int \rho(r)\, dv$$

where r represents the coordinates in real space.

In the case of a spherical homogeneous particle ($\rho(r) = \rho$) becomes

$$R_g = \sqrt{3/20}\ D$$

where D is the particle diameter.

3.9.2 Guinier's Law

Guinier [3.23] has shown that the following approximation is valid for very small angles

$$I(s) = I_e N \Delta\rho^2 v^2 \exp[-1/3\ R_g^2\ (2\pi s)^2] \qquad (3.13)$$

Equation (3.13) is known as Guinier's law. The region of validity of this equation depends on the shape of the particles. For spherical particles it is valid up to about $D.s = 0.6$.

The plot of log I(s) vs. s^2 (or ε^2) is a straight line in the Guinier region, the slope of which is proportional to $-R_g^2$, and from this, D may be determined.

The extrapolated value I(0) is proportional to the square of the volume of the particle and to the number of particles

$$I(0) = I_e N \Delta\rho^2 v^2 \qquad (3.14)$$

3.9.3 Integrated intensity

If the sample is isotropic (contains identical particles of random orientation) the observed intensity is the average value of $I(\vec{s})$ for a given value of s. Thus

$$\int I(\vec{s})dv_s = \int_0^\infty 4\pi s^2 I(s)ds \qquad (3.15)$$

Although I(s) is not known experimentally up to s = 0, the extrapolation of $s^2I(s)$ can be made with accuracy. It can be shown that the integral Equation (3.15), usually denoted as Q_0, is proportional to the total volume of the precipitated phase (N.v)

$$Q_0 = I_e \Delta\rho^2 Nv \qquad (3.16)$$

Absolute measurements of I(s) allow the determination of v if $(\rho-\rho_0)$ is known or, conversely, of $(\rho-\rho_0)$ if v is known. Equations (3.14) and (3.16) give the volume of the particle in terms of relative measurements only:

$$\frac{I(0)}{Q_0} = \frac{I_e \Delta\rho^2 Nv^2}{I_e \Delta\rho^2 Nv} = v \qquad (3.17)$$

3.9.4 Porod's Law

The solid line in Figure 3.10 shows the intensity diffracted by a dilute assembly of spheres of diameter D. For the wings (high angle end) of the scattering curve, Porod [3.24] has shown that if the particles are not strictly monodisperse the oscillations shown in Figure 3.10 disappear from the curve and

$$I(s) \underset{s\to\infty}{=} \frac{I_e \Delta\rho^2 S}{8\pi^3 s^4} \qquad (3.18)$$

where S is the total surface of the particles. Scattering from nearly identical particles show the Porod behaviour because small fluctuations in

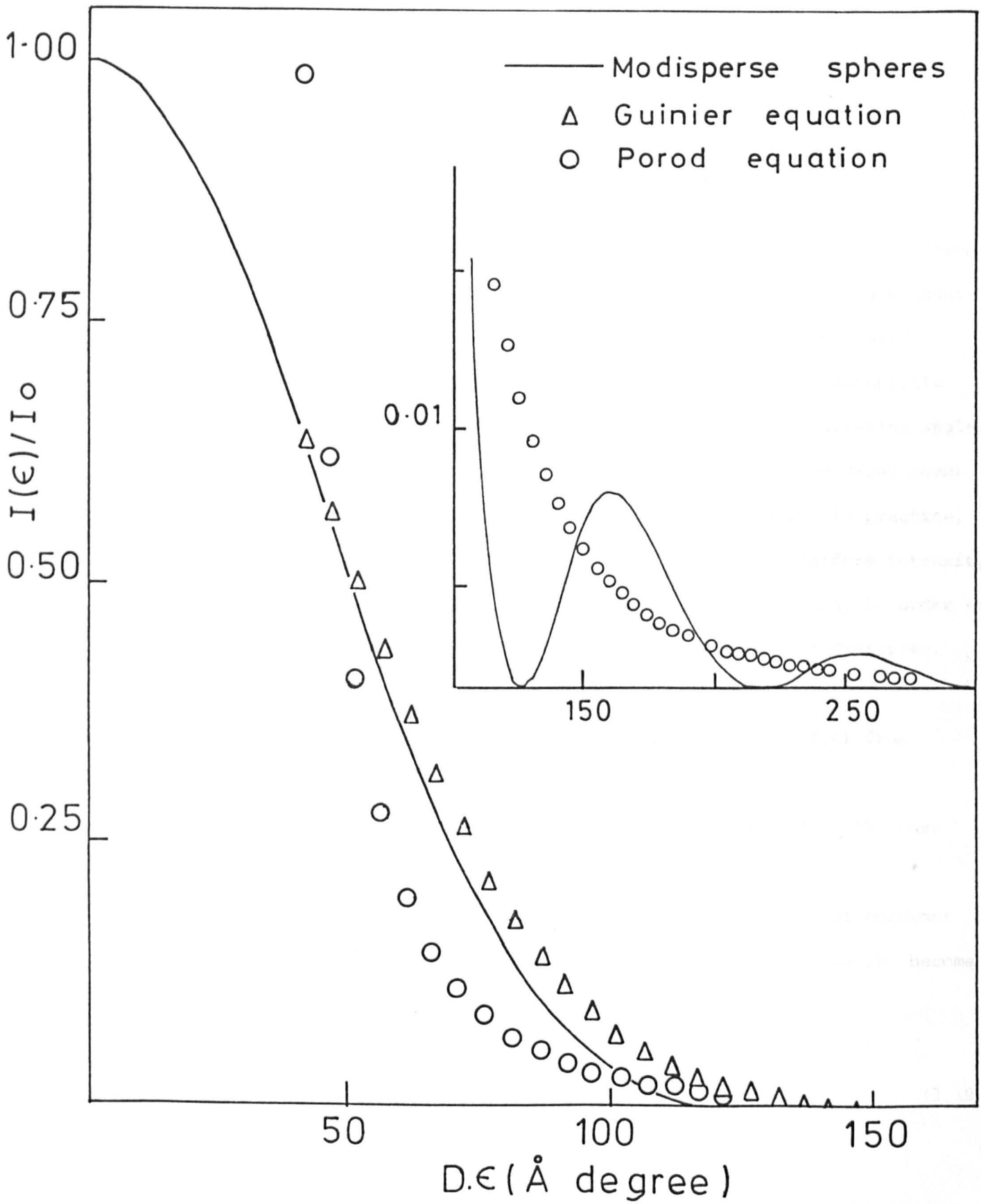

Fig. 3.10 Intensity scattered by a monodispersed system of spheres. The triangles represent the curve calculated from the Guinier equation and the spheres represent the Porod equation.

size are enough to supress the oscillations. This equation is valid for any shape of particle, so long as the orientations are random and none of the particle dimensions approach zero (needle or plate shaped). It is also valid for dissimilar particles and for a close-packed system of particles. Positive deviation from Porod's law can occur due to electron density fluctuations within the phases whilst diffuse inter-phase boundaries cause negative deviations [3.25]. The triangles in Figure 3.10 represent the Guinier equation and the dotted line shows the asymptotic function $9/2\ \pi^4\ (Ds)^4$ of Equation (3.18), in terms of the scattering angle, ε.

The equations of the preceding sections are valid if the X-ray beam has an infinitely small cross-section (point collimation). In practice, most of the experiments are carried out with flat beams (uniform intensity), obtained with a system of slits or with crystal monochromators, in order to achieve higher intensities. The scattering pattern is then distorted.

The experimental intensity J(s) can be used in two ways:

(a) It is possible to deduce the true scattering function I(s) from J(s) [3.26,3.27].

(b) The different laws established for I(s) may be adapted to the case of a flat beam.

It can be shown that for an 'infinitely high' flat beam of constant intensity and negligible width, Equations (3.13), (3.15) and (3.18) become [3.28] (Appendix 2).

$$J(s) = J(0)\ \exp\left[-\ 1/3\ R_g^2 (2\pi s)^2\right] \qquad (3.19)$$

where $J(0) = \dfrac{\sqrt{3\pi}}{2\pi R_g} I(0)$

$$\int_0^\infty 4\pi s^2 I(s)\,ds = \int_0^\infty 2\pi s J(s)\,ds \tag{3.20}$$

$$I(s)s^4 = \frac{\pi}{2} J(s)s^3 \tag{3.21}$$

respectively.

3.9.5 Debye's approach

Debye et al. [3.29] have shown that a completely random two phase system has an exponential correlation function. For slit-smeared intensities [3.30] (See Appendix 2 for definition of $J^1(s)$)

$$J^1(s) = \frac{A}{(1 + 4\pi^2 s^2 \bar{\ell}^{-2})^{3/2}} \tag{3.22}$$

where A is a constant and $\bar{\ell}$ is related to surface area per unit volume of glass, S_V, by

$$S_V = \frac{4\phi_1(1 - \phi_1)}{\bar{\ell}} \tag{3.23}$$

where ϕ_1 is the volume fraction of the dispersed phase.

A plot of $J(\varepsilon)^{-2/3}$ vs. ε^2 , ε (degrees), is thus linear and $\bar{\ell}$ may be derived from the relationship

$$\bar{\ell} = \frac{180\lambda}{2\pi^2}\left[\frac{\text{slope}}{\text{intercept}}\right] \tag{3.24}$$

The advantage of the Debye method is that experimentally and computationally it is much more rapid than the Porod method, since it is not necessary to collect data over the whole angular range and no graphical

integrations or extrapolations are required. However, it must be emphasised that the method is confined to completely random systems.

Brown et al. [3.31] have measured the surface areas of silica fillers in silicone rubber. Longman et al. [3.32] have determined the pore diameters and surface areas of a range of porous silicas used in gel permeation chromatography. Agreement between various techniques and the Debye method was satisfactory in both cases.

3.9.6 Polydispersed system of particles

When dealing with a system of particles of various shapes and sizes, the Guinier plot deviates from linearity, while the limiting tangent as $s \to 0$ gives a weighted gyration radius, defined by

$$R_g^2 = \frac{\Sigma R_i^2 v_i^2 \phi_i}{\Sigma v_i^2 \phi_i}$$

where R_i, v_i and ϕ_i are respectively, gyration radius, volume and fraction of particles of species i. If the particles are spherical, differing only in size

$$R_g^2 = \frac{\Sigma R_i^8 \phi_i}{\Sigma R_i^6 \phi_i} \qquad (3.25)$$

which defines an average diameter

$$D = \sqrt{20/3}\, R_g$$

heavily weighted towards the larger particles of the population.

For a polydispersed system Equation (3.17) may be written in terms of average values

$$\frac{I(0)}{Q_0} = < v^2 > / < v > \tag{3.26}$$

From equations (3.25) and (3.26), the following are obtained

$$D^2 = \frac{80}{3} < D^8 > / < D^6 > \tag{3.27}$$

$$D_v^3 = \frac{6}{\pi} \frac{I(0)}{Q_0} = < D^6 > / < D^3 > \tag{3.28}$$

where D_v is an average diameter calculated from the average volume of the particles. For a polydispersed system D is, in general, different from D_v. In practice it is not possible to obtain the limiting tangent for $s \to 0$. From an experimental curve, the maximum tangent gives information about the size of particles producing the scattering. However, larger particles can also be present.

3.9.7 Dense systems of identical particles

If the particles are close to each other the observed intensity is not the sum of the intensities scattered by the individual particles, since interference enters into play. If the particles are identical, distributed uniformly, and the orientations are completely random, the distribution is given by a function P(r), such that $4\pi r^2 P(r)dr$ is the number of particles whose centres are between r and r + dr of the origin chosen. For particles with spherical symmetry, the scattering power per particle, I(s), is [3.33]

$$I(s) = F^2(s)\left[1 + 2/sv_1 \int_0^\infty [P(r) - 1] \sin(2\pi sr)dr\right] \tag{3.29}$$

where $F^2(s)$ is the scattering power per particle when there is no inter-

ference and v_1 is the average volume available for each particle.

As the concentration increases (v_1 decreases), the second term in the bracket reduces the intensity scattered at the centre, since it is negative when s is very small. The curve then has a *hump* which becomes a maximum at high concentrations. There is no significant interference when s increases; thus the Porod formula (Equation (3.18)) is valid even for close-packed particles.

An approximation of Equation (3.29) for the scattering by spherically symmetrical particles is [3.34]

$$I(s) = I_e N F^2(s)\ v_1/(v_1 - (2\pi)^{3/2}\ \varepsilon_0\ \beta(s)) \tag{3.30}$$

where $\varepsilon_0 \sim 1$ and the interparticle interferences which modify the curve $F^2(s)$ are taken into account in the function $\beta(s)$, where

$$s\beta(s) = K \int_0^\infty r\alpha(r)\ \sin(sr)dr \tag{3.31}$$

with $\alpha(r) = e^{-\phi(r)/kT} - 1$; $\phi(r)$ being the potential energy function of a pair of particles whose centres are separated by a distance r, and K a constant.

If the concentration of the particles is not too high, the function $\beta(s)$ only slightly modifies the curve of $F^2(s)$. We can again trace the usual log I(s) vs. s^2 curve and verify that it still has a linear portion at small angles. The apparent radius of gyration R_1 determined in this way is not the true radius of gyration R_g. Mathematical manipulation of Equation (3.30) leads to [3.35]

$$R_1^2 = R_g^2 - \frac{3}{2}\ \frac{\beta''(0)}{v_1(2\pi)^{-3/2} - \beta(0)} \tag{3.32}$$

where $\beta''(0)$ is the value of the second derivative of B(s) for s = 0. R_1 approached R_g as the concentration decreases, i.e. the average volume v_1 increases. Furthermore, the experimentally observable decrease of the intensity I(0) with increasing concentration, together with certain theoretical considerations [3.36], have shown that, if Equation (3.30) is to be used, it is necessary to adopt a function $\beta(s)$, which is negative for small values of s. Now, when $|\beta(s)|$ is a maximum at s = 0, $\beta''(0)$ is of the opposite sign to that of $\beta''(0)$, so in our case $\beta''(0)$ must be positive. Therefore, R_1 *is less than* R_g and becomes even smaller, the greater the concentration of particles.

When considering a fluid of hard spheres showing no interactions other than impenetrability, $\beta(s)$ can be calculated [3.34], and Equation (3.30) becomes

$$I(s) = I_e N\phi^2(sR) \frac{1}{1 + (8v/v_1)\varepsilon_0\phi(2sR)} \qquad (3.33)$$

The corresponding curves are given in Figure 3.11 for various values of concentration $c = v/v_1$, where v is the volume of each particle. The intensity maxima are produced at larger and larger angles, the greater the concentration of scattering matter.

The curves of log I(s) vs. s^2 for c equal to: 0.00, 1/32 and 1/16 are plotted in Figure 3.12. These curves verify not only that the slope at the origin varies with concentration in the manner indicated before, but also that the curves depart more and more from linearity as the concentration increases.

Rothwell [3.37] has measured the scattering produced by a colloidal dispersion of uniform silica spheres in water (Ludox AS). Volume concentrations of 0.16, 0.08. 0.04, 0.02 and 0.01 were prepared. The diameter

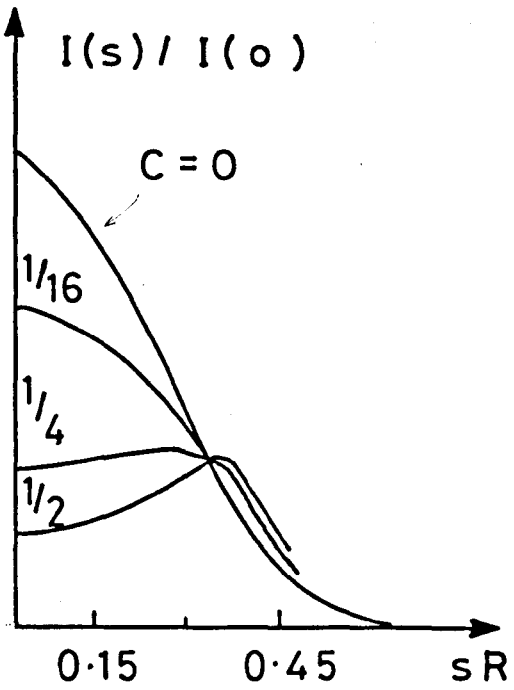

Fig. 3.11 Scattered intensity for spherical particles in increasing concentrations.

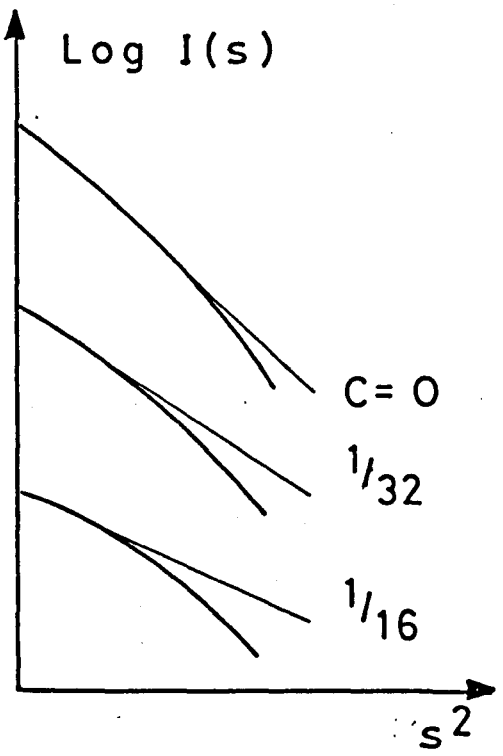

Fig. 3.12 Log I(s) vs. s^2 (Guinier plots) for spherical particles packed together in increasing concentrations.

of the particles was measured from the Guinier plots for the different concentrations. The experimental results shown in Table 3.7 are in

Table 3.7

SAXS DIAMETERS FOR DIFFERENT CONCENTRATIONS [3.37]

ϕ_1 (vol. fraction)	0.0	0.01	0.02	0.04	0.08	0.16
D(Å)	216	211	202	175	163	151

qualitative agreement with the preceding theory, showing that the Guinier diameter is *less than* the real diameter of the particles when dealing with concentrated systems, the discrepancy increasing with concentration.

The incipient peak observed in the scattering curves at about $s = 0.0091$ corresponds to the first subsidiary maximum in the theoretical scattering function for uniform spheres at $D.s = 1.84$. This gives $D = 202$ Å in good agreement with the Guinier plot values for low concentrations [3.37].

A complicated expression based on the preceding arguments was derived by Fournet [3.35] and applied to mixtures of homogeneous spheres of radii R and 2R. The curves representing the variation of scattered intensity as a function of angle are given in Figure 3.13. Two parameters were included in the calculation: ϕ_1, the ratio of the volume occupied by the particles to the total volume available; and x, the ratio of the mass of smaller particles to the total mass of the particles. Short-dashed curves correspond to $\phi_1 = 0.5$, long dashed curves to $\phi_1 = 0.125$ and full-line curves to the case of infinitely separated particles ($\phi_1 \to 0$). One feature of the

Fig. 3.13 Scattered intensity from mixtures of spheres of radii R and 2R. The parameter x denotes the ratio of the mass of the small spheres to the total mass of the mixture, and ϕ_1 represents the ratio of the effective volume of the spheres to the total volume.

——— $\phi_1 \to 0$; —— $\phi_1 = 0.125$; --- $\phi_1 = 0.50$.

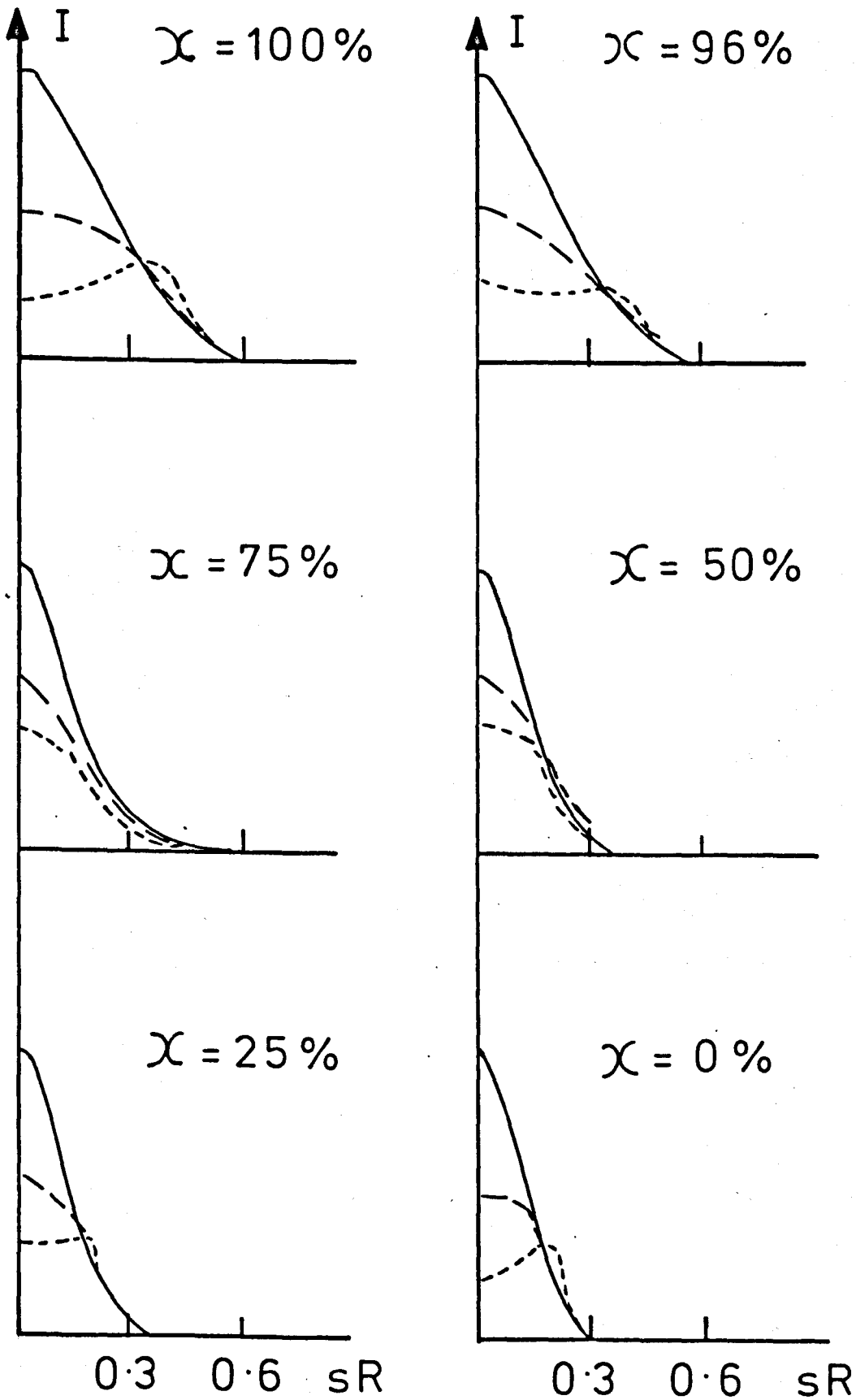
I
χ = 100%
I
χ = 96%
χ = 75%
χ = 50%
χ = 25%
χ = 0%
0·3
0·6
sR
0·3
0·6
sR

intensity curves is that for constant ϕ_1, the more homogeneous the mixture the more they tend to show maxima. For example, the curve for $\phi_1 = 0.5$ possesses a maximum only if the mass of smaller particles represents more than 95 or less than 25 per cent of the total mass.

Based on this work Guinier and Fournet [3.38] concluded that "In a mixture of non-identical particles of arbitrary forms and with random distribution (no long-range order) it is improbable that the packing of particles will lead to large changes in the scattering curves and that thus the laws for widely separated particles can furnish the orders of magnitude of the scattering phenomena."

3.9.8 Experimental

The X-ray intensity versus scattering angle (ε) curves were obtained with Rigaku-Denki equipment using the CuKα radiation, a graphite monochromator and a scintillator detector. A schematic diagram of the experimental set up is shown in Figure 3.14. G is the X-ray source, f1, f2, f3, f4 and f5 slits used to collimate the beam and to decrease the parasitic (air and slits) scattering, S the specimen, M a graphite monochromator and D the scintillator detector.

Absorption of X-rays

The scattered intensity depends on the volume V of irradiated material and also on its absorption characteristics. This may be expressed in the following way:

$$I = KI_0V \exp(-\mu\rho x) \qquad (3.34)$$

where K is a constant, I_0 the intensity of the incident radiation and I the

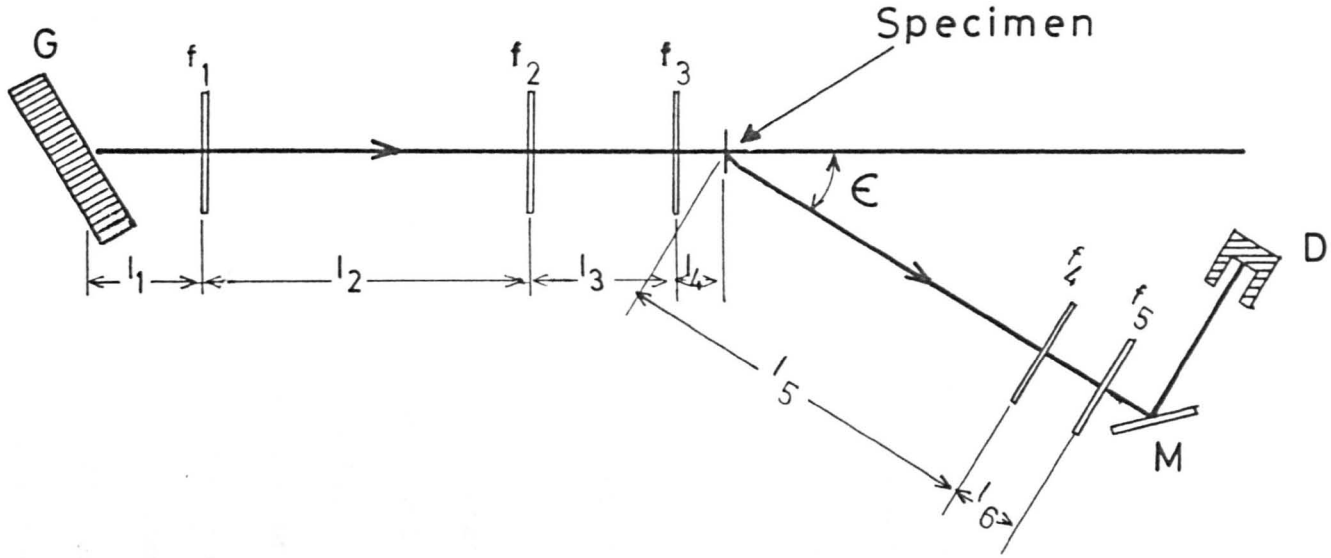

Fig. 3.14 Schematic diagram of the SAXS equipment.

l_1 = 80; l_2 = 220; l_3 = 95; l_4 = 30; l_5 = 500 and l_6 = 40 mm

f_1 = 0.1; f_2 = 0.05; f_3 = 0.05; f_4 = 0.3 and f_5 = 0.1 mm

intensity of the transmitted radiation at $\varepsilon = 0$, ρ the mass density of the specimen, μ the mass absorption coefficient and x the effective thickness of the sample. From Equation (3.34) it can be easily shown that for $x = 1/\mu\rho$ the ratio I/I_0 is a maximum. For a glass with 28.3 mol% BaO; $\rho = 3.40$ g cm^{-3} and $\mu = 179.8$ cm^2/g (calculated from international tables of crystallography). Therefore, the optimum thickness of the specimens for SAXS is 0.016 mm. The actual samples used were ground and polished to approximately 20 x 6 x 0.03 mm, because it was difficult to obtain specimens thinner than 0.03 mm having such a relatively large area.

The attenuation coefficient (A) of each sample was calculated by means of the equation $A = \ln(I_0/I)$, where I_0 and I were measured experimentally at $\varepsilon = 0°$. For this, 20 KV and 35 mA were applied to the X-rays generator and Ni filters were placed in front of the detector.

Measurement of the scattered intensities by the air and by the glass specimens

40 KV and 35 mA were applied to the X-rays generator. The samples (IS) and air (IA) scattering intensities were measured independently, by step scanning from 0.10 to 1.2°, in 0.025° intervals. The 'counting' times varied from 400 to 2000 sec at each angle, depending on the scattering intensity of the specimen. All the measurements were automatically recorded. Also, the intensity of the scattered radiation of a standard porous vitreous carbon (IVC) sample was measured twice (IVC_1 and IVC_2), at a fixed angle ε_1, in order to correct the experimental curves for variations in the intensity of the primary beam. The background intensity BK was measured at the end. The overall sequence of measurements was:

$$A \rightarrow IS(\varepsilon) \rightarrow IVC_1(\varepsilon_1) \rightarrow IA(\varepsilon) \rightarrow IVC_2(\varepsilon_1) \rightarrow BK$$

Corrections and normalization of the experimental curves

The results were normalized to a constant sample thickness, and corrected for absorption, fluctuations in the intensity of the primary beam, and parasitic (air and slits) and background intensity (cosmic rays and electronic noise) by means of the following equation

$$J(\varepsilon) = \frac{1}{\ln A}\left[\frac{IS(\varepsilon)A}{IVC_1} - \frac{IA(\varepsilon)}{IVC_2} - \frac{BK}{IVC}(A-1)\right] \text{ (a.u.)} \qquad (3.35)$$

where $J(\varepsilon)$ is the normalized and corrected intensity used to compute the results, BK is the background intensity, which was much smaller than IS and IA, and IVC is the average of IVC_1 and IVC_2.

Infinitely high X-ray beam

For the primary beam to be of 'infinite' length, the radiation at the ends of the beam cross-section must not be able to send radiation into the counter slit [3.39]. This can be expressed in terms of the following relation

$$\varepsilon_0 \text{ (degrees)} = \frac{(L-\ell)}{2R}\frac{180}{\pi} \qquad (3.36)$$

where L is the length of the homogeneous part of the X-rays bean, ℓ is the length of the measuring slit and R is the distance sample-detector. For the experimental set up used, $\varepsilon_0 \simeq 0.8°$, i.e. the beam could be considered 'infinite' if the intensity $J(\varepsilon)$ was negligible at $\varepsilon = 0.8°$. This condition was verified for most specimens studied.

CHAPTER 4

EXPERIMENTAL RESULTS

The preparation of the glasses and chemical analysis were described in Chapter 3. The designation of each glass indicates the molar percentage of BaO or Li_2O, e.g. glass 17.7Li_2O contains 17.7 mol% Li_2O by analysis.

4.1 Crystal Nucleation in $BaO-SiO_2$ Glasses

4.1.1 Crystal nucleation in glasses undergoing phase separation

Having heat-treated and prepared the specimens, as described in section 3.5, micrographs were obtained and the size distributions and number of crystals per unit area were measured. The numbers of crystals per unit volume of glass were then calculated by means of Equation (3.1). Typical micrographs of the several glasses studied are shown in Figures 4.1a, b and c.

The heterogeneous nucleation of $BaO.2SiO_2$ spherulites was observed to occur on the surface of bubbles, cracks and external surfaces of the heat-treated glasses. Some examples are shown in Figure 4.2. It should be emphasized, however, that the number of heterogeneously nucleated crystals was negligible compared with the number of crystals in the bulk of the glass. It is considered probable that these crystals in the bulk were nucleated *homogeneously* due to the very high undercoolings necessary to observe internal nucleation.

Figures 4.1a and b show that the $BaO.2SiO_2$ (BS_2) spherulites in glasses 27.0, 28.3A, 28.3B, 29.7H and 29.0 are very similar in shape, being approximately spherical. The stoichiometric glasses 33.1U, 33.2B, 33.2C, 33.3A and 33.3P have more "spiky" crystals, especially when the "development" heat-treatment was short, i.e. for specimens nucleated at temperatures close to

Fig. 4.1a Optical micrographs (reflected light) of $BaO-SiO_2$ glasses. From left to right and from top to bottom:
Glass 27.0: 7 h at 752°C + 22 min at 815°C
Glass 28.3B: 7 h at 752°C + 22 min at 815°C
Glass 28.3B: 9.5 h at 752°C + 22 min at 815°C
Glass 33.2C: 40 min at 765°C + 14 min at 815°C
⊢—⊣ = 20 µm

Fig. 4.1b Optical micrographs (reflected light) of $BaO-SiO_2$ glasses. From left to right and from top to bottom:
Glass 28.3A: 6.5 h at 760°C + 22 min at 815°C
Glass 28.3A: 8.0 h at 760°C + 22 min at 815°C
Glass 28.3A: 15.3 h at 760°C
Glass 33.3A: 8.0 h at 760°C
⊢—⊣ = 10 µm

Fig. 4.1c Optical micrographs (transmitted light) of $BaO-SiO_2$ glasses. From top to bottom:
Glass 28.3B: 1.5 h at 800°C
Glass 29.9: 1.5 h at 800°C
Glass 33.3P: 30 min at 800°C
⊢—⊣ = 40 µm

Fig. 4.2 Heterogeneous nucleation of BS_2 spherulites in $BaO-SiO_2$ glasses
⊢—⊣ = 10 µm

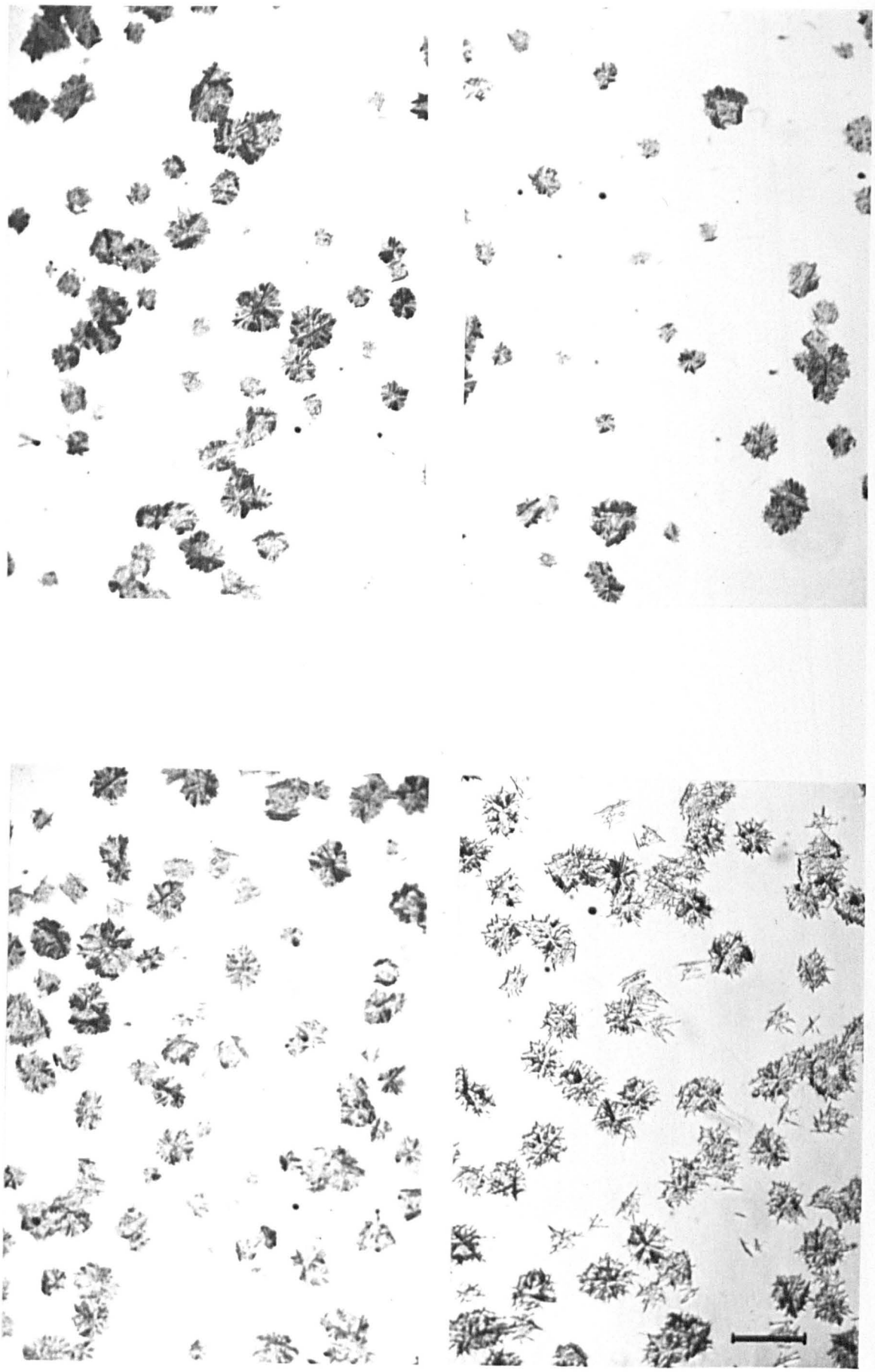

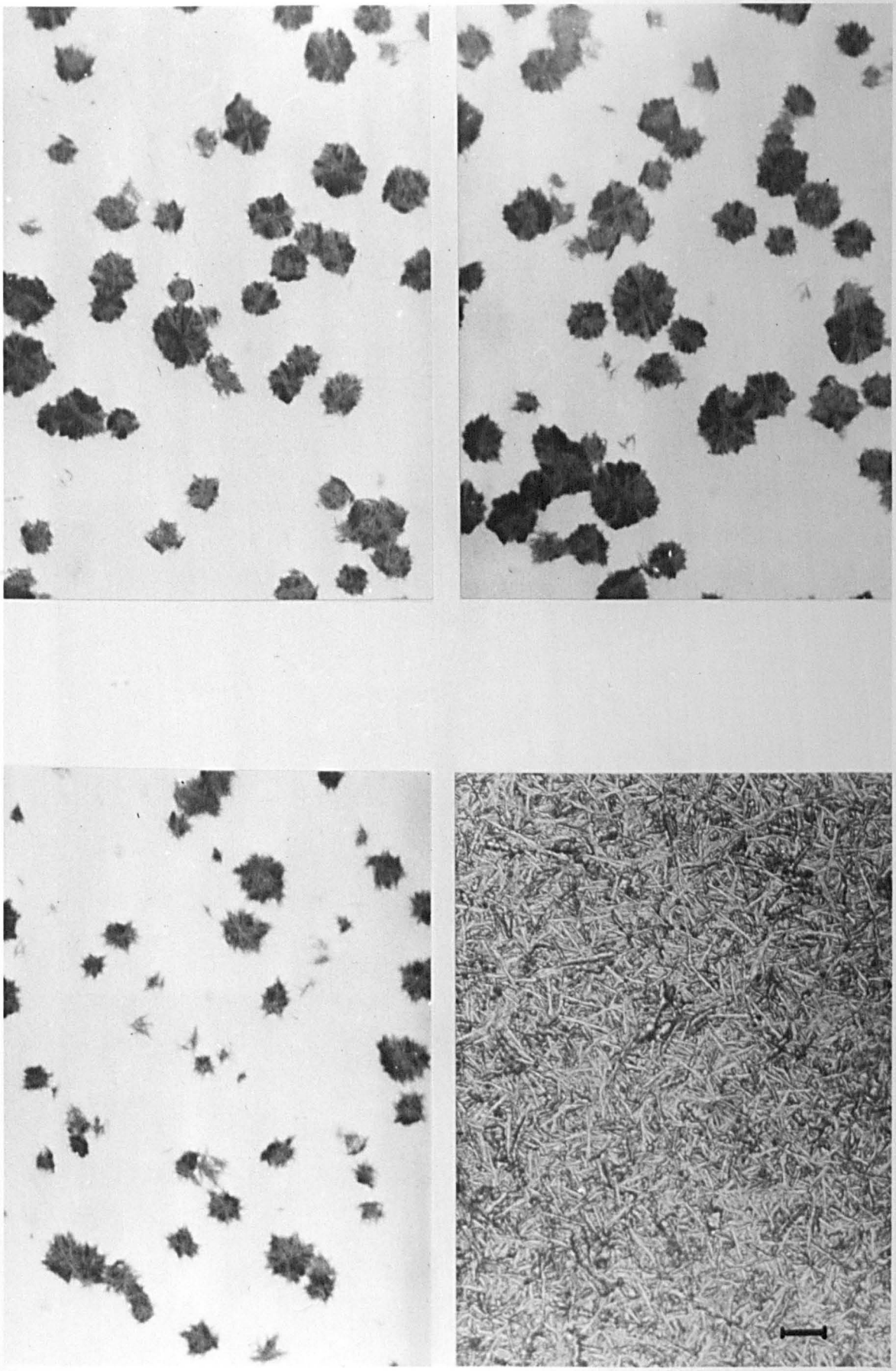

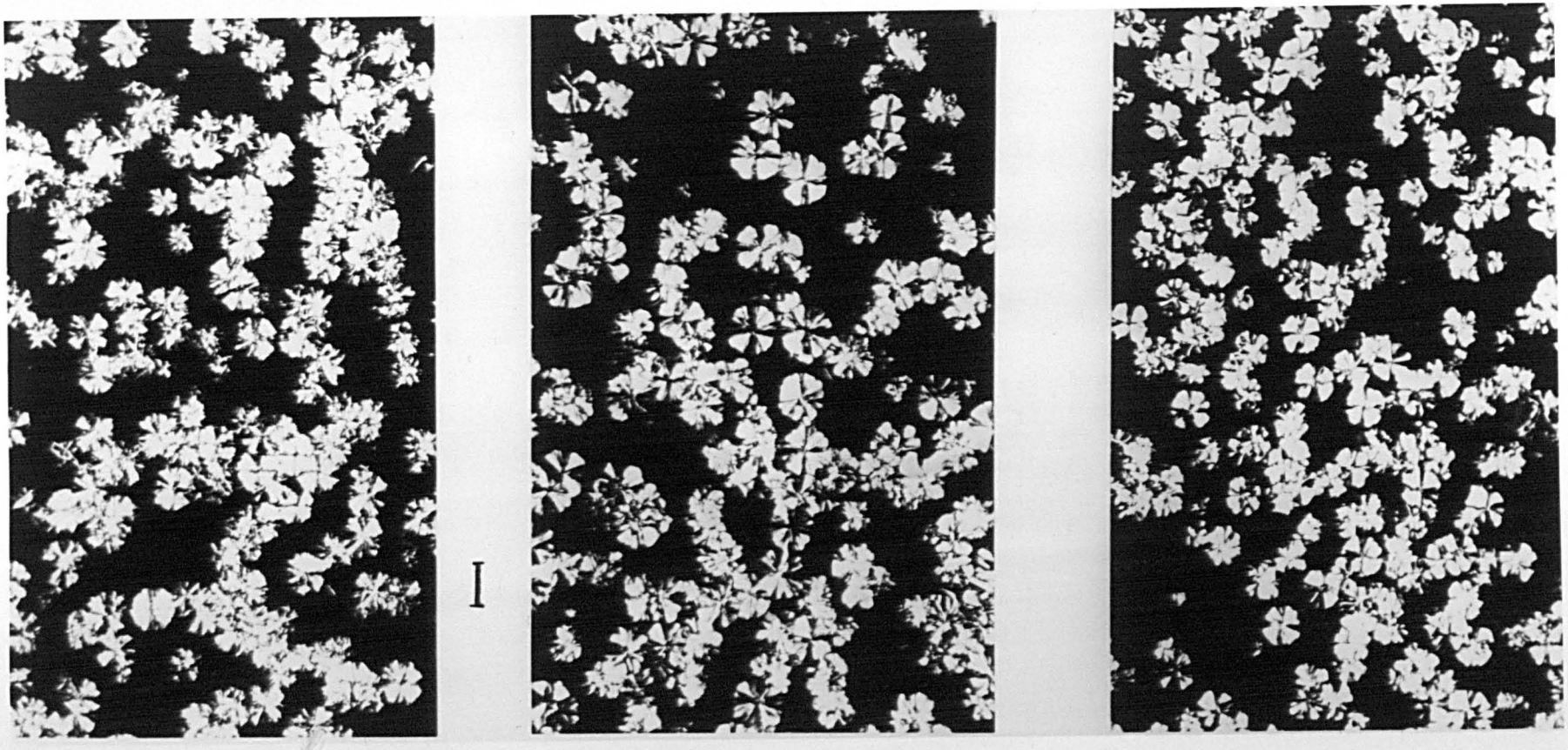

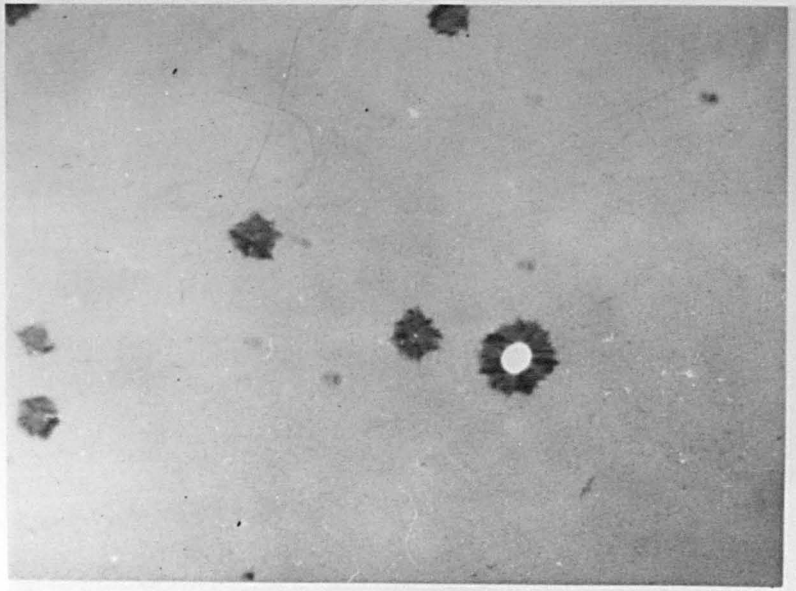

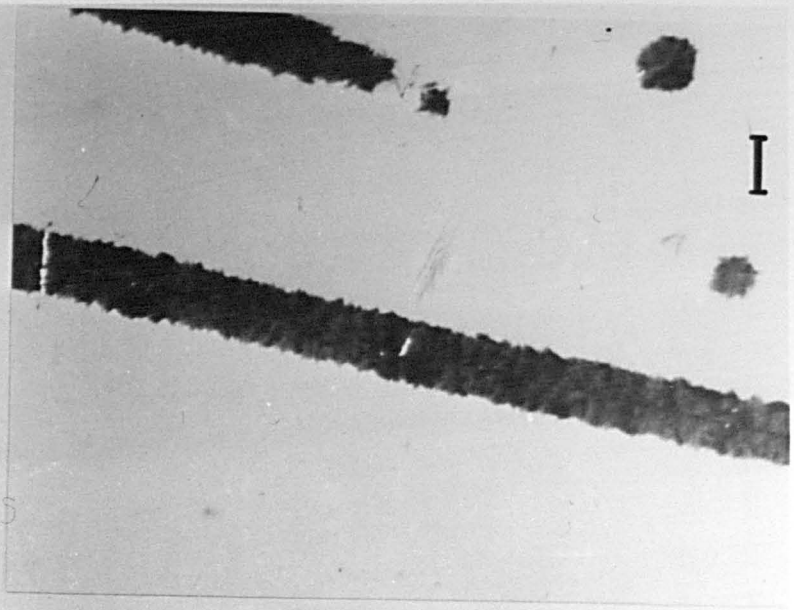
I

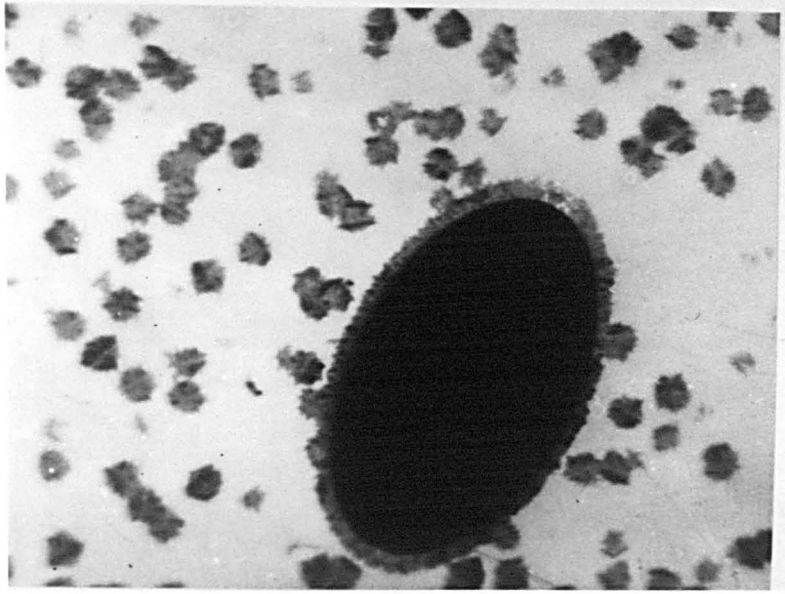

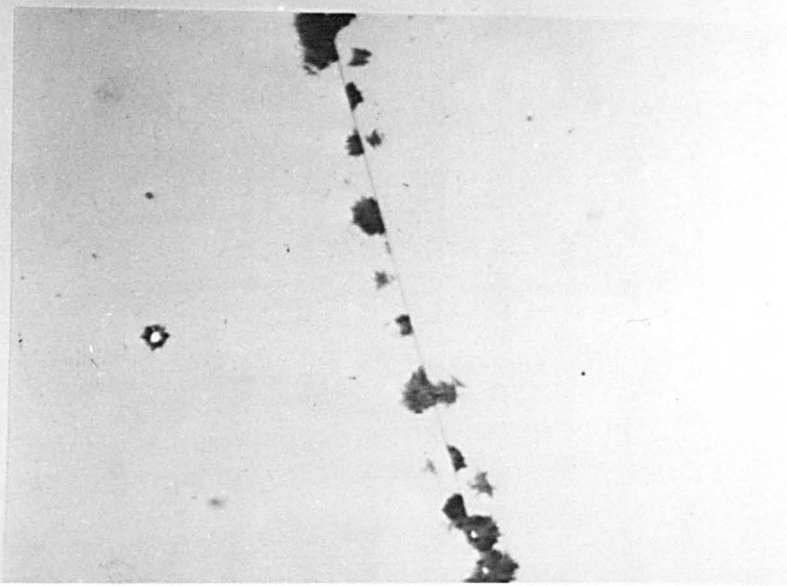

the maximum rate of nucleation (~ 700°C). The spherulitic character of the BS_2 crystals can be clearly seen in the transmission micrographs of Figure 4.1c.

At this stage, it must be stressed that the objective of the nucleation studies described below was the establishment of possible relationships between amorphous phase separation (APS) and the nucleation and growth of crystals. For that purpose, the nucleation behaviour of several glasses with compositions inside the miscibility gap (glasses 27.0, 28.3A, 28.3B, 29.7H and 29.9), and some glasses close to the barium disilicate composition, i.e. outside the gap (33.3A, 33.2C and 33.3P), was studied at several temperatures above the transformation range. These studies were correlated with SAXS and TEM studies of the liquid-liquid immiscibility in the same system.

In Figure 4.3, crystal nucleation density (N_V) versus time curves are plotted for glasses 28.3A and 29.7H nucleated at 718°C . The nucleation rate, dN_V/dt, is *constant* for glass 29.7H and *increases* continuously with time for glass 28.3A.

Figure 4.4 shows a similar trend for both glasses nucleated at 745°C. The nucleation rate of glass 28.3A *increases* gradually up to about 7 hours, *overcomes* dN_V/dt of glass 29.7H, and becomes *constant*. The experimental points obtained with a single stage heat-treatment (•) are also shown, and are lower than the values obtained with a double stage treatment. Detailed explanations for this apparent discrepancy were discussed in section 3.5 and are given in Appendix 1. The same figure shows that the nucleation rate of the stoichiometric glass 33.3A is about 20 times higher than the maximum dN_V/dt of glass 28.3A, and 40 times higher than dN_V/dt of glass 29.7H. As will be shown later, the nucleation rate of glasses having compositions close to the stoichiometric composition of the crystals, BS_2, are much higher than dN_V/dt of other compositions at all temperatures.

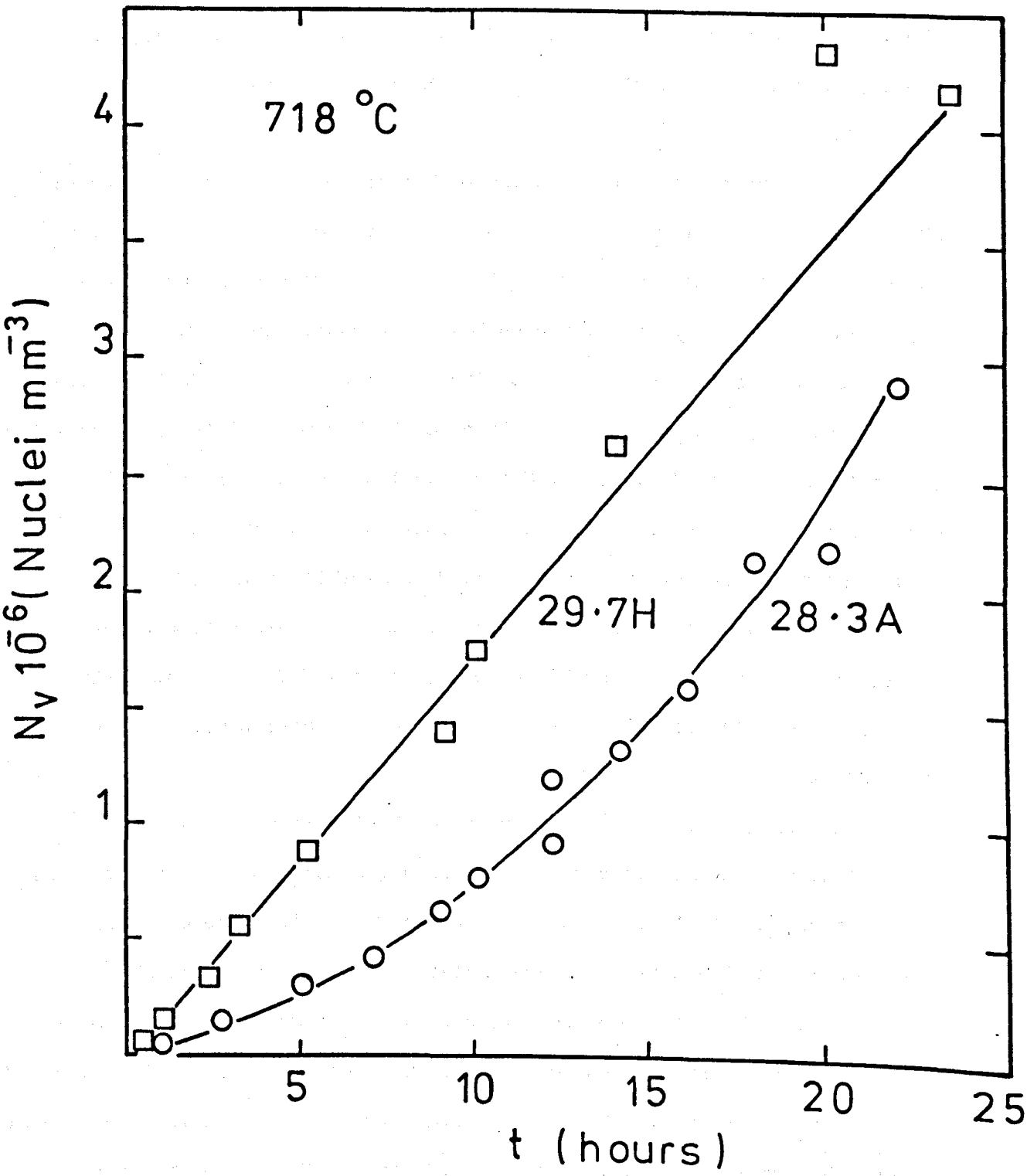

Fig. 4.3 Number of crystals per unit volume (N_v) versus time plots for glasses 28.3A and 29.7H nucleated at 718°C.

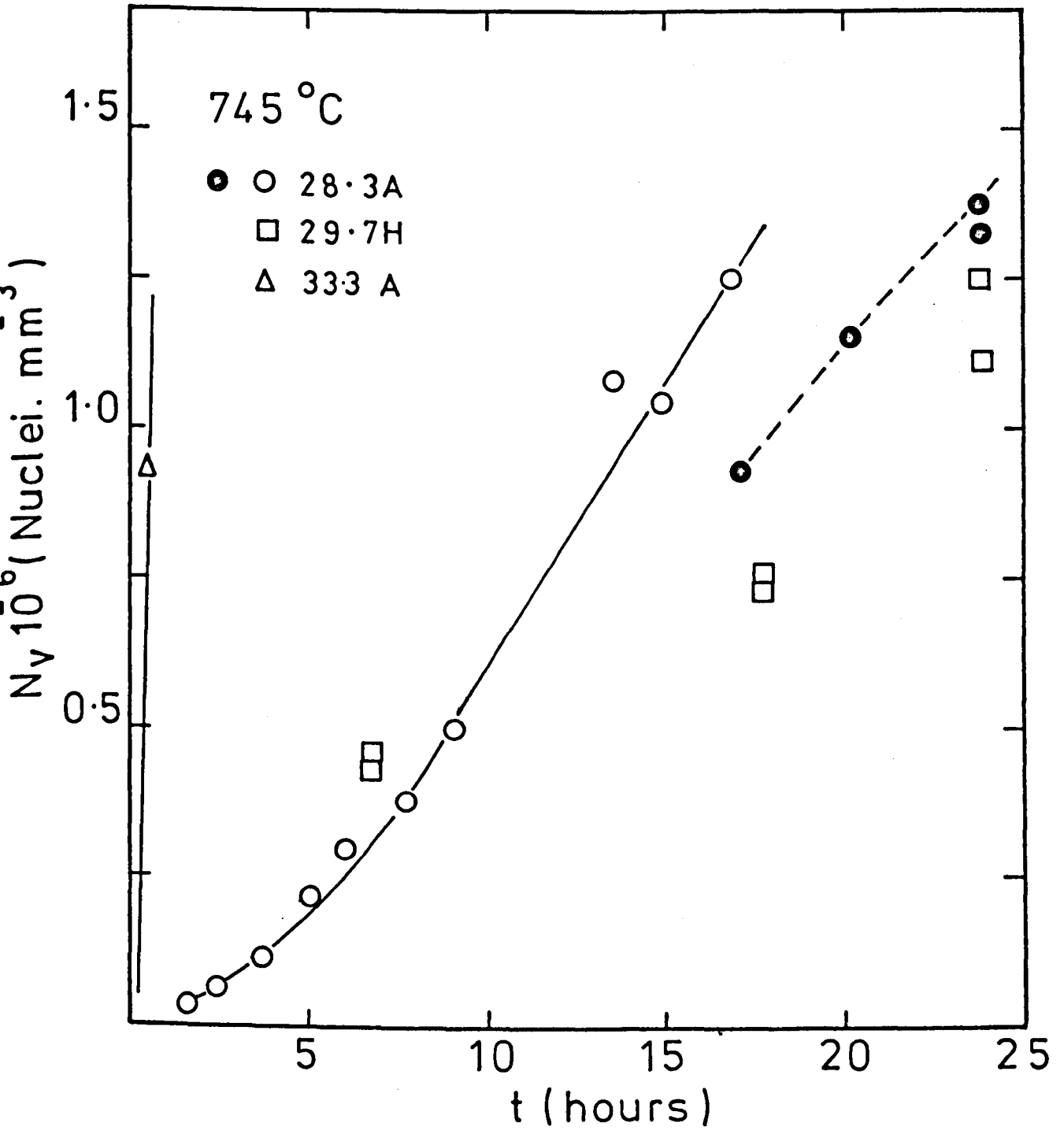

Fig. 4.4 Crystal nucleation (N_V versus time) plots for glasses 28.3B, 29.7H and 33.3A nucleated at 745°C.
(●) single stage heat treatment

Glasses 28.3A and 29.7H were also nucleated at 760°C, and the N_V versus time curves are shown in Figure 4.5. The nucleation rate of glass 28.3A is initially lower, reaches a *maximum* value at about 2.5 hours, overcoming the constant rate of glass 29.7H, and levels off after 3 hours approaching a constant value. Even at this stage, dN_V/dt for glass 28.3A is *higher* than the steady state rate of glass 29.7H. With the exception of the inflexion, which gives a maximum value for dN_V/dt of glass 28.3A at 760°C, the general behaviour is similar at 718°C, 745°C and 760°C.

In order to check the reproducibility of the experimental data, and to test the possibility that the observed inflexion in the nucleation curve of glass 28.3A was caused by the "development" heat treatment, a further "growth" treatment of 8 min at 815°C was given to the same specimens used before. The new values of N_V are compared with the old ones in Figure 4.6. The agreement is excellent.

Figure 4.7 shows the nucleation curve for glass 28.3B *first* heat-treated at 821°C for 22 min to cause a pronounced development of the amorphous phase separation. The blueish appearance of the glass samples and the rather large size of the silica-rich droplets (Figure 4.14a) after this treatment was an indication that the APS had reached an advanced stage. These specimens will be called 28.3BPS. Then, the same specimens were subjected to the common double-stage heat-treatment at 743°C and 820°C. A few crystals, much bigger than the average size, could be seen in the micrographs. These were formed during the first heat treatment and were neglected. The nucleation rate in glass 28.3BPS is *constant* and *higher* than the *constant* dN_V/dt of glass 29.7H. The nucleation rates of glasses 28.3A and 28.3B (two different melts of the same chemical composition) are equal, showing the reproducibility of the present experiments, and *increase* continuously up to about 7 hours, when they approach a constant value which is *higher* than dN_V/dt for glasses 28.3BPS and 29.7H.

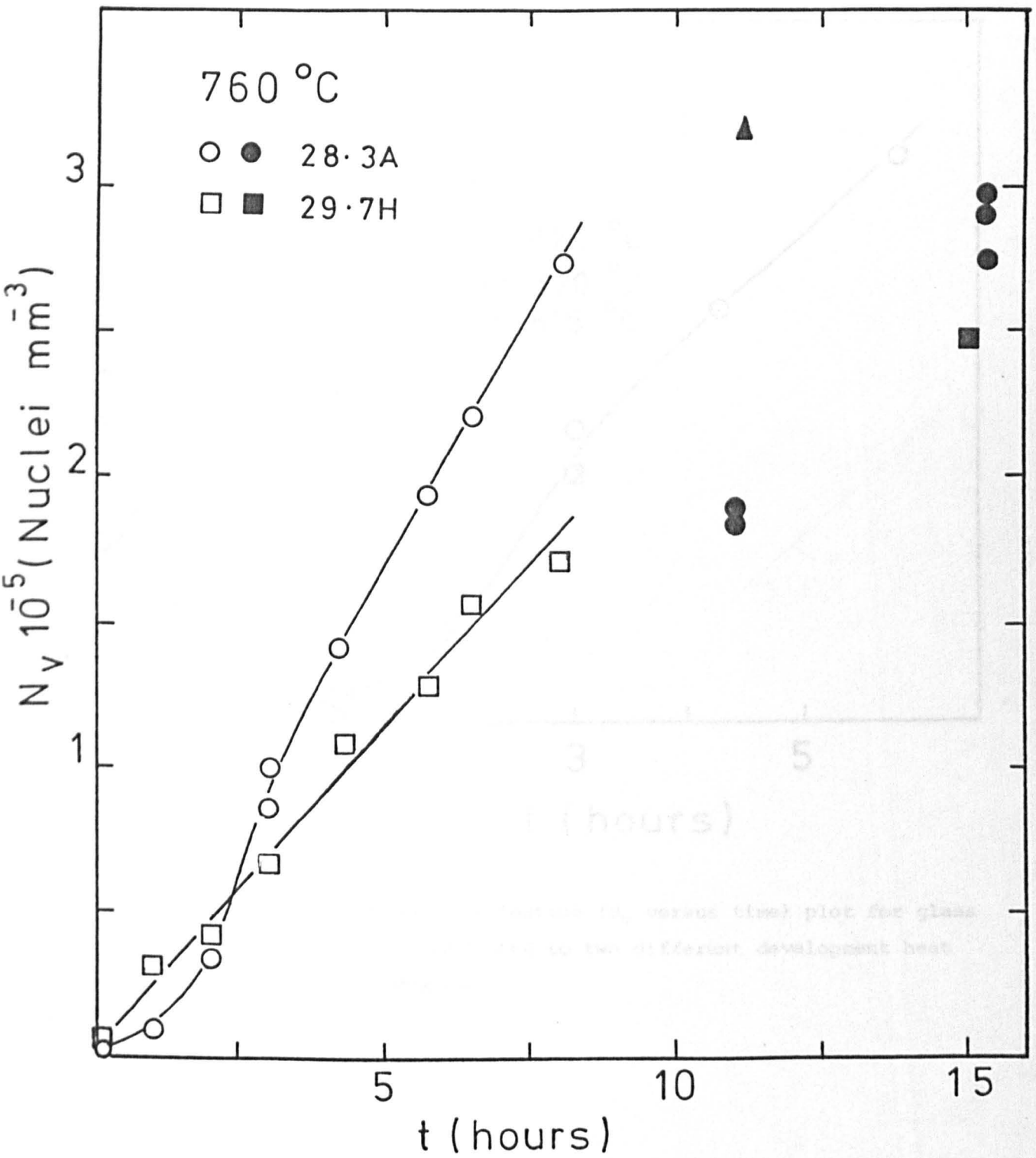

Fig. 4.5 Crystal nucleation (N_v versus time) plots for glasses 28.3A and 29.7H nucleated at 760°C. (○, □) double-stage; (●,■) single-stage heat treatment; (▲) short development treatment.

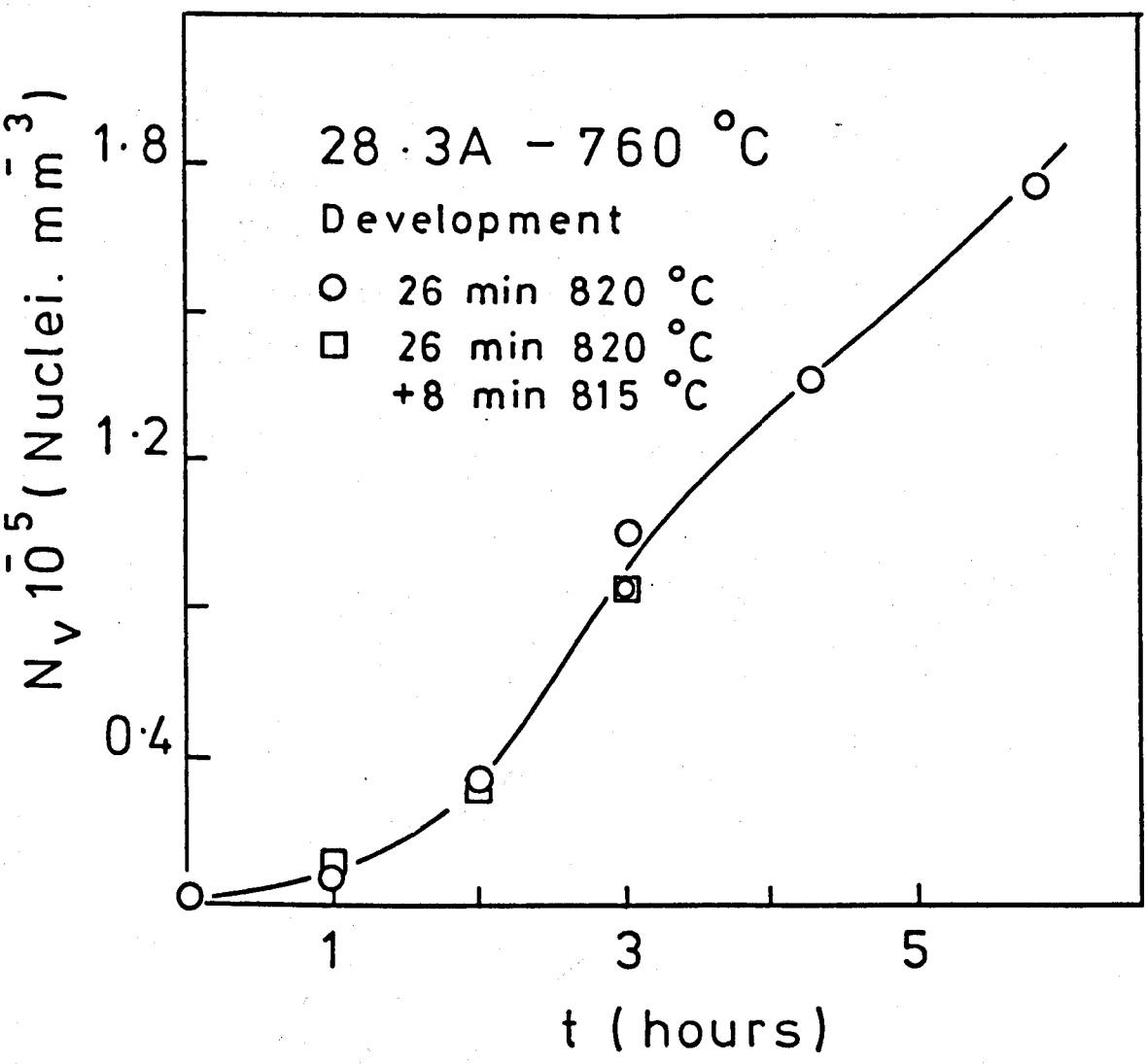

Fig. 4.6 Crystal nucleation (N_v versus time) plot for glass 28.3A subjected to two different development heat treatments.

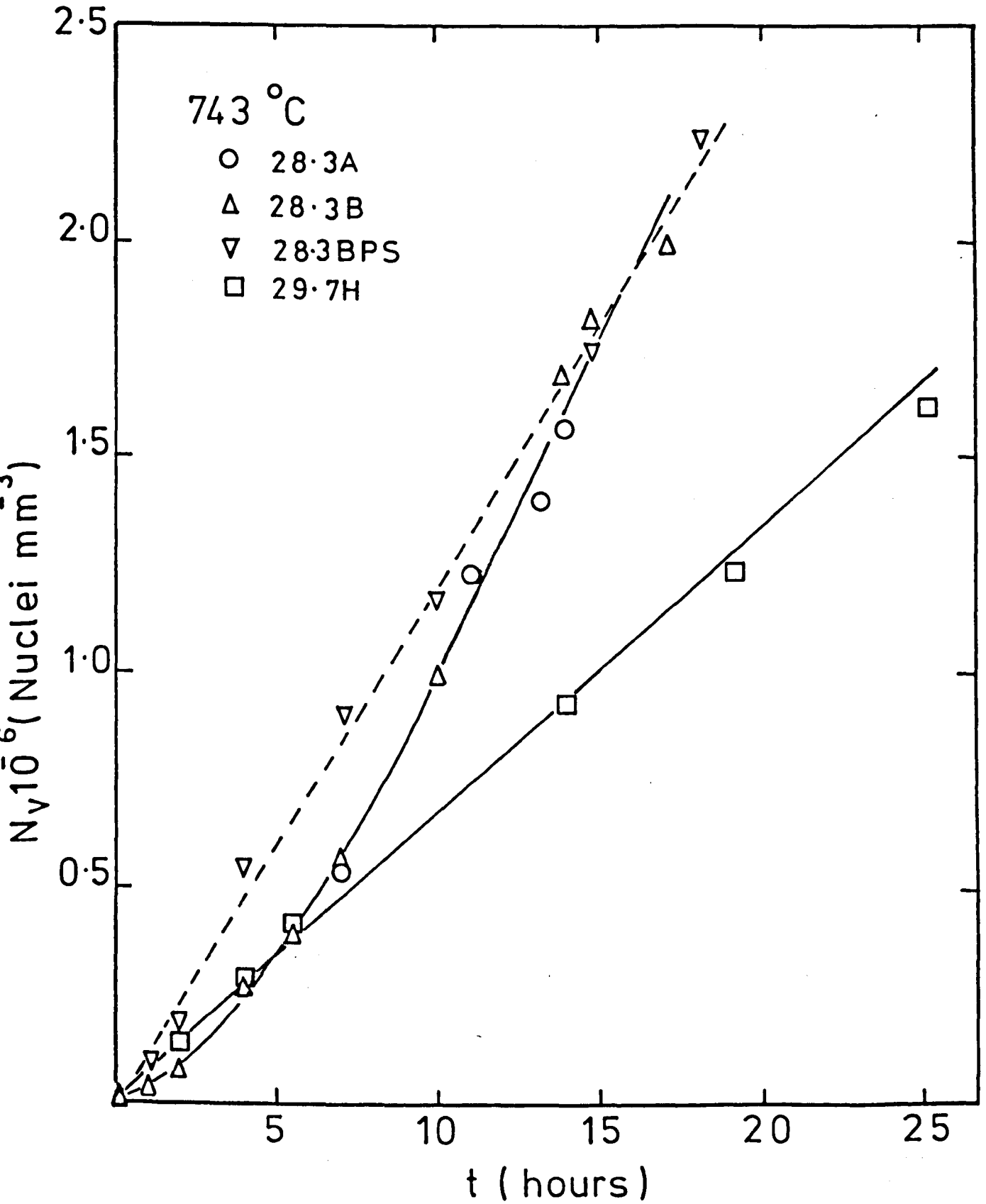

Fig. 4.7 Crystal nucleation (N_V versus time) plots for glasses 28.3A, 28.3B, 28.3BPS and 29.7H nucleated at 743°C.
---- phase separated at 821°C for 22 min, ——— as quenched.

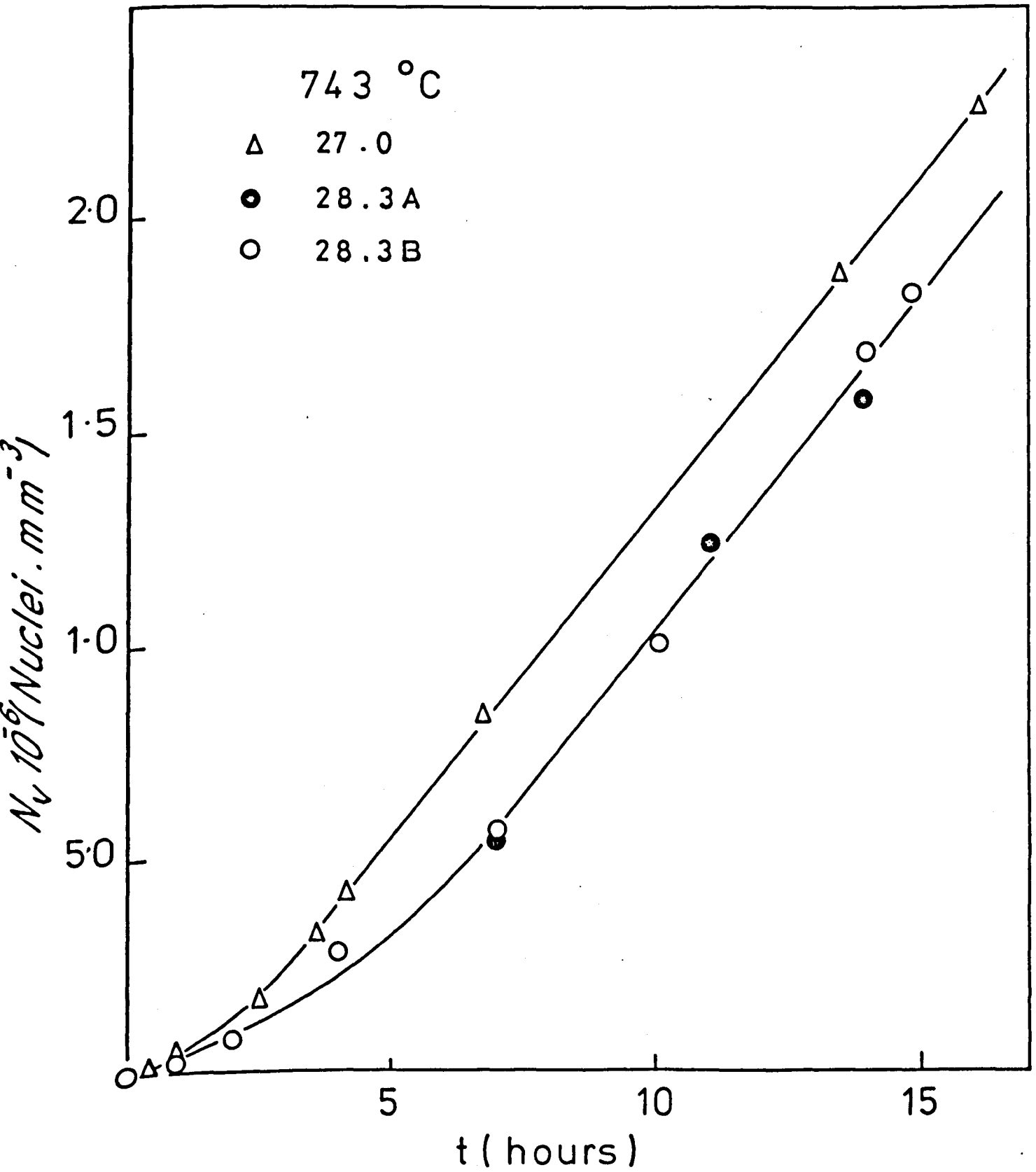

Fig. 4.8 Crystal nucleation (N_v versus time) plots for glasses 27.0, 28.3A and 28.3B nucleated at 743°C.

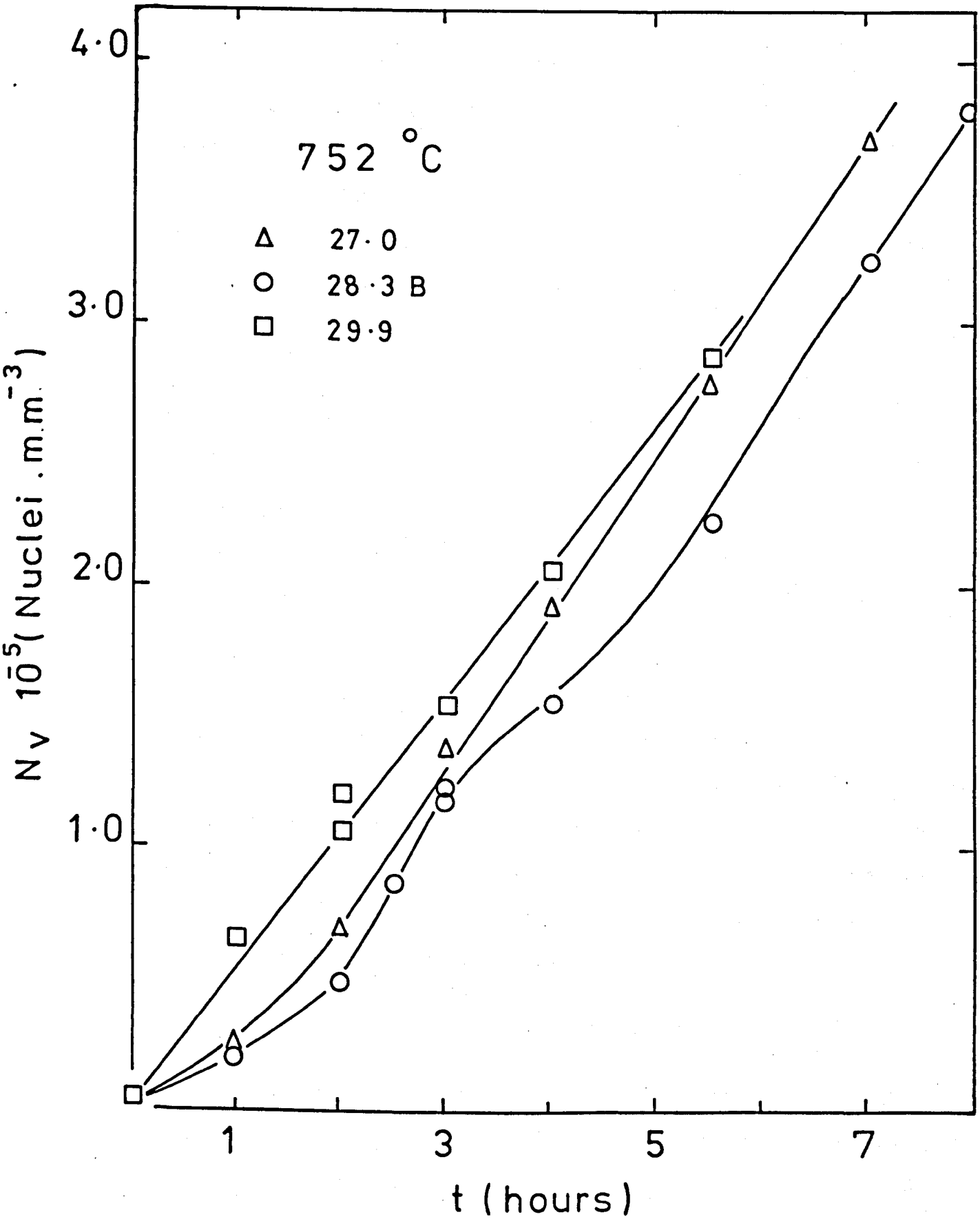

Fig. 4.9 Crystal nucleation (N_v versus time) plots for glasses 27.0, 28.3B and 29.9 nucleated at 752°C.

The nucleation curve of glass 27.0 heated at 743°C is shown in Figure 4.8 together with the curve for glasses 28.3A and 28.3B. The nucleation rate of glass 27.0 *increases* up to about 2 hours, which is much shorter than the 7 hours period required for glasses 28.3A and 28.3B to reach an equilibrium rate. After these periods, the crystal nucleation rates of the three glasses are *constant* and *equal*.

Figure 4.9 shows the crystal nucleation density (N_V) versus time curves for glasses 27.0, 28.3B and 29.9 nucleated at 752°C. dN_V/dt of glass 28.3B *increases* up to about 3 hours passing through a *maximum*, decrease and becomes *constant* after about 5 hours of heat treatment. The nucleation rate of glass 27.0 *increases* up to about 2 hours, when it approaches a constant value *equal* to the nucleation rate of glass 28.3B, and higher than the constant rate of glass 29.9.

Comments

It is clear that the crystal nucleation rates of glasses 27.0, 28.3A and 28.3B, which are undergoing amorphous phase separation, *increase* with time, in some cases passing through a maximum, and approach a *constant* value. The nucleation rates of glasses 29.7H and 29.9, which do not phase separate as will be shown later, are *constant* from the beginning, being higher than dN_V/dt of the phase separating glasses only in the initial parts of the nucleation curves (for short nucleation treatments).

4.1.2 Crystal nucleation in stoichiometric $BaO.2SiO_2$ (BS_2) glasses

It was of interest to study the nucleation behaviour of spherulites in BS_2 glasses for comparison with glasses inside the miscibility gap, and also for a quantitative test of the classical nucleation theory to be described later. In these glasses, the shape of the spherulitic crystals departs from the spherical symmetry making the determination of the shape factor,

K(q), in Equation (3.1) very difficult. Therefore, only the minor axis of the *largest* crystal, D_M, on the micrographs was measured, and the following relation was used for the calculation of N_V:

$$N_V = N_S/D_M \qquad (4.1)$$

This equation is strictly applicable only if all crystals are spheres of equal size. However, it can be shown by mathematical manipulation of Equations (3.1) and (3. 2), that the errors in neglecting the factors $2\bar{z}/\pi$ and K(q) are in opposition, which can lead to a substantial decrease in the error in using Equation (4.1). For the case under study, i.e. a size distribution of elongated crystals, this is particularly true. Hence, equation (4.1) is a reasonably good approximation. It should also be mentioned that due to the very high nucleation rates in BS_2 glasses, the times of heat-treatment were limited to two hours, causing the values of nucleation rates to be underestimated, especially at temperatures close and below the transformation range, due to non-steady state effects.

Figure 4.10 shows the crystal nucleation densities versus time curves of glasses 33.2C and 33.3A from 685°C to 765°C. Pronounced induction periods are observed below 718°C, steady state conditions being rapidly established for higher temperatures. Table 4.1 shows the crystal nucleation rates calculated from the slopes of these curves, together with the values obtained by Rowlands [1.47] for a glass very close in composition to 33.2C and 33.3A, but with 0.33 wt% Al_2O_3 and a higher water content. The general agreement is good. These nucleation rates are much *higher* than that in glasses 27.0, 28.3A, 28.3B, 29.7H and 29.9.

Table 4.1

CRYSTAL NUCLEATION RATES IN BARIUM DISILICATE GLASSES ($mm^{-3}.s^{-1}$)

BS_2 [1.47]		33.3A		33.2C	
T(°C)	I	T(°C)	I	T(°C)	I
662	42*	-	-	-	-
680	206*	-	-	685	125*
700	1870*	-	-	706	1490*
718	1450	718	1042	-	-
729	798	-	-	731	644
740	459	-	-	-	-
748	280	745	461	749	415
760	134	760	222	-	-
-	-	765	163	765	163
780	27	-	-	-	-

* underestimated due to induction periods

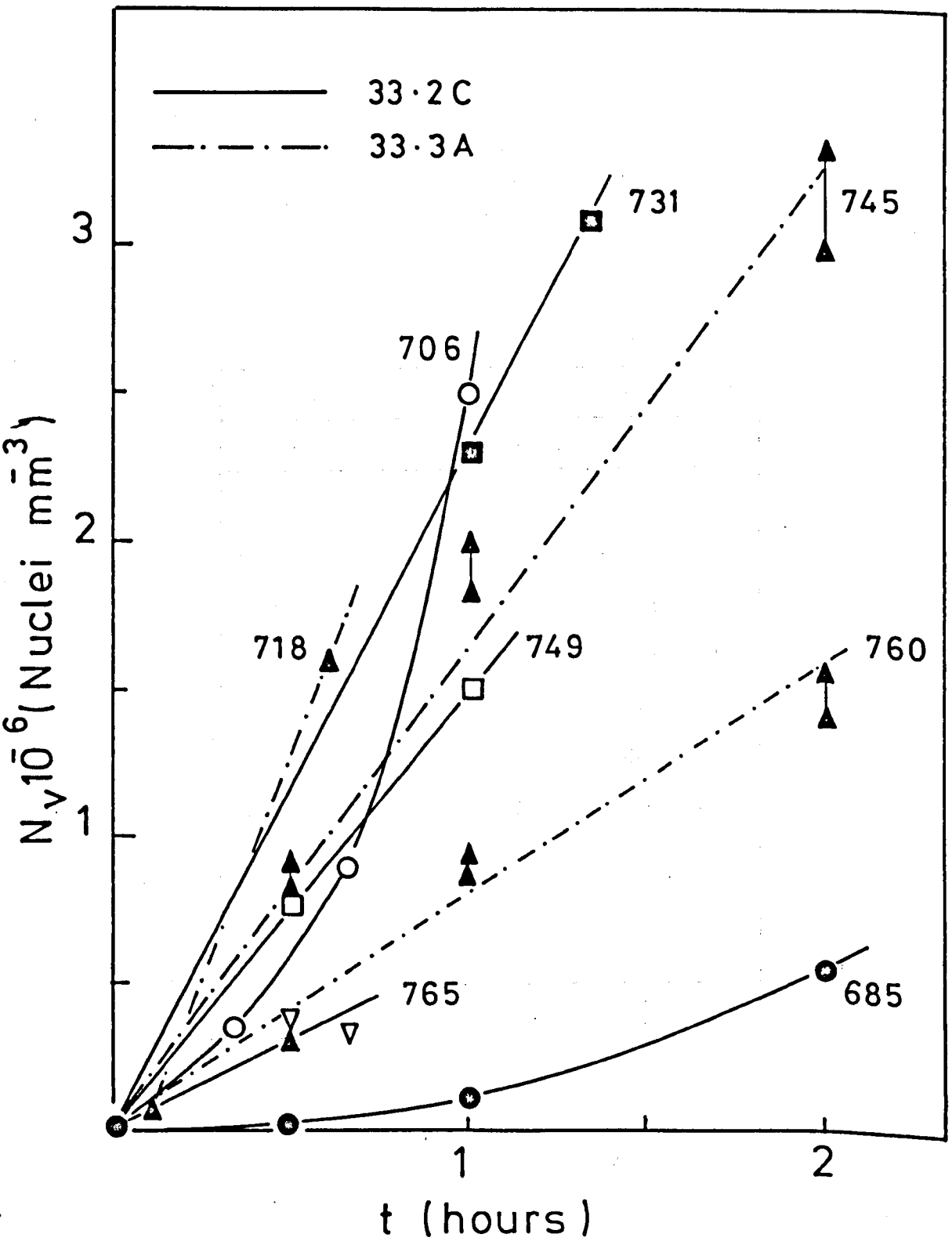

Fig. 4.10 Crystal nucleation (N_v versus time) plots for glasses 33.2C and 33.3A nucleated at several temperatures.

4.1.3 Effect of impurities on the nucleation rates

It is well established that most impurities *reduce* the nucleation rate of crystals in glasses [2.51,2.52]. For instance, in Li_2O-SiO_2 glasses, only nucleating agents like P_2O_5 [2.45,2.52], water [1.53] and possibly a few others, increase the nucleation rate of crystals. Ramsden [2.54] has demonstrated that TiO_2 and Al_2O_3 dramatically decrease the crystal nucleation rates in BaO-SiO_2 glasses. Water has probably a catalyzing effect on the nucleation rates but its level, and the level of other impurities, is low and *similar* in all glasses used in this study (sections 3.2 and 3.3). As the main impurity in the BaO-SiO_2 glasses melted in this work was SrO, an experiment was devised to test the effect of this oxide on the nucleation of crystals.

Figure 4.11 clearly shows that the nucleation rate of glass 33.3P (0.004 wt% SrO) is about 1.5 times higher than dN_v/dt of glasses 33.2C and 33.3A (0.290 wt% SrO) at 749°C and 765°C. This effect should therefore be taken into account when comparing nucleation rates of BaO-SiO_2 glasses having different SrO contents. Among the glasses actually used in this study, only glass 29.7H (0.54 wt% SrO) had a substantially higher SrO level than the others.

4.2 Crystal Growth in BaO-SiO_2 Glasses

The early stages of crystal growth in BaO-SiO_2 glasses have been studied in detail by other authors and discussed in chapter 2. As in this work the relationship between APS and crystal growth was of particular interest, a simple experiment was devised and will be described below.

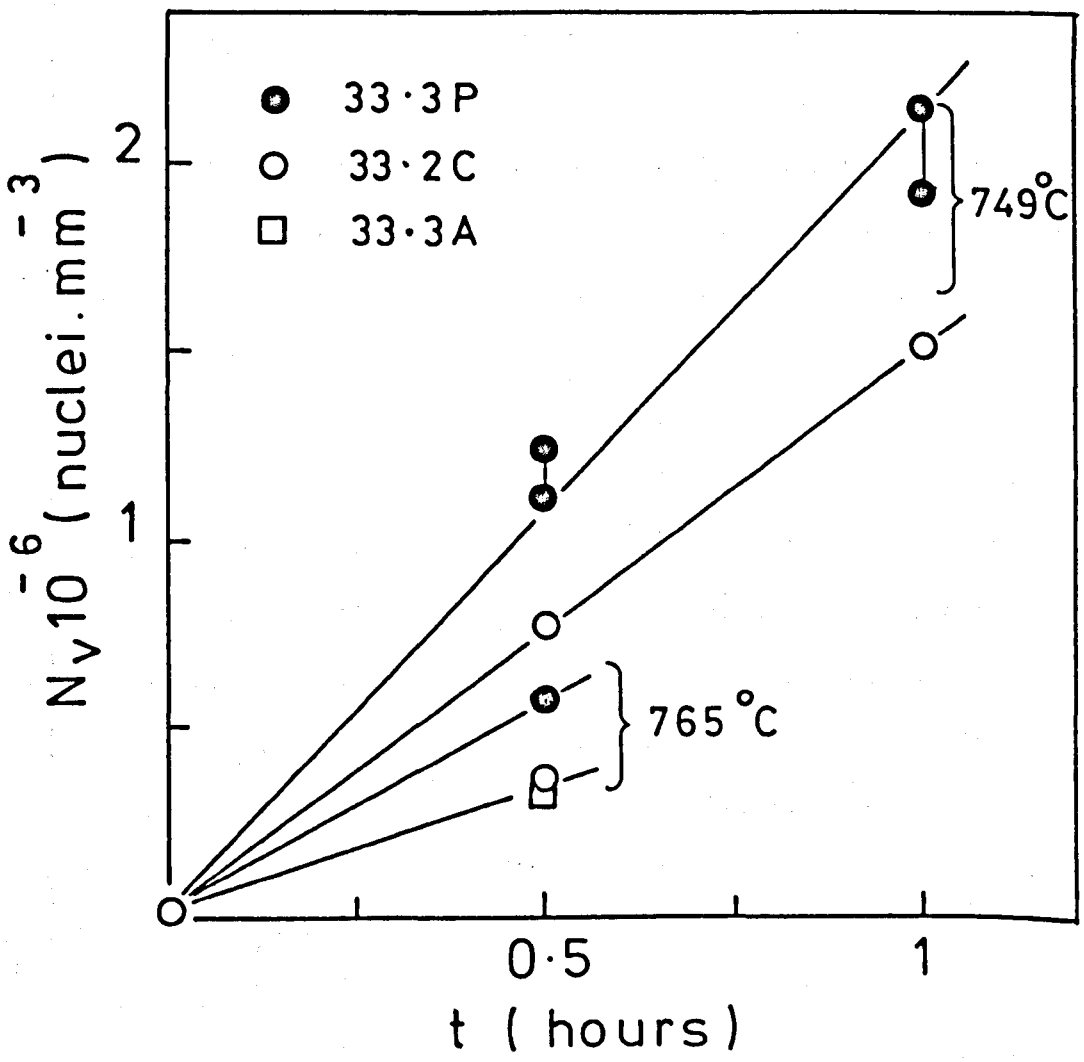

Fig. 4.11 Crystal nucleation (N_v versus time) plots for glass 33.3P (0.004 wt% SrO) and glasses 33.3A, 33.2C (0.290 wt% SrO).

4.2.1 Effect of amorphous phase separation

Specimens of glasses 28.3A and 29.7H, which have been nucleated for increasingly longer periods of time at 718°C, 745°C and 760°C and then "developed" at a higher temperature (the same temperature and time of development were employed for each particular glass composition and nucleation temperature), show larger crystal diameters with increasing nucleation periods. Therefore, by measuring the maximum diameters of the spherulites shown in optical micrographs and assuming that: (i) the growth rate of the crystalline nucleus is independent of its size and (ii) the "development" heat treatment brings an equal additional growth to each nucleus, it was possible to estimate the *growth* rates of the nuclei in the *nucleation range* of temperatures.

Figure 4.12a shows the maximum spherulite diameters as a function of nucleation time at 718°C, 745°C and 760°C for glasses 28.3A and 29.7H. The plots are straight lines and the growth rates, $\frac{1}{2}dD_M/dt$, clearly increase with temperature. The growth rate of glass 28.3A is *higher* at 760°C and 745°C than in 29.7H, and approximately equal at 718°C to the growth rate in glass 29.7H (Table 4.2a). These observations suggest that APS has the remarkable effect of increasing the growth rate of glass 28.3A, so that it is greater than the growth rate of the non-phase separating glass 29.7H, which in overall composition is higher in BaO. The APS at 718°C (as will be discussed later) takes a long time to proceed towards the final stage, and the effect on crystal growth is not detected.

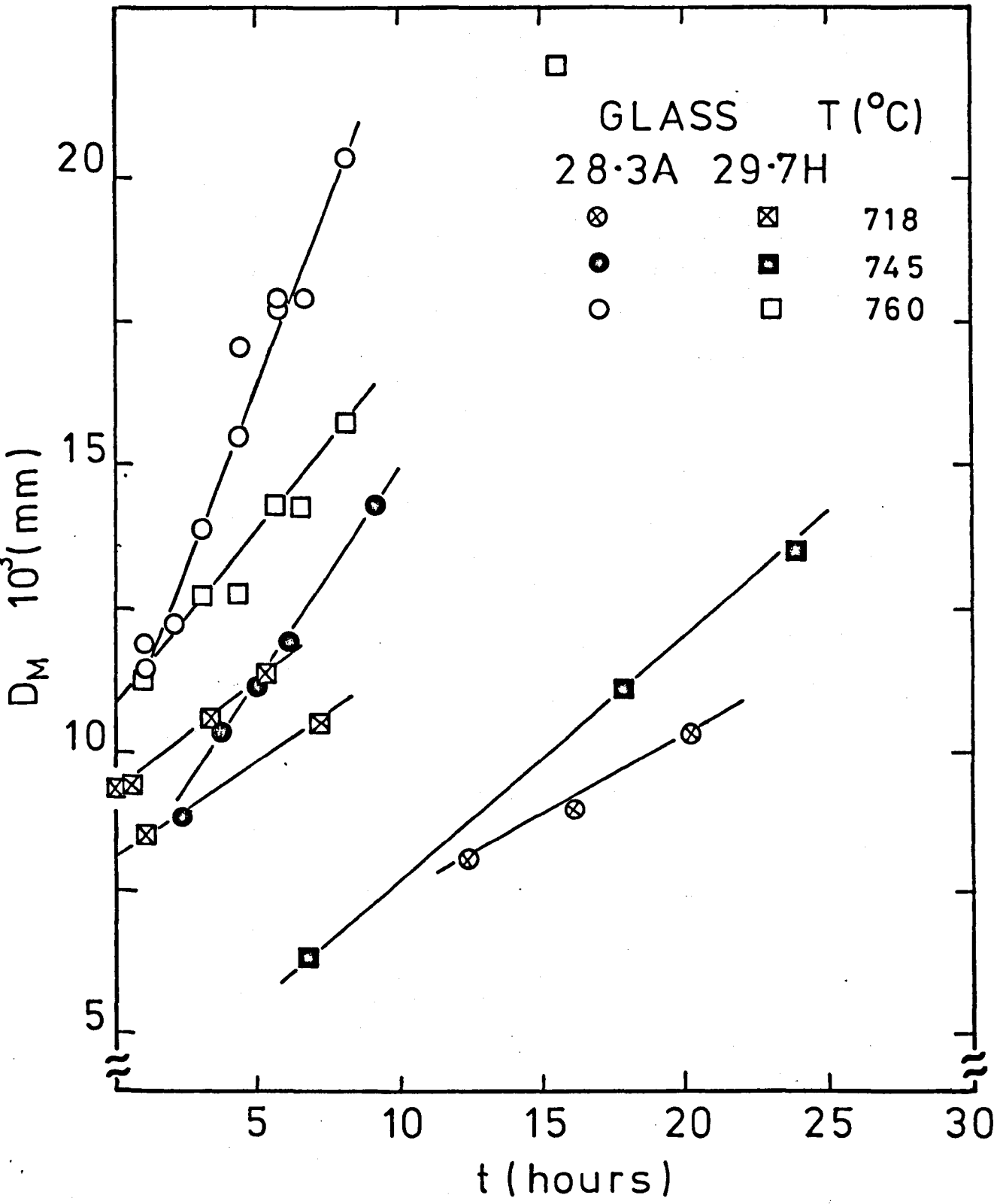

Fig. 4.12a Largest diameters of BS_2 spherulites versus time of heat treatment at 718°C, 745°C and 760°C (after a development treatment).

Table 4.2a

CRYSTAL GROWTH RATES IN GLASSES 28.3A AND 29.7H ($m.s^{-1}$)

Glass	718°C	745°C	760°C
28.3A	0.40×10^{-10}	1.0×10^{-10}	1.8×10^{-10}
29.7H	0.45×10^{-10}	0.61×10^{-10}	0.95×10^{-10}

4.2.2 Crystal growth in the stoichiometric glass 33.3A

The crystals growing in glass 33.3A do not have a spherical morphology and the growth rate is much higher than for glasses 28.3A and 29.7H. In this case, the largest crystalline spikes were measured after a *single* stage heat treatment at 745°C and 760°C.

The growth rates, $\frac{1}{2}dD_M/dt$, and induction times measured in the plots of Figure 4.12b were used in the analysis of the fraction crystallinity versus time curves (Figure 4.13) discussed below.

4.3 Overall Crystallization - the Johnson-Mehl-Avrami (JMA) Theory

The JMA theory [4.1,4.2] predicts the evolution with time of the fraction of crystallized material, α, as a function of the steady state nucleation rate, I, and constant growth rate, U, as follows:

$$\alpha = 1 - \exp[-gIU^p t^n] \qquad (4.2)$$

where g is a shape factor, p and n depend on the dimensionality of the crystals and growth process (diffusion or interface controlled) and t is the time of isothermal heat treatment.

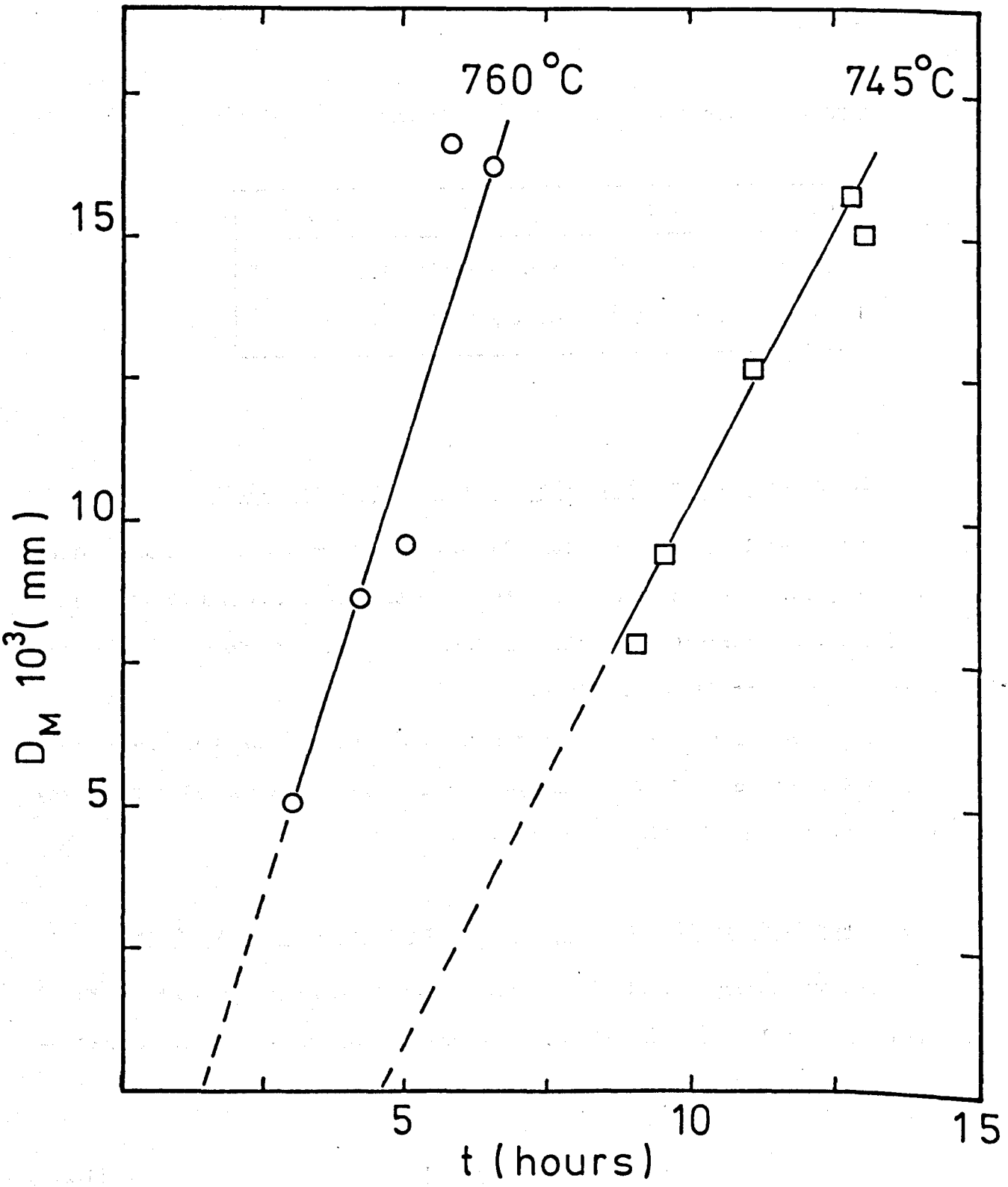

Fig. 4.12b Length of largest crystal spike versus time in glass 33.3A at 745°C and 760°C.

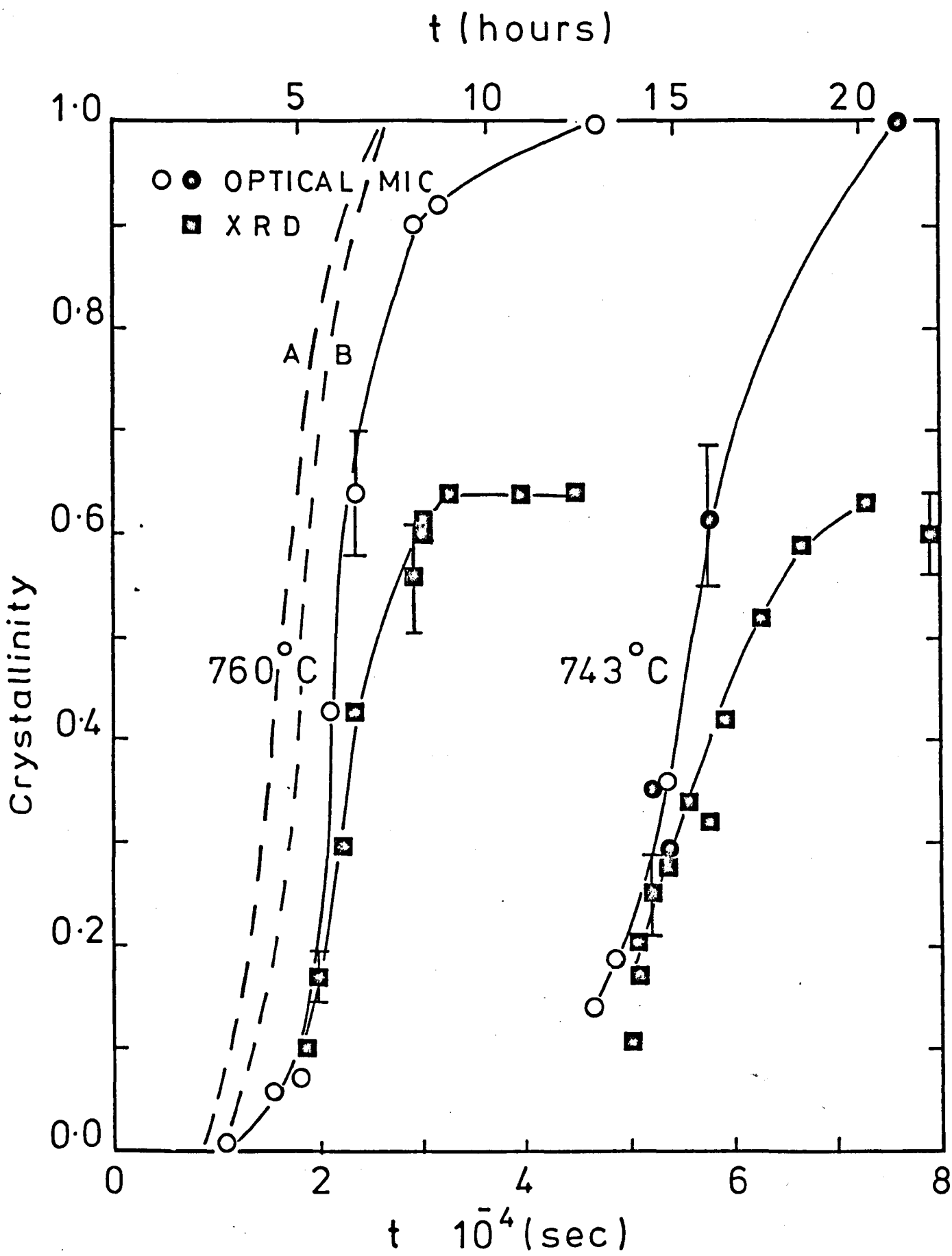

Fig. 4.13 Volume fraction of crystallinity versus time curves for glass 33.3A (O) and glass 33.2B (●, ■). Curves A and B were calculated by Eqs. 4.3 and 4.2, respectively.

The JMA theory is often used to access the factor n, which can partially describe the transformation under study, through $\ln \ln(1 - \alpha)^{-1}$ versus log t plots. Recently the JMA theory has been extensively employed in the formulation of theories of glass formation by Uhlmann and co-authors [4.3,4.4,4.5, 4.6,4.7]. It also provides an alternative and more rapid way of calculating crystal nucleation rates from measured values of U and α, and has been used recently in an attempt to test the classical nucleation theory [1.71,1.77]. As far as this author is aware, however, *no* quantitative test of the JMA theory has so far been made. Therefore, the experimental crystal nucleation and growth rates of glass 33.3A at 745°C and 760°C (Table 4.2b) were used to calculate the curves α versus time, which could then be compared with the measured α versus time curves plotted in Figure 4.13.

Table 4.2b

EXPERIMENTAL PARAMETERS USED TO TEST THE JMA THEORY
(GLASS 33.3A)

	745°C	760°C
I ($mm^{-3}.s^{-1}$)	461	222
U ($mm.s^{-1}$)	3.24×10^{-7}	4.63×10^{-7}
t_0 (s)	16500	5400
N_0 (mm^{-3})	7.6×10^{6}	1.2×10^{6}

It can be shown [4.8] that in the case of a fixed number of nuclei, N_0, growing with a constant rate U, Equation (4.2) is modified to give

$$\alpha = 1 - \exp [- g' N_0 U^p t^{n-1}] \qquad (4.3)$$

For the crystallization of glass 33.3A at 745°C and 760°C, there are appreciable induction periods (t_0) before detectable growth occurs (Figure 4.12b). Hence ($t - t_0$) should be substituted for t in Equations (4.2) and (4.3). For spherically growing crystals, the factors p and n are equal to 3 and 4 respectively [4.8].

Curve B in Figure 4.13 is the calculated curve at 760°C, obtained by means of Equation (4.2) with the parameters mentioned above, and reflects the situation where the rate of nucleation is constant and each nucleus is growing with a constant rate. It must be realised, however, that for glass 33.3A appreciable *growth* of the nuclei only occurs after a certain induction period, t_0, so a great number of nuclei, $N_0(t_0)$, is already formed when crystal growth begins. Assuming that no more nucleation occurs after the starting of the growth process, α can be calculated by Equation (4.3), and is plotted as curve A in Figure 4.13. The real fraction transformed is then given by the *combination* of curves A and B.

The experimental curves in Figure 4.13 were obtained by XRD, and a point-counting method described in section 3.7. There is a large discrepancy between the Optical Microscopy (point-counting) and XRD curves, but this can be explained if we realise that the spherulites are not entirely crystalline, some residual, uncrystallised glass remaining inside them. Results similar to those obtained by XRD here, have also been found for the spherulitic crystallization of polymers [4.8,4.9]. It is also of interest to observe that the maximum degree of crystallinity, as measured by XRD at 745°C and 760°C, is indicating that *each* BS_2 spherulite is only 64% crystalline. Schultz [4.28] also shows that bulk polyethylene crystallizes very slowly after a volume fraction of about 60% crystallinity is reached.

4.3.1 Comparison of experimental and calculated curves

Figure 4.13 shows that the calculated and experimental curves at 760°C are displaced on the time axis. The discrepancy is even greater if we realise that the real calculated curve is the combination of curves A and B. At 745°C, the calculated curves (not shown in Figure 4.13 for clarity) nearly coincide with the experimental curves for 760°C, being a long way from the measured curves for the isothermal treatment at 743°C. Some explanations for this discrepancy will be given in chapter 5.

4.3.2 XRD - phase analysis

Some heat treated speciment of glass 33.3A were analysed in the standard way by XRD to reveal the crystalline phases. For all heat treatments given at temperatures below about 970°C, the XRD patterns consisted of very broad peaks, characteristic of the small size of the crystals. These were probably the fine spikes of the spherulites. Above 970°C, when the spherulites transform to lath-shaped crystals, sharp peaks corresponding to the low form of $BaO.2SiO_2$ (ℓ-BS_2) were clearly identified. These observations are very similar to those of Rowlands [1.47].

4.4 Amorphous Phase Separation (APS) in $BaO-SiO_2$ Glasses

The quantitative study of APS involves techniques capable of high resolution such as TEM and SAXS. In this work, both techniques were used for the characterization of the structural parameters which describe phase separated glasses and their evolution with heat treatment.

4.4.1 Transmission Electron Microscopy (TEM)

The morphology of APS in several $BaO-SiO_2$ glasses was studied by TEM of thin foils by Seward et al. [2.6], who also determined the miscibility gap

at high temperatures. Ramsden [2.54] made some semi-quantitative estimations of volume fractions, number of droplets and surface areas of phase-separated $BaO-SiO_2$ glasses using surface carbon replicas. The TEM techniques employed in this work were described in section 3.8 and micrographs of several $BaO-SiO_2$ glasses melted in this study are shown in Figures 4.14a-4.14e.

Figure 4.14a shows thin foil TEM micrographs of glass 28.3B heat treated for up to 14.4 h at 743°C. The as-quenched specimen shows *no* detectable phase separation. The nearly spherical droplets shown in the heat treated glasses clearly increase in size with time. The last micrograph is for glass 28.3B heated at 821°C for 22 minutes (glass 28.3BPS). The size of the droplets (~ 400 Å) is much larger while the number of droplets is smaller. This specimen was slightly blue while the others, heat treated at 743°C, were clear and transparent.

Figure 4.14b shows that *no* phase separation could be detected by TEM in glass 29.7H even after a treatment of 5.5 h at 743°C + 4.2 h at 690°C + 1.0 h at 750°C. Specimens of this glass heated for 23 hours at 710°C or 718°C for 48 hours were also free of submicroscopic structural features, suggesting that this glass does not phase separate even when heated inside the miscibility gap. A similar observation was made by Burnett and Douglas [4.10] in their study of APS in $Na_2O-CaO-SiO_2$ glasses. They suggested that this behaviour is due to a lack of thermodynamic driving force for compositions and temperatures which lie near to the binodal curve. Ramsden [2.54] also observed *no* trace of immiscibility in a glass with 30.4 mol% BaO heated inside the miscibility gap. For a glass with 28.7 mol% BaO phase separation could be detected only for undercoolings larger than about 80°C. Therefore, it can be concluded that temperatures lower than 690°C (higher undercollings) would be required before nucleation of

Fig. 4.14a TEM micrographs of glass 28.3B phase separated at 743°C. From top to bottom on the first page and from bottom to top on the second page: 0, 3, 5, 10 and 14.4 hours, respectively. On the top of the second page a micrograph of glass 28.3BPS, i.e. glass 28.3B heated at 821°C for 22 minutes, is shown.
⊢——⊣ = 0.1 μm.

Fig. 4.14b TEM micrographs of $BaO-SiO_2$ glasses. From left to right and top to bottom respectively:
glass 29.7H: 5.5 h at 743°C + 4.2 h at 690°C + 1.0 h at 750°C
glass 27.0: 4.1 h at 743°C
glass 28.3B: 17 h at 743°C + 15 min at 821°C
glass 28.3BPS: 6 h at 743°C
The bar on the first figure indicates the magnification of the first three figures.
⊢——⊣ = 0.1 μm

Fig. 4.14c TEM micrographs of glass 28.3B at 760°C. From left to right and top to bottom: 1.0, 3.7, 8.4 and 8.4 hours respectively.
The bar on the third figure (⊢——⊣) indicates the magnification of the first three figures (0.1 μm).
The bar on the fourth figure indicates 0.5 μm.

Fig. 4.14d Replica micrographs of glass 28.3A at 760°C. From top to bottom: 1.0, 5.8 and 8.0 hours respectively.
⊢——⊣ = 0.1 μm

Fig. 4.14e TEM micrographs of glass 28.3B heated for 30.2 hours at 743°C (top figures) and glass 29.9 heated for 13.1 and 17 hours at 752°C (bottom figures). The bar on the first figure indicates the magnification on the first three figures.
⊢——⊣ = 1 μm

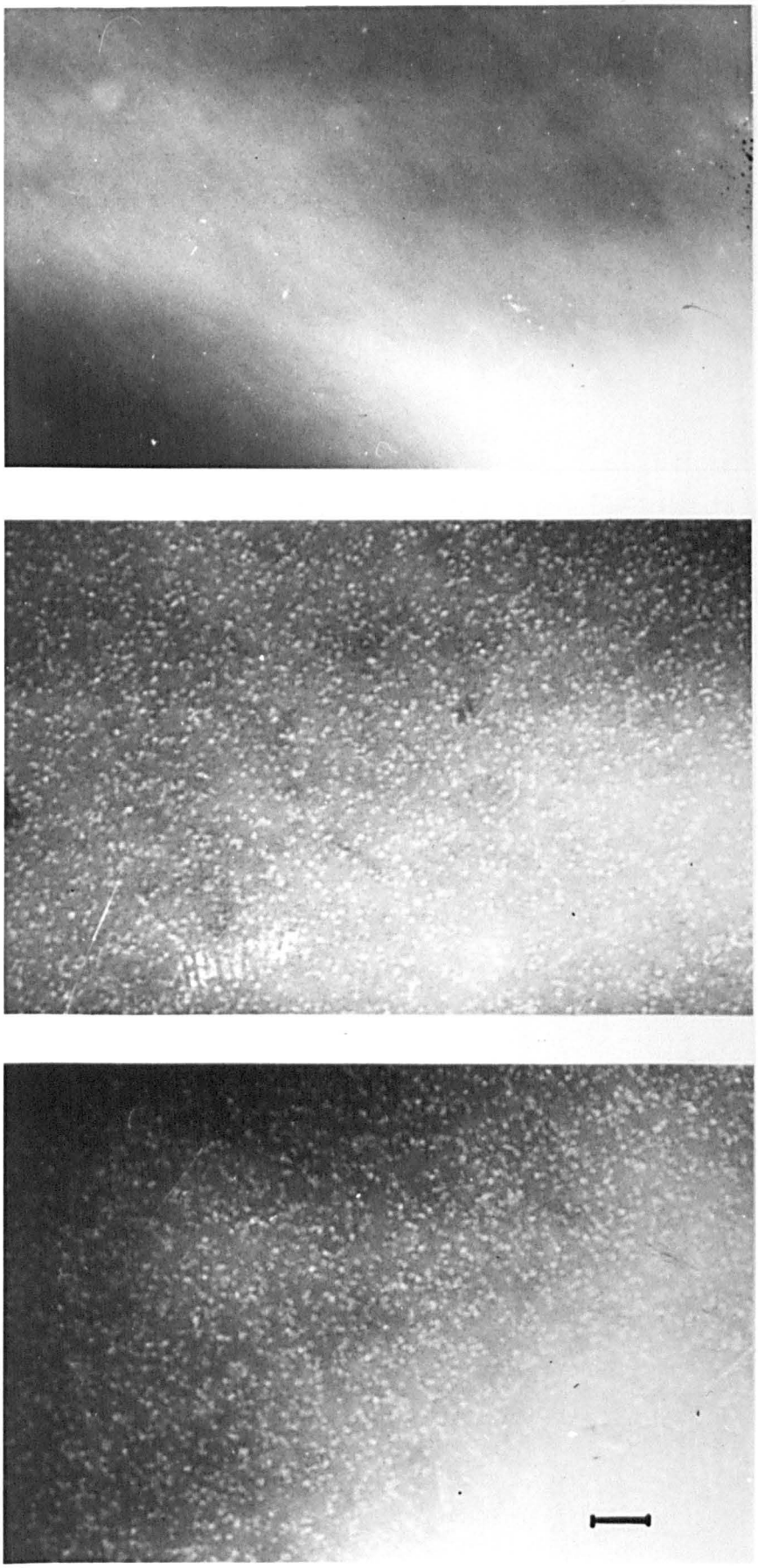

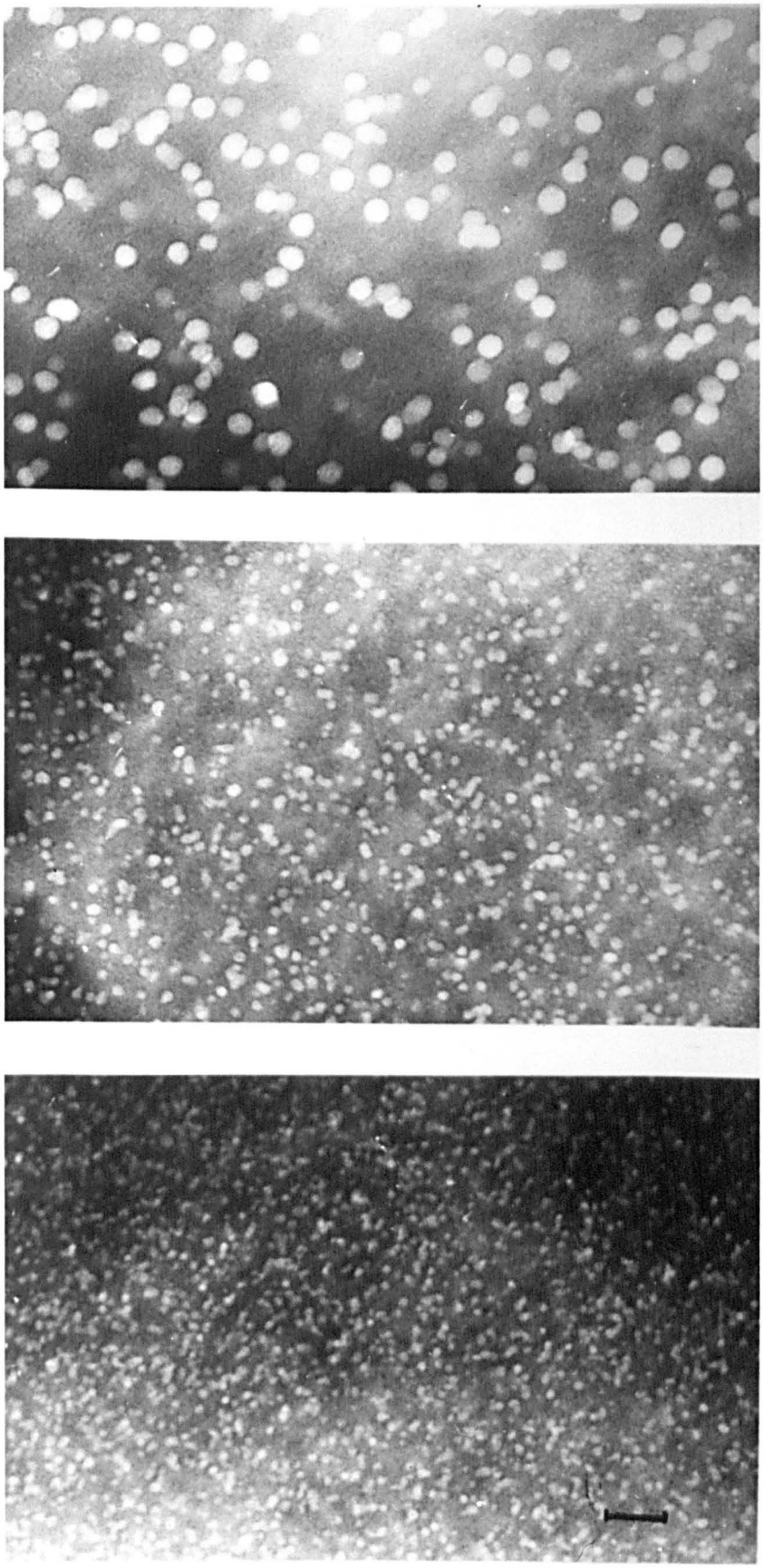

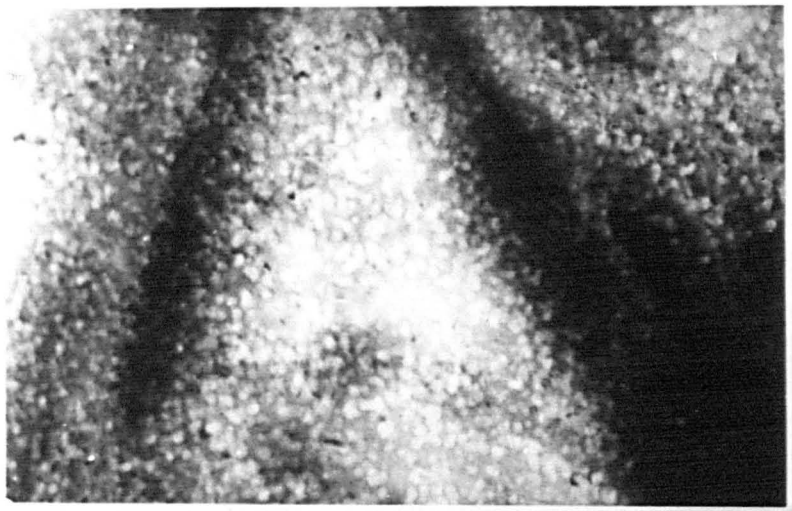

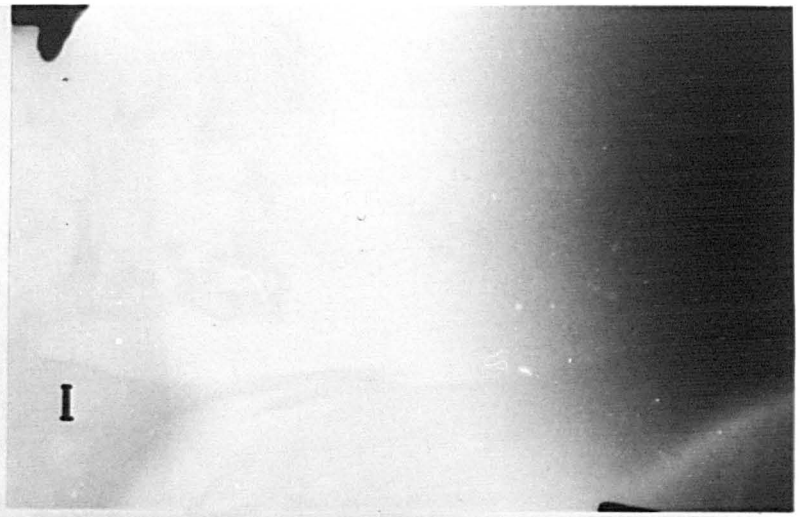

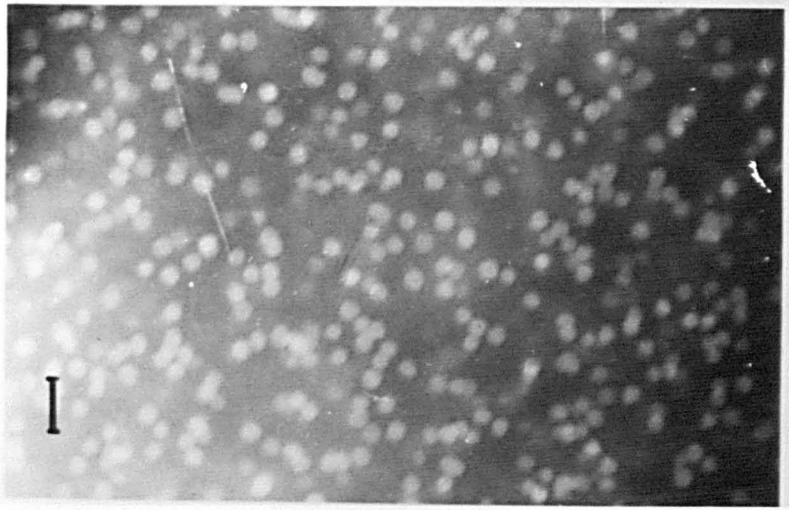

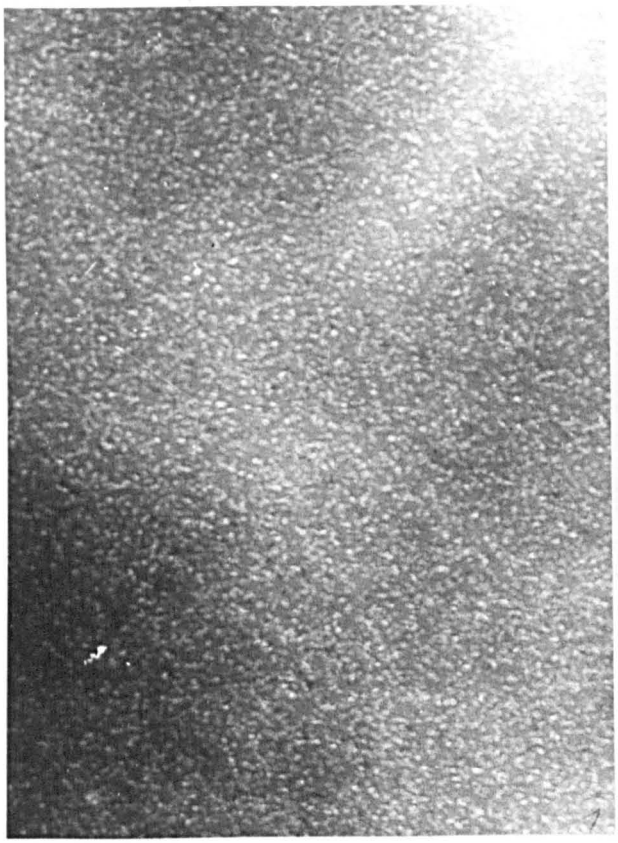

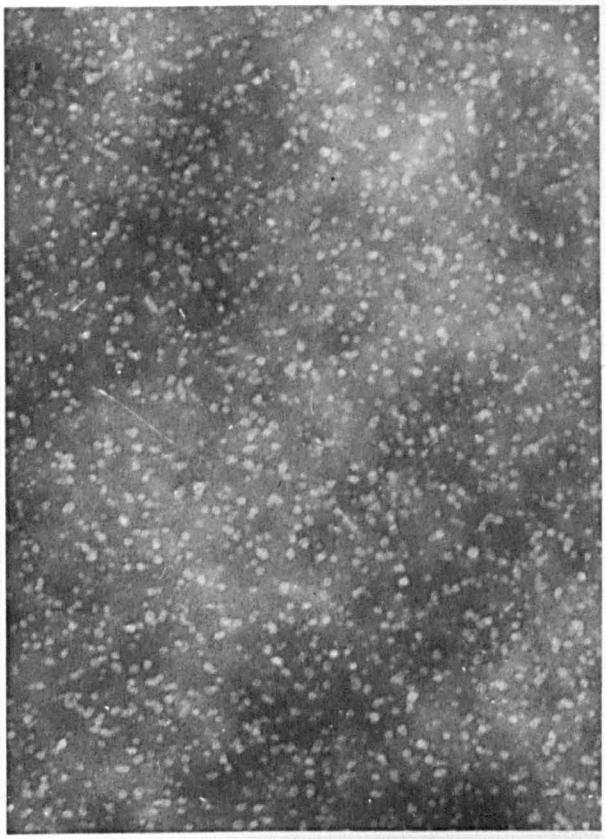

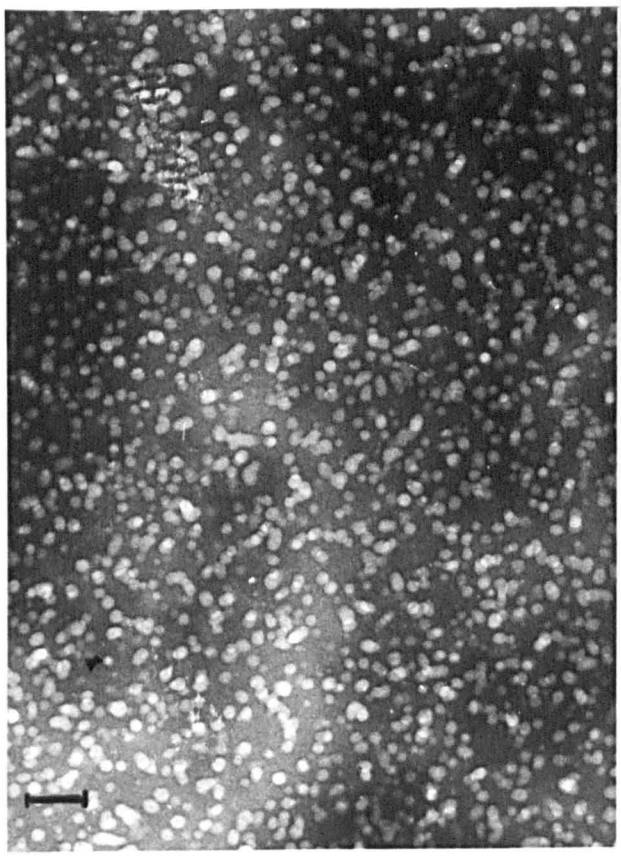

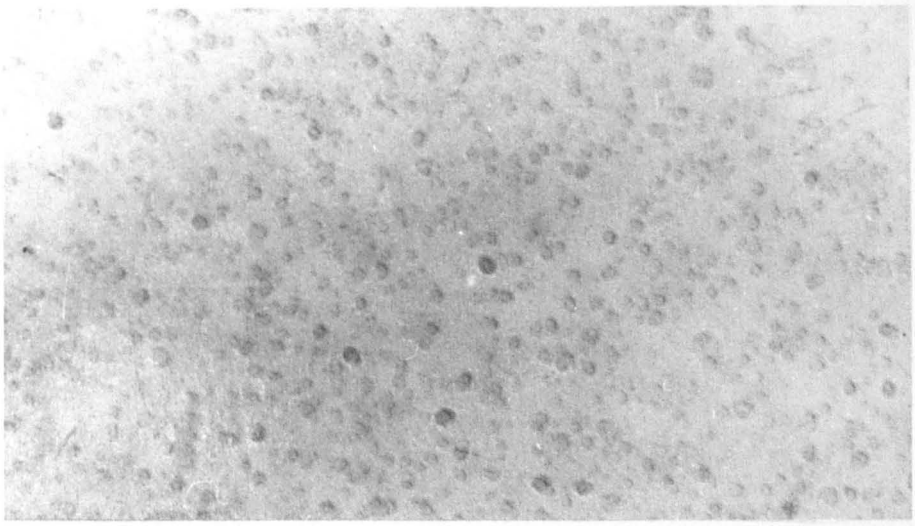

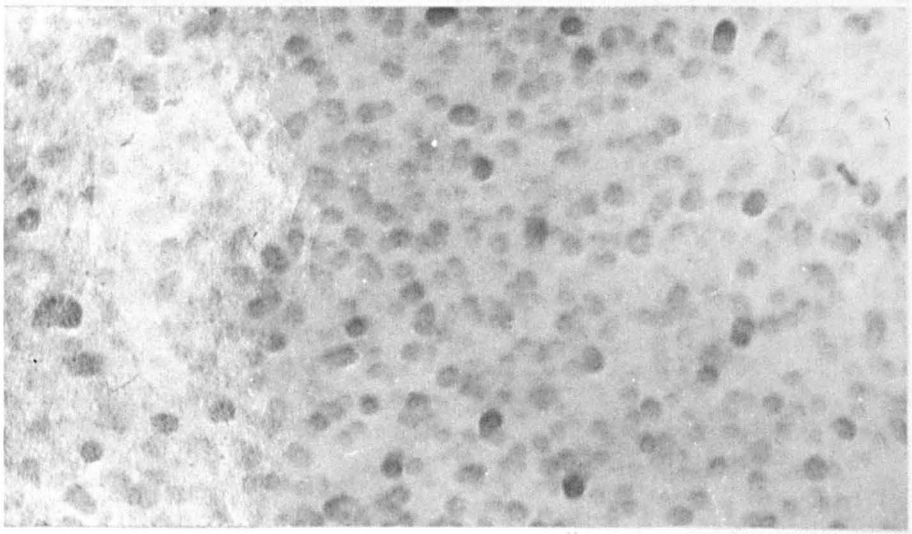

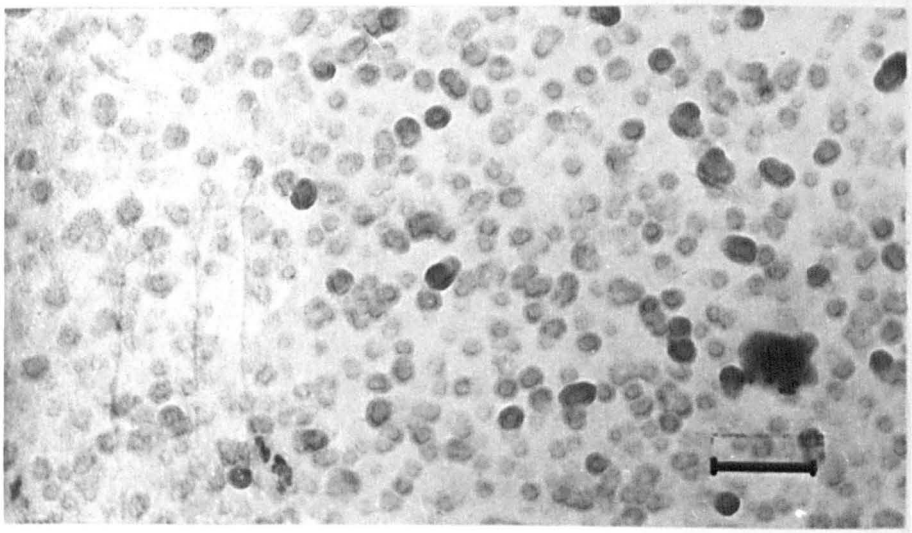

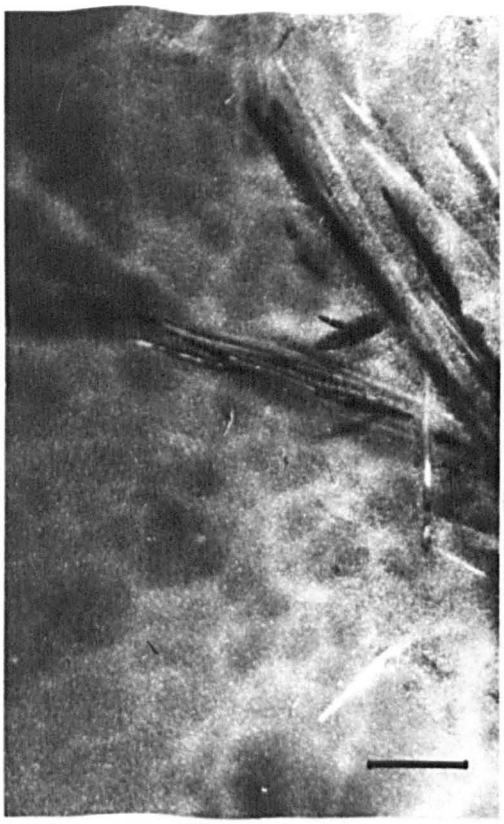

amorphous droplets could occur in glass 29.7H.

Supporting this conclusion is the observation that the development of APS occurs more rapidly as the SiO_2 content of the base glass is *increased* (moving towards the centre of the gap), as observed by Ramsden [2.54], and in section 4.4.2, i.e. the attainment of the equilibrium composition of the baria-rich matrix is much faster for glass 27.0 (72.6 mol% SiO_2) than for glass 28.3B (71.3 mol% SiO_2). Quantitative studies of APS in Li_2O-SiO_2 glasses also show the same pattern (section 4.8). This means that nucleation can begin at much higher temperatures (due to higher undercoolings below the gap) allowing growth to proceed at a much faster rate in high SiO_2 glasses.

Figure 4.14b also shows a fine scale phase separation in glass 27.0 heated for 4.1 hours at 743°C. Glass 28.3B nucleated at 743°C and "developed" at 821°C for 15 minutes (for crystal nucleation studies) still retains the amorphous droplets apparently undisturbed by the growing crystalline spikes. The same behaviour was shown by other phase separated glasses nucleated and "developed" at different temperatures. Finally, there is *no* evidence for secondary phase separation in glass 28.3BPS after further treatment at 743°C for 6 hours (Figure 4.14b). Micrographs obtained with higher magnifications confirm this observation, which is in agreement with the previous discussion concerning the absence of phase separation in glass 29.7H. In the case of glass 28.3 BPS, the initial treatment at 821°C caused the baria-rich matrix to shift to about 30.1 mol% BaO (given by the binodal boundary) rendering difficult the nucleation of droplets in the amorphous matrix.

Figure 4.14c shows the increase in size of the SiO_2-rich droplets in glass 28.3B heated at 760°C for 1.0, 3.7 and 8.4 hours. Some crystalline spikes can be seen in the 8.4 hours specimen.

Some replica micrographs of glass 28.3A heated at 760°C are shown in Figure 4.14d. The droplet diameters estimated in the thin foil and replica

micrographs of Figures 4.14e and 4.14d are compared with the diameters measured by SAXS in Figure 4.22.

Figure 4.14e shows crystalline BS_2 spikes growing through the phase separated matrix in glass 28.3B heated at 743°C for 30.2 hours. In glass 29.9 heated at 752°C for 13.1 and 17 hours the crystalline spikes grow in a homogeneous (non-phase separated) matrix.

Conclusions from TEM study

These TEM studies of $BaO-SiO_2$ glasses allow the following conclusions to be drawn:

The as-quenched glasses show *no* detectable phase separation. Particles smaller than the resolution limit of the Hitachi HU 11A electron microscope (20-30 Å) may, however, be present.

Glasses with compositions close to the immiscibility boundary (29.7H and 29.9) showed *no* sign of phase separation even when heated inside the gap. This observation is in agreement with other authors, but does not exclude the possibility of phase separation occurring when lower temperatures (higher undercoolings) are employed. Also, no secondary separation was detected in glass 28.3BPS heated at 743°C.

Glasses 27.0, 28.3A and 28.3B show extensive phase separation at 743°C, 760°C and higher temperatures. The silica-rich droplets are nearly spherical.

BS_2 crystalline spikes can be detected for samples subjected to long heat treatments growing through the amorphous matrix in phase separated glasses and leaving the silica-rich droplets undisturbed.

4.4.2 Small Angle X-ray Scattering (SAXS)

In section 3.9 the theory and experimental part of SAXS were described. It was also shown how the structural parameters (D, N, S_V, v, etc.) which characterize phase separated glasses can be obtained from experiment. The

quantitative results for phase separation in $BaO-SiO_2$ glasses are now presented.

The amorphous phase separation in glass 27.0 heated at 743°C from 0 to 17 h, and glass 28.3B heated at 743°C from 0 to 30 h and at 760°C from 0 to 8 h, was studied by SAXS. From the normalised $J(\varepsilon)$ versus ε curves Guinier [$\log J(\varepsilon)$ vs. ε^2] plots and Porod plots [$J(\varepsilon).\varepsilon^3$ vs. ε] were made. From these plots the following parameters were calculated: average diameter of the amorphous particles D, surface area of the particles per unit volume S_V, relative number of particles per unit volume N, integrated intensity in reciprocal space Q, and average volume of particles v.

From the analysis of these data and based on the existing theories of nucleation, growth and coarsening of liquid-liquid immiscibility, the kinetics of the phase separation in these glasses was defined and correlated with the nucleation and growth behaviour of the $BaO.2SiO_2$ spherulites in the same glasses.

Scattering curves

The normalised SAXS curves, $J(\varepsilon)$ vs. ε, in arbitrary units, for glass 27.0 heated at 743°C from 0 to 17 h, and glass 28.3B heated at 743°C from 0 to 14 h and at 760°C from 0 to 8 h are plotted in Figures 4.15, 4.16 and 4.17 respectively. All curves, except the ones for very short heat treatments, show a hump which is associated with interparticle interferences, as discussed in section 3.9.7. This phenomenon is to be expected because the volume fraction of the amorphous (SiO_2) scattering particles, calculated from the binodal boundary, approached 0.19, 0.15 and 0.11 respectively as the equilibrium composition of the amorphous phase separation was reached in the above glasses.

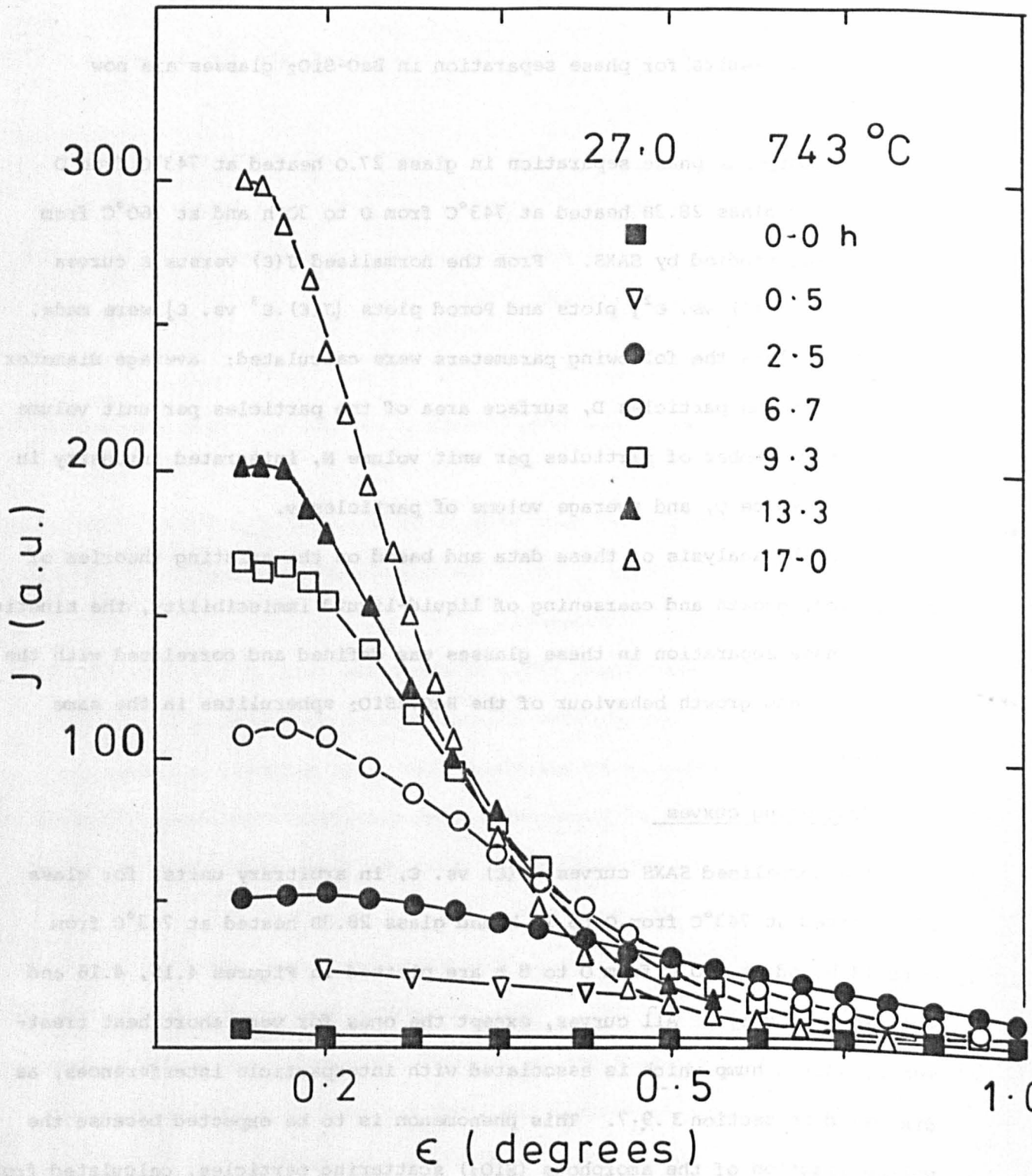

Fig. 4.15 SAXS curves of glass 27.0 heat treated at 743°C.

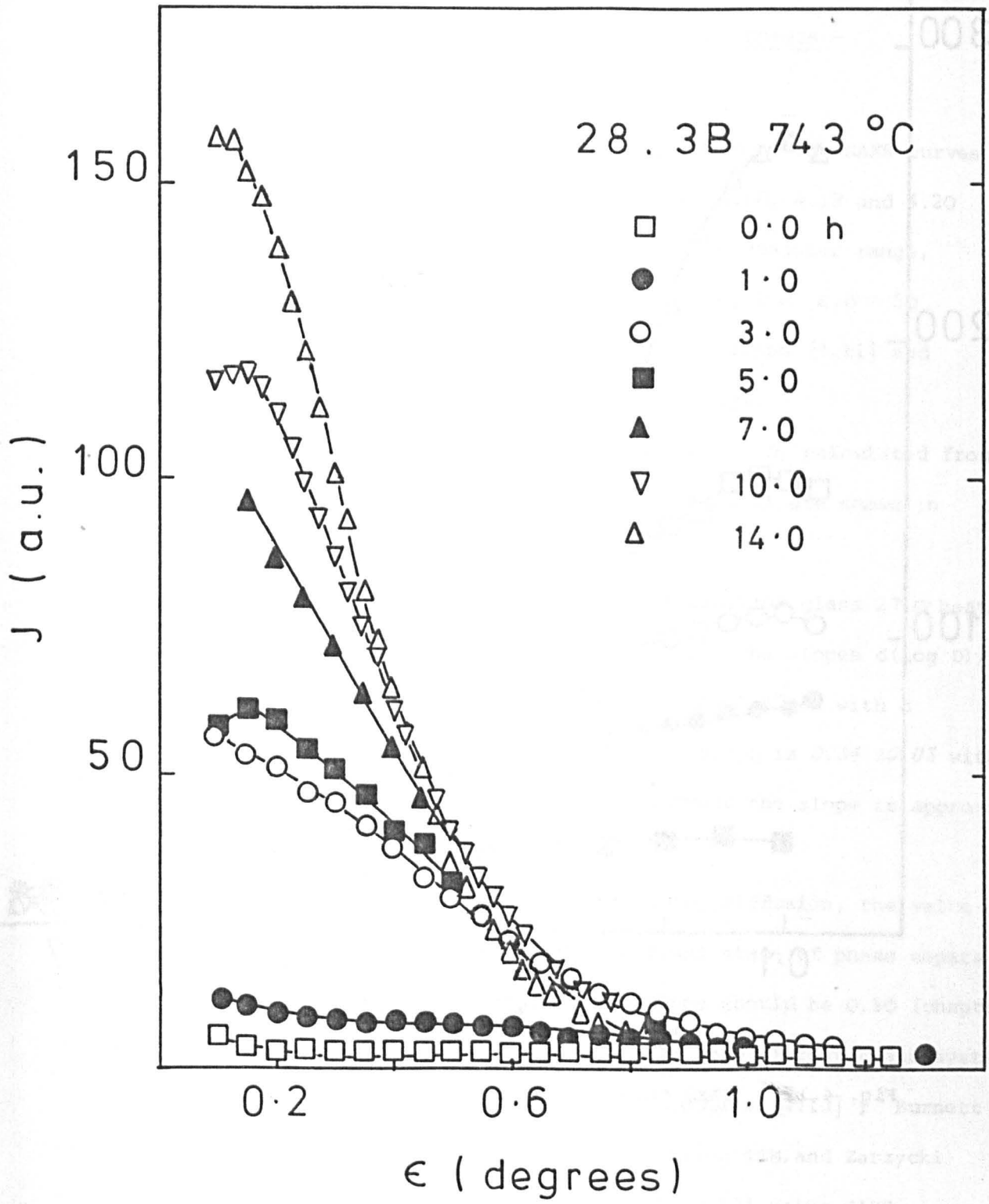

Fig. 4.16 SAXS curves of glass 28.3B heated treated at 743°C.

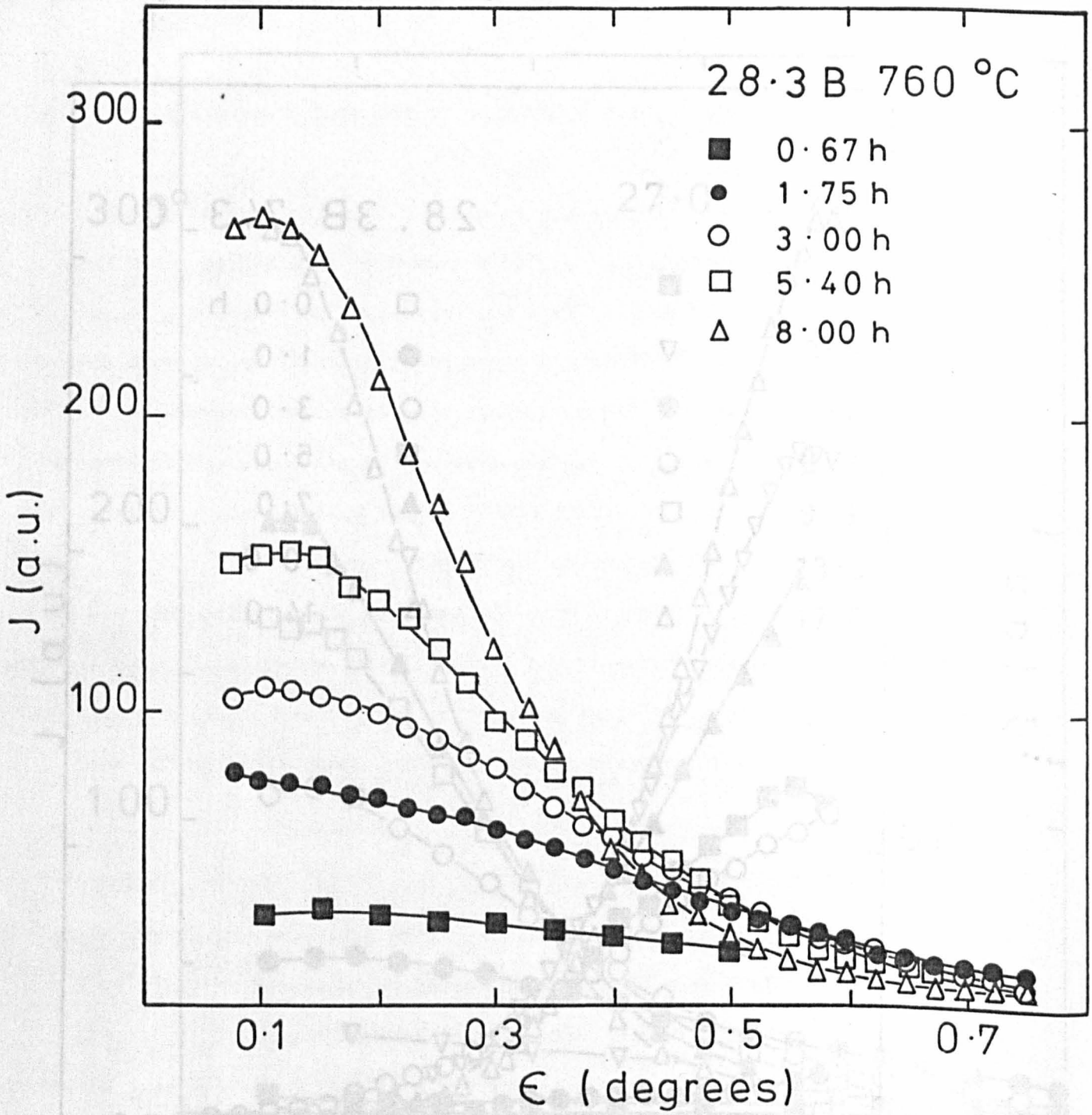

Fig. 4.17 SAXS curves of glass 28.3B heat treated at 760°C.

4.4.2.1 Growth kinetics of the amorphous droplets - Guinier's Law

The Guinier plots, log $J(\varepsilon)$ vs. ε^2, corresponding to the SAXS curves of Figures 4.15, 4.16 and 4.17 are shown in Figures 4.18, 4.19 and 4.20 respectively. The linearity is maintained in a large angular range, extending over the limit of validity of Guinier's Law, i.e. $\varepsilon.D \simeq 50$ (Degrees Å). This behaviour was also observed by Neilson [4.11] and Gerold [4.12] for different glasses and metallic alloys.

The average diameters of the scattering particles, D, calculated from the Guinier curves by means of Equation (8A) (Appendix 2) are shown in Table 4.3.

Figure 4.21 shows the plots of log D vs. log(time) for glass 27.0 heated at 743°C and glass 28.3B heated at 743°C and 760°C. The slopes d(log D)/ d(log t), for glass 28.3B heat treated at 760°C is *0.32 ±0.02* with a correlation coefficient r = 0.991. At 743°C, the slope is *0.34 ±0.03* with r = 0.975, whereas for short periods of heat treatment the slope is approximately 0.5.

If the growth of the particles is controlled by diffusion, the value of 0.33 is predicted for d(logD)/d(log t) in the final stage of phase separation. In the nucleation and growth stage the slope should be 0.50 (chapter 1). Similar behaviour has been verified experimentally in different glass systems by a number of authors, among them, McCurrie and Douglas [4.13] ; Burnett and Douglas [4.10] and James and McMillan [4.14] using TEM, and Zarzycki and Naudin [4.15]; Neilson [4.16] and Craievich [4.17] using SAXS.

For glass 27.0 heated at 743°C the slope is *0.43 ±0.03* with r = 0.994 or *0.48 ±0.05* with r= 0.988 if the first point (t = 2.5 h) is disregarded. Therefore, in this case, the slope is close to 0.5, implying that the

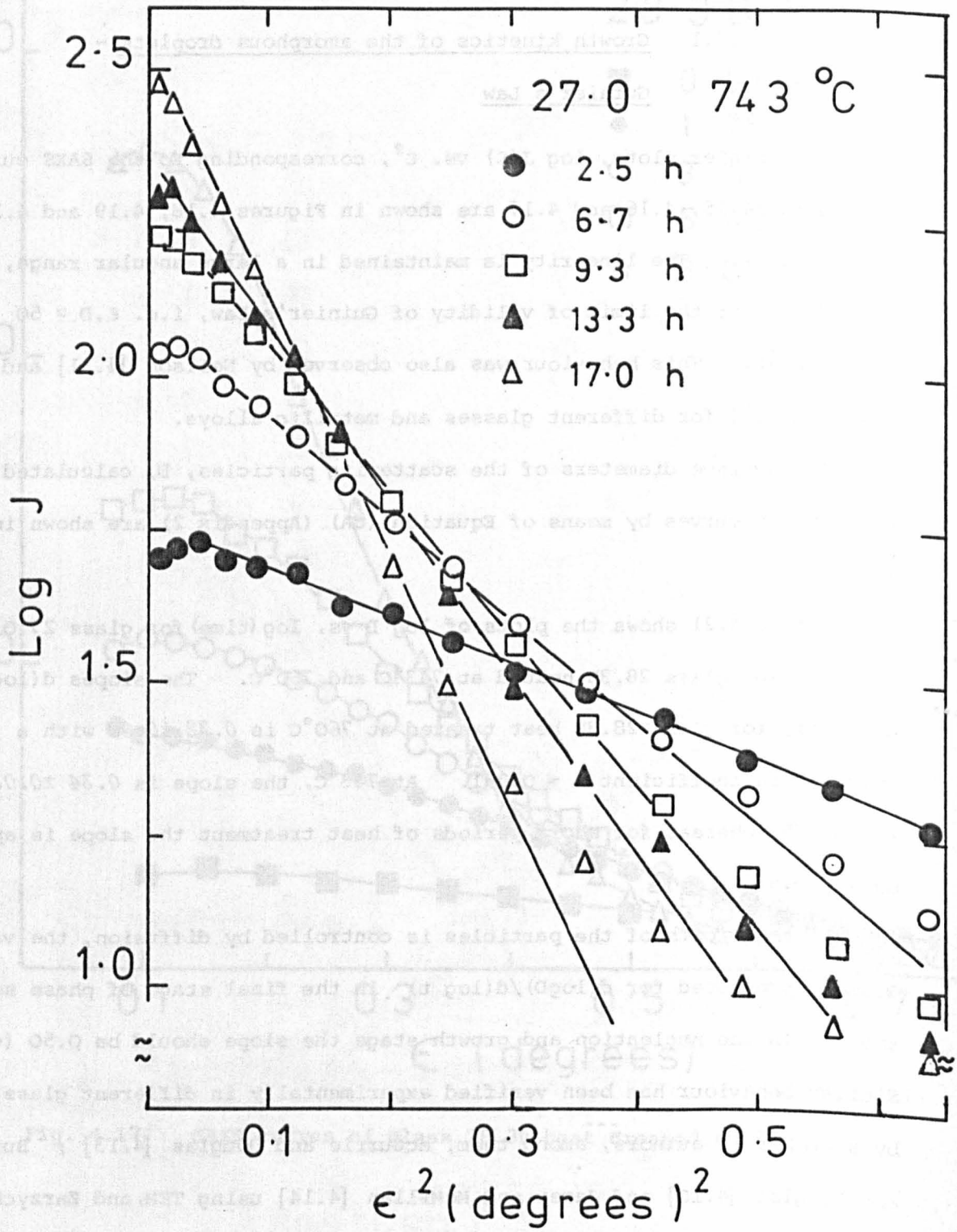

Fig. 4.18 Guinier plots for glass 27.0 heat treated at 743°C.

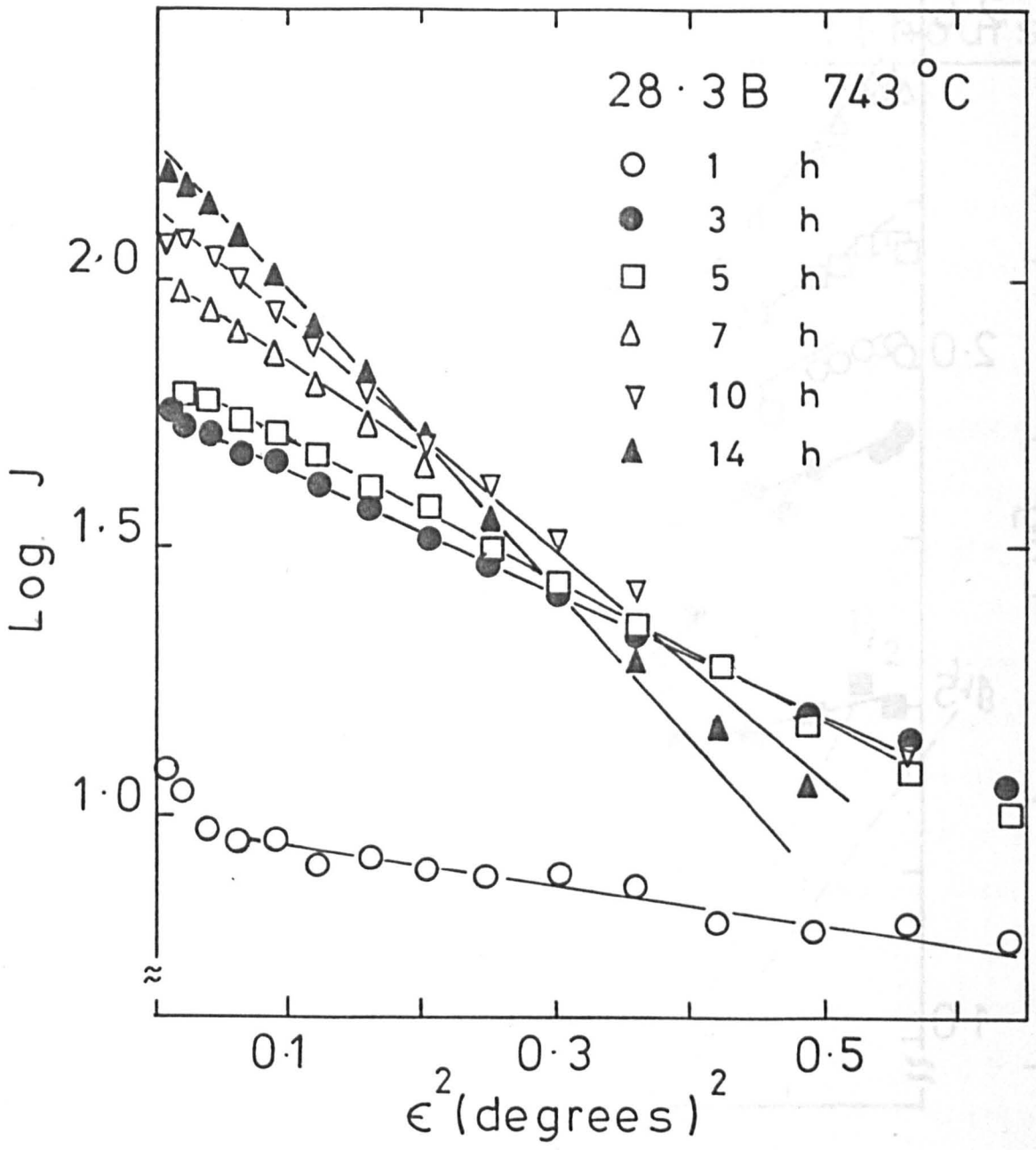

Fig. 4.19 Guinier plots for glass 28.3B heat treated at 743°C.

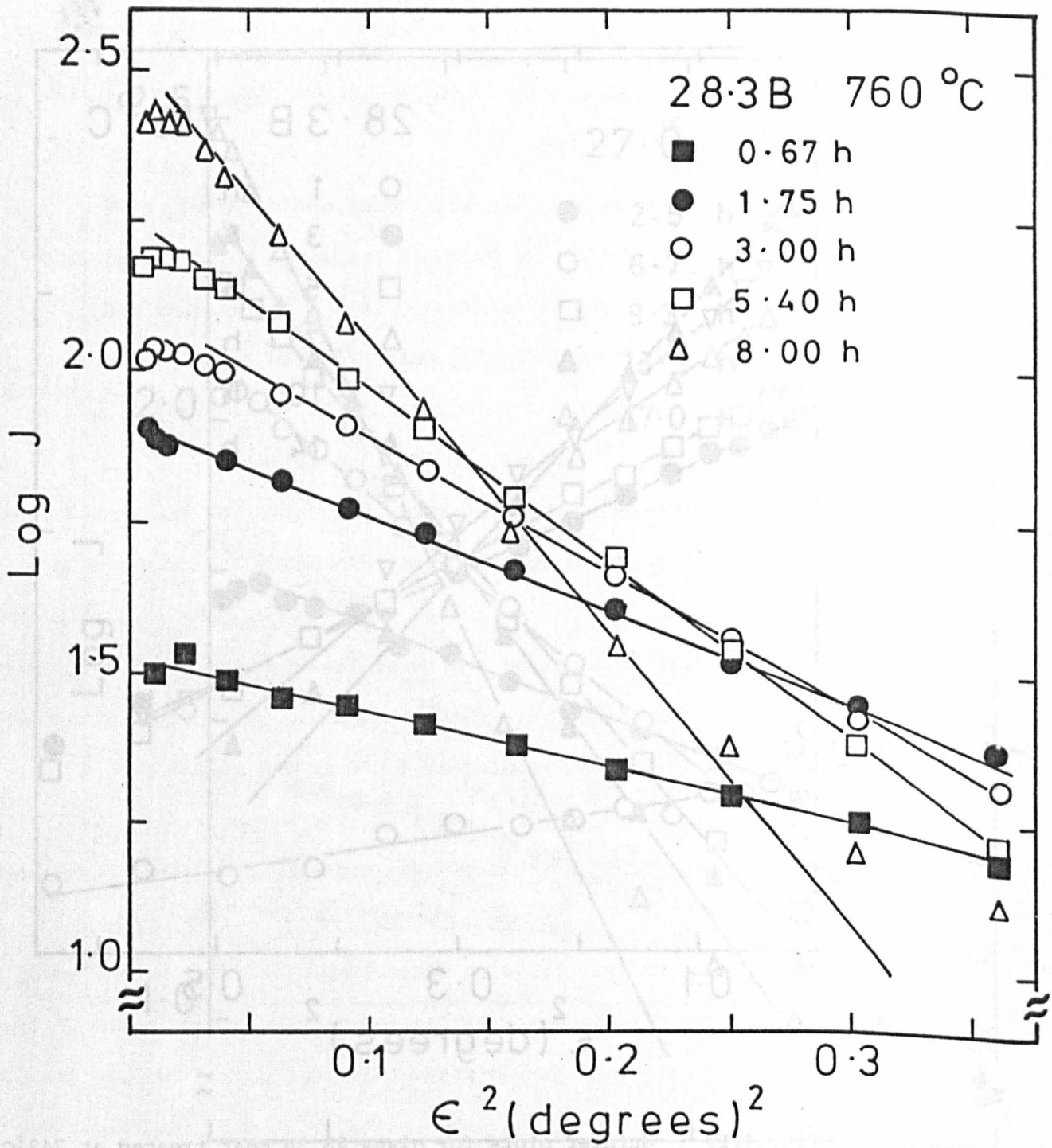

Fig. 4.20 Guinier plots for glass 28.3B heat treated at 760°C.

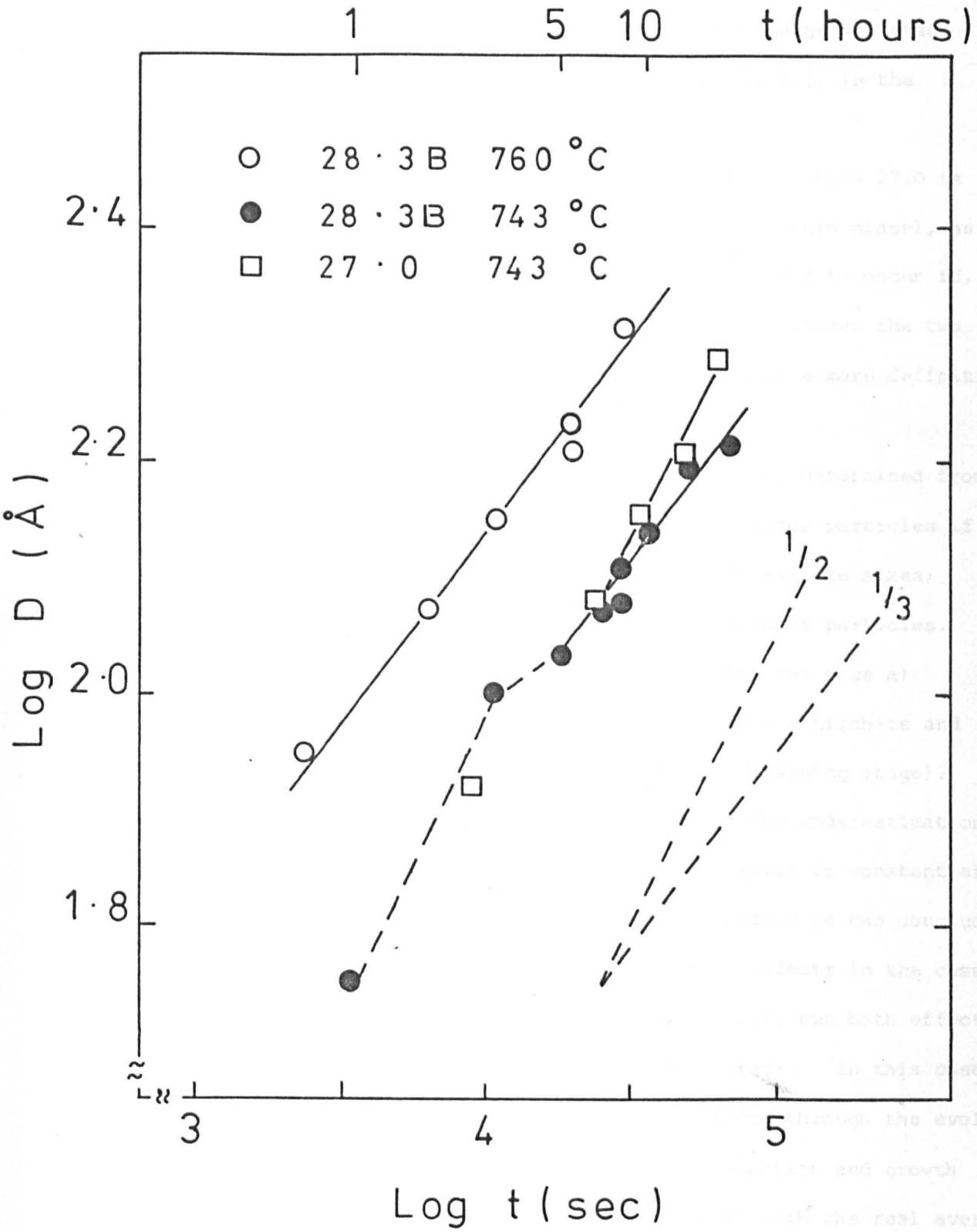

Fig. 4.21 Log D vs. Log (time) plots for glass 27.0 at 743°C, and glass 28.3B at 743°C and 760°C.

amorphous phase separation is either in the nucleation and growth stage (diffusion controlled growth) or, according to Wagner [1.24], in the coarsening stage for interface controlled growth.

The first possibility is ruled out because the APS in glass 27.0 is *not* in the nucleation and growth stage (Q is constant for this glass), as will be shown later. The second possibility is more likely to occur if, for example, there is an impurity layer at the interfaces between the two phases. However, more measurements would be necessary if a more definitive conclusion is to be taken.

It should be emphasized that the average diameter, D, determined from the Guinier plots is: a) strongly biased towards the *large* particles if the phase separated system consists of a wide range of particle sizes; b) *less* than the real diameter for a concentrated system of particles. Zarzycki and Naudin [4.15] have shown theoretically that for case a) D = 1.17 x average diameter of the distribution (assuming a Lifshits and Slyozov distribution which normally fits well in the coarsening stage). For case b) as shown in section 3.9.7, the magnitude of the underestimation depends only on the volume fraction of the particles, which is constant after the matrix reaches its equilibrium composition. Therefore, we can conclude that the Guinier diameters are subject to two opposite effects in the case under study (close-packed size distribution of particles), but both effects have a constant magnitude if the APS is in the final stage. In this case, the growth kinetics of the droplets can still be followed through the evolution of the SAXS diameters. If the APS is in the nucleation and growth stage, the correlation of the measured Guinier diameter with the real average diameter of the distribution changes with time, rendering the interpretation very difficult.

For glass 28.3B heated at 760°C, the diameter of the droplets was large

enough to be estimated in electron micrographs of replicas and thin foils. The results of such measurements are compared with the Guinier diameters in Figure 4.22. It can be seen that the diameters measured in replica micrographs are much larger than both SAXS and thin foil diameters. The magnitude of this discrepancy was shown by Burnett and Douglas [4.10] to depend on the etching conditions of the glass specimens. The diameters determined in the thin foil micrographs are slightly higher than the SAXS diameters, and give an idea of the width of the size distribution of amorphous particles. This difference can be attributed to the underestimation of the SAXS diameters due to interparticle interferences as discussed above.

A set of experiments was performed employing slightly modified experimental conditions, with some repolished specimens of glass 28.3B heated at 743°C to check the reproducibility of the SAXS technique. The newly measured values of D given in Table 4.3b compare well with the old values.

Table 4.3b

DROPLET DIAMETERS IN GLASS 28.3B AT 743°C

t(h)	8	14	19	30	5.4 (760°C)
new D(Å)	129	164	166	228	171
old D(Å)	120	159	165	238	163
% Error	7.5	3.1	0.6	-4.4	4.9

4.4.2.2 Porod's Law

Figures 4.23 and 4.24 show the curves $J(\varepsilon).\varepsilon^3$ vs. ε for glass 27.0 heated at 743°C and glass 28.3B heated at 760°C. According to Equations (3.18) and (3.21) such curves, at large angles, should approach a constant

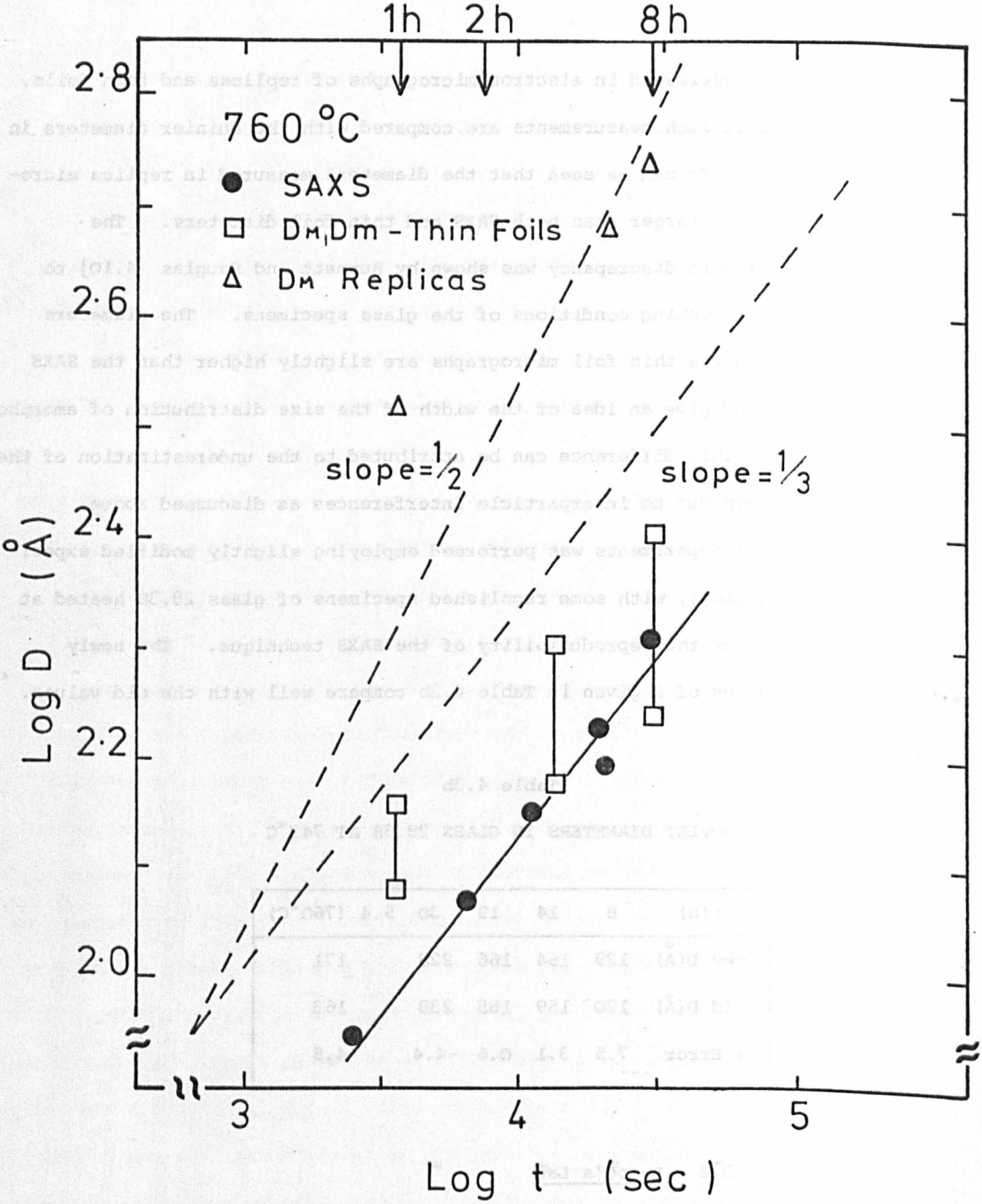

Fig. 4.22 Comparison of droplet diameters in a glass 28.3 mol% BaO measured by different techniques.

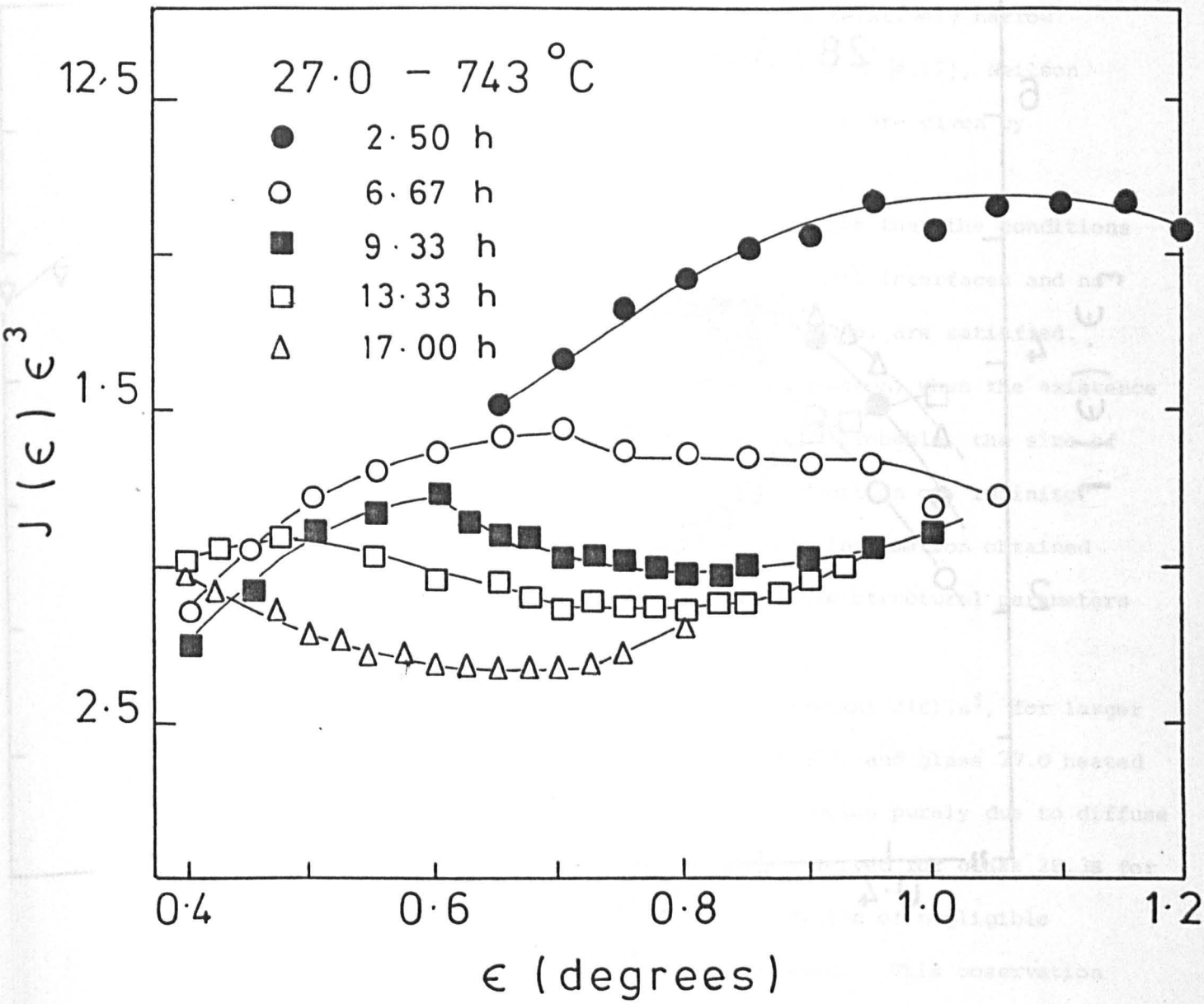

Fig. 4.23 Porod plots for glass 27.0 heat treated at 743°C.

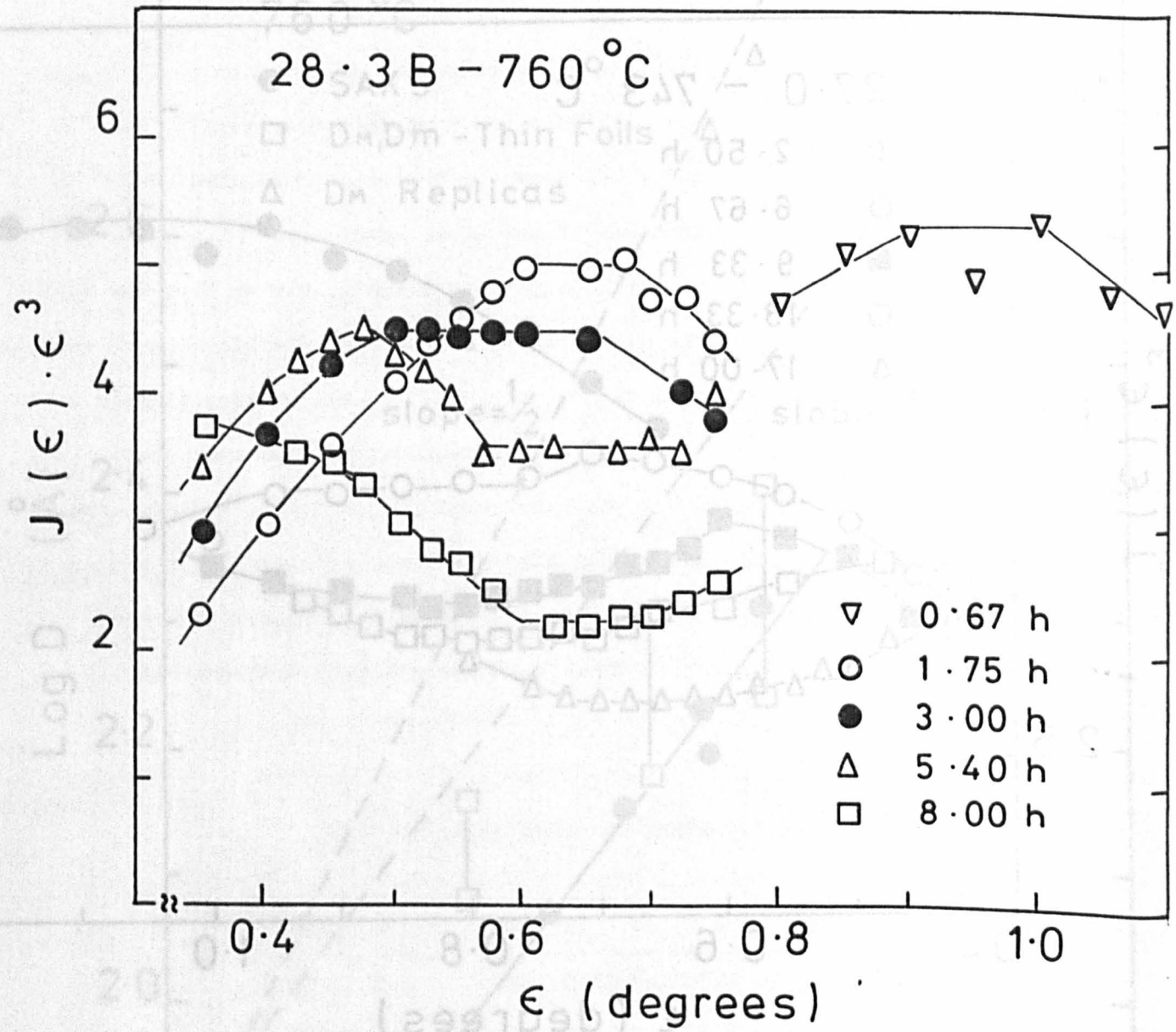

Fig. 4.24 Porod plots for glass 28.3B heat treated at 760°C.

value proportional to the total surface area of the particles. It can be seen that a constant value is observed only within a relatively narrow angular range. Similar observations were made by Gerold [4.12], Neilson [4.11] and Tomozawa [2.28]. Reasons for this behaviour are given by Guinier [3.23].

If Porod's law [$J(\varepsilon).\varepsilon^3$ = const.] holds, it implies that the conditions stated in section 3.9.4, i.e. sharp droplet-glass matrix interfaces and no appreciable compositional fluctuations within each phase, are satisfied. Unfortunately in the very *early* stages of phase separation, when the existence of compositional profiles around the droplets is most probable, the size of the droplets is very small and, in this case, the condition of "infinite" X-ray beam was not completely fulfilled. Thus, the information obtained from the SAXS experiment gives only an estimate of the structural parameters involved.

Therefore, the decrease in the value of the constant $J(\varepsilon).\varepsilon^3$, for larger ε, observed for glass 28.3B heated for 0.67 h at 760°C, and glass 27.0 heated for 2.5 h at 743°C, cannot be seen unambiguously as being purely due to diffuse interfaces. However, the same decrease was also observed for glass 28.3B for 1.75 and 3.0 h at 760°C and, in this case, the condition of negligible scattering at 0.8° (section 3.9.8) was nearly achieved. This observation could suggest the existence of diffuse interfaces in these glasses; however, SAXS experiments employing an intense point-like X-ray beam (e.g. from a Synchrotron source) could be needed to verify quantitatively this suggestion.

It should also be emphasized that the observed angular range of validity for Porod's law begins at $\varepsilon.D \sim 70\text{-}120$, values which are lower than the theoretical lower limit of validity, i.e. $\varepsilon.D \sim 180$ (Degrees Å).

4.4.2.3 Integrated SAXS intensity

It was shown in section 3.9.3 that the scattered intensity integrated over all reciprocal (Fourier) space Q_0, is related only to the volume fractions and chemical compositions of the separated phases (Equation 3.16). If Q_0 becomes constant after a certain period of isothermal treatment, the APS is in the final stage since, in that case, the compositions and volume fractions of the droplets and matrix are constant.

It is demonstrated in Appendix 2 that, for a linear and "infinite" beam, $Q_0 = \text{const. } Q$; $Q = \int_0^\infty J(\varepsilon).\varepsilon.d\varepsilon$. However, it is experimentally impossible to determine the scattering curve over all the extent of reciprocal space, the limits being imposed by a very high parasitic scattering at $\varepsilon < \varepsilon_m$ ($\varepsilon_m = 0.10°$ for the SAXS collimation system utilized) and too low scattering intensity for $\varepsilon > \varepsilon_f$ (ε_f depending on the specimen being studied). To obtain the integral Q, the intensity $J(\varepsilon)$ was determined for $\varepsilon < \varepsilon_m$ by linear extrapolation of the curves $J(\varepsilon).\varepsilon$ (Figure 4.25), and for $\varepsilon > \varepsilon_f$ by means of Porod's equation. Therefore, the final value of Q was obtained by the expression

$$Q = \int_0^{\varepsilon_p} J(\varepsilon).\varepsilon.d\varepsilon + J(\varepsilon_p).\varepsilon_p^2 \qquad (4.4)$$

where ε_p and $J(\varepsilon_p)$ are values within the range of validity of Porod's law. The integral in the expression was evaluated numerically, and by choosing several values of ε_p and $J(\varepsilon_p)$ an estimate of the error in Q was obtained.

The values of Q for glass 27.0 heated at 743°C and glass 28.3B heated at 743°C and 760°C, as a function of time, are plotted in Figure 4.26. It can be seen that a constant value of Q (equilibrium composition of the matrix) is approached after approximately *3-4 h at 760°C* and *7 h at 743°C* for *glass 28.3B*. For glass *27.0 at 743°C*, Q is constant from

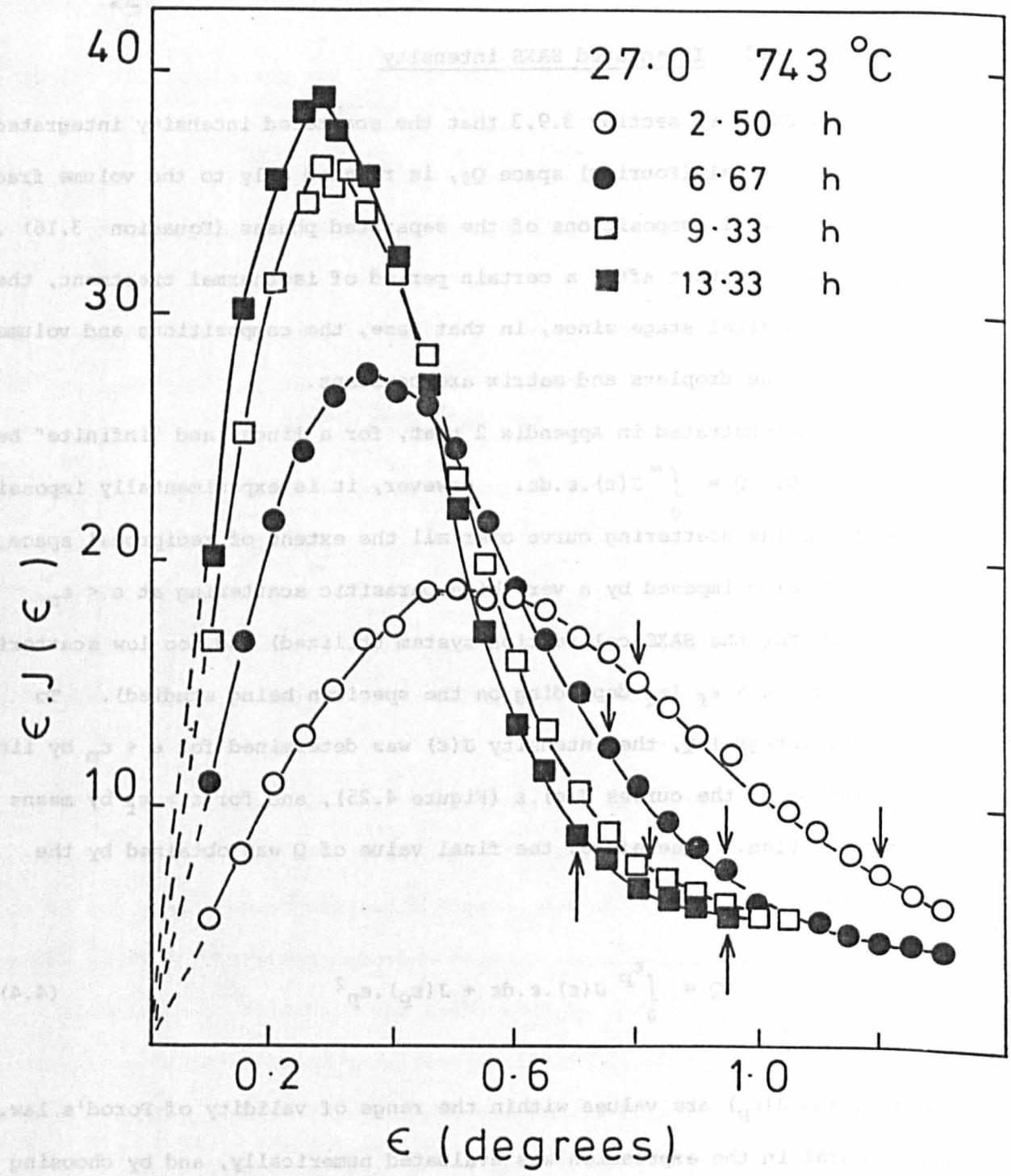

Fig. 4.25 J(ε).ε versus ε curves for glass 27.0 at 743°C. The arrows indicate the regions of validity of Porod's law.

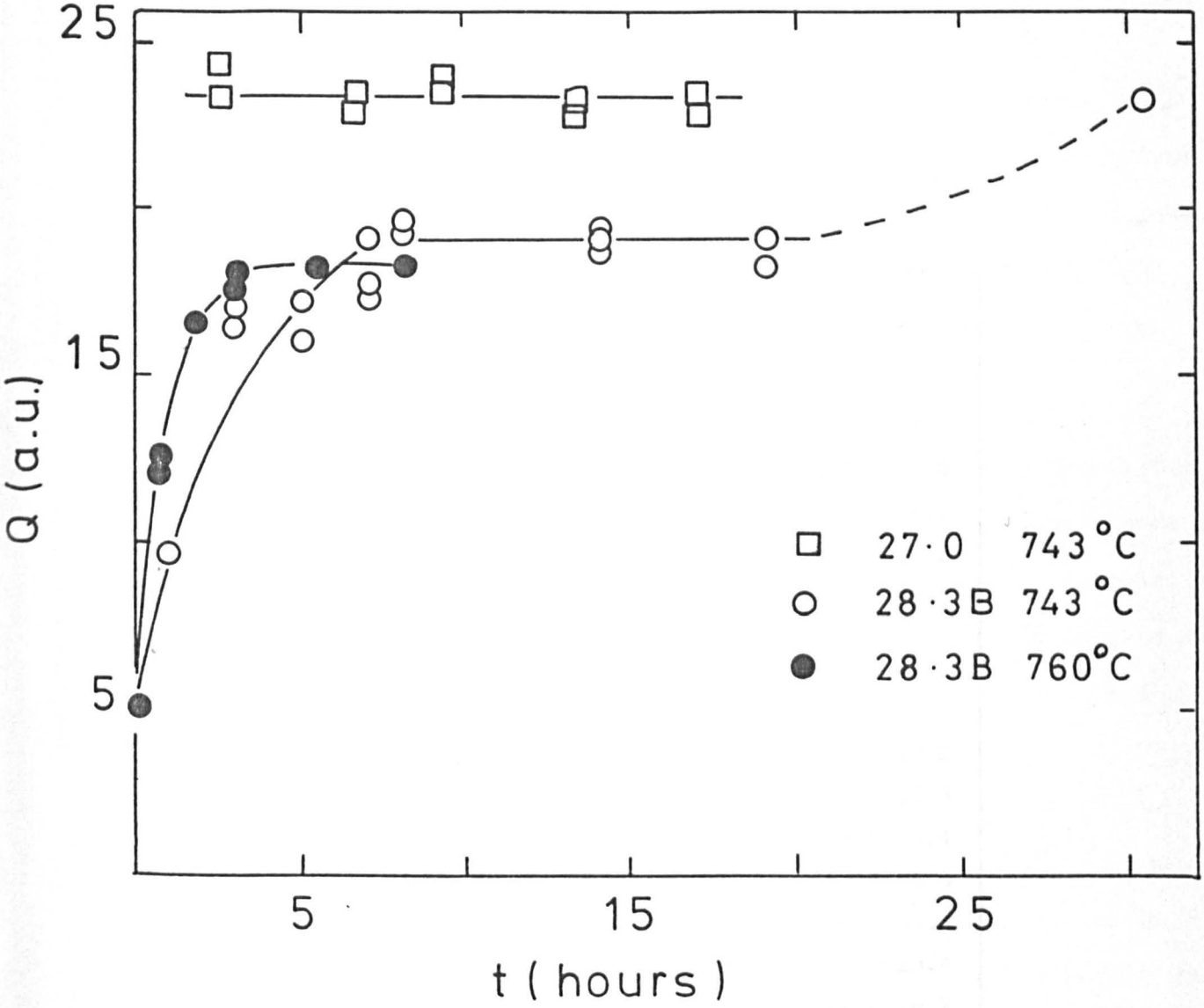

Fig. 4.26 Integrated SAXS intensity for $BaO-SiO_2$ glasses heat treated at 743°C and 760°C.

Table 4.3

SAXS PARAMETERS FOR PHASE SEPARATED

$BaO-SiO_2$ GLASSES

t(h)	J(0)	D(Å)	D_v**(Å)	$J(\varepsilon_p).\varepsilon_p^3$	Q(a.u)
			27.0 - 743°C		
2.50*	58	83	73	10.8	23.7-24.5
6.67	125	121	107	6.8	23.1-23.6
9.33	186	145	129	5.0	23.7-24.1
13.33	225	162	144	4.4	22.6-23.2
17.00	347	195	176	3.4	22.6-23.5
			28.3B - 743°C		
1.0*	10	56	47	>6.3	9.7
3.0*	58	102	87	6.3	16.6-17.2
5.0*	67	108	93	5.3	17.0-17.3
7.0	105	121	107	5.5	17.8-19.4
8.0	96	120	104	6.1	19.4-19.8
10.0	133	138	119	5.3	20.5-20.8
14.0	178	159	140	4.1	18.9-19.4
19.0	173	165	141	4.1	18.6-19.2
30.2	480	238	209	3.0	23.4-24.0
			28.3B - 760°C		
0.67*	32	90	77	5.4	12.1-12.5
1.75	81	119	103	5.0	16.6
3.00	129	142	124	4.5	17.7-17.9
5.40	182	163	145	3.6	18.3
8.00	316	207	188	2.2	18.5

* The condition of linear and "infinite" X-ray beam was not completely fulfilled.

** $D_v = (6v/\pi)^{1/3}$; v = average volume (Equation 9A)

$t < 2.5\ h$ of heat treatment. The increase in Q observed for glass 28.3B heated at 743°C for 30.2 hours could be associated with the advanced stage of crystallization in this specimen (Figure 4.14e). Tomozawa [2.28] made a similar observation when studying the APS in Li_2O-SiO_2 glasses by SAXS.

4.4.2.4 Structural parameters of the phase separated glasses

Having obtained the average diameter of the SiO_2-rich droplets D, the constant of Porod $[J(\varepsilon_p).\varepsilon_p^3]$, the intensity at $\varepsilon = 0$, $J(0)$, extrapolated from Guinier plots, and the Q values (Table 4.3), it was possible to calculate the relative number of particles per unit volume of glass N, the surface area per unit volume of glass S_v, the average volume of the particles v, and the position of the binodal boundary.

a) Relative number of droplets (N)

According to the Appendix 2 (Equation 11A), $N = KJ(0)/\Delta\rho^2 D^5$. If we assume that the difference in electronic densities of the two phases, $\Delta\rho$, is constant (this assumption is strictly valid only for the final stage of the APS), it is possible to follow the variation of N as the isothermal treatment time increases. The N values are listed in Table 4.4.

In Figure 4.27 the inverse of the relative number of droplets vs. time of heat treatment, is plotted. It can be seen that straight lines fit the experimental data reasonably well for glass 27.0 heated at 743°C and 28.3B heated at 760°C. For glass 28.3B heated at 743°C there is a change in the slope after 8 h, when N begins to decrease more rapidly. Of particular interest is the observation that the number of droplets *decreases* from the first heat treatment time given, suggesting that most of the *nucleation* of amorphous particles occurs either during cooling from the melt or within a very short time of heat treatment. The highest rate of dissolution of

particles, however, occurs when the composition of the matrix reaches its equilibrium composition. This point becomes clearer if we compare the evolution of Q (Figure 4.26) and N^{-1} (Figure 4.27) for glass 28.3B heated at 743°C.

It should be stressed that the N^{-1} values for different glasses, or the same glass heated at different temperatures, are not directly comparable because $\Delta\rho^2$ is not the same in each case. Also, the N^{-1} values would be smaller for glasses in which the phase separation was in the early stages, as in this case, $\Delta\rho^2$ would be smaller. This observation reinforces the conclusion that N begins to decrease well before the attainment of the equilibrium composition by the matrix.

(b) Specific surface area of particles (S_V)

Equation (3.18) shows that the surface area of the particles is proportional to Porod's constant $I(s).s^4$. In Appendix 2 (Equation 10A) it is shown that the specific surface, S_V, can be calculated even for the case of scattering curves obtained in an arbitrary scale with a linear and "infinite" X-ray beam.

An independent method was given by Debye, as shown in section 3.9.5. In Figure 4.28, $J(\varepsilon)^{-2/3}$ is plotted as a function of ε^2 for glass 28.3B heated for increasing periods of time at 743°C and 760°C. The slopes and intercepts of the straight lines give the correlation distance $\bar{\ell}$ (Equation 3.24). The specific surface can then be calculated by means of Equation (3.23) [$S_V = 4\phi_1(1 - \phi_1)/\bar{\ell}$].

The volume fraction of the droplets, ϕ_1, was estimated from the position of the co-existence boundary (binodal) at 760°C and 743°C, and the values of S_V calculated by the Porod and Debye methods are given in Table 4.4. It can be seen that there is a reasonable agreement between the two methods, the Porod values being approximately 1.2-2.0 times smaller than Debye values.

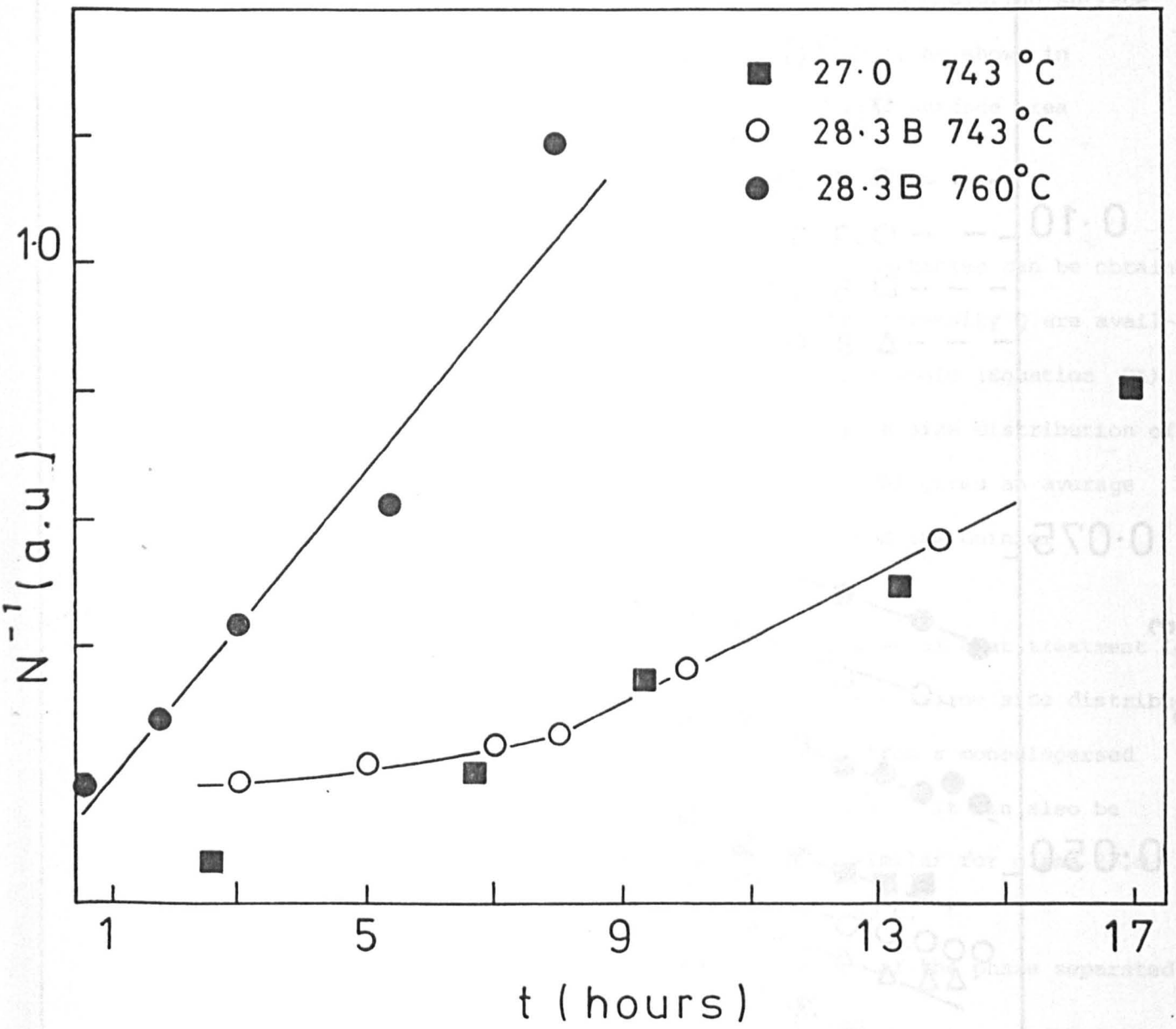

Fig. 4.27 Inverse of the number of amorphous droplets versus time of heat treatment in $BaO-SiO_2$ glasses.

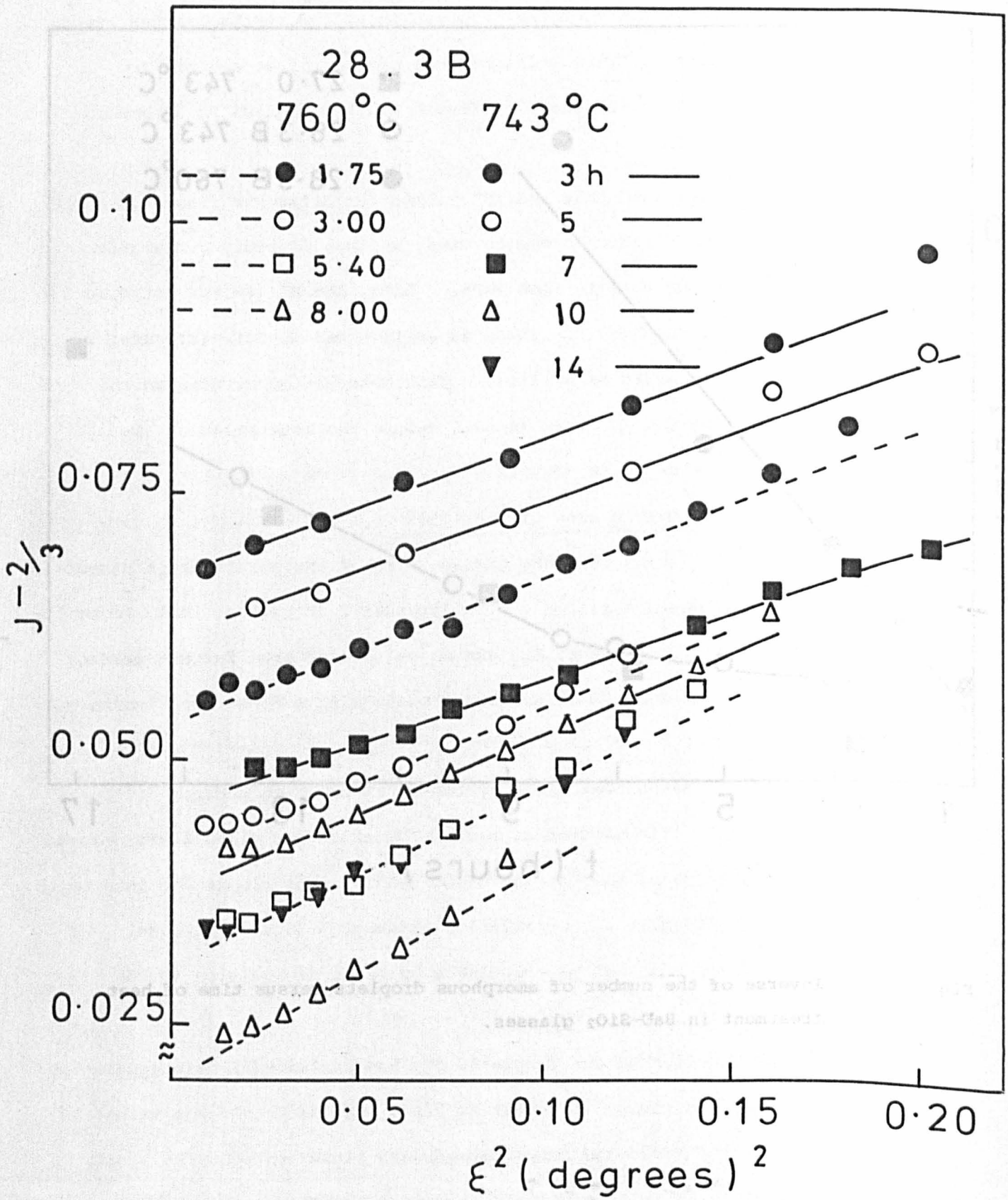

Fig. 4.28 Debye plots for glass 28.3B heat treated at 743°C and 760°C.

A similar result was obtained by Brown et al. [3.31] when measuring surface areas of fillers in polymers. It can be also seen that, as shown in chapter 1, for the coarsening stage of APS the specific surface area *decreases* with the time of heat treatment.

c) Average volume of the particles (v)

It is shown in Appendix 2 that the volume of the particles can be obtained if the extrapolated intensity J(0), and the integrated intensity Q are available, even for scattering curves obtained in a relative scale (Equation 9A). Equations (3.26) and (3.28) also show that if there is a size distribution of particles, the average volume determined by Equation (9A) gives an average diameter $D_V = (6v/\pi)^{1/3}$, which is slightly different from the Guinier diameter D (Table 4.3).

The ratio D_V/D (Equations (3.27) and (3.28) vs. time of heat treatment is plotted in Figure 4.29. It can be seen that there is a narrow size distribution of particles, and the magnitude of the departure from a monodispersed system decreases only slightly with heat treatment time. It can also be concluded that the shape of the size distribution is similar for glass 27.0 heated at 743°C and glass 28.3B heated at 743°C and 760°C.

Table 4.4 shows the various structural parameters of the phase separated glasses determined by SAXS.

4.4.2.5 Determination of the binodal boundary

According to Guinier [3.23], the integrated intensity, Q, is proportional to the compositional difference between the scattering particles and matrix and volume fractions of the two phases

$$Q = K \phi_1 (1 - \phi_1) (C_1 - C_m)^2 \qquad (4.5)$$

Table 4.4

STRUCTURAL PARAMETERS CALCULATED BY MEANS OF SAXS

t(h)	N(a.u.)	$S_v.10^{-5}$ (mm^2/mm^3) Debye	Porod	$v.10^{-6}$ ($Å^3$)
		27.0 - 743°C (ϕ_1 ~ 0.19)		
2.50*	1.460	$26.9\phi_1\phi_2$	$12.6-13.0\phi_1$	0.200
6.67	0.480	11.8	8.2-8.4	0.632
9.33	0.287	10.6	5.9-6.0	1.113
13.33	0.202	10.4	5.4-5.5	1.556
17.00	0.124	9.4	4.1-4.3	2.856
		28.3B - 743°C (ϕ_1 ~ 0.15)		
1.0*	1.700	-	-	-
3.0*	0.534	$20.2\phi_1\phi_2$	$10.4-10.8\phi_1$	0.055
5.0*	0.455	20.0	8.7-9.4	0.342
7.0	0.405	17.1	8.1-8.8	0.417
8.0	0.380	-	8.8-9.0	0.585
10.0	0.270	13.9	7.0-7.3	0.880
14.0	0.175	12.1	6.0-6.2	1.431
19.0	0.144	-	6.0-6.2	1.471
30.2	0.063	-	3.6-3.7	4.80
		28.3B - 760°C (ϕ_1 ~ 0.11)		
0.67*	0.550	$22.8\phi_1\phi_2$	$12.5\phi_1$	0.237
1.75	0.347	16.9	8.6	0.572
3.00	0.227	13.3	7.2	1.001
5.40	0.161	12.1	5.6	1.587
8.00	0.084	8.8	3.4	3.464

* The condition of linear and "infinite" X-ray beam was not completely fulfilled.

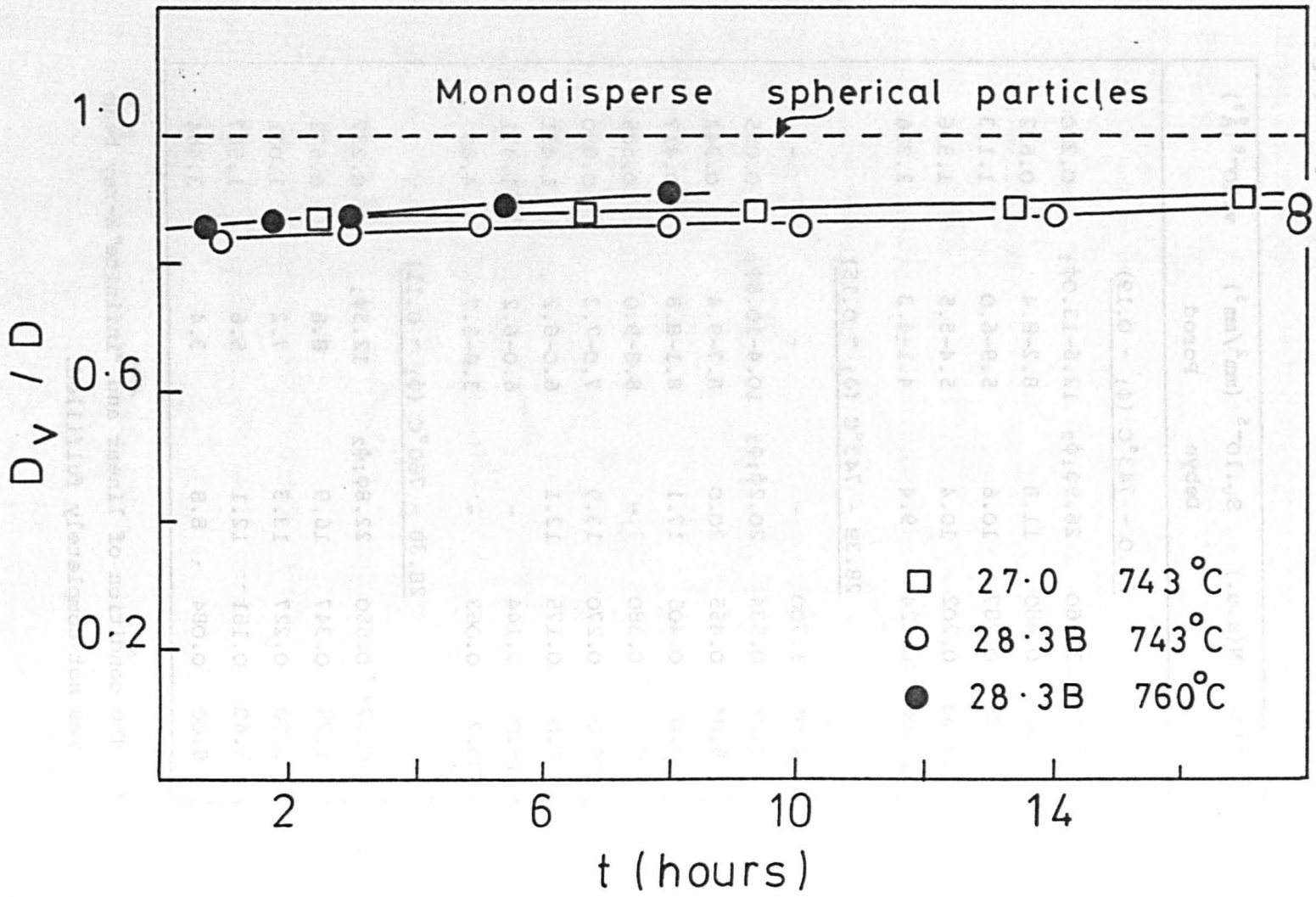

Fig. 4.29 Ratio D_v/D versus time plots for glasses 27.0 and 28.3B.

where C_1 and C_m are the compositions of the dispersed phase and matrix respectively. Thus, from the ratio of Q for two compositions (glass a and b) which were heat treated at the same temperature, C_m the composition of the matrix phase can be determined using the relation

$$\frac{Q_a}{Q_b} = \frac{\phi_{1a}(1 - \phi_{1a})}{\phi_{1b}(1 - \phi_{1b})} \tag{4.6}$$

where ϕ_{1a} and ϕ_{1b} represent the volume fractions of the dispersed phases in glasses a and b respectively, and

$$1 - \phi_1 = \frac{\rho_1(C_g - C_1)}{\rho_1(C_g - C_1) + \rho_m(C_m - C_g)}$$

In this equation, compositions C_1, C_m and C_g (glass composition) are expressed in wt.%, and ρ_1 and ρ_m are the densities of the two phases. A similar expression can be used to find $C_m(T_2)$ when $C_m(T_1)$ is known, by comparing Q at these two temperatures for the same glass composition.

For the present calculation, the constant value for Q for glasses 27.0 and 28.3B heated at 743°C and glass 28.3B heated at 760°C were used. Assuming C_1 = 0 - 1 mol% BaO, ρ_1 = 2.21 - 2.26 g/cm^3, ρ_m = 3.5 - 3.6 g/cm^2, and considering the variations of all the parameters involved in the calculation (within experimental error), the composition of the binodal at 743°C and 760°C were obtained. These values are shown in Table 4.5 together with the values calculated by Haller et al. [2.7] by fitting thermodynamic parameters to the high temperature data of Seward et al. [2.6]. There is a 1 - 2 mol% BaO discrepancy, but it should be emphasized that Seward et al. estimated the determined binodal to be within ±50-100°C and ±1 mol% BaO. Different levels of SrO, the main impurity present in BaO-SiO_2 glasses, could also account for the observed discrepancy.

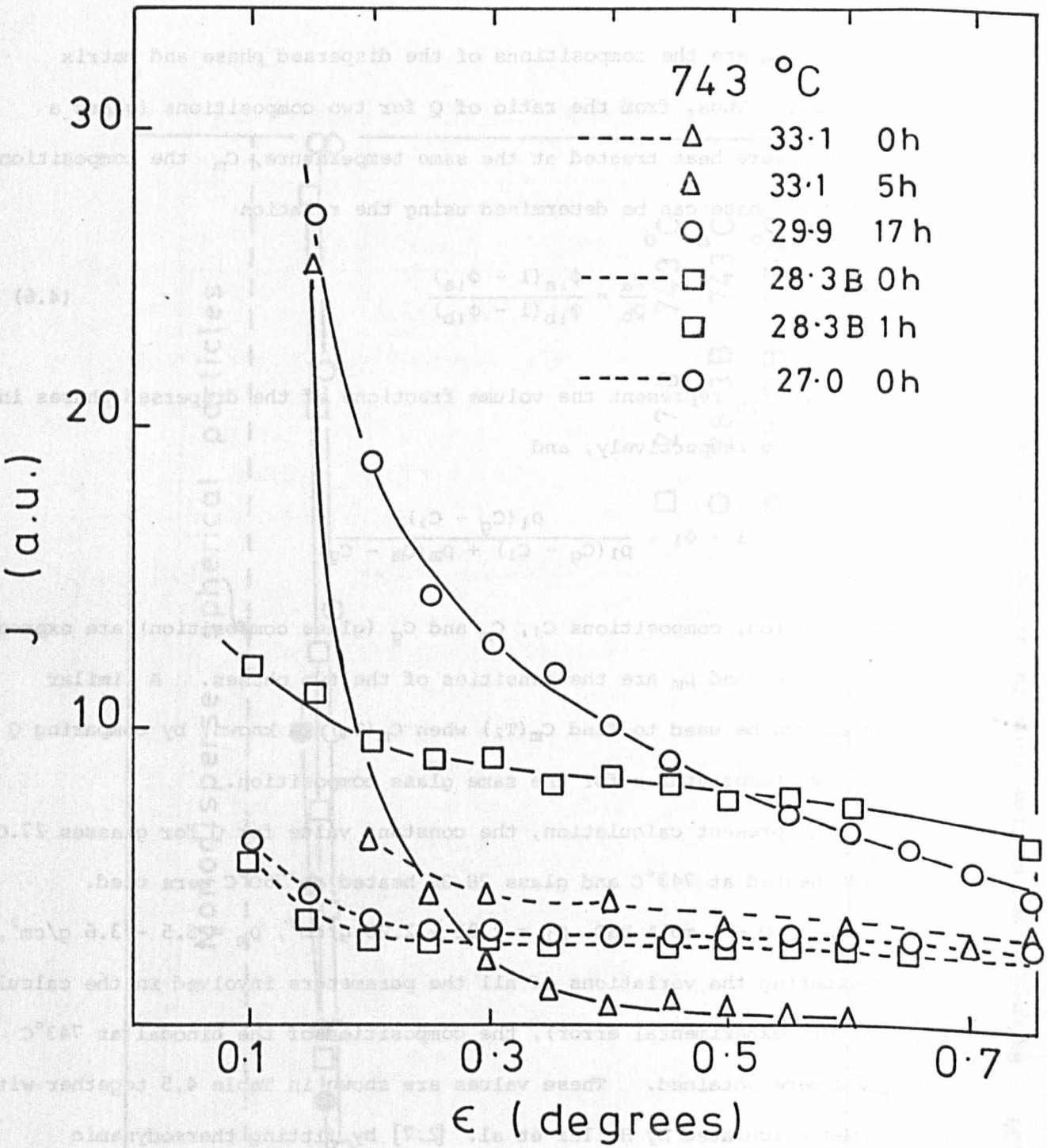

Fig. 4.30 SAXS curves for weakly scattering samples.

Table 4.5

EXPERIMENTAL AND CALCULATED COMPOSITIONS OF THE BINODAL

T(°C)	Experimental	Calculated [2.7]
743	32.0 - 33.0	30.8
760	31.5 - 32.0	30.5

4.4.2.6 Samples with a very weak scattering

As-quenched glasses

It was of interest to test the scattering produced by *as-quenched* samples having compositions inside and outside the miscibility gap. The SAXS curves for as-quenched specimens of glasses 27.0 and 28.3B and the stoichiometric 33.1U (Figure 4.30), show that there is a very weak scattering (compare the values with the scattering curves of glasses 27.0 and 28.3B; Figures 4.15, 4.16 and 4.17) which is similar for the three compositions. The relatively high scattering for $\varepsilon < 0.3°$ could be due to surface imperfections, as observed experimentally by Zanotto [4.18]. According to Williams et al. [4.19] a glass surface needs to be perfectly polished, under 100x magnification, if one needs to eliminate completely the surface scattering. The residual, almost angle independent, scattering observed for $\varepsilon > 0.3°$ could be associated with atomic scale compositional fluctuations. Guinier plots for these curves give equivalent spherical diameters of 20-30 Å. This could imply an incipient phase separation for glasses 27.0 and 28.3B but it would be difficult to explain this phenomenon for glass 33.1U (outside the miscibility gap) on the same basis.

Glasses heat treated at 743°C

Glass 28.3B heated for 1 h shows an increased but still weak scattering. TEM shows that this scattering is produced by a fine scale phase separation. Glass 33.1U heated for 5 h, shows a weak scattering which could be produced by an incipient spherulitic crystallization of BS_2 crystals or by the surface of the specimen. Glass 29.9 heated for 17 h, shows a weak detectable scattering which could be associated with the presence of the BS_2 crystalline spikes (Figure 4.14e). The absence of amorphous droplets in glass 29.9 is very clear if this micrograph is compared with that for glass 28.3B heated for 30.2 h.

Conclusions from SAXS study

The SAXS curves of glass 27.0 heated at 743°C and glass 28.3B heated at 743°C and 760°C show that after a few hours of heat treatment they contain closely spaced distributions of amorphous particles.

Guinier's law is followed over a large angular range for all heat treatments. The average particle diameters D, obtained from the Guinier plots, indicate that the growth kinetics of the amorphous SiO_2-rich droplets are well described by the existing theories for the early and advanced stages. The error in D is estimated to be smaller than 7.0%. Porod's law is valid in narrow angular ranges, in agreement with observations made by other authors. The droplet diameters determined directly in TEM micrographs are in reasonably good agreement with the SAXS diameters.

The evolution of the integrated intensity Q, with heat treatment time indicates that the final stage of liquid-liquid immiscibility (equilibrium composition of the matrix) is approached after about 3-4 h for glass 28.3B heated at 760°C; 7 h for glass 28.3B heated at 743°C and $t < 2.5$ h for glass heated 27.0 heated at 743°C. The maximum error in the Q values is estimated to be 10%, and it is mainly due to the uncertainty in the Porod constant $[J(\varepsilon).\varepsilon^3]$.

The number of droplets decreases with time of heat treatment at 743°C and 760°C in both glasses, implying that most particles nucleate either during cooling from the melt or within a short time of heat treatment. In this case, the coarsening stage begins well *before* the attainment of the equilibrium composition of the matrix, which is given by a constant value of Q.

The specific surface areas of the particles, S_v, calculated by the Debye and Porod methods are in reasonably good agreement. S_v decreases with time as expected for the coarsening stage of amorphous phase separation.

The average volume of the particles, v, was calculated by means of the ratio $J(0)D^5/Q$. The diameter D_v, obtained from v, is slightly smaller than the Guinier diameter D, suggesting that there is a relatively narrow size distribution of particles which changes very little in shape with time of heat treatment.

The binodal boundary on the baria-rich side, determined experimentally, is 1-2 mol% BaO wider than given by the calculations of Haller et al. [2.7].

4.5 Viscosity

4.5.1 Testing the penetration technique and indentors

To test the applicability of the theories (chapter 3) and the accuracy and reproducibility of the viscosity measurements, two standard glasses supplied by the National Bureau of Standards were used (NBS 710 and NBS 711).

NBS 710

Several 3 mm thick samples ≃ 1 cm in diameter were ground parallel and the surfaces to be indented were polished. The viscosity vs. temperature standard curve and the experimental points obtained with different indentors are shown in Figure 4.31. A significant discrepancy can be observed, all

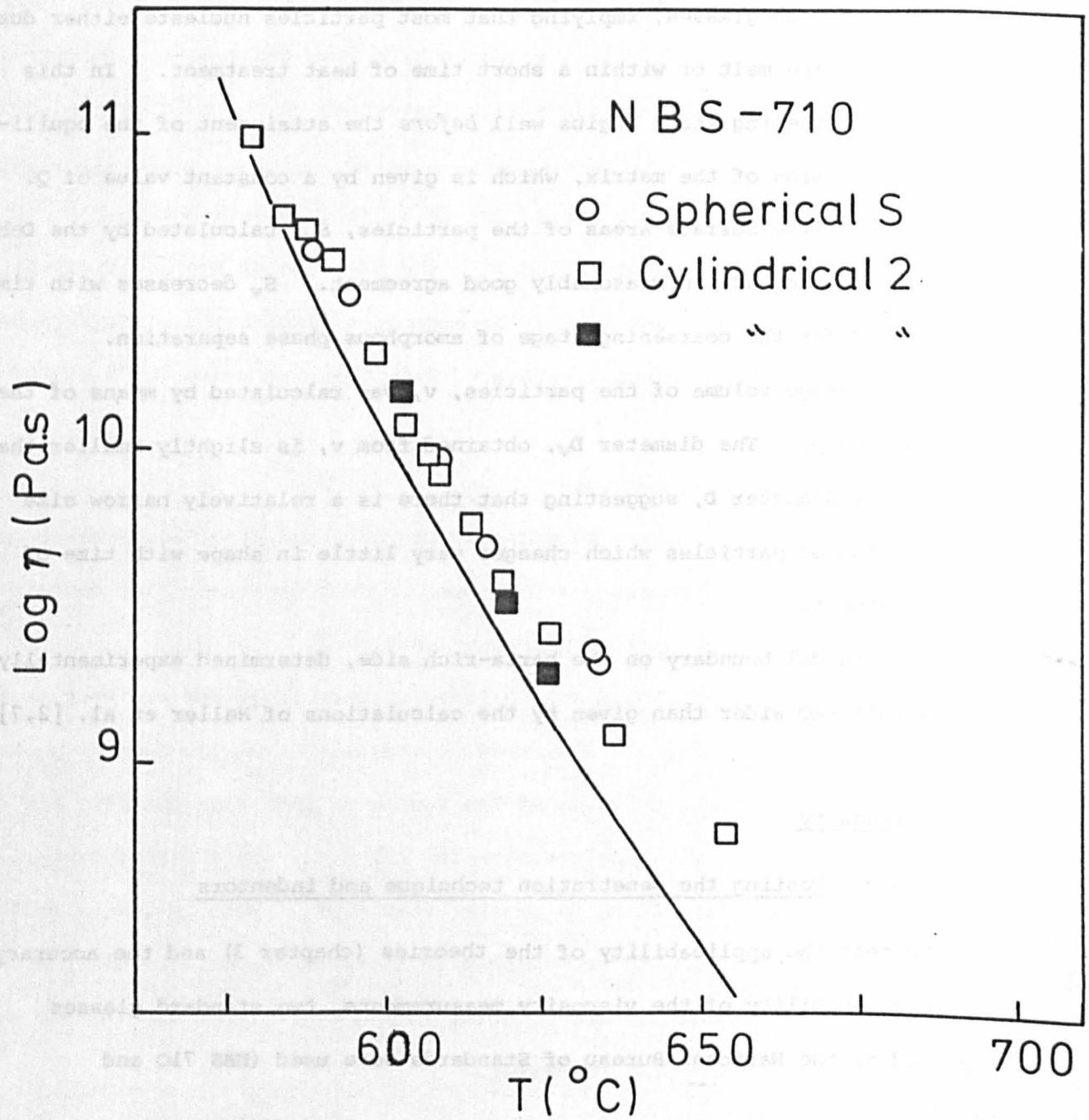

Fig. 4.31 Standard viscosity curve for glass NBS 710 (solid line). Experimental points obtained with:

- o spherical indentor, sample 2.3 mm thick
- □ cylindrical indentor, sample 2.3 mm thick
- ■ cylindrical indentor, sample 4.3 mm thick

experimental points lying above the standard curve. It was also noted that this discrepancy tends to increase with increasing depth of indentation used. In order to clarify this point, and to test the possible influence of sample size on the measured viscosity values, a more detailed study was made employing glass NBS 711 because our stock of glass 710 was quite low.

NBS 711

Figure 4.32 shows the standard viscosity vs. temperature curve and the experimental points, obtained with different indentors, for large (8-10 mm thick, 20-30 mm in diameter) and small (3 mm thick, 10 mm in diameter) samples. For large samples, there is good agreement between the experimental curve obtained with all kinds of indentors employed and the standard curve, in the range 10^8-10^{11} Pa.s, with some deviation (0.1-0.2 in log η) for higher viscosities. For small samples, a pronounced discrepancy is again observed. The agreement of the determination employing the spherical Nimonic indentor with the standard curve, allowed us to use it in the measurements of viscosity of the more refractory BaO-SiO_2 glass because in this case, strong oxidation of the steel indentor would occur.

Cylindrical indentors

In order to gain more insight into the problem of sample size, the penetration velocity of cylindrical indentors (v) versus penetration depth (ε) is plotted in Figure 4.33 for small and large samples. For large samples, it can be seen that initially v decreases by a large amount, tending to a *constant* value as the penetration depth increases. For small samples, there is a continuous and more pronounced decrease in v with increasing penetration depths. This explains why the measured viscosity values tend to depart more from the standard curve as the penetration depth increases, a constant value not being attained with small specimens.

Fig. 4.32 Standard viscosity curve for glass NBS 711 (solid line). Experimental points obtained with:

indentor	sample thickness (mm)
spherical steel	(●) 9.0
spherical nimonic	(○) 9.0; (▽) 2.8
cylindrical (ϕ = 1 mm)	(□) 9.0
cylindrical (ϕ = 2 mm)	(△) 9.0; (⊠) 2.8
cylindrical (ϕ = 3.85 mm)	(■) 9.0

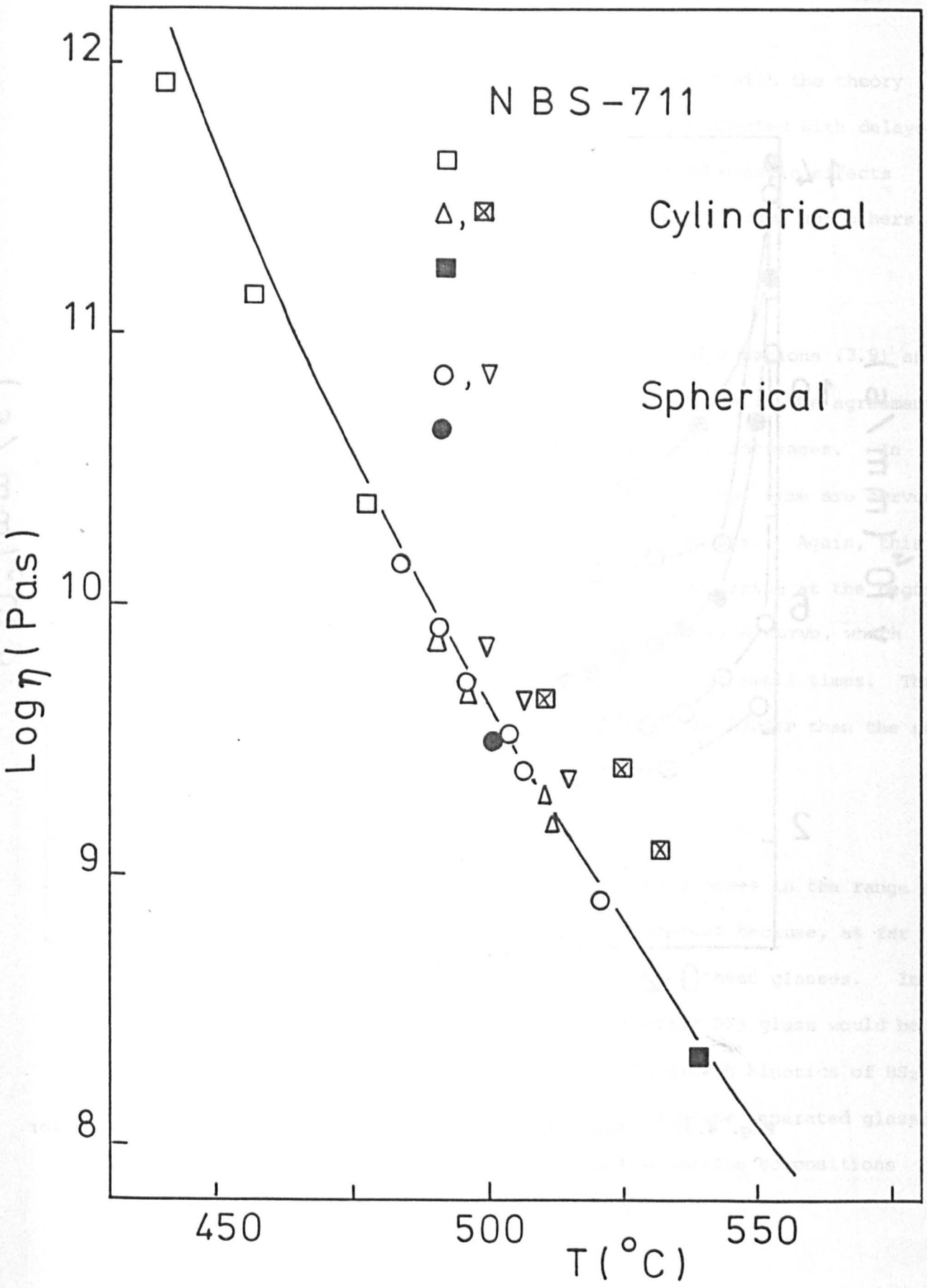
NBS-711
Cylindrical
Spherical
Log η (Pa.s)
T (°C)
12
11
10
9
8
450
500
550

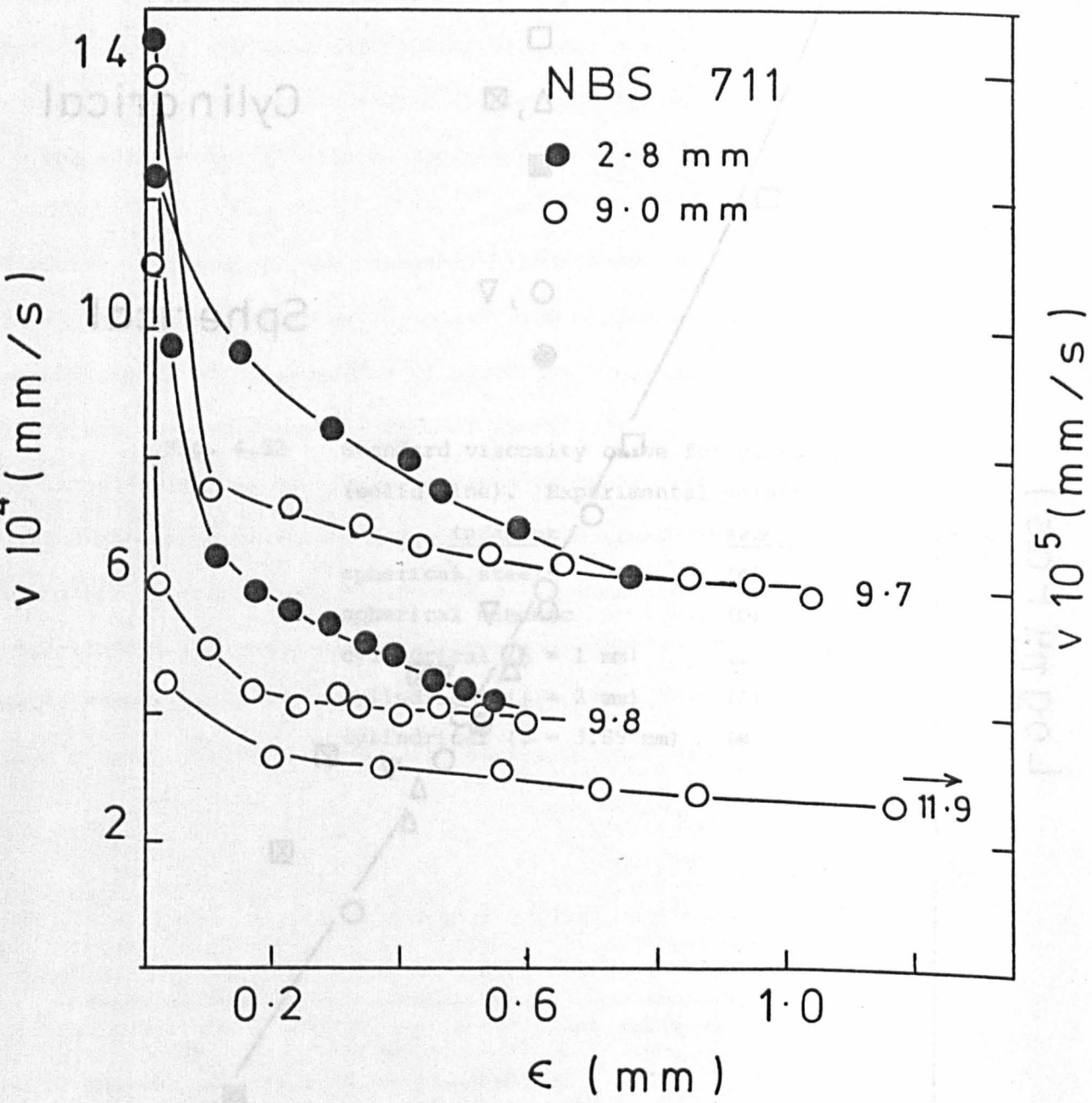

Fig. 4.33 Penetration velocity versus depth of indentation for thin (2.8 mm) and thick (9.0 mm) samples of glass NBS 711.

The behaviour of v for *large* samples is consistent with the theory developed in section 3.6, the initial large v being connected with delayed elastic effects. It must be pointed out that delayed elastic effects above T_g have also been observed by Visser and Stevels [4.20] and others [4.21,4.22].

Spherical indentors

In Figure 4.34 the two functions $\varepsilon^{3/2}$ and $F(\varepsilon)$, of Equations (3.9) and (3.10), are plotted as a function of depth of penetration. The agreement is very good for small penetrations becoming worse as ε increases. In Figure 4.35 it can be clearly seen that the plots $F(\varepsilon)$ vs. time are curved for short times (small ε), becoming straight as ε increases. Again, this behaviour could reflect delayed elastic deformation occurring at the beginning. Figure 4.35 also shows that the slope of the $F(\varepsilon)$ vs. time curve, which determines the viscosity coefficient, is not constant at small times. Thus, any viscosity value calculated from $\varepsilon^{3/2}$ curves, will be *larger* than the real viscosity value the smaller the depth of penetration.

4.5.2 Viscosity of $BaO-SiO_2$ glasses

The determination of the viscosity of $BaO-SiO_2$ glasses in the range of high viscosities ($\log \eta > 8$ Pa.s) was of great interest because, as far as we knew, there was no previous literature data for these glasses. In particular, the viscosity curve for the stoichiometric BS_2 glass would be very helpful in the analysis of the nucleation and growth kinetics of BS_2 crystals. In addition, the viscosity behaviour of phase separated glasses, and the comparison of the viscosity values for the various compositions utilized in nucleation studies was of importance.

4.5.2.1 Stoichiometric glass (BS_2)

The viscosity vs. temperature curve for the 33.2C BaO glass is shown in Figure 4.36. Large samples (~ 10 mm thick, 20 mm in diameter) were used in

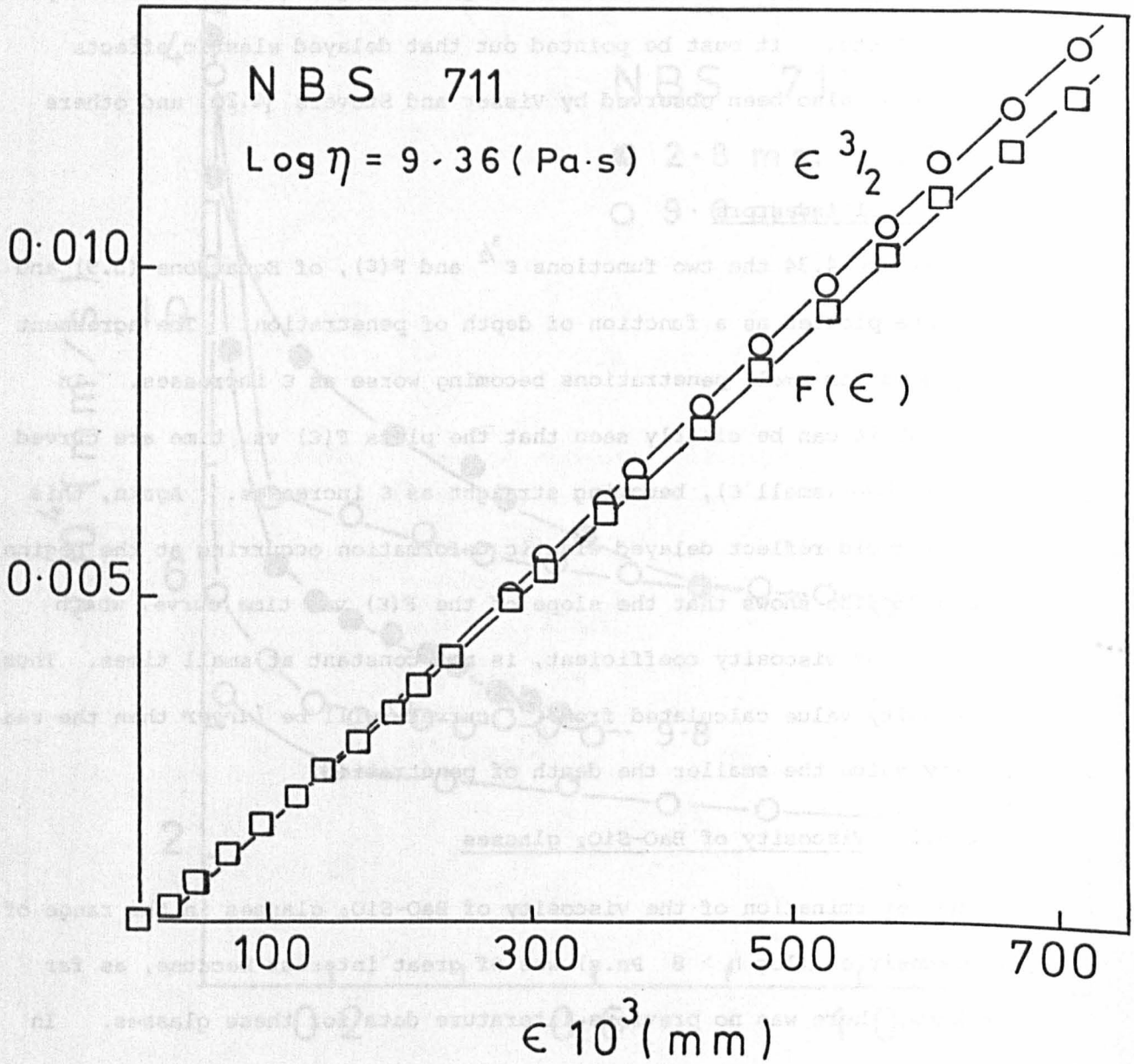

Fig. 4.34 $F(\varepsilon)$ and $\varepsilon^{3/2}$ versus depth of penetration for glass NBS 711 (spherical steel indentor).

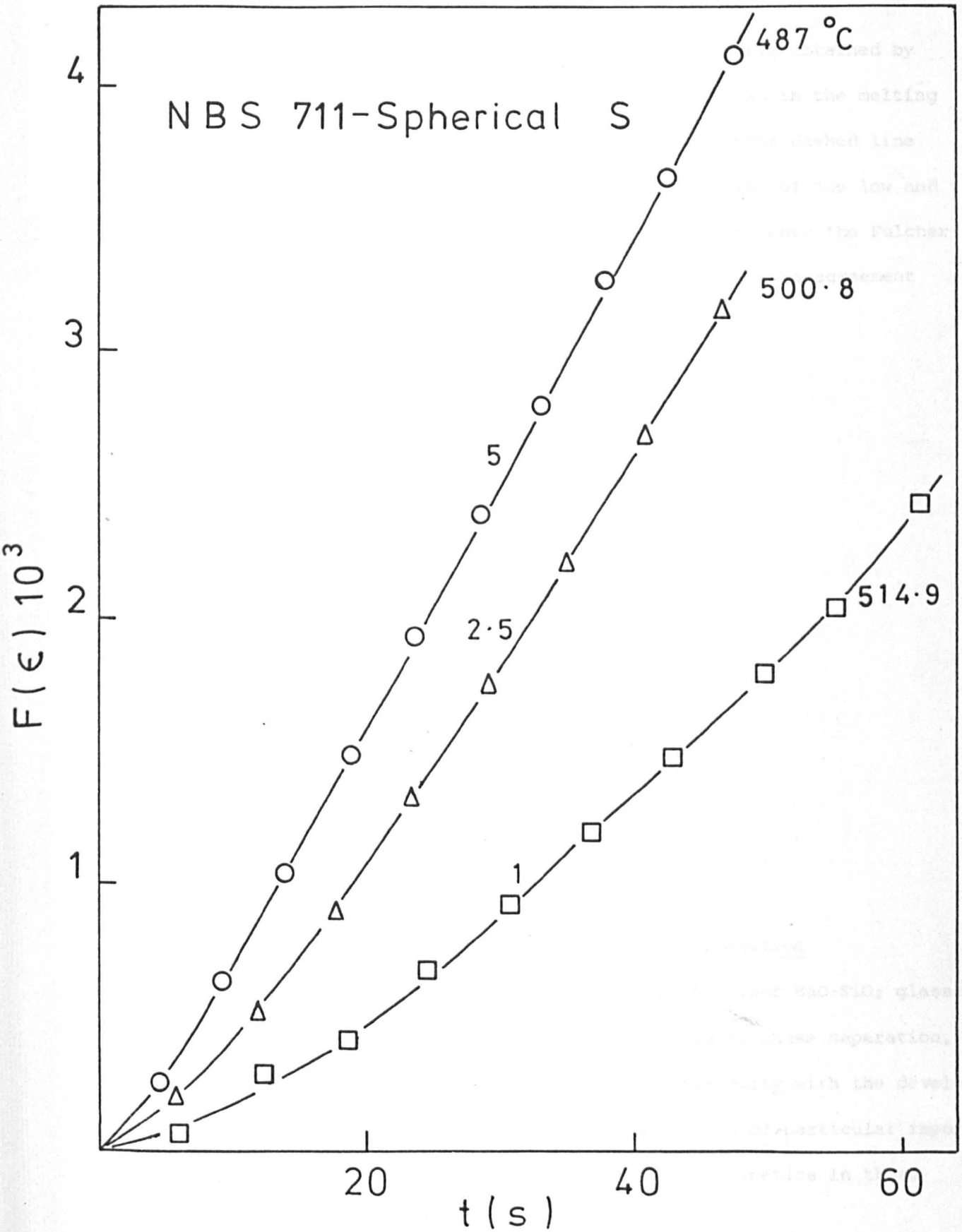

Fig. 4.35 F(ε) versus time curves for glass NBS 711 (spherical steel indentor.

the measurements. In the same figure, the viscosity curve obtained by Bockris et al. [4.23], for a glass with 33.5 ±0.2 mol% BaO in the melting range, using the rotating cylinders method, is shown. The dashed line represents the Fulcher curve obtained with the combination of the low and high temperature viscosity values. The solid line represents the Fulcher equation for the high viscosity range only (Table 4.6). The agreement between both Fulcher curves is quite good.

Table 4.6

FULCHER PARAMETERS* FOR GLASS 33.2C BaO

	High η	Full curve
A	1.83	-3.47
B	1701.90	4283.80
T_0	521.60	411.77

* $\text{Log } \eta = A + B/(T - T_0)$; $T(T_0)$ [°C]; η [Pa.s].

4.5.2.2 Effect of phase separation and composition

The determination of the viscosity curve for the other $BaO-SiO_2$ glasses, including those compositions which undergo liquid-liquid phase separation, was also of interest. The possible variation of viscosity with the development of the amorphous phase separation, would have been of particular importance for the interpretation of the crystal nucleation kinetics in these glasses, i.e. 27.0, 28.3A and 28.3B.

Unfortunately, it was virtually impossible to obtain thick glass

Fig. 4.36 Viscosity curve for glass 33.2C obtained with different indentors at low temperatures. The results of Bockris et al. [4.23] for the melting range are also shown. The dashed line represents the Fulcher equation obtained with a combination of the low and high temperature data.

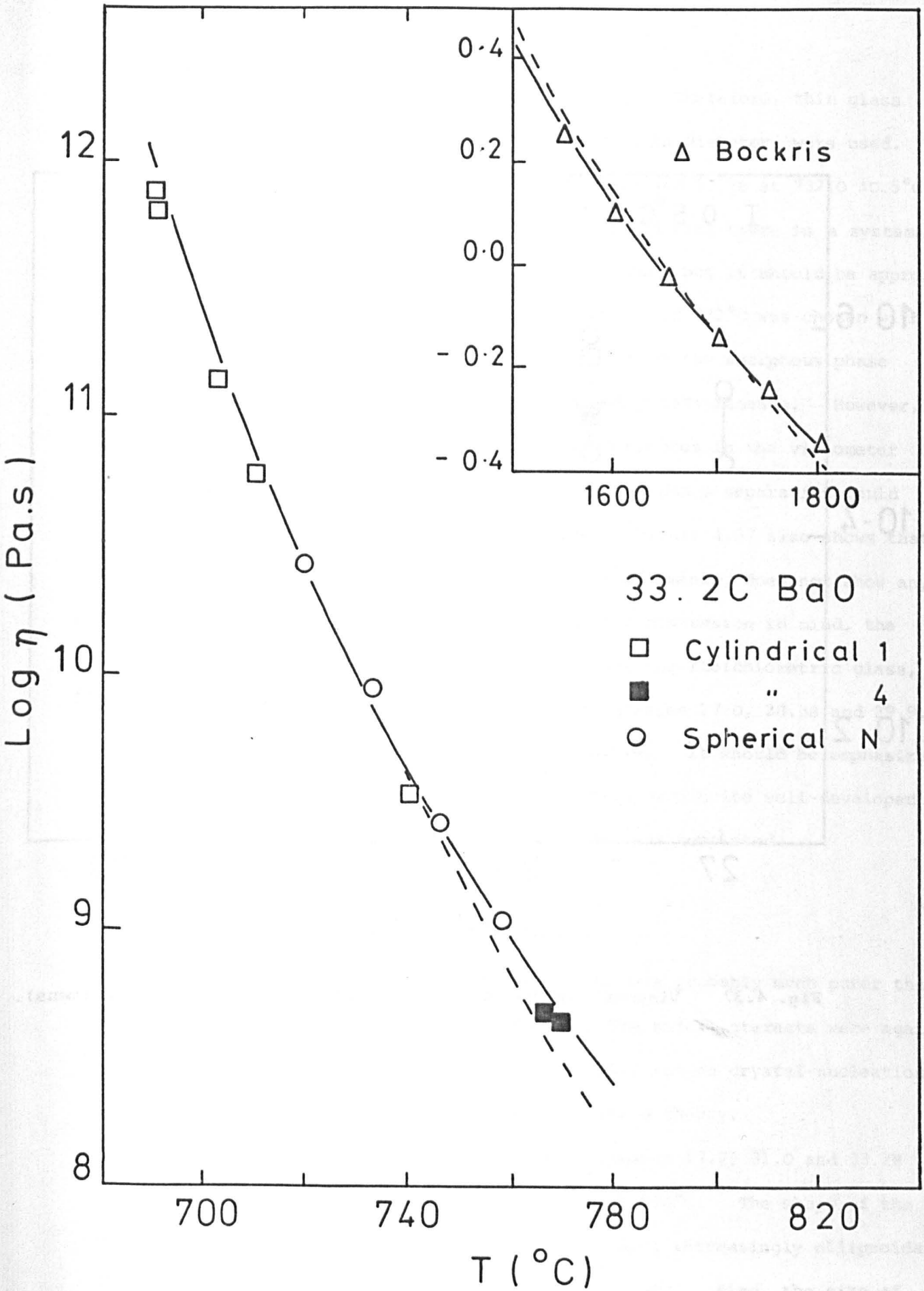
12
11
10
9
8
Log η (Pa.s)
700
740
780
820
T (°C)
0·4
0·2
0·0
- 0·2
- 0·4
1600
1800
Δ Bockris
33.2C BaO
Cylindrical 1
" 4
Spherical N

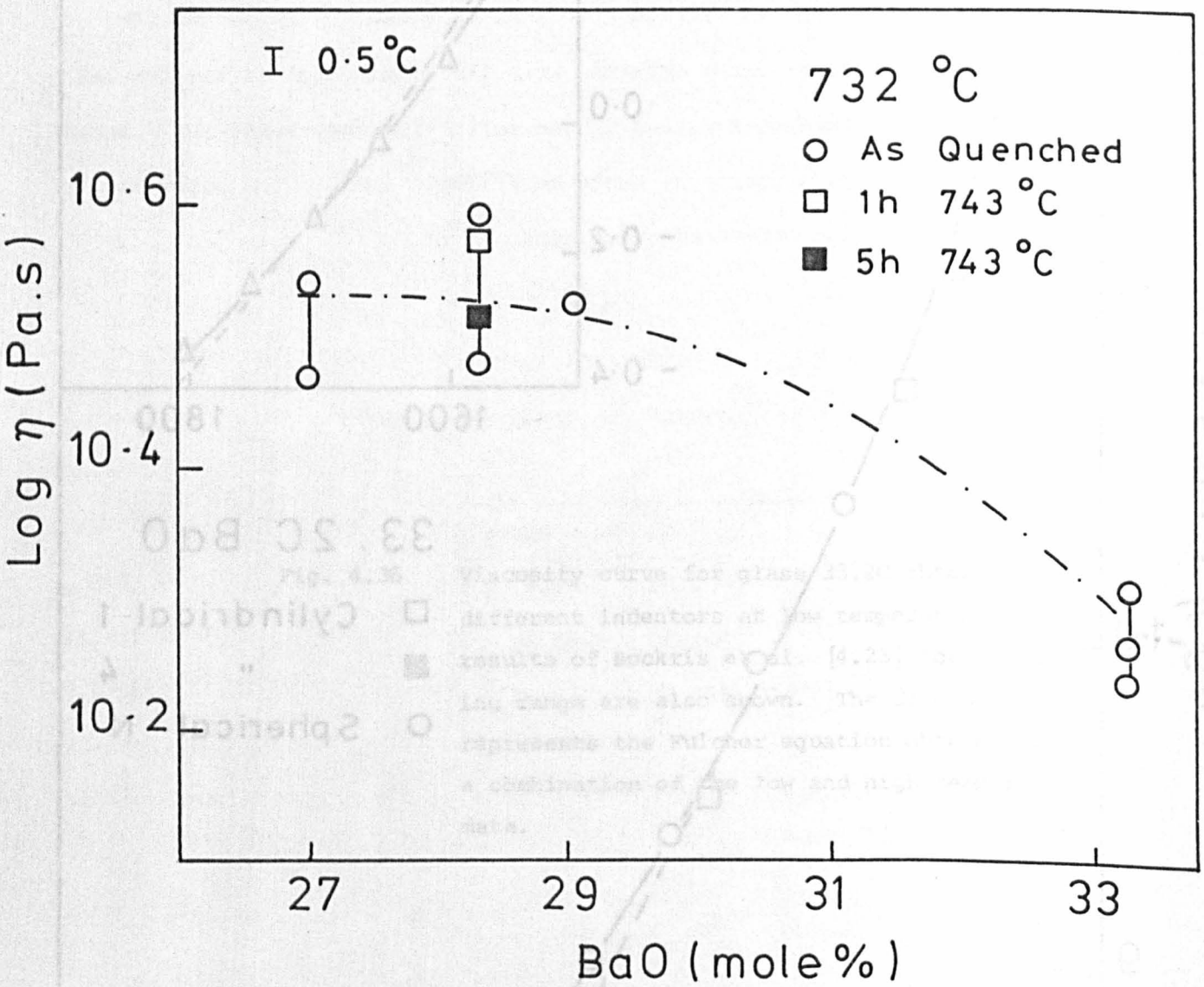

Fig. 4.37 Viscosity of $BaO-SiO_2$ glasses at 732 ±0.5°C (thin specimens).

specimens free of well-developed phase separation. Therefore, thin glass specimens 1.60 to 1.75 mm thick and about 12.0 mm in diameter, were used. The viscosity values of glasses 27.0, 28.3B, 29.9 and 33.2B at 732.0 ±0.5°C are plotted in Figure 4.37. It should be stressed that there is a systematic error in these values due to the small sample sizes, but it should be approximately constant for all samples. The temperature of 732°C was chosen with the requirements of a relatively slow development of the amorphous phase separation and a reasonable time for the viscosity measurements. However, it was necessary to leave the samples for 30-40 minutes in the viscometer furnace in order to obtain equilibrium, and the amorphous separation could have developed substantially during that time. Figure 4.37 also shows that glass 28.3B, heated for 1 and 5 h before the measurements, does not show any appreciable variation in viscosity. Having this discussion in mind, the only general conclusion which can be made is that the stoichiometric glass, 33.2B, has an appreciable *lower* viscosity than glasses 27.0, 28.3B and 29.9, which have *similar* viscosities at this temperature. It should be emphasized, however, that the amorphous separation could have been quite well-developed in glasses 27.0 and 28.3B before the measurement was completed.

4.6 Crystal Nucleation in Li_2O-SiO_2 Glasses

The Li_2O-SiO_2 glasses melted in this study were probably much purer than Li_2O-SiO_2 glasses utilized by other authors. The major interests were again to determine the effects of amorphous phase separation on crystal nucleation and to test quantitatively the classical nucleation theory.

Figure 4.38 shows typical micrographs of glasses 17.7, 31.0 and 33.2B nucleated for 5 hours at 481°C and "developed" at 570°C. The shape of the crystals is different in the three glasses, becoming increasingly ellipsoidal as the stoichiometric composition (LS_2) is approached. Also, the size of

Fig. 4.38 Optical micrographs (reflected light) of Li_2O-SiO_2 glasses. From left to right and top to bottom:

glass 17.7: 5 h at 481°C + 55 min at 570°C

glass 31.0: 5 h at 481°C + 55 min at 570°C

glass 33.2B: 5 h at 481°C + 40 min at 570°C

glass 33.2B: 3 h at 481°C + 40 min at 570°C (transmitted light)

⊢——⊣ = 30 µm

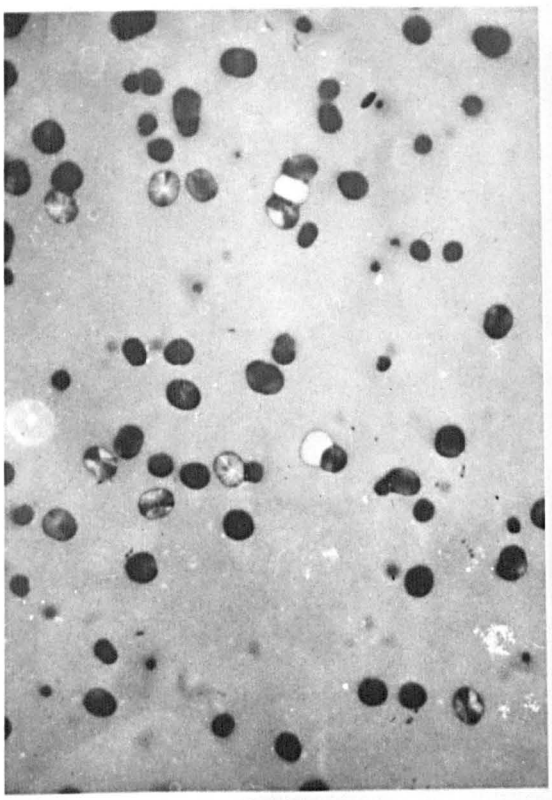

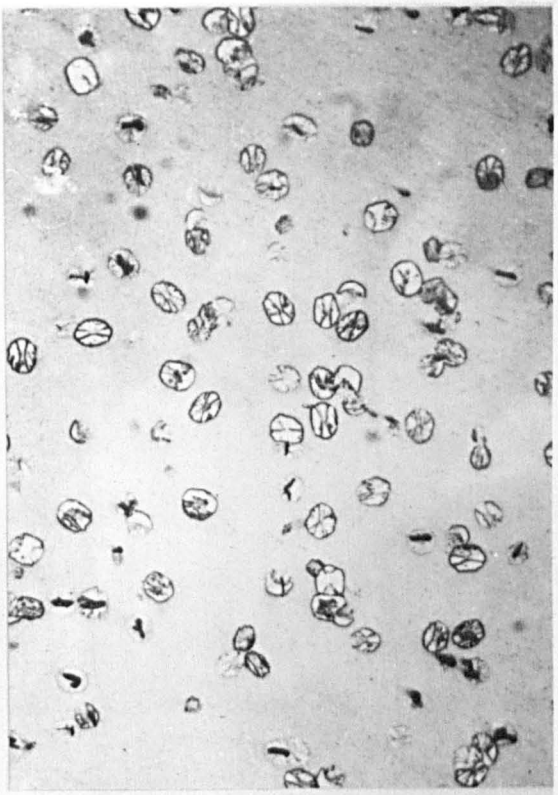

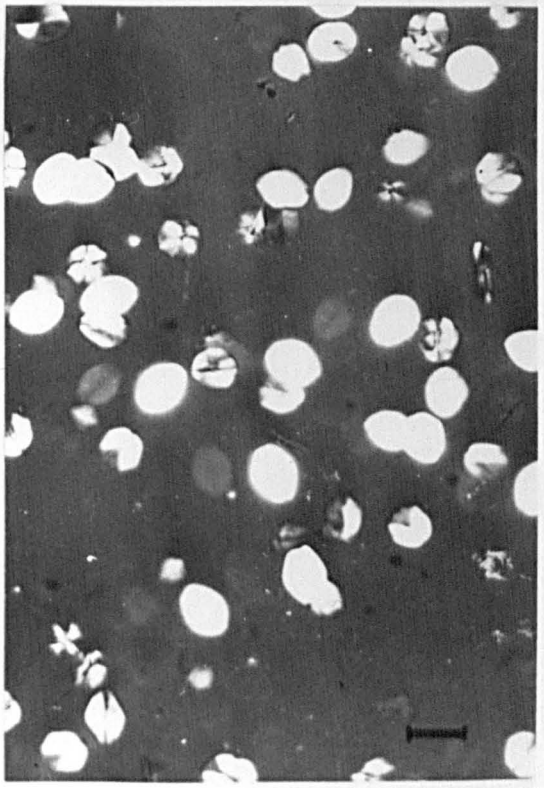

the crystals in the stoichiometric glass 33.2B is clearly larger (reflecting a higher growth rate) than in glasses 17.7 and 31.0. These general features were observed for all heat treatments employed.

4.6.1 Crystal nucleation in phase separated glasses

The transformation range for these Li_2O-SiO_2 glasses is situated around 450°C and a steady-state nucleation rate is rapidly established for temperatures higher than about 475°C, as shown by Figure 4.41 and in [1.62]. Also, it was shown by Zanotto and Craievich [2.50] that the time required for the APS to reach the final stage, in a glass with 31.0 mol% Li_2O, was about 15 hours at 475°C. Therefore, 481°C was the temperature chosen for the study of crystal nucleation in the present Li_2O-SiO_2 glasses. The amorphous phase separation should reach its final stage in a reasonable period at this temperature and non-steady state effects should be negligible. Much higher temperatures would cause the nucleation rates to be too low rendering their accurate measurement more difficult.

Figure 4.39 shows the crystal nucleation densities (N_V) of glasses 17.7, 31.0 and 33.2B at 481°C. The first and most striking observation is that the crystal nucleation rates in glasses 17.7 and 31.0, increases with time and after about 4 hours, are *equal* and about 3.6 times *higher* than the constant rate in glass 33.2B. Another, less obvious observation, is that for glass 17.7, between 1 and 3 hours, there are a number of experimental points systematically higher than the smooth curve drawn. The same phenomenon is observed for glass 31.0 between 2 and 4 hours. Very similar inflexions in nucleation curves of Li_2O-SiO_2 glasses undergoing phase separation have also been observed by Tomozawa [2.28] and Zanotto and Craievich [2.50]. Furthermore, humps of the same kind were observed earlier on the nucleation curves for the BaO-SiO_2 glass 28.3B in the present work. We therefore

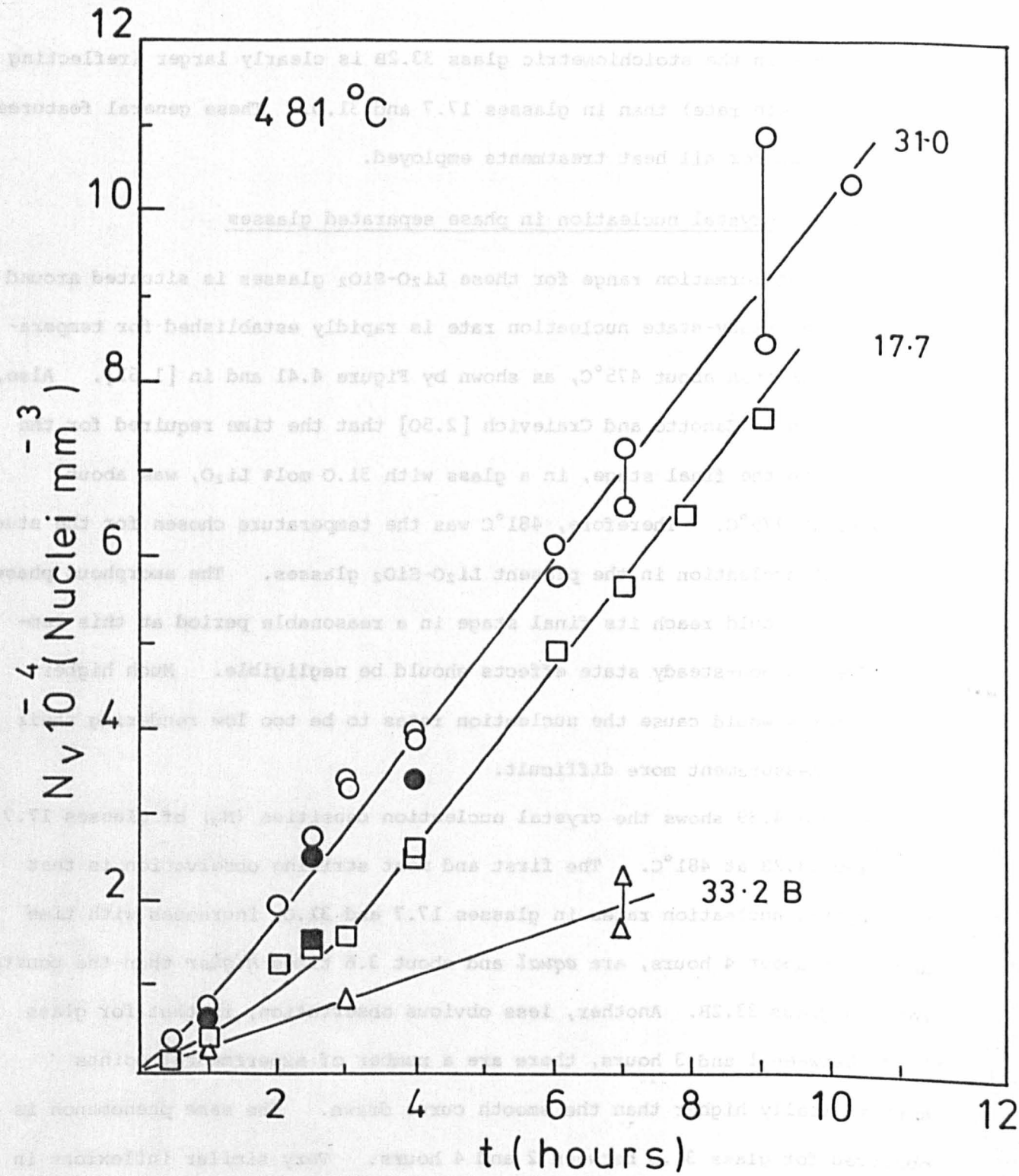

Fig. 4.39 Number of crystals per unit volume (N_v) versus time plots for Li_2O-SiO_2 glasses nucleated at 481°C.
(●, ■) T_d = 600°C ; (○, □) T_d = 570°C

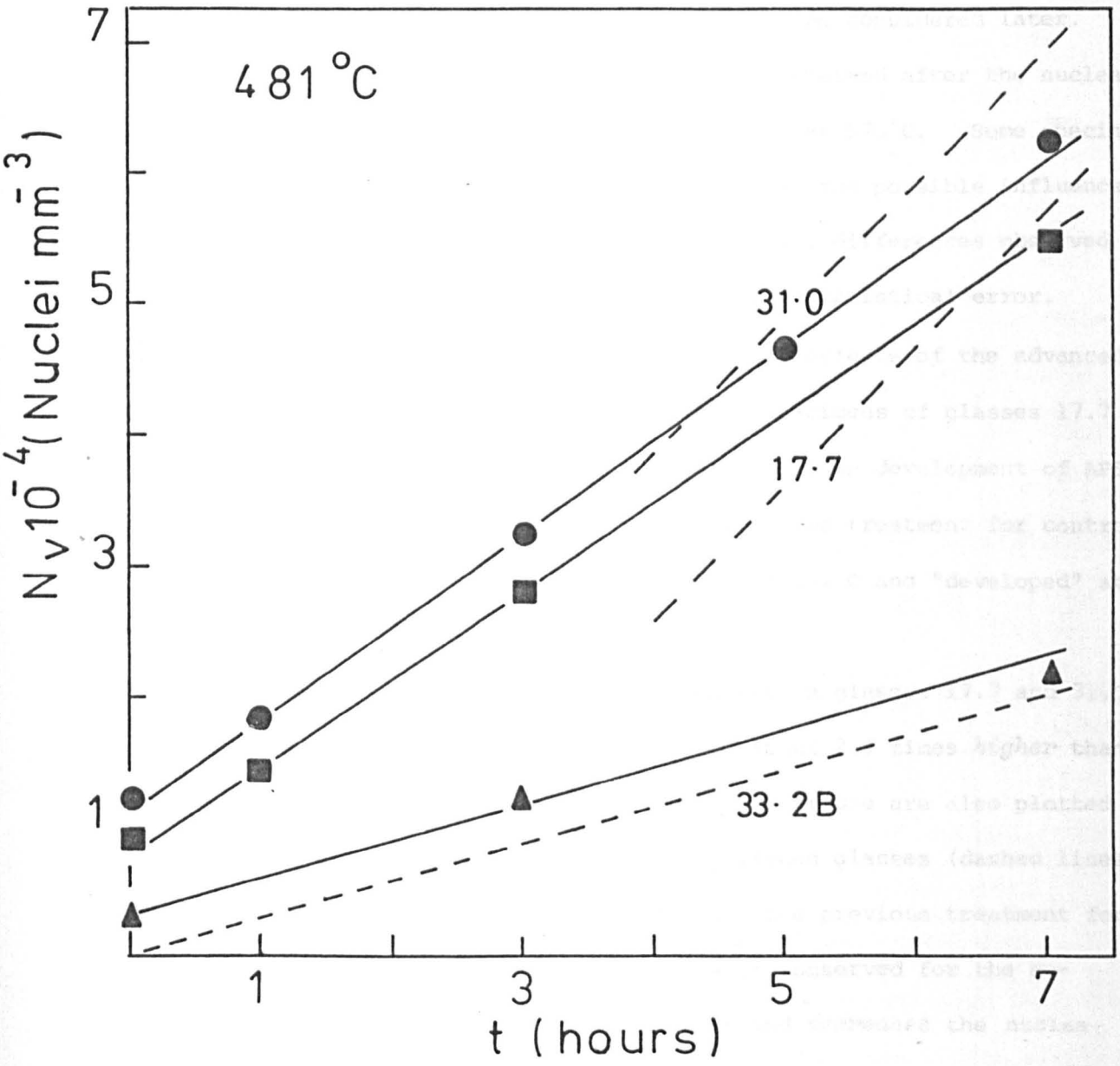

Fig. 4.40 Number of crystals per unit volume (N_V) versus time plots for Li_2O-SiO_2 glasses nucleated at 481°C.

----- as-quenched glasses

——— phase separated for 5 h at 497°C.

tentatively suggest that the small additional effects in glasses 17.7 and 31.0 are genuine. Reasons for this behaviour will be considered later.

Most experimental points in Figure 4.39 were obtained after the nucleated glasses were subjected to a "development" treatment at 570°C. Some specimens, however, were "developed" at 600°C (■ , ●) to test the possible influence of the growth treatment on the N_v values. The small differences observed for the two development temperatures are within the statistical error.

A different experiment was devised to test the effects of the advanced coarsening stage of APS on crystal nucleation. Specimens of glasses 17.7 and 31.0 were *first* heated at 497°C for 5 hours to cause development of APS. Samples of glass 33.2B were also subjected to the same treatment for control purposes. After that, they were all nucleated at 481°C and "developed" at 570°C.

Figure 4.40 shows that the crystal nucleation in glasses 17.7 and 31.0 are *equal* and constant at all times. They are about 2.4 times *higher* than the nucleation rates in glass 33.2B. In the same figure are also plotted the steady-state nucleation curves of the as-quenched glasses (dashed lines) obtained from Figure 4.39. It can be seen that the previous treatment for phase separation at 497°C eliminates the curvature observed for the as-quenched phase separating glasses (Figure 4.39) and *decreases* the nucleation rates. For the non-phase separating glass 33.2B, there is no modification in the nucleation rates. The intercept on the N_v axis is due to nucleation in the initial heat treatment at 497°C.

4.6.2 Crystal nucleation in the stoichiometric glass 33.2B

The composition of glass 33.2B was very close to the stoichiometric phase $Li_2O.2SiO_2$, and the establishment of nucleation rates at different temperatures, together with viscosity and thermodynamic data could be used

to test the classical nucleation theory, as discussed in the first chapter.

Figure 4.41 shows the crystal nucleation density (N_V) versus time curves for glass 33.2B at several temperatures. Pronounced induction periods are observed even above the transformation range ($T_g \simeq 454°C$), i.e. up to 464°C, in good agreement with the results of James [1.62]. The nucleation rates, calculated from the slopes of the curves in Figure 4.41 are tabulated in chapter 5 and are discussed there. It should be stressed that, in this case, the results are more precise than the values obtained for the stoichiometric BS_2 glasses, because the nucleation rates are lower for the 33.2B Li_2O glass, allowing the nucleation curves to be obtained for extended periods of time. Also, the ellipsoidal shape of the crystals could be very well-defined and measured allowing the accurate Equation (3.1) to be used for the calculation of N_V.

4.7 X-ray Diffraction Study of Li_2O-SiO_2 Glasses

It was shown by West and Glasser [2.21] that the first crystallization product of Li_2O-SiO_2 glasses is a metastable lithium disilicate *solid solution*, its composition ranging from 38 to 28 mol% Li_2O. The solid solutions persist indefinitely at $T < 700°C$ and the extent of solution is limited by amorphous phase separation. Several structural variants of the silica-rich solid solutions have been characterized by their X-ray diffraction patterns, which exhibited systematic variations in intensities and sharpness of some reflections.

In this thesis, a study was undertaken to characterize the crystalline phases in the heat-treated Li_2O-SiO_2 glasses. Such characterization could be helpful in the interpretation of the nucleation behaviour of both phase separating and non-phase separating glasses.

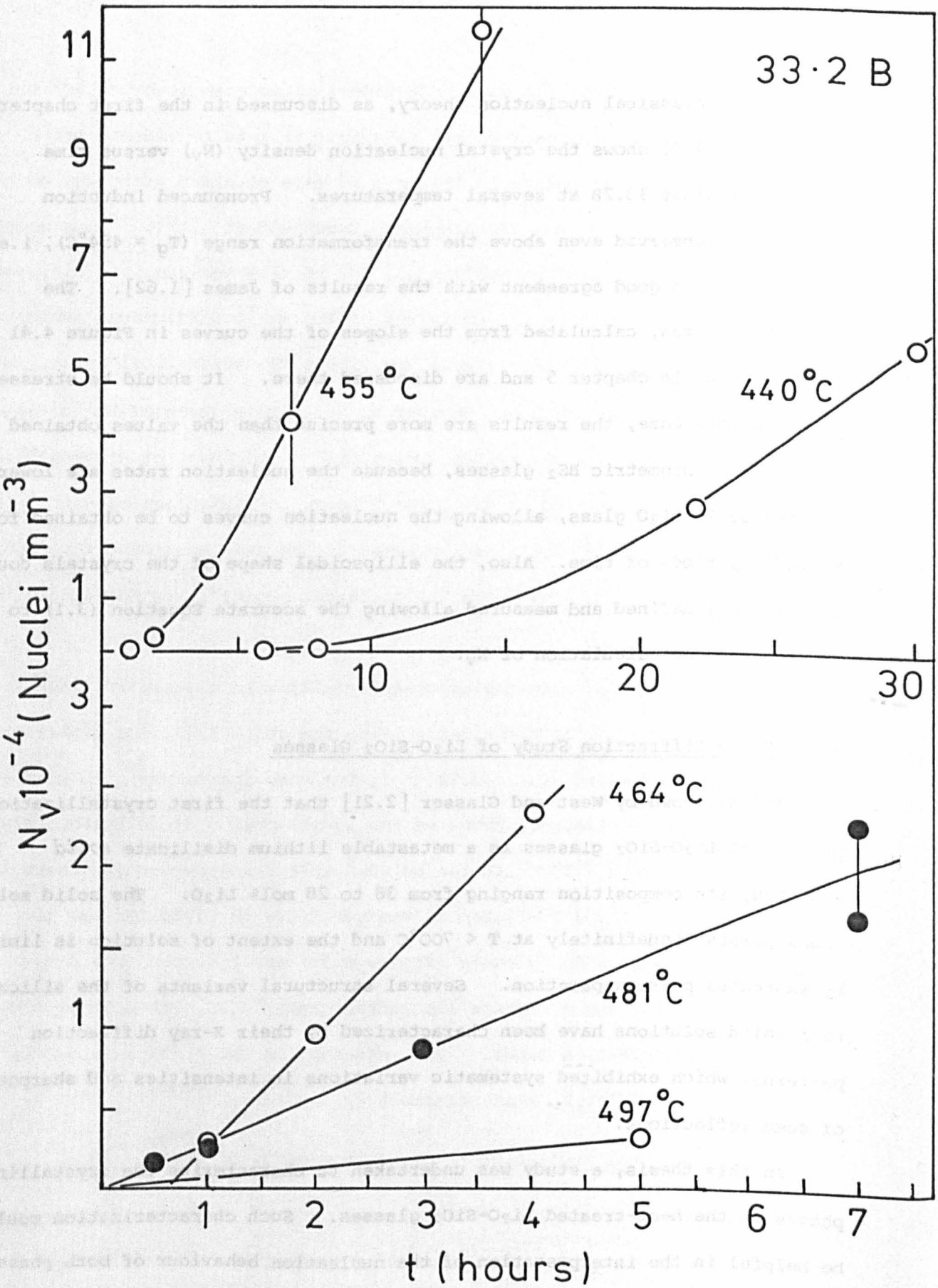

Fig. 4.41 Number of crystals per unit volume (N_v) versus time plots for glass 33.2B.

In order to minimize preferential orientation of crystals, which normally occurs when using powders, monolithic pieces of about 2 x 10 x 20 mm were nucleated at 464°C for 18 h and "developed" at 570°C for 1.5 hours. In this way a large number of randomly oriented crystals were formed in the bulk of the specimens. The diffraction experiments were carried out after the removal of the crystallized surface layer, in a Philips 1730 PW 1050 diffractometer fitted with a graphite monochromator. Copper Kα radiation was used and the calibration of the goniometer was performed by a Si polycrystalline standard. The interplanar spacings (d) and relative intensities of the reflections (I_r) for glasses 17.7, 31.0 and 33.2B are given in Table 4.7.

The values of Table 4.7 are shown schematically in Figure 4.42. It can be seen that the phases crystallizing in glasses 17.7 and 31.0 give very similar diffraction patterns and can be identified as a *solid solution* structure given by West and Glasser (Figure 6.c in [2.21]). The diffraction pattern of glass 33.2B is identified with the low temperature form of LS_2 (Figure 6.a in [2.21]). The results for glass 33.2B are also compared with literature data for ℓ-LS_2 in Table 4.8. In no instance were the main lines of lithium metasilicate (4.70, 3.31, 2.71, 1.56, 1.57 Å) or h-LS_2 (3.73, 3.61, 2.40, 1.99 Å) detected.

Table 4.8 shows that the most important lines for the ℓ-LS_2 crystal phase are the 3.72, 3.63, 3.56, 2.38 and 1.97 Å lines. The maximum difference between the results of several authors is 0.03 Å for these spacings. The large discrepancies observed in the relative intensity values of these lines are probably due to preferential orientation of the crystals during the preparation of the powdered specimens for the X-ray experiments.

Table 4.7

X-RAY DIFFRACTION RESULTS FOR Li_2O-SiO_2 GLASSES

2θ(Deg)	d (Å)	I_r
	Glass 17.7	
16.55	5.351	4
24.00	3.704	39
24.60	3.615	61
24.95	3.566	100
30.80	2.900	6
37.60	2.390	26
	Glass 31.0	
16.45	5.384	7
23.90	3.720	34
24.48	3.633	60
24.89	3.574	100
30.45	2.933	4
30.75	2.905	7
37.60	2.390	24
	Glass 33.2B	
16.50	5.368	12
23.93	3.715	67
24.48	3.633	48
24.98	3.561	100
30.50	2.928	3
30.83	2.898	9
37.73	2.382	62
38.35	2.345	11
39.45	2.282	5

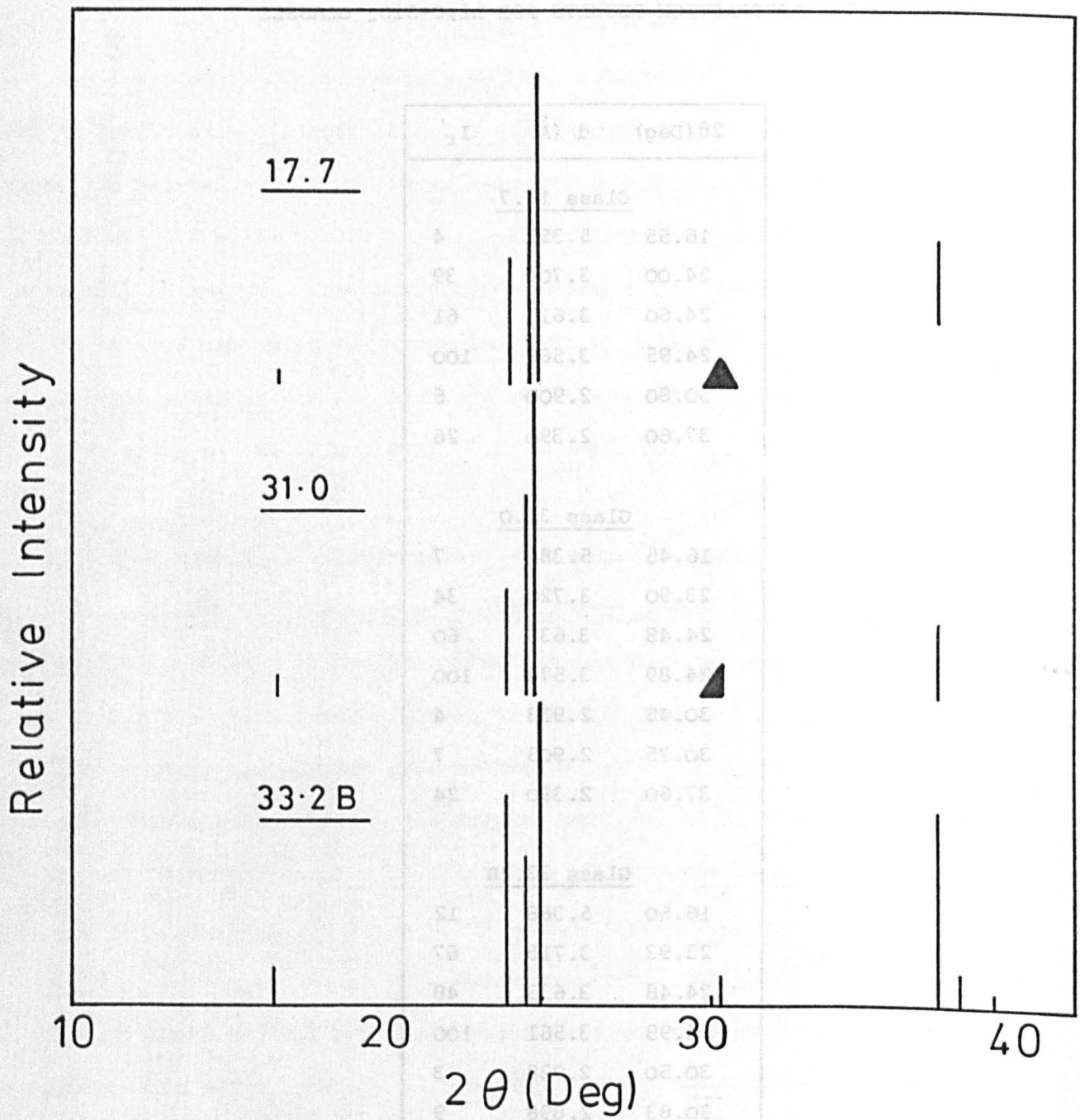

Fig. 4.42 Schematic XRD patterns for Li_2O-SiO_2 glasses nucleated for 18 h at 464°C and developed for 1.5 hours at 570°C.

Table 4.8

X-RAY DIFFRACTION DATA OF LOW-LITHIUM DISILICATE

ASTM [4.29]		Roy [4.30]		Rindone [4.31]		Gruner [4.32]		Noshiro [4.33]		Kalinina [2.19]		Present Work	
7.31	12	7.35	4	7.332	4	7.38	5	7.37	20	7.26	5	-	-
5.41	6	5.39	12	5.392	8	5.42	5	5.44	7	5.38	20	5.37	12
4.02	2	4.10	4	-	-	-	-	4.04	3	-	-	-	-
3.75	45	3.73	80	-	-	3.75	100	3.72	50	3.721	75	3.72	67
3.66	100	3.64	65	3.666	52	3.65	95	3.65	100	3.640	65	3.63	48
3.61	30	3.58	100	3.588	100	3.59	80	3.58	12	3.567	100	3.56	100
-	-	2.93	10	2.950	5	-	-	-	-	2.937	27	2.93	3
2.91	2	-	-	2.900	12	2.921	5	2.91	5	2.902	16	2.90	9
2.39	4	2.385	30	2.403	29	2.392	40	2.39	4	2.387	62	2.38	62
2.35	4	2.36	10	2.352	8	2.356	10	2.36	4	2.353	46	2.35	11
2.295	2	2.30	5	2.299	14	2.298	7	2.29	6	2.284	27	2.28	5
2.054	2	2.06	7	2.056	7	2.058	4	2.06	4	2.050	24		
2.012	2	2.00	5	2.010	5	2.014	3	-	-	2.010	15		
1.966	30	1.96	15	1.97	12	1.973	30	1.969	20	1.980	57		
1.847	2	1.84	4	1.85	5	1.852	2	1.860	4	1.866	5		

4.8 Liquid-liquid Immiscibility in Li_2O-SiO_2 Glasses

The liquid-liquid immiscibility in Li_2O-SiO_2 glasses has been studied by TEM by several investigators, among them a number of Russian authors [4.24,4.25],Vogel [2.33] and James and McMillan [4.14]. Porai-Koshits and Goganov [4.26], employing the SAXS technique, found that the maximum integrated SAXS intensity, Q, occurred between 15 and 17 mol% Li_2O for samples quenched from the melt between two steel plates. For a glass with 23.5 mol% Li_2O heated at 475°C, they showed that the average radius of the droplets increased up to about 10 hours, slowing down and approaching a constant value after about 30 hours. The experimental points for Q showed that this parameter increased from 0.5 to 1.0 in 3 hours,and remained constant up to 96 hours of heat treatment. It was also suggested that the growth of LS_2 crystals (detectable by XRD for t > 20 h) retarded the growth of the droplets. Tomozawa [2.28] also used SAXS and concluded that the integrated intensity approached a constant value (final stage of APS) after about 11 hours at 475°C, 6 hours at 500°C and 4 hours at 525°C for a glass with 29.5 mol% Li_2O. For a glass with 27.4 mol% Li_2O a constant value of Q was achieved within a few minutes of heat treatment at these temperatures. For long periods of heat treatment the Q values increased due to crystallization of the specimens. Zanotto and Craievich [2.50] have shown that the attainment of a constant value of Q takes about 15 hours at 475°C for a glass with nominally 31.0 mol% Li_2O.

Although most of the TEM studies were of a qualitative character, James and McMillan [4.14] were able to determine the true size distribution of the particles and values of mean diameter, particle concentration and volume fraction, and studied the kinetics of phase separation at 550°C in Li_2O-SiO_2 glasses with and without P_2O_5. At this temperature, the separation was complete within a very short period, the particles growing by diffusion controlled

Ostwald ripening thereafter. For a glass with 30 mol% Li_2O, the average radius of the particles increased according to the $t^{1/3}$ law and the number of particles per unit volume decreased proportionally to t^{-1}.

Therefore, it is clear that the development of phase separation in Li_2O-SiO_2 takes a longer time the closer the composition of the glass is to the binodal boundary and the lower is the temperature. These data from the literature will be used together with the TEM results described below in the interpretation of the crystal nucleation behaviour of Li_2O-SiO_2 glasses undergoing phase separation.

4.9 Transmission Electron Microscopy of Li_2O-SiO_2 Glasses

The TEM micrographs of glasses 17.7, 31.0 and 33.2B heated for 24 h at 440°C and 15 min at 570°C are shown in Figures 4.43a and 4.43b. A very fine scale interconnected phase separation can be seen in glass 17.7. The growing crystals (not shown on the micrograph) were nearly spherical. Glass 31.0 shows some crystals growing in a phase separated background, i.e., some fine droplets can be observed in the micrograph. The crystalline particles growing in glasses 33.2c have the well-known [2.14,2.15,2.16] rosette morphology, and *no* phase separation was observed in this glass. For the Li_2O-SiO_2 glasses, beam damage occurred in a matter of seconds at 100 KV making it difficult to obtain well focused photographs. However, it can be concluded that the amount of phase separation (volume fraction and interfacial area) was much greater in glass 17.7 than in glass 31.0. Also, the shape of the crystal particles were different in the three glasses.

Fig. 4.43a TEM micrographs of Li_2O-SiO_2 glasses nucleated for 24 hours at 440°C and developed for 15 minutes at 570°C. From left to right and from top to bottom: 17.7, 31.0, 31.0 and 33.2B. The magnification is identical in the micrographs shown at the bottom.

⊢——⊣ = 1 μm

Fig. 4.43b TEM micrographs of glass 33.2C nucleated for 24 hours at 440°C and developed for 15 minutes at 570°C. Typical LS_2 crystal clusters are shown.

⊢——⊣ = 1 μm

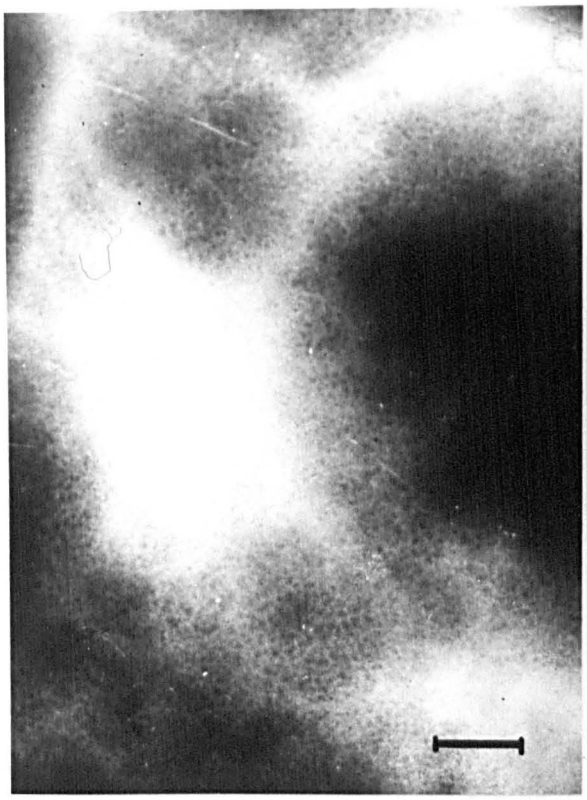

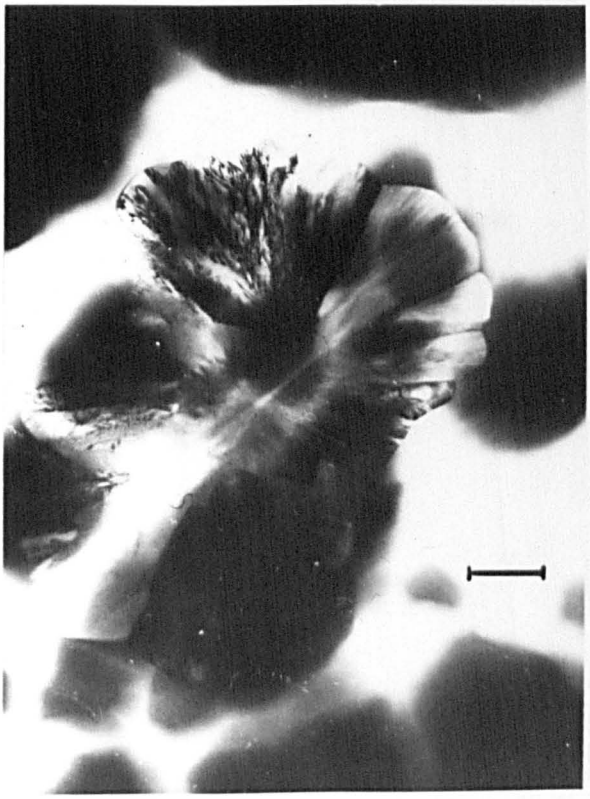

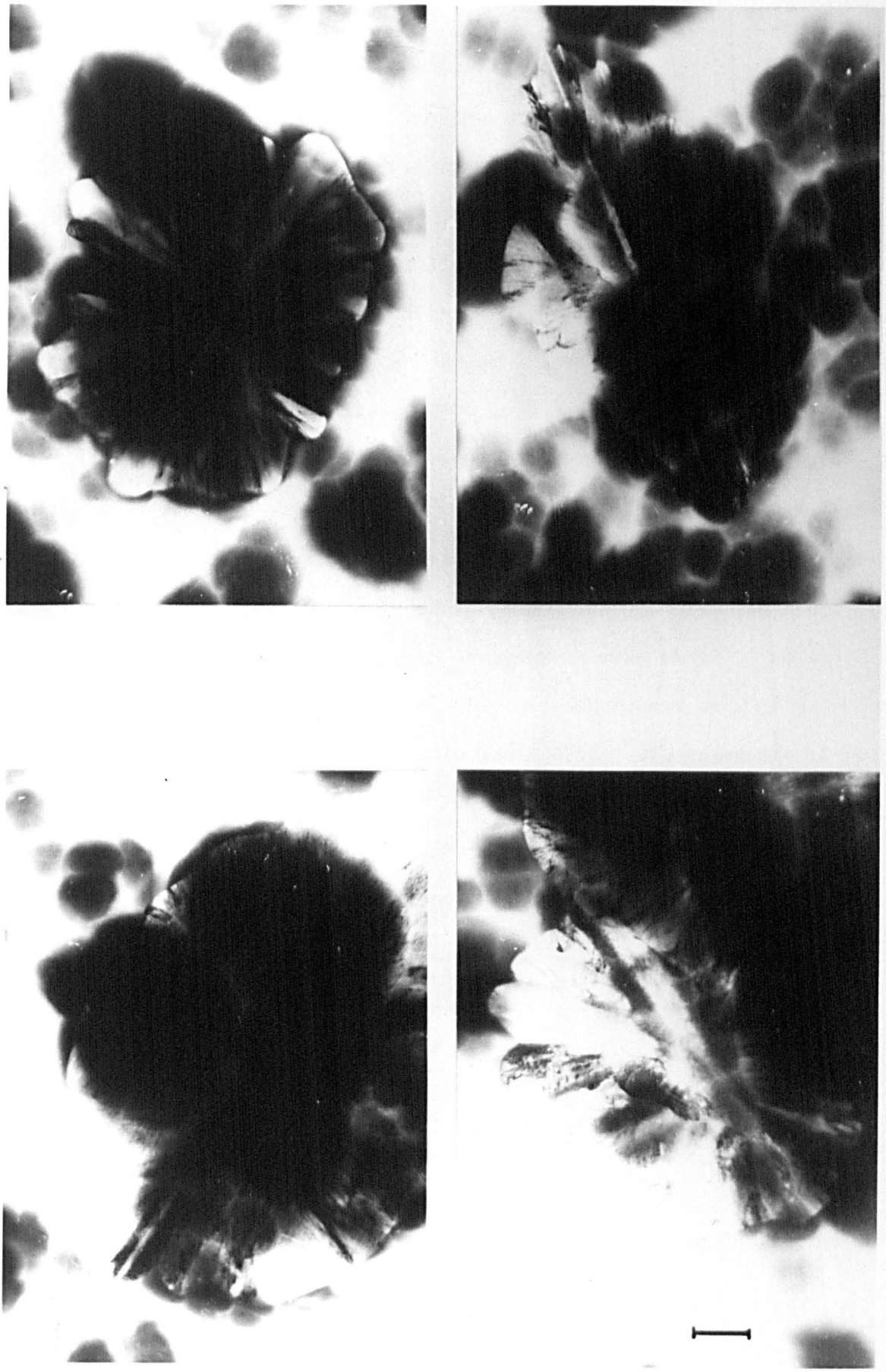

4.10 Viscosity of the Stoichiometric Glass LS_2

The nucleation and crystal growth kinetics in glasses can be related to the viscosity. On the other hand, small variations in some trace components, e.g. "water" can affect the viscosity. Therefore, even when there is viscosity data available in the literature for a glass composition, it is necessary to measure the viscosity for the *particular* glass being used if comparisons with the nucleation and growth rates of crystals are to be made.

The viscosity curve of glass 33.2B Li_2O was determined by indenting large glass specimens with a cylindrical (ϕ = 1 mm) Nimonic indentor. The experimental results are plotted in Figure 4.44 together with some literature data. The dashed line represents the Fulcher curve obtained with a combination of the high temperature data of Bockris et al. [4.23] and Shartsis et al. [4.27], and the low temperature data obtained in this work. The solid line represents the Fulcher curve through the low temperature data only. The actual Fulcher constants are listed in Table 4.9. The agreement of both

Table 4.9

FULCHER PARAMETERS FOR GLASS 33.2B

	High η	Full Curve
A	1.81	-2.55
B	1346.62	3385.50
T_0 (°C)	321.82	218.05

Fulcher equations is excellent from 10^0 to 10^{11} Pa.s, a small underestimation with the full curve occurring for $\eta > 10^{11}$ Pa.s.

Fig. 4.44 Viscosity curves for $Li_2O.2SiO_2$ glasses obtained by different authors. The dashed line represents the Fulcher equation obtained with a combination of the low and high temperature data.

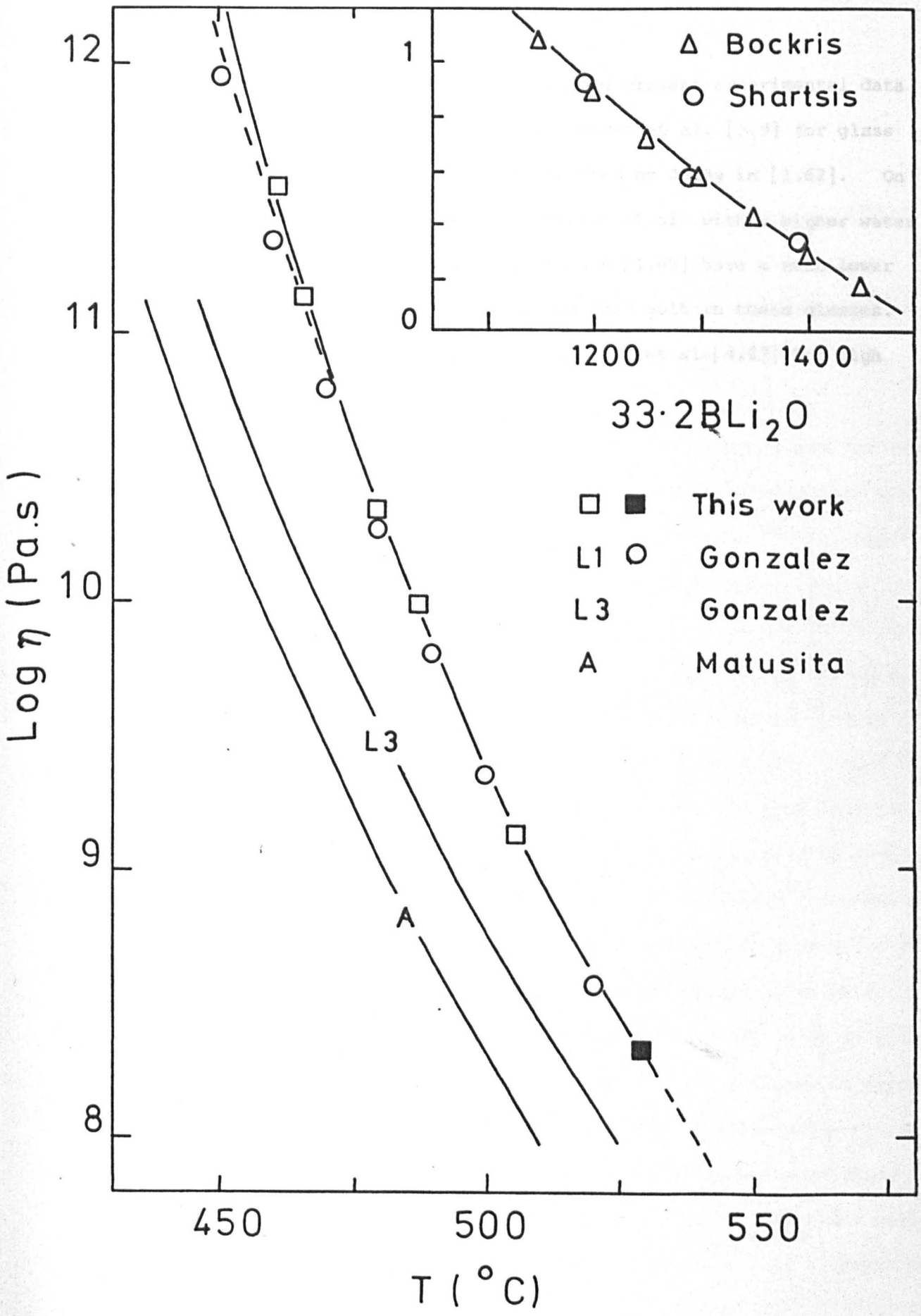
12
11
10
9
8
Log η (Pa.s)
450
500
550
T (°C)
L3
A
1
0
1200
1400
Bockris
Shartsis
33·2BLi2O
This work
L1 Gonzalez
L3 Gonzalez
A Matusita

In the same figure it can be seen that the present experimental data agree quite well with the data of Gonzalez-Oliver et al. [3.9] for glass L1 which contained 0.02 wt% H_2O, and was studied by James in [1.62]. On the other hand, the glass L3 of Gonzalez-Oliver et al. with a higher water content (0.136 wt% H_2O), and Matusita's glass A [1.69] have a much lower viscosity. The nominal content of Li_2O was 33.3 mol% in these glasses. The results of Bockris et al. [4.23] and Shartsis et al. [4.27] for high temperatures agree very well.

CHAPTER 5

DISCUSSION

5.1 Effect of Phase Separation on Crystal Nucleation in $BaO-SiO_2$ Glasses

In this section the results of the crystal nucleation studies are correlated with the kinetics of amorphous phase separation in the same glasses. Some figures of former chapters are reproduced here to facilitate the present discussion.

It was shown in section 4.1 that the crystal nucleation rates for the phase separating glasses 27.0, 28.3A and 28.3B, increase with time in the early stages, approaching constant values for longer times. This time decreases with increasing temperature. The nucleation density plots for the non-phase separating glasses, 29.7H, 29.9, 33.2C, 33.3A and 33.3P, are straight lines from the beginning. If we look specifically at the curves of Figure 4.8, it is clear that the crystal nucleation rates in glasses 27.0 and 28.3B, heated at 743°C, increase for times up to 2 and 7 hours respectively. After these periods they remain *constant* and *equal* for the two glasses. The integrated SAXS intensity at 743°C (Figure 4.26) also *increases* up to $t < 2.5$ hours for glass 27.0 and up to 7 hours for glass 28.3B, remaining unchanged after these periods. As discussed previously, the increase in Q indicates that the composition of the amorphous matrix is changing with time until equilibrium is approached (constant value at Q). Therefore, this is strong experimental evidence that the increase in crystal nucleation rates is due to the compositional shift of the amorphous matrix (enrichment in BaO) brought about by phase separation. This conclusion is further supported by the curves of Figures 4.5 and 4.26 for the glass with 28.3 mol% BaO at 760°C which show that both the nucleation rate of crystals

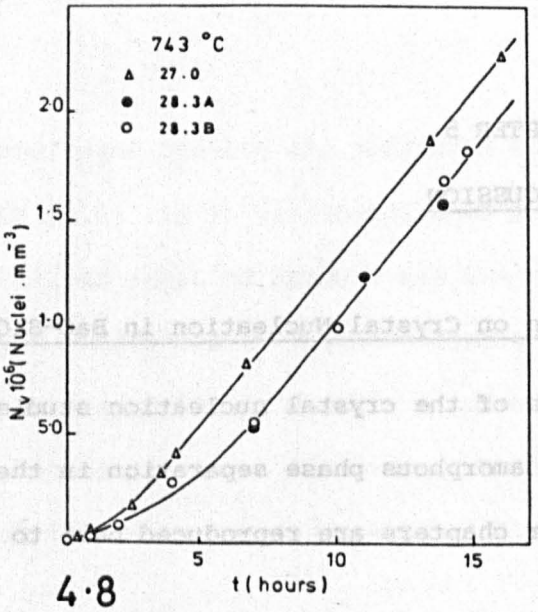

4·8

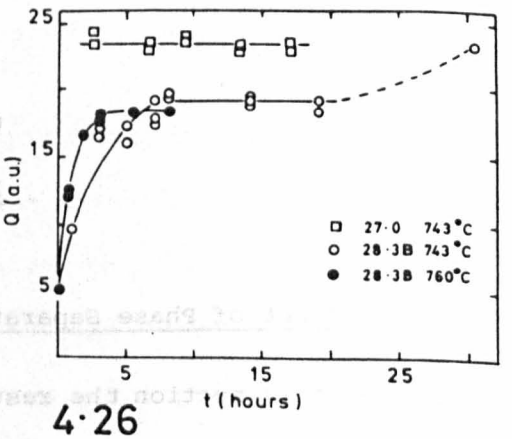

4·26

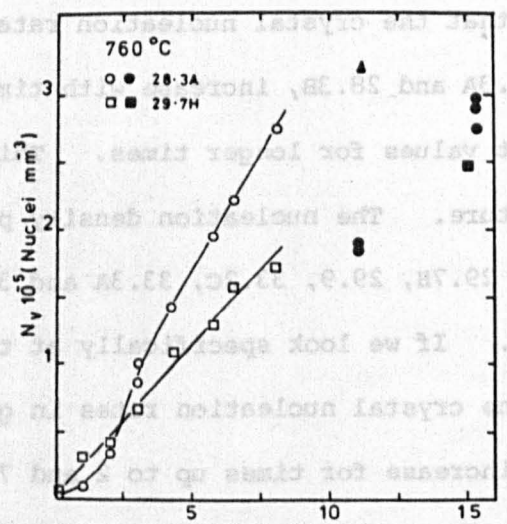

4·5

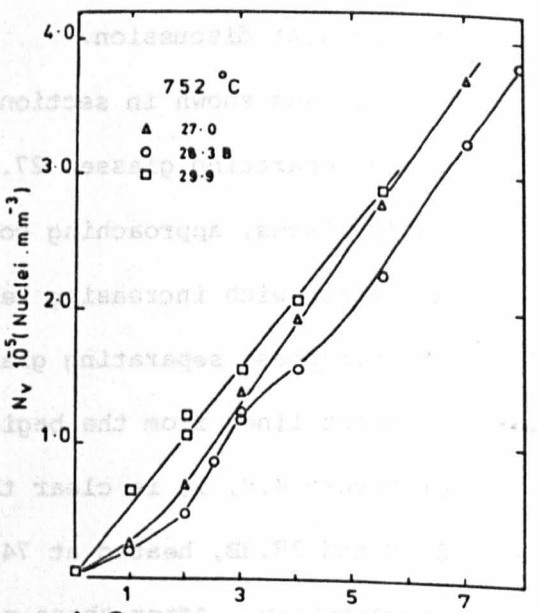

4·9

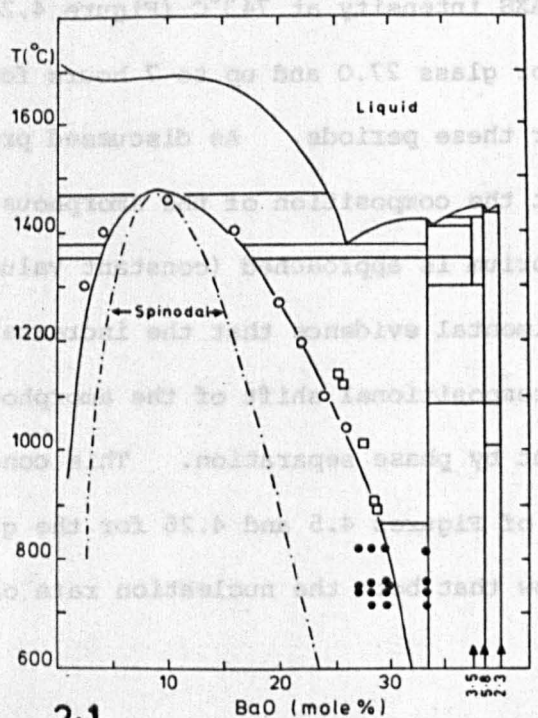

2·1

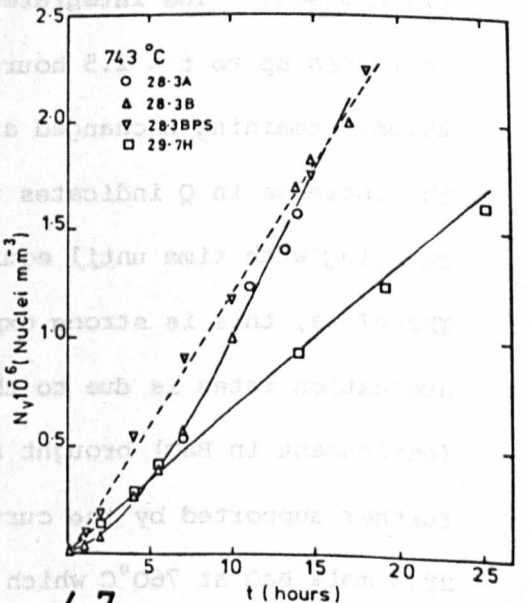

4·7

and integrated intensity *increase* for times up to about 3 hours.

The fact that the "equilibrium" nucleation rates, I, of glasses 27.0 and 28.3B at longer times, are *equal* at two temperatures (Figures 4.8 and 4.9), implies that I is only a function of the chemical composition of the phase separated matrix and does *not* depend on the volume fraction of the amorphous droplets. This statement becomes clearer if we refer to the miscibility gap shown in Figure 2.1. For a given glass, the composition of the amorphous phase (binodal line) is only a function of temperature, being therefore *equal* for glasses 27.0 and 28.3B when phase separated at the same temperature. On the other hand, the volume fraction of droplets given by the lever rule, is larger for glass 27.0 than for glass 28.3B.

Figure 4.7 shows that the crystal nucleation rate in glass 28.3BPS, which was fully phase separated at 821°C before the nucleation treatment at 743°C, is constant from the beginning, and initially higher than the nucleation rate of the as-quenched glass 28.3B, for which phase separation proceeded simultaneously with crystal nucleation. When the matrix reached its equilibrium composition in glass 28.3B, i.e. after 7 hours at 743°C (Figure 4.26) its nucleation rate *overtook* that of glass 28.3BPS. This is due to the asymmetrical shape of the immiscibility boundary, the BaO content in the amorphous matrix being lower at 821°C than at 743°C. It should be mentioned however that, if secondary phase separation had occurred in glass 28.3BPS when nucleated at 743°C, the composition of the matrix would be equal for both glasses. However, TEM micrographs (Figure 4.14b) show *no* evidence for secondary phase separation in this glass. Probably, a very long time is required for further phase separation to fully develop at 743°C.

At this point, the possible influence of interfaces of the phase separated structure on the nucleation of crystals must be discussed. According to the SAXS results of section 4.4.2, the average size of the droplets increases and

the number and specific surface area of the droplets decrease from the very beginning of heat treatment. Therefore, the number of crystals which could eventually nucleate at the interfaces between the amorphous phases, if any, should also decrease with time. However, a decrease in crystal nucleation was never observed.

Finally, the fact that crystal nucleation rates in the phase separating glasses, 27.0, 28.3A and 28.3B, increase with time overtaking the constant nucleation rates in the non-phase separating glasses, 29.7H and 29.9, which are situated just inside the miscibility gap (Figure 2.1), at 718°C, 743°C, 745°C, 752°C and 760°C, reinforces the conclusion that the observed increase in crystal nucleation rates is due to the enrichment in BaO (of the matrix) caused by phase separation. After the completion of phase separation, the matrix in glasses 27.0, 28.3A and 28.3B have the same percentage of BaO, which is higher than the BaO content in glasses 29.7H and 29.9.

Basically the same conclusion was taken by Ramsden [2.54] in his studies of $BaO-SiO_2$ glasses at 700°C. Although only a semi-quantitative estimate of amorphous phase separation was made on replica micrographs, he deduced that the morphology of the phase separation had little or no influence on crystal nucleation, and the effects observed were due predominantly to the progressive shift in composition of the matrix phase with time as a result of phase separation.

An additional, smaller effect to that of compositional changes was observed in the nucleation curves. Thus, an *inflexion* was clearly observed in the nucleation curve for glass 28.3A nucleated at 760°C (Figures 4.5 and 4.6), corresponding to a maximum value in dN_v/dt higher than the constant nucleation rate achieved at longer times. An inflexion was also observed for glass 28.3B nucleated at 752°C (Figure 4.9). A similar effect may just be detected at 745°C and 743°C (some points are higher than the "smooth"

curves in Figures 4.4 and 4.8), but no inflexion can be seen at 718°C (Figure 4.3). In all cases, the inflexion in N_v occurred before the attainment of the equilibrium composition by the baria-rich amorphous phase as given by a constant value of Q (Figure 4.26). A similar effect was observed by Tomozawa [2.28] and Zanotto and Craievich [2.50] in phase-separating Li_2O-SiO_2 glasses. Their results were explained as being due to some enhanced heterogeneous nucleation in the diffusion zones, which exist around the amorphous droplets when the amorphous phase separation was in the early stages. The fact that the maximum in the nucleation rate (inflexion in N_v) is more pronounced as the temperature increases (nucleation rates decrease) shows that this is a relatively minor effect, being masked when the nucleation rates are too high, i.e. for temperatures approaching T_g.

Another important observation is that the stoichiometric glasses 33.2C, 33.3A and 33.3P have much *higher* crystal nucleation rates than the other compositions (higher in silica) at all temperatures. The classical nucleation theory would predict this result, because the viscosity is lower and the thermodynamic driving force is expected to be higher for the stoichiometric composition. Therefore, the enrichment of the amorphous matrix in BaO, due to phase separation, render the glasses that phase separate more prone to crystal nucleation, as shown schematically in Figure 2.3. Thus, the thermodynamic driving force for crystal nucleation is increased as the composition approaches that of the nucleating phase. Also, the viscosity decreases when the stoichiometric composition is approached (Figure 4.37). Although no data for the crystal-glass interfacial energy are available for phase separating glasses, it is reasonable to assume that σ is lower the closer the compositions of the glass and the nucleating phase because the structural similarity between parent glass and crystal is then greater.

5.2 Effect of Phase Separation on Crystal Growth in $BaO-SiO_2$ Glasses

It was shown in section 4.2.1, that the growth rate U of BS_2 spherulites in glass 28.3A is higher than in glass 29.7H at 745°C and 760°C, and is approximately equal to that in glass 29.7H at 718°C. The crystal growth rate in the stiochiometric glass 33.3A is the highest, as expected.

Again, the higher growth rate in glass 28.3A (lower BaO content than glass 29.7H) can be explained if the BS_2 spherulites grow in an amorphous matrix enriched in BaO due to phase separation. Indeed, the TEM micrographs of Figure 4.14e show that crystal growth proceeds undisturbed through the matrix. At 718°C, the amorphous phase separation takes a long time to fully develop and longer heat treatments would be required if an increased growth rate were to be detected. If the differences in U for the two glasses, observed at 745°C and 760°C, were due to difference in the level of SrO impurity, it should also show at 718°C, but at this temperature the growth rates are about the same.

In view of the precision of these measurements and the assumptions involved (section 4.2.1) these results on growth rates are regarded as tentative until further experimental work can be done. The general conclusion, however, is in agreement with that of other authors [2.54, 2.55, 2.56].

5.3 Effect of Phase Separation on Crystal Nucleation in Li_2O-SiO_2 Glasses

The nucleation curves of Figure 4.39 show that, for phase separating glasses, there is a small inflexion (points higher than the "smooth" curves) between 1 and 3 hours for glass 17.7, and between 2 and 4 hours for glass 31.0. Although these points are within the 95% confidence limits for the statistical error in N_V, they were confirmed by repeated measurements.

Similar inflexions have also been observed by Tomozawa [2.28] and Zanotto and Craievich [2.50] and, as discussed previously, it was suggested that the effects are associated with nucleation of crystals in the diffusion zones around the droplets because the inflexions occur in the *early* stages of the amorphous phase separation. However, this is only a minor effect.

For longer times, the crystal nucleation rates in glasses 17.7 and 31.0 are *equal* but *higher* than the constant nucleation rate of the stioichiometric glass 33.2B. The same argument used to explain the nucleation in the $BaO-SiO_2$ glasses undergoing phase separation can be applied again, i.e., the only parameter which is the *same* for glasses 17.7 and 31.0, after nucleation at 481°C, is the composition of the amorphous (lithia-rich) matrix phase. The morphology (and probably kinetics also) of the phase separation in the two glasses were quite different. Thus isolated silica-rich droplets were observed in glass 31.0, which were probably produced by nucleation and growth, whereas in glass 17.7 an interconnected microstructure, possibly the result of spinodal decomposition, was observed (Figure 4.43a). Therefore, the nearly identical crystal nucleation rates observed in these glasses is probably because the lithia-rich matrix has the same *composition* in both glasses after the completion of phase separation.

Figure 4.40 shows that the crystal nucleation rates in the fully phase-separated glasses 17.7 and 31.0 (17.7PS and 31.0PS) are equal and constant from the beginning, being lower than the nucleation rates of the as-quenched glasses (dashed lines in Figure 4.40). This behaviour is very similar to that found in the $BaO-SiO_2$ glasses, and is probably because in the glasses first phase-separated at 497°C the lithia-rich matrix has a slightly lower Li_2O content than the matrix of glasses only heated at 481°C. In principle, further phase separation (nucleation of new droplets and/or growth of the existing ones) could occur at 481°C for glasses 17.7PS and

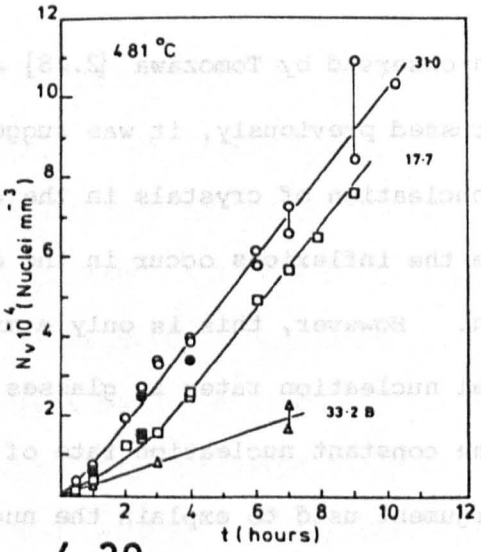

4·39

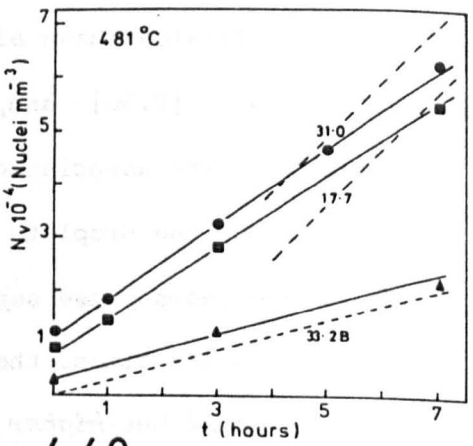

4·40

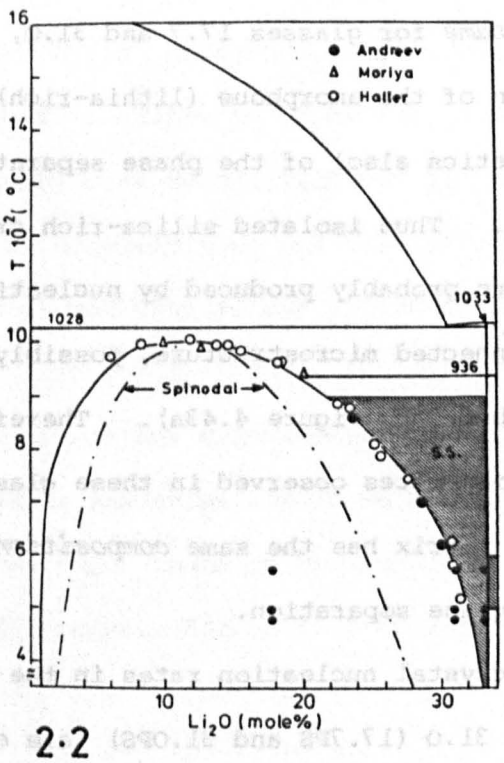

2·2

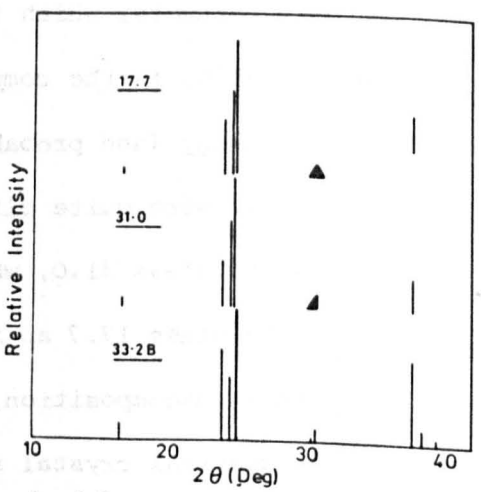

4·42

31.OPS. However, since the matrix compositions after heat treatment at 497°C would be only *just inside* the immiscibility boundary corresponding to 481°C, the kinetics of secondary phase-separation would probably be very very slow. Therefore, it is likely that the composition of the matrix phase did not reach the equilibrium value at 481°C even after 7 hours (Figure 4.40), whereas equilibrium was attained much more quickly in the as-quenched glasses at 481°C (Figure 4.39).

The fact that the almost stoichiometric glass 33.2B has a *lower* crystal nucleation rate than the phase separated glasses, differs strikingly from the observations in the $BaO-SiO_2$ glasses, and cannot be explained by the same (compositional) arguments if the crystal phase is the stoichiometric $Li_2O.2SiO_2$ in all glasses. However, it was shown in section 4.7 that the crystalline phases in glasses 17.7 and 31.0 are *solid solutions* which gave nearly identical diffraction patterns. In glass 33.2C, the low-$Li_2O.2SiO_2$ stoichiometric crystal phase was clearly identified (Figure 4.42). Therefore, the crystalline phase in the stoichiometric glass *differs* from that in the phase-separated glasses. In this case, the thermodynamic driving force (and interfacial energy) could be more favourable for crystal nucleation in the phase-separated glasses than for the low-LS_2 phase in the nearly stoichiometric glass, giving higher nucleation rates for the former. The compositional effect is, however, clearly realized because the nucleation rates in glasses 17.7 and 31.0, which have widely different average composition are *identical* for two heat-treatment conditions. In both cases the amorphous matrix has the same Li_2O content.

5.4 Analysis of Nucleation Data for $Li_2O.2SiO_2$ Glasses

The steady-state crystal nucleation rates in $Li_2O.2SiO_2$ glasses obtained by several authors are shown in Table 5.1, and plotted in Figure 5.1.

There are appreciable variations between the various sets of data; differences as great as a factor of 2 to 3 times being observed for a given temperature. There is, however, good agreement for the temperature dependence of the nucleation rates, the maximum being at 450-455°C. The technique employed by all authors (except Ito et al. [5.4]) was similar, i.e. a double-stage heat treatment followed by stereological measurements, as described in chapter 3, the development temperatures varying from 560°C to 630°C. The accuracy of the measurements was not stated in most cases (it is 10-20% in this work). Therefore, this could in part account for the observed differences. Chemical analyses of glasses studied were given by some authors and are shown in Table 5.2. Significant differences in the levels of various impurities and in the percentages of the major components are observed for the three glasses reported, and are also expected for the other glasses where no chemical analyses were given. In the case of glass L1 used by James [1.62], and glass 33.2B used in this work, the water contents (determined by the author) and the Li_2O contents are very close. The overall level of other impurities is larger in glass L1. Exactly the same stereological technique was used by the two authors. Therefore, the observed differences in nucleation rates are apparently due to differences in the level of one or more impurities. The glass of Tuzzeo [5.2], on the other hand, has a much higher impurity content than the other two glasses. Also, the SiO_2 and Li_2O contents are different. The nucleation rates reported by Tuzzeo, however, are quite close to the nucleation rates of the much purer glass 33.2B.

Table 5.1

CRYSTAL NUCLEATION RATES IN $Li_2O.2SiO_2$ GLASSES

Ito [5.4]		Filipovich [5.1]		James [1.62]	
T (°C)	I ($mm^{-3}.s^{-1}$)	T (°C)	I ($mm^{-3}.s^{-1}$)	T (°C)	I ($mm^{-3}.s^{-1}$)
-	-	-	-	425	0.045
430	0.10	-	-	430	0.368
-	-	-	-	435	1.041
-	-	440	1.28	440	1.147
450	0.92	450	1.50	445	3.761
-	-	-	-	454	4.253
-	-	460	1.34	465	2.863
-	-	-	-	476	1.868
480	2.80	480	0.80	489	0.639
500	0.80	500	0.25	502	0.149
520	0.07	-	-	516	0.025
-	-	-	-	527	0.006

Tuzzeo [5.2]		Fokin [5.3]		This Work	
T (°C)	I ($mm^{-3}.s^{-1}$)	T (°C)	I ($mm^{-3}.s^{-1}$)	T (°C)	I ($mm^{-3}.s^{-1}$)
430	0.24	430	0.23	-	-
-	-	440	0.86	440	1.05
446	1.263	-	-	-	-
455	2.224	451	1.33	455	2.63
465	1.967	465	2.43	464	1.90
475	1.260	485	0.72	481	0.80
498	0.126	-	-	497	0.19
528	0.009	-	-	-	-

Table 5.2

CHEMICAL ANALYSES OF $Li_2O.2SiO_2$ GLASSES (wt%)

Oxide	James		Tuzzeo	This Work		Nominally
	EPMA	XRF	GRA	FES	EPMA	
Li_2O	-	19.72	20.20	-	-	19.91
SiO_2	79.84	79.50	78.66	-	80.19	80.09
Al_2O_3	0.04	0.07	[0.79	<0.05	-	
Fe_2O_3	0.02	0.01		<0.0004	-	
Na_2O	0.07	0.05	-	0.01-0.02	-	
H_2O	0.02	0.02	-			
CaO	-	0.07	-			
H_2O*	-	0.02	<0.03		0.02	

* IR Spectroscopy

EPMA = Electron Probe Microanalysis

XRF = X-ray Fluorescence Analysis

GRA = Gravimetric Analysis

FES = Flame Emission Spectroscopy

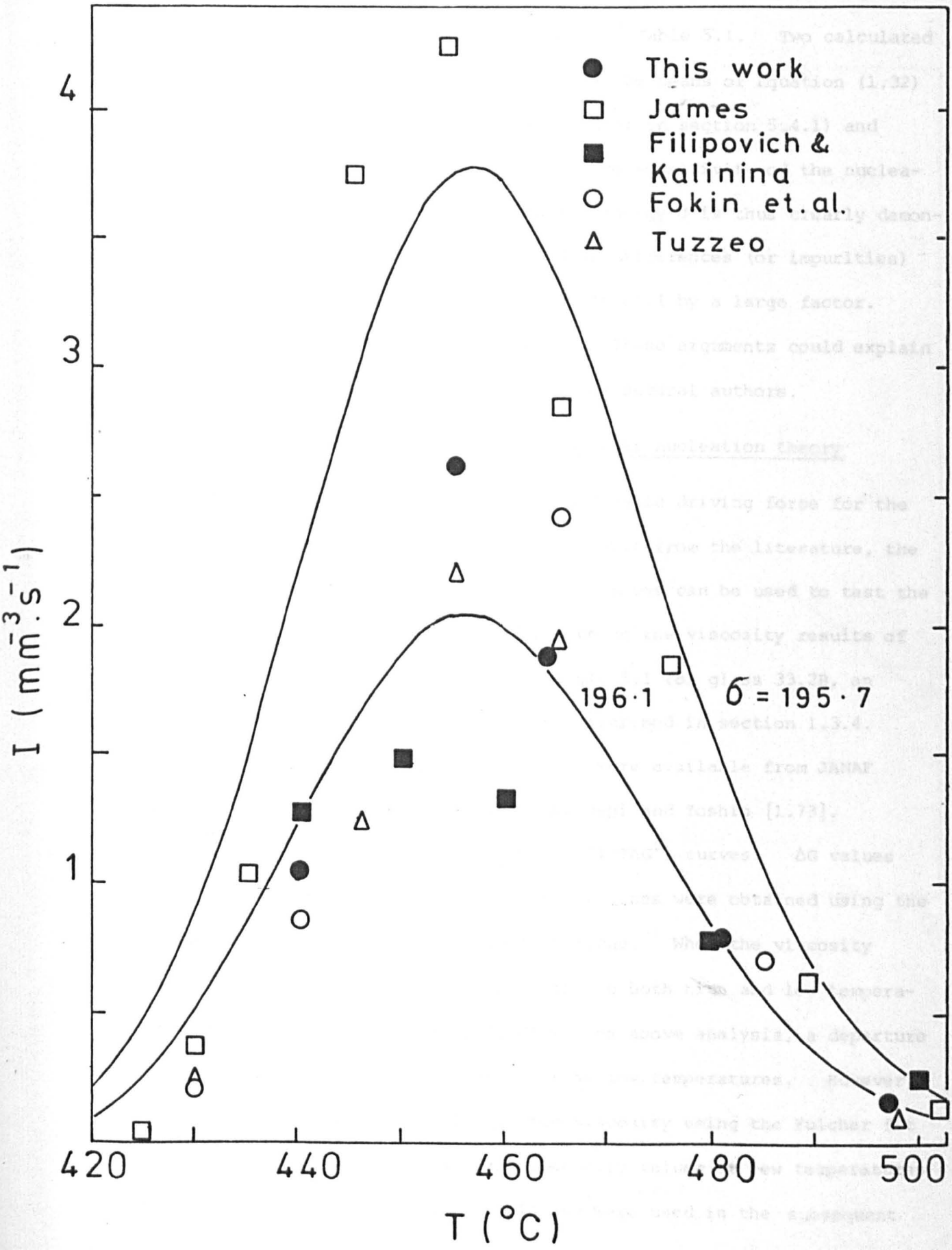

Fig. 5.1 Calculated and experimental nucleation rates versus temperature curves for $Li_2O.2SiO_2$ glasses.

Figure 5.1 shows the experimental data of Table 5.1. Two calculated curves are also plotted. They were obtained by means of Equation (1.32) assuming log A = 62 $m^{-3}.s^{-1}$ (as described later in section 5.4.1) and σ = 196.1 and 195.7 $mJ.m^{-2}$ respectively. The sensitivity of the nucleation rates to the values of the interfacial energy σ is thus clearly demonstrated. Therefore, if minor compositional differences (or impurities) affect σ by a very small amount this will affect I by a large factor. Variations in viscosity are also expected. These arguments could explain the differences in the nucleation data of the several authors.

5.4.1 Experimental tests of the classical nucleation theory

As discussed previously, if the thermodynamic driving force for the glass → crystal transformation, ΔG, is available from the literature, the experimental nucleation rates and viscosity values can be used to test the classical nucleation theory. Therefore, using the viscosity results of section 4.10 and the nucleation data of Table 5.1 for glass 33.2B, an analysis was made according to the method described in section 1.3.4. Thermodynamic data for the $Li_2O.2SiO_2$ glass were available from JANAF thermochemical tables [1.51] and from Takahashi and Yoshio [1.73].

Figure 5.2 shows the $\log(I\eta/T)$ versus $(1/T\Delta G^2)$ curves. ΔG values from both sources were used. Good straight lines were obtained using the measured viscosity data in the nucleation range. When the viscosity values were calculated from the Fulcher fit to both high and low temperatures viscosity data (see section 4.10) in the above analysis, a departure from linearity was observed for one point at low temperatures. However, this arose from an underestimation of the viscosity using the Fulcher fit at lower temperatures. The measured viscosity values at low temperatures were therefore considered more reliable and were used in the subsequent analyses.

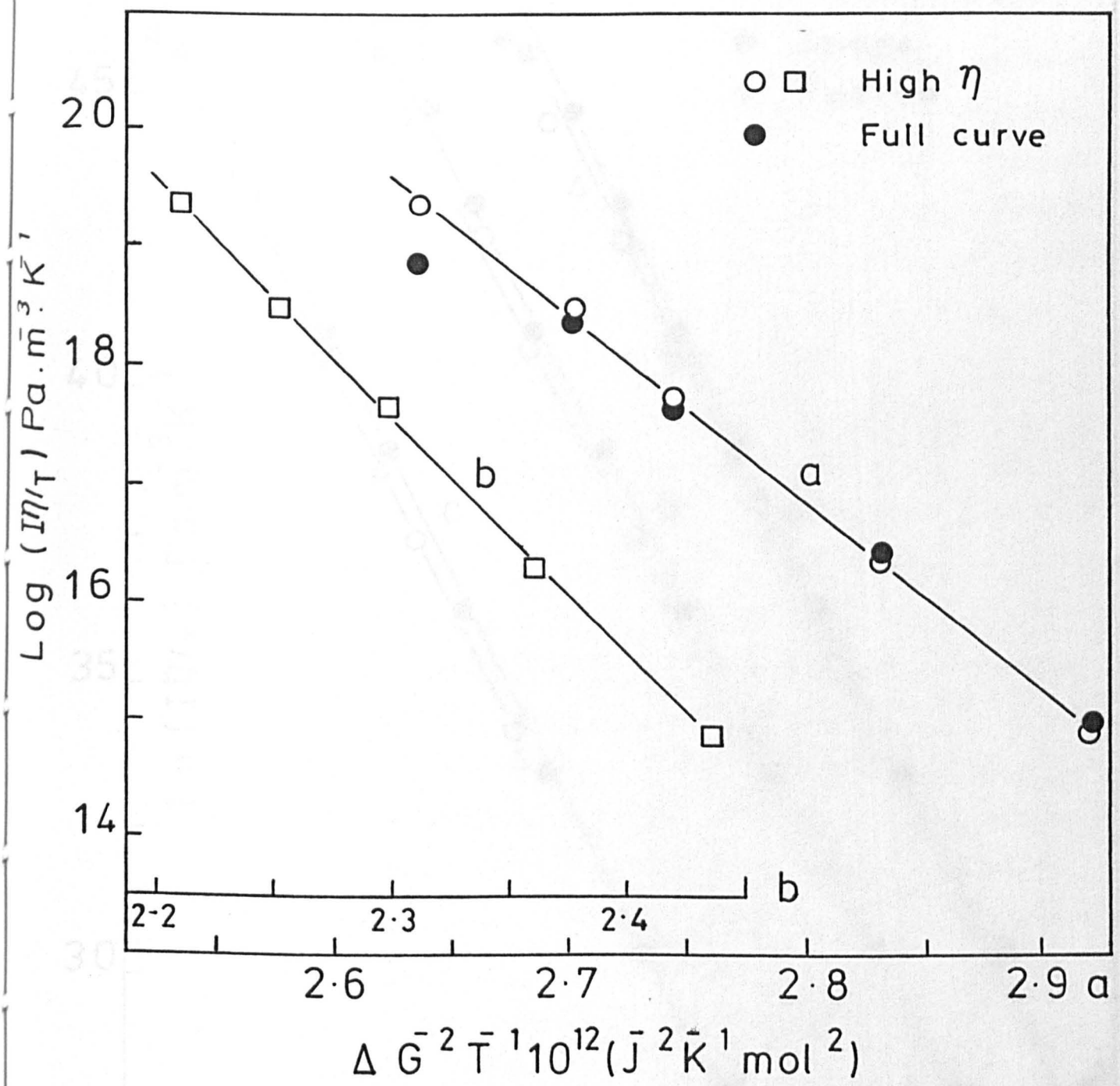

Fig. 5.2 Log(Iη/T) versus $1/T\Delta G^2$ for glass 33.2B. Thermodynamic data from a) JANAF [1.51] b) Takahashi and Yoshio [1.73].

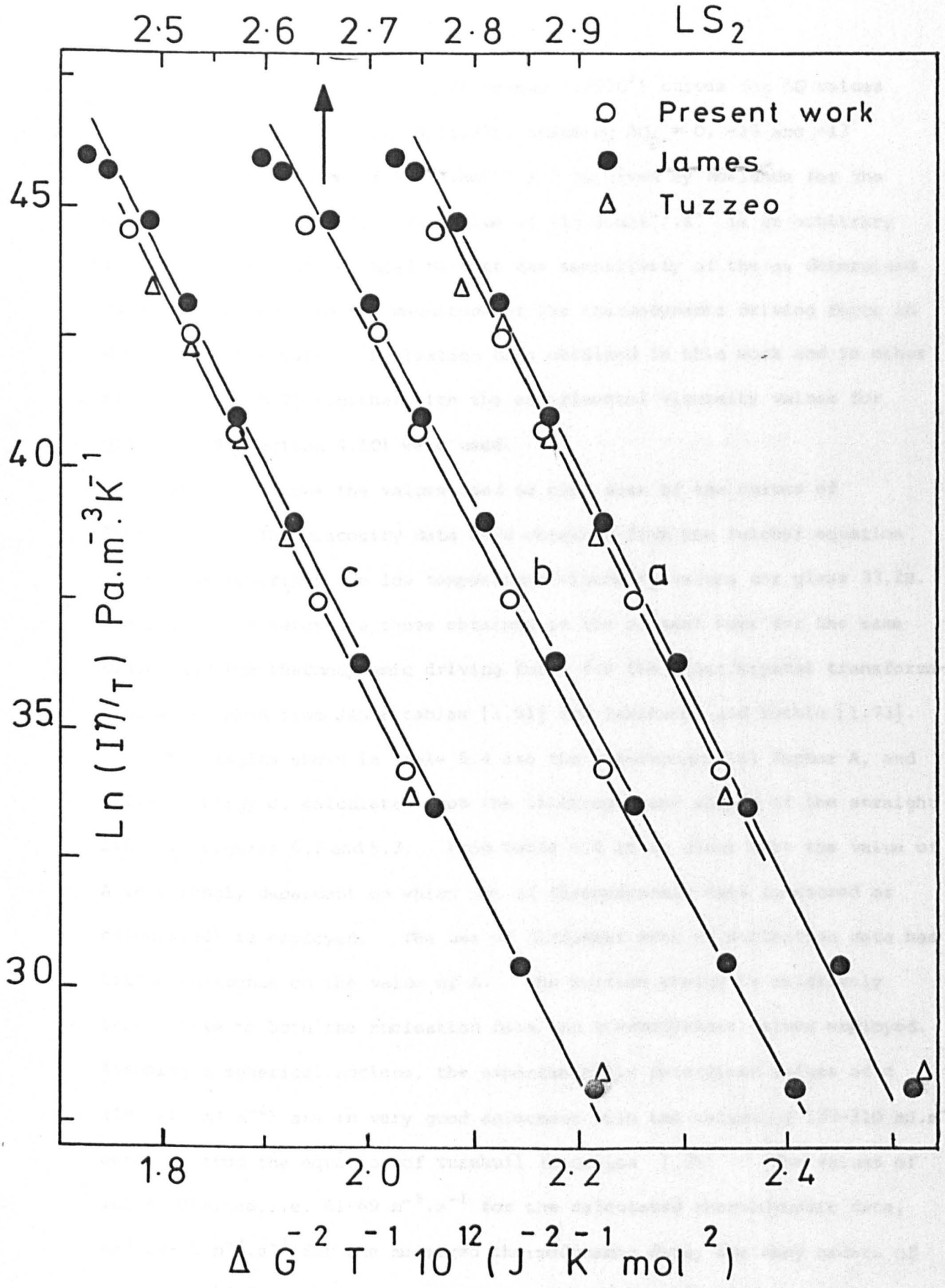

Fig. 5.3 Ln(Iη/T) versus $1/T\Delta G^2$ for LS_2 glasses. ΔG from Equation 1.28 with: a) $\Delta C_p = 0$, b) $\Delta C_p = -13$, c) $\Delta C_p = 13$ J.mol^{-1}.K^{-1}.

Figure 5.3shows the $\ln(I\eta/T)$ versus $(1/T\Delta G^2)$ curves for ΔG values when calculated from Equation (1.28), assuming ΔC_p = 0, -13 and +13 $J.mol^{-1}.K^{-1}$ The value of -13 $J.mol^{-1}.K^{-1}$ is given by Rowlands for the $Li_2O.2SiO_2$ glass [1.47]. The value of +13 $J.mol^{-1}.K^{-1}$ is an arbitrary (too high) value of ΔC_p used to test the sensitivity of the as determined parameters A and σ to the magnitude of the thermodynamic driving force ΔG used in the analysis. Nucleation data obtained in this work and in other studies [1.62,5.2] together with the experimental viscosity values for glass 33.2B (section 4.10) were used.

Table 5.3 shows the values used to plot some of the curves of Figure 5.2. The viscosity data were obtained from the Fulcher equation which best described the low temperature viscosity values for glass 33.2B. The nucleation rates are those obtained in the present work for the same glass, and the thermodynamic driving force for the glass/crystal transformation were taken from JANAF tables [1.51] and Takahashi and Yoshio [1.73].

The results shown in Table 5.4 are the pre-exponential factor A, and surface energy σ, calculated from the intercepts and slopes of the straight lines in Figures 5.2 and 5.3. From Table 5.4 it is clear that the value of A is strongly dependent on which set of thermodynamic data (measured or calculated) is employed. The use of different sets of nucleation data has little influence on the value of A. The surface energy is relatively insensitive to both the nucleation data and thermodynamic values employed. Assuming a spherical nucleus, the experimentally determined values of σ (197-211 $mJ.m^{-2}$) are in very good agreement with the values of 187-210 $mJ.m^{-2}$ obtained from the equation of Turnbull (Equation 1.31) The values of log A obtained, i.e. 61-69 $m^{-3}.s^{-1}$ for the calculated thermodynamic data, and 69-71 $m^{-3}.s^{-1}$ for the measured thermodynamic data, are many orders of magnitude *higher* than the theoretical value of 41 $m^{-3}.s^{-1}$.

Table 5.3

PARAMETERS FOR ANALYSIS OF NUCLEATION IN GLASS 33.2B

T (K)	I ($m^{-3}.s^{-1}$)	Log η(Pa.s)	- ΔG ($J.mol^{-1}$) JANAF	Takahashi
713	1.05×10^{9}	13.21	23.06×10^{3}	25.2×10^{3}
728	2.63	11.92	22.54	24.7
737	1.90	11.28	22.23	24.3
757	0.80	10.27	21.64	23.7
770	0.19	9.50	21.08	23.1

Table 5.4

EXPERIMENTAL PARAMETERS FROM THE ANALYSES OF NUCLEATION IN LS_2 GLASSES

	This Work			
	Eq. (1.26)	Eq. (1.28)	JANAF	Takahashi
Log A ($m^{-3}.s^{-1}$)	61 ±2	69 ±2	70 ±2	71 ±2
σ ($mJ.m^{-2}$)	199.3	198.6	197.6	210.7
	Tuzzeo			
Log A ($m^{-3}.s^{-1}$)	61 ±2	69 ±2	69 ±2	
σ ($mJ.m^{-2}$)	199.3	199.6	195.8	
	James			
Log A ($m^{-3}.s^{-1}$)	61 ±2	69 ±2	70 ±2	
σ ($mJ.m^{-2}$)	198.3	198.6	196.9	

$\text{Log } \eta = 1.81 + 1346.6/(T - 594.8)$; η(Pa.s), T (K)

$\Delta G = - 57400\ (1307 - T)/1307\ (J.mol^{-1})$; Eq. (1.26) ($\Delta C_p = 0$)

$\Delta C_p = - 13\ J.mol^{-1}.K^{-1}$ in Eq. (1.28)

When the arbitrary (too high) value of +13 $J.mol^{-1}K^{-1}$ is used for ΔC_p, the value of log A obtained is 57 ±2 for the three different sets of nucleation data. The values of σ are 201.0, 199.8 and 199.6 $mJ.m^{-2}$ for the nucleation data of this work, Tuzzeo [5.2] and James [1.62], respectively.

If the Hoffman expression (Equation 1.30) is used for ΔG, the $\ln(I\eta/T)$ versus $1/T\Delta G^2$ plots are *not* straight lines. Indeed, Figure 1.4 shows that Equation (1.30) is not a good approximation for ΔG for the $Li_2O.2SiO_2$ glass.

Rowlands and James [1.72], using the nucleation data of James [1.62] and the viscosity data of Matusita and Tashiro [1.69], obtained a value of 190 $mJ.m^{-2}$ for σ and log A = 62 $m^{-3}.s^{-1}$ for JANAF thermodynamic data; and σ = 197 $mJ.m^{-2}$ and log A = 59 $m^{-3}.s^{-1}$ for Takahashi and Yoshio's thermodynamic data. From a plot of $(T \ln I - T' \ln I')/(T - T')$ against $(T - T')^{-1}$ $(1/\Delta G^2 - 1/\Delta G_1^2)^{-1}$, according to Equation (1.45), Rowlands and James [1.72] obtained values of 222 $mJ.m^{-2}$ and 900 $kJ.mol^{-1}$ for σ and ΔH_D respectively.

Neilson and Weinberg [1.74] in an independent analysis of the same nucleation and viscosity data, obtained very similar values for σ and log A. In both studies, however, a marked departure from linearity was observed in the $\log(I\eta/T)$ vs. $1/T\Delta G^2$ plots for temperatures lower than the maximum crystal nucleation rate temperature (T_{max}). It is now clear that this effect was due to the use of the viscosity data of Matusita and Tashiro [1.69]. However, when the viscosity data obtained in the present work are used the linearity is maintained even for $T < T_{max}$. A few experimental points lower than the straight lines are due to an experimental underestimation of viscosity values, and probably also some underestimation of the nucleation rates, when $T < T_g$ (see curve a in Figure 5.2).

As discussed previously, the viscosities measured by Matusita and Tashiro were lower than in the present work although nominally the glasses were both of the same lithium disilicate (LS_2) composition. The glass in the present work was close to the exact LS_2 composition and made from very pure starting materials. The glass of Matusita and Tashiro may have differed from ours in its base composition or in its impurity levels. One possibility is that it had a much higher water content.

Several explanations readily come to mind which might account for the large discrepancy between the theoretical and experimental pre-exponential factors.

(a) Non-steady state nucleation: Transient effects could cause some underestimation of I at the lowest temperatures used. This would affect the linearity of the plot at these temperatures. However, transient effects were negligible at higher temperatures above the maximum in the nucleation rate versus temperature curve. So over most of the temperature range, transient effects would not affect the slope of the $\ln(I\eta/T)$ vs. $1/T\Delta G^2$ plots, and the value of the pre-exponential A determined from them.

(b) Possibility of heterogeneous nucleation: It is unlikely that the disagreement can be attributed to heterogeneous nucleation. The high undercoolings below the liquidus necessary to observe internal nucleation of crystals and the experimental evidence presented by James et al. [1.66] strongly suggest that a homogeneous nucleation mechanism is predominant in LS_2 glasses. Furthermore, even using the experimental nucleation data of several investigators made no significant difference in the values of the pre-exponential A.

Let us now consider the possibility of a heterogeneous catalyst distributed throughout the supercooled liquid or glass. Comparison of Equations (1.20) and (1.44) shows that the pre-exponential factors are approximately in the ratio $n:n_h$, where n represents the number of formula units of the

nucleating component per unit volume of liquid (homogeneous nucleation), and n_h the number of formula units of the nucleating component in contact with the catalyst surface per unit volume of liquid (heterogeneous nucleation). In most cases $n_h << n$. Therefore, according to theory, the pre-exponential factor for heterogeneous nucleation will be many orders of magnitude less than that for homogeneous nucleation. So, there is an even *greater* discrepancy between the heterogeneous nucleation theory and experiment.

(c) Experimental errors in the nucleation rates: Measurement errors do exist and probably in part account for the differences in the results obtained by several authors for nominally the same glass composition (Table 5.1). One source of errors is the possible dissolution of nuclei during the growth (development) treatment mentioned previously. However, James [1.62] and Kalinina and Filipovitch [5.1,5.3,1.70] have investigated nuclei dissolution and have shown that the effects on measured steady state nucleation rates are negligible provided the nucleation temperature is sufficiently high (i.e. not too far below the maximum nucleation rate temperature where transient nucleation occurs) and the development temperature is not too high. These conditions certainly applied in the present study. Another source of error is the stereological effect (Appendix 1) also discussed earlier. This would cause a small systematic underestimation in the nucleation rates.

It should be stressed, however, that the magnitude of the systematic errors introduced from these two sources are very small in relation to the large discrepancy in the pre-exponential factor A observed between theory and experiment. Furthermore, the above effects would tend to produce an underestimate in the experimental nucleation rates. Thus, if anything, disagreement with theory would be *increased* if perfectly accurate data were used.

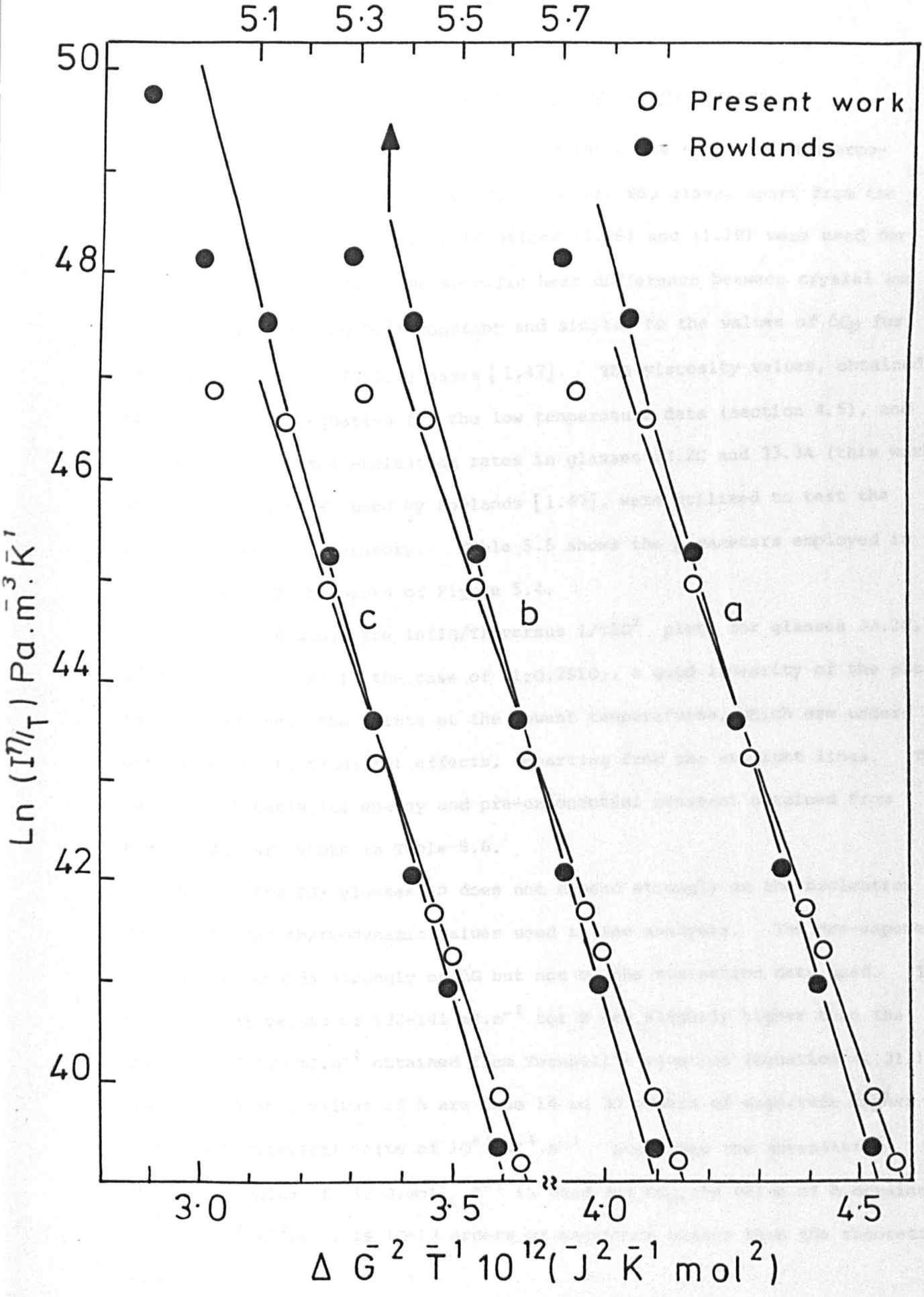

Fig. 5.4 Ln(Iη/T) versus $1/T\Delta G^2$ for BS_2 glasses. ΔG from Equartion 1.28 with: a) $\Delta C_p = 0$, b) $\Delta C_p = -12$, c) $\Delta C_p = 12$ $J.mol^{-1}.K^{-1}$.

5.5 Analysis of the Nucleation Data for $BaO.2SiO_2$ Glasses

Unlike the lithium disilicate glass there are no detailed thermodynamic data available for the stoichiometric BS_2 glass, apart from the heat of fusion [1.47]. Hence Equations (1.26) and (1.28) were used for the calculation of ΔG. The specific heat difference between crystal and glass ΔC_p was assumed to be constant and similar to the values of ΔC_p for $Na_2O.2SiO_2$ and $Li_2O.2SiO_2$ glasses [1.47]. The viscosity values, obtained from the Fulcher equation for the low temperature data (section 4.5), and the measured crystal nucleation rates in glasses 33.2C and 33.3A (this work) and in the BS_2 glass used by Rowlands [1.47], were utilized to test the classical nucleation theory. Table 5.5 shows the parameters employed in the construction of the plots of Figure 5.4.

Figure 5.4 shows the $\ln(I\eta/T)$ versus $1/T\Delta G^2$ plots for glasses 33.2C, 33.3A and BS_2. As in the case of $Li_2O.2SiO_2$, a good linearity of the plots is obtained, only the points at the lowest temperatures, which are underestimated due to transient effects, departing from the straight lines. The values of interfacial energy and pre-exponential constant obtained from these plots are shown in Table 5.6.

As for the LS_2 glasses, σ does not depend strongly on the nucleation data or on the thermodynamic values used in the analysis. The pre-exponential constant A depends strongly on ΔG but not on the nucleation data used. The experimental values of 132-141 $mJ.m^{-2}$ for σ are slightly higher than the value of 97-130 $mJ.m^{-2}$ obtained from Turnbull's equation (Equation (1.31)). The experimental values of A are from 14 to 30 orders of magnitude *higher* than the theoretical value of 10^{41} $m^{-3}.s^{-1}$ Even when the unrealistic (too high) value of +12 $J.mol^{-1}.K^{-1}$ is used for ΔC_p, the value of A obtained, 10^{50} - 10^{53} $m^{-3}.s^{-1}$, is 10-13 orders of magnitude higher than the theoretical value.

Table 5.5

PARAMETERS FOR ANALYSIS OF NUCLEATION IN GLASSES 33.2C AND 33.3A

T (K)	I ($m^{-3}.s^{-1}$)	Log η(Pa.s)	$1/T\Delta G^2$ ($J^{-2}.mol^2.K^{-1}$) Eq. (1.26)	Eq. (1.28)
958	125×10^9	12.25	3.94×10^{-12}	5.32×10^{-12}
979	1490	11.06	4.08	5.46
991	1042	10.50	4.17	5.54
1004	644	9.96	4.28	5.64
1018	461	9.45	4.39	5.76
1022	415	9.31	4.43	3.79
1033	222	8.97	4.53	5.89
1038	163	8.82	4.58	5.93

$\text{Log } \eta = 1.83 + 1701.9/(T - 794.6)$; η (Pa.s), T (K)

$\Delta G = -37500\ (1693 - T)/1693$ $(J.mol^{-1})$; Eq. (1.26)

$\Delta C_p = -12\ J.mol^{-1}.K^{-1}$ in Eq. (1.28) [1.47]

Table 5.6

PARAMETERS OBTAINED FROM THE ANALYSIS OF NUCLEATION DATA FOR BS_2 GLASSES

	Eq. (1.26) ($\Delta C_p = 0$)	Eq. (1.28) ($\Delta C_p = -12$)	Eq. (1.28) ($\Delta C_p = 12$)*
		This work	
Log A($m^{-3}.s^{-1}$)	55 ±2	65 ±3	50 ±1
σ ($mJ.m^{-2}$)	131.6	133.1	134.0
		Rowlands	
Log A($m^{-3}.s^{-1}$)	58 ±1	70 ±2	53 ±1
σ ($mJ.m^{-2}$)	137.3	139.2	140.5

The headings "This Work" and "Rowlands" indicate the source of nucleation data.

* The value of +12 $J.mol^{-1}$ K^{-1} is an arbitrary (too high) value chosen to test the sensitivity of A and σ on the magnitude of the thermodynamic driving force ΔG used in the analysis.

As in the case of LS_2 glasses, when the Hoffman expression (Eq. 1.30) is used for ΔG, the $\ln(I\eta/T)$ vs $1/T\Delta G^2$ plots are *not* straight lines.

From a plot of $(T \ln I - T' \ln I')/(T - T')$ versus $(T - T)'(1/\Delta G^2 - 1/\Delta G_i^2)^{-1}$ James and Rowlands [1.75], assuming a spherical nucleus, obtained values of 132 $mJ.m^{-2}$ for σ and 741 $kJ.mol^{-1}$ for ΔH_D between 700°C and 780°C. They employed a different method of analysis (see chapter 1), avoiding the use of viscosity data by assuming that ΔH_D was independent of temperature over the range of nucleation measurements. However, this is an approximation since the viscosity data indicate that ΔH_D does vary with temperature (see sections 5.6 and 5.8). Hence it would seem preferable to use the present method of analysis with viscosity data when available. Nevertheless, the result of James and Rowlands [1.75] for σ is in good agreement with the present results.

It should be emphasized that for barium disilicate more accurate thermodynamic data are required if the nucleation theory is to be tested with greater certainty. This applies in particular to the determination of the parameter A and its comparison with theory. However, it should also be pointed out that the large discrepancy in A (14-30 orders of magnitude) between theory and experiment was very similar for both the $BaO-SiO_2$ and Li_2O-SiO_2 systems and, in the latter system, reliable thermodynamic data was available. In the only other work where viscosity, thermodynamic and nucleation data were available for the *same* glass, carried out by Gonzalez-Oliver and James [1.76], an even larger discrepancy between theory and experiment was observed.

A more general problem is the uncertainty of the assumption that the diffusion process required for nucleation is closely related to the process of viscous flow. Turnbull and Cohen [1.59] suggested that for the crystallization of network liquids, interatomic bonds in the network must be broken.

As interatomic bonds must also be broken for viscous flow or self-diffusion, the activation energy for these processes must be of the same magnitude. One justification for the procedure of identifying ΔH_D with ΔH_η (activation enthalpy for viscous flow) is that the diffusion coefficients calculated from measured viscosity values using the Stokes-Einstein equation have been found to agree with measured values for the diffusion of oxygen in silicate glasses to within an order of magnitude [5.5]. Also, the apparent activation enthalpies $\Delta H_{D_{ox}}$ for diffusion of oxygen were close to those of viscous flow for three different silicate glasses, and increased with falling temperature in the transformation range for a Na_2O-CaO-SiO_2 glass [5.5]

5.6 Further Test of the Nucleation Theory

It was shown in chapter 1 that the steady-state nucleation rate is given by

$$I = n \frac{kT}{h} \exp\left[- \frac{\Delta G_D}{RT} \right] \exp\left[- \frac{K_5 \bar{\sigma}^3 V_m^2}{\Delta G^2 \, kT} \right] \qquad (1.20)$$

where $\Delta G_D = \Delta H_D - T\Delta S_D$. Therefore, if the activation enthalpy for molecular transport across the nucleus-matrix interface ΔH_D is independent of temperature, a plot of $(\ln I + \Delta H_D/RT)$ versus $1/(T\Delta G^2)$ should yield a straight line. However, a very pronounced curvature was observed in such plots when a value of 535 $kJ.mol^{-1}$ (or other arbitrary values) were used for ΔH_D. This behaviour indicates that ΔH_D does *vary* with temperature and gives some support for the procedure of substituting ΔH_D by ΔH_η.

5.7 Further Discussion of the Classical Theory of Homogeneous Nucleation

The basic assumptions that embryos and nuclei may be treated as macroscopic quantities of bulk material having definite geometrical surfaces, and the interfacial energy of the embryo-parent phase boundary does not depend on embryo size, deserve attention. As discussed in the first chapter, these conditions are probably far from reality and it has been shown [1.54] that if a spherical embryo is assumed to have a well-defined geometrical surface, the interfacial energy will decrease with decreasing embryo size. Neglect of this effect is often referred to as the capillary approximation. Since direct measurements of interfacial energy refer to a planar interface, they should give values larger than those obtained from nucleation kinetics. This discrepancy is perhaps about 15% for a critical nucleus containing 13 atoms [1.54]. Unfortunately, no independent value of σ is available for baria-silica or lithia-silica glasses, and since σ was derived from nucleation measurements it is difficult to see how such an argument could explain the discrepancy in the factors A between theory and experiment.

5.7.1 Statistical mechanical contributions to the free energy of formation of embryos

Lothe and Pound [1.86] concluded that several important contributions to the free energy of formation of an embryo are neglected in the classical derivation of W^*. These arise from a consideration of the translational and rotational free energy of the embryo, and the probability of finding a critical nucleus per unit volume is increased considerably by these additional free energy terms. This causes an *increase* in the value of the pre-exponential factor. On the basis of results for supercooled mercury [1.83] an approximate value of the pre-exponential factor was calculated to be

10^{48} m^{-3} s^{-1} compared with the experimental value of 10^{41} m^{-3} s^{-1}. Lothe and Pound [1.86] also suggested that these contributions may be smaller in the case of more complex liquids, leading to better agreement with classical theory. The discrepancy between classical theory and experiment, found in the present study, especially for the Li_2O-SiO_2 glasses for which thermodynamic data were available, is far greater than the correction factor calculated by Lothe and Pound.

5.7.2 The effect of a temperature dependent interfacial energy

The experimental results for homogeneous nucleation of supercooled gallium [1.88] indicate a pre-exponential factor of 10^{45} - 10^{47} $m^{-3}.s^{-1}$, similar to the value of 10^{48} $m^{-3}.s^{-1}$ obtained for supercooled mercury [1.83], but 5-7 orders of magnitude greater than the theoretical value of 10^{40} $m^{-3}.s^{-1}$. This discrepancy was explained by assuming an interfacial free energy which *decreased* with decreasing temperature, according to $\sigma = \sigma_0 - bT$, the interfacial entropy, b, being negative. An analysis of the results for mercury yielded similar results. The authors concluded that classical theory is able to explain nucleation data for metals, without recourse to statistical mechanical corrections. Rowlands and James [1.72] analysed their results for LS_2 glass, based on the equations given in [1.88] , and found that the experimentally obtained value of A was reduced to the theoretical value if σ is expressed as: $\sigma = 64.0 + 0.109T$ ($mJ.m^{-2}$). The value of b was similar in magnitude to the value of -0.055 $mJ.m^{-2}.K^{-1}$ obtained for gallium and also to the value of -0.090 $mJ.m^{-2}.K^{-1}$ obtained for the homogeneous nucleation of mercury.

Many of the above ideas were discussed by Rowlands and James [1.72] who also considered the possibility that the nuclei of the LS_2 crystal phase were non-spherical.

Uhlmann and coworkers tested the theory for a $Na_2O.2SiO_2$ glass [1.71] and for a $CaO.Al_2O_3.2SiO_2$ glass [1.77]. In both studies a nearly perfect agreement was found with theory. However, three points should be emphasised: (i) the crystal nucleation rates were obtained indirectly by means of the Johnson-Mehl-Avrami (JMA) equation, (ii) the Hoffman expression was used for ΔG and (iii) *no* evidence of internal nucleation of crystals was given for these glasses. Let us now discuss these points: (i) no experimental test of the JMA has been performed to date and because of the exponential form of the JMA equation, small systematic errors in the measured volume fraction of crystalliniaty and/or in the crystal growth rates can lead to large errors in I. (ii) The Hoffman expression is *not* a good approximation for ΔG of $Li_2O.2SiO_2$ and $Na_2O.2SiO_2$ glasses, and the pre-exponential factor is strongly dependent on the values of ΔG. Therefore the use of uncorrect values for ΔG can lead to serious errors in A. (iii) *No* internal nucleation was detected in a $Na_2O.2SiO_2$ glass melted in this work. Also, several literature references show clearly that only surface nucleation occurs in this glass. The same restrictions are expected to apply for the $CaO.Al_2O_3.2SiO_2$ glass. Therefore, the work described in [1.71] and [1.77] did not provide a test of the classical theory.

Apart from the possibility of a temperature dependent σ, the explanations considered previously do not seem to be adequate to account for the divergence between the calculated and experimental pre-exponential factors. Therefore, we conclude that either there are some flaws in the classical theory or some unknown difficulties regarding the selection of the parameters that enter into the theory. The application of computer simulations to test new atomistic theories could be a very important development [5.7,5.8] in the future.

Finally, it is worth pointing out again that the temperature dependence of the nucleation rates appears to be well described by the classical theory.

5.8 Analysis of Non-steady State Nucleation in $Li_2O.2SiO_2$ Glasses

It was demonstrated in the first chapter that the induction period for crystal nucleation could be expressed by the following equation:

$$\tau = \frac{16\ h\ \lambda^2\ \sigma}{\pi^2\ \Delta G^2}\ \exp(\Delta G_D/kT) \qquad (1.39)$$

where the activation free energy for self diffusion ΔG_D is not necessarily the same as the kinetic barrier for nucleation. If ΔG_D is constant, a plot of $\ln(\tau\ \Delta G^2)$ versus $1/T$ should give a straight line. The activation enthalpy for self diffusion $\Delta H_D (= \Delta G_D + T\Delta S_D)$ could then be estimated from the slope.

Figure 5.5 shows the plots of $\ln(\tau.\Delta G^2)$ and $\ln(\eta)$ versus $1/T$ for the experimental values of τ obtained by several authors (Table 5.7), and the viscosity data of this work. The thermodynamic driving force ΔG was obtained from JANAF tables [1.51]. From Figure 5.5, ΔH_D is estimated to be 535 $kJ.mol^{-1}$, and the activation enthalpy for viscous flow ΔH_η varies from 555 to 1085 $kJ.mol^{-1}$ in the *same* temperature range (485°C - 430°C). It can be concluded, therefore, that *different* mechanisms are responsible for the structural re-arrangements in the two processes (non-steady state nucleation and viscous flow).

Gonzalez-Oliver [1.53] made a similar analysis for the nucleation of $Na_2O.2CaO.3SiO_2$ crystals in a glass of the same composition. He found a value of 327 $kJ.mol^{-1}$ for ΔH_D, and an average value of 820 $kJ.mol^{-1}$ for ΔH_η in the same temperature range.

Kalinina et al [5.9] recently carried out a similar study in a $2Na_2O.CaO.3SiO_2$ glass. They found that the activation enthalpy for the induction period, ΔH_D, was 610 $kJ.mol^{-1}$ between 450°C and 500°C. The average value of ΔH_η was 824 $kJ.mol^{-1}$ for temperatures between 462°C and 509°C.

Therefore, the three studies agree that the activation enthalpy for non-steady state nucleation is constant and smaller than the activation enthalpy for viscous flow, which varies with temperature.

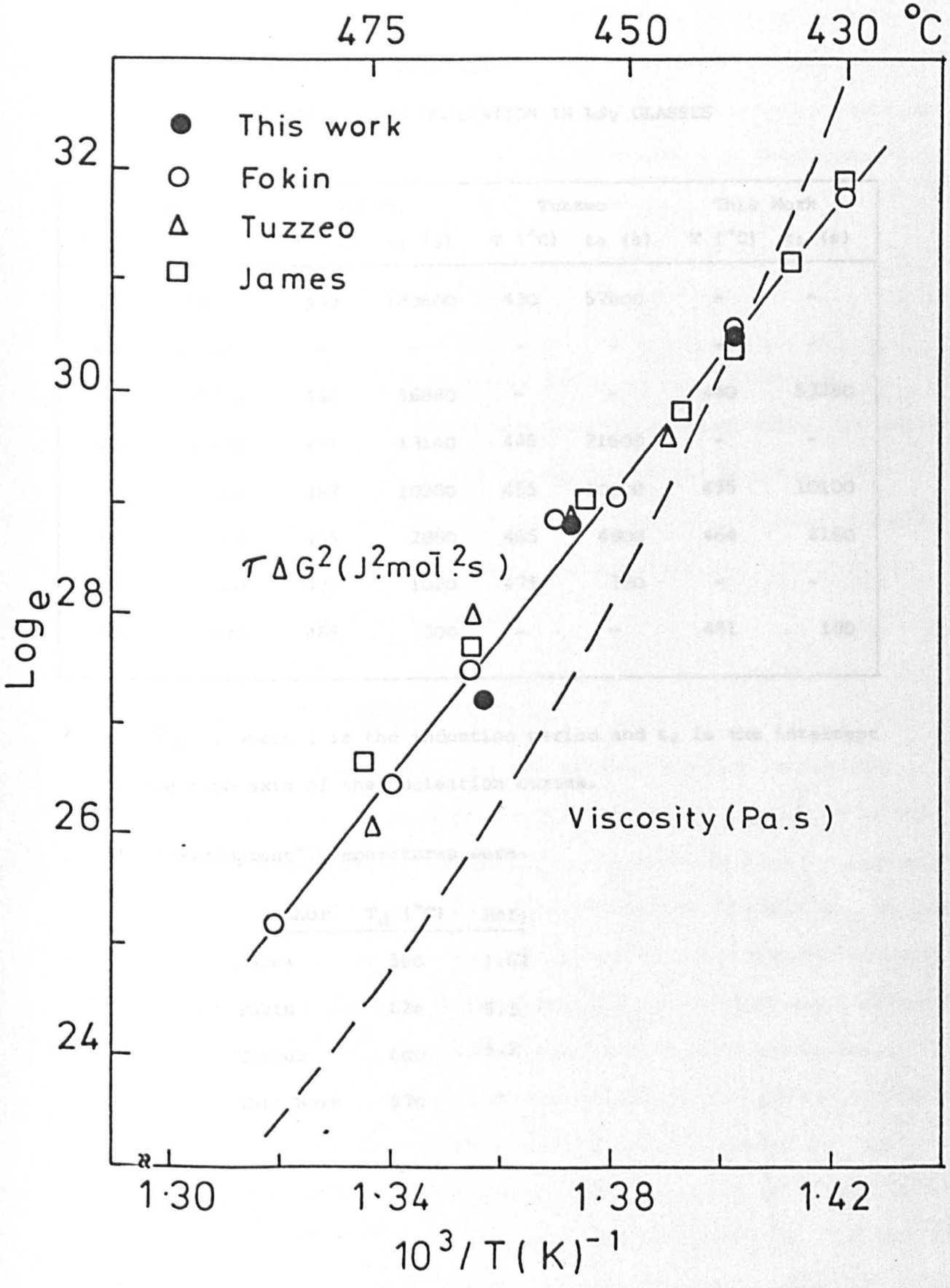

Fig. 5.5 Ln(η) vs. 1/T and Ln(τ.ΔG^2) vs. 1/T plots for LS_2 glasses.

Table 5.7

INDUCTION PERIODS FOR NUCLEATION IN LS_2 GLASSES

James		Fokin		Tuzzeo		This Work	
T (°C)	t_0 (s)*	T (°C)	t_0 (s)	T (°C)	t_0 (s)	T (°C)	t_0 (s)
430	214170	430	183600	430	57600	-	-
435	102645	-	-	-	-	-	-
440	47375	440	56880	-	-	440	53280
445	28425	451	13140	446	21600	-	-
454	13500	457	10980	455	10800	455	10100
465	3600	465	2880	465	4800	464	2160
476	1260	473	1020	475	720	-	-
489	690	485	300	-	-	481	180

* $\tau = \frac{6\ t_0}{\pi^2}$; where τ is the induction period and t_0 is the intercept on the time axis of the nucleation curves.

The "development" temperatures were:

Author	T_d (°C)	Ref.
James	560	1.62
Fokin	626	5.3
Tuzzeo	600	5.2
This Work	570	-

However, it should be stressed that the apparent intercept time t_0 is the *sum* of the true intercept time due to non-steady state nucleation, t_n, and the time t_g at the temperature of nucleation T_n, for nuclei to grow to sizes greater than the critical size at T_d (temperature of development). The time t_g is given approximately by

$$t_g = \frac{r^* (T_d) - r^* (T_n)}{U (T_n)} \qquad (5.1)$$

where U is the average rate of growth of nuclei at T_n. Therefore, the closer T_n is to T_d, i.e. with increasing nucleation temperatures, the smaller is t_g and the measured intercept time t_0 approaches the true t_n. Thus, the slope of the $\ln(T.\Delta G^2)$ versus $1/T$ plot in Figure 5.5, would be slightly decreased if correction for t_g was made. Hence, this would increase the observed difference between ΔH_D and ΔH_η.

5.9 The Johnson-Mehl-Avrami (JMA) Theory

As discussed in section 4.3, the JMA equation has been extensively applied to studies of phase transformations in materials but as far as the author is aware no quantitative test of this equation has been carried out. Such a test would involve comparison of the percentage crystallinity determined experimentally (e.g. by using X-ray diffraction) as a function of time, with the percentage crystallinity calculated from the JMA equation using independent measurements of crystal nucleation rates and crystal growth rates. In the present work a lack of agreement was found between the measured crystallinity vs. time curves and those calculated using the JMA equation for the barium disilicate glasses 33.3A and 33.2B heat treated at 743°C and 760°C.

There are a number of reasons for this lack of agreement. The form of equations (4.2) and (4.3) show clearly that very *accurate* experimental values

of the shape factor g, nucleation rate I and especially growth rate U are needed if comparison between theory and experiment is to be made. As discussed previously, however, the shape of the spherulites is very irregular (nearly 'star-like') in the BS_2 glasses. Further complications are that the spherulites are apparently only about 64% crystalline (see chapter 4) and the first phase to nucleate (as small spheres) is the high temperature form of barium disilicate (h-BS_2), the stable low temperature form (ℓ-BS_2) nucleating on the spheres and growing as needles or "spikes". Also the growth rates of the two forms of barium disilicate are quite different. The result is that the spherulites grow very slowly in the early stages but after a certain period of time when the spikes appear the crystallinity develops much more rapidly.

All these factors make a reliable test of the JMA equation very difficult in this system.

It is suggested, therefore, that another glass system be chosen with the following requirements:

i) The shape of the crystals can be clearly defined and determined.

ii) Crystal nucleation and growth in the volume of the glass predominates over surface nucleation and growth.

iii) Both nucleation and growth rates are constant with time.

iv) The phase precipitating in the supercooled liquid is 100% crystalline.

Under these circumstances the JMA theory could be compared accurately with experiment. Suitable systems might be $Li_2O.2SiO_2$, $Na_2O.CaO.3SiO_2$ or $2Na_2O.CaO.3SiO_2$.

CHAPTER 6

CONCLUSIONS AND SUGGESTIONS FOR FURTHER WORK

The main objective of this work was to study the effect of amorphous phase separation (APS) on crystal nucleation and growth in glasses. A second objective was to investigate as far as possible the validity of the classical nucleation theory for crystal nucleation in supercooled glass-forming liquids. Finally, it was intended to test the applicability of the Johnson-Mehl-Avrami theory to the glass/crystal transformation.

A series of baria-silica and lithia-silica glasses were melted and homogenized in electric furnaces. The major components and levels of minor impurities in the glasses were thoroughly analysed. The combination of several techniques, i.e. Atomic Absorption Spectroscopy, Flame Emission Spectroscopy, Flame Photometry, Electron Probe Microanalysis and Gravimetric Analysis, showed that the overall level of impurities in the Li_2O-SiO_2 glasses was very low (< 0.05 wt%). The Bao-SiO_2 glasses contained from 0.7 to 0.004 wt% SrO, depending on the $BaCO_3$ used. The total level of other impurities was about 0.1 wt%.

The "water" content was very similar in all the BaO-SiO_2 glasses and was much lower than that in glasses melted in gas furnaces by other authors. The Li_2O-SiO_2 glasses also contained very similar water contents. The homogeneity of the glasses was carefully checked by measuring the number of crystals (after heat treatment) in several different glass samples using different sizes of the field of view in the optical microscope. The observed variations were within the statistical error.

The Small Angle X-ray Scattering (SAXS) results showed that amorphous phase separation developed rapidly in some BaO-SiO_2 glasses heated at 50-70°C

above the transformation range. The number of silica-rich droplets and their specific surface area decreased from the earliest stage of heat treatment, indicating that most nucleation occurred during quenching from the melt or within a short period of heat treatment. The attainment of the equilibrium composition of the matrix, however, required 3 to 4 hours at 760°C and about 7 hours at 743°C for a glass with 28.3 mol% BaO. The average droplet diameters determined by SAXS increased according to well established laws for the early and more advanced stages of APS, and agreed reasonably well with the diameters determined directly from thin foil TEM micrographs, giving some support for the approximations involved in the SAXS technique. The low temperature binodal boundary determined by SAXS was about 1 mol% BaO higher than the value given by the equations of Haller et al. [2.7]. This could be due to a difference in the levels of SrO between the glasses used here and those used in the calculations of Haller et al.

Transmission Electron Microscopy of the $BaO-SiO_2$ glasses revealed that only glasses with 28.3 mol% (or less) BaO phase separated. Glasses with 29.7 and 29.9 mol% BaO, although clearly situated inside the miscibility gap, did *not* phase separate. This observation is in agreement with other authors. For glasses situated close to the binodal line, the absence of amorphous phase separation is probably due to a lack of thermodynamic driving force for nucleation. TEM studies also showed that the crystalline $BaO.2SiO_2$ needles grew undisturbed by the droplets in the amorphous phase separated matrix.

A remarkable correlation was found at two temperatures between the times required for the amorphous (baria-rich) matrix to reach the equilibrium composition, revealed by a constant value of the integrated SAXS intensity, and the period of *increasing* crystal nucleation rates in glasses undergoing

phase separation. The crystal nucleation rates in non phase separating glasses were *constant* with time at all temperatures above the transformation range. No correlation was found between the nucleation rates of crystals and the interfacial area and number of the amorphous droplets determined by SAXS. The comparison of nucleation rates in glasses with different percentages of BaO revealed that the crystal nucleation rates increased with BaO content in the non phase separated glasses. In the phase separated glasses, the nucleation rates increased with the BaO content in the matrix (baria-rich) phase. The stoichiometric $BaO.2SiO_2$ glass gave the *highest* nucleation rates as expected from the classical theory.

The phase-separated glasses with 27.0 and 28.3 mol% BaO showed nearly identical crystal nucleation rates at the same temperature. Again there was no direct correlation between the volume fraction and specific surface area of the amorphous droplets with the crystal nucleation rates in these glasses. These observations indicate that the crystal nucleation rates depend mainly on the *composition* of the baria-rich matrix, because the baria content in the matrix was the same for glasses 27.0 and 28.3 after phase separation at the same temperature.

Similarly, the *enhanced* crystal growth rates observed in phase separating glasses were probably due to compositional changes in the matrix resulting from amorphous phase separation.

The viscosities of $BaO-SiO_2$ glasses situated inside the miscibility gap (27.0, 28.3B and 29.9) were equal within experimental error, reflecting the similarity of the BaO content in the matrix of the three glasses at a given temperature. The stoichiometric glass 33.3A had a lower viscosity.

Therefore, we conclude that there is no direct relation between the morphology of phase separation and crystal nucleation in $BaO-SiO_2$ glasses. The enhanced crystal nucleation and growth rates, observed for glasses under-

going phase separation, is mainly due to enrichment in BaO of the matrix caused by amorphous phase separation. This causes a decrease in viscosity, and increases the thermodynamic driving force for crystal nucleation by bringing the composition of the matrix closer to the stoichiometric crystal phase $BaO.2SiO_2$.

The crystal nucleation rates in Li_2O-SiO_2 glasses undergoing phase separation also increased initially, approaching a constant value with time for isothermal heat treatment. These constant nucleation rates were nearly identical for glasses of widely different Li_2O content, situated in the unstable (spinodal) and metastable regions of the miscibility gap, showing that the composition of the amorphous matrix is the main responsible for the nucleation. No correlation was found between crystal nucleation and the morphology of amorphous phase separation studied by TEM. In the Li_2O-SiO_2 system, in contrast to the BaO-SiO_2 system, the nearly stoichiometric glass, 33.2B, had *lower* crystal nucleation rates than that in the glasses undergoing phase separation. This was probably due to the nucleation of a solid solution crystal phase in the phase separated glasses, whereas the stoichiometric ℓ-$Li_2O.2SiO_2$ phase crystallized in glass 33.2B. In this case, the thermodynamic driving force (and interfacial energy) could be more favourable for nucleation in the phase separated glasses, giving higher nucleation rates.

A minor, additional effect was detected in the nucleation (N_V vs. time) plots of both baria-silica and lithia-silica glasses. In some cases, an inflexion was observed in the N_V vs. time plots, corresponding to a temporary maximum in the nucleation rate I, the effect disappearing at longer times. These inflexions occurred when the amorphous phase separation was in the early stages (before attainment of the equilibrium composition of the matrix). Therefore, they may be related to the *diffusion zones* (silica-depleted regions) which exist around the amorphous droplets when the phase separation is in

the early stages. Some preferential nucleation (perhaps heterogeneous) may occur in these zones. This is a minor effect because these inflexions are more pronounced at high temperatures (lower nucleation rates), being undetectable in the region of higher nucleation rates.

Generalizing, we can say that the *enhancement* in crystal nucleation and growth rates, caused by amorphous phase separation, is mainly due to the *compositional shift* of the matrix. The observed increase in nucleation rates, however, are relatively small (less than one order of magnitude) when compared with the effect of nucleating agents which, in some cases, can increase the nucleation rates by 6-7 orders of magnitude.

An experimental test of the classical nucleation theory was performed with $Li_2O.2SiO_2$ and $BaO.2SiO_2$ glasses. Apart from the present results, several authors have measured the crystal nucleation rates in $Li_2O.2SiO_2$ glasses, and thermodynamic data were available from the literature. The test was carried out with a combination of different nucleation and thermodynamic data; and the viscosity results obtained in this work. The experimentally determined values of interfacial energy σ were not strongly dependent on which combination of data was used. The pre-exponential factor A, however, was strongly dependent on the thermodynamic data, i.e. 10^{61} $m^{-3}.s^{-1}$ and 10^{70} $m^{-3}.s^{-1}$ for calculated and measured values of thermodynamic driving force, respectively. These values are much *higher* than the theoretical value of 10^{41} $m^{-3}.s^{-1}$. The experimentally determined values of σ, 197-211 $mJ.m^{-2}$, agree well with the values calculated from the Turnbull equation (187-210 $mJ.m^{-2}$).

For the $BaO.2SiO_2$ glass, crystal nucleation rates obtained in this work and those obtained by Rowlands, were used in conjunction with the viscosity data obtained here. For this glass, no thermodynamic data are available in

the literature apart from the measured heat of fusion. Therefore, calculated free energies were used. Again, the experimental values of the pre-exponential constant depended strongly on the thermodynamic data used and varied from 10^{55} to 10^{70} $m^{-3}.s^{-1}$. The experimental values of interfacial energy, 132-139 $mJ.m^{-2}$, were slightly higher than the values expected from Turnbull's equation, i.e. 97-130 $mJ.m^{-2}$.

For both $Li_2O.2SiO_2$ and $BaO.2SiO_2$ glasses the temperature dependence of nucleation rates was *well* described by the classical theory.

Several possible reasons for the discrepancy in the pre-exponential constants between theory and experiment were discussed including transient nucleation effects, experimental errors in the nucleation rates, the possibility of heterogeneous nucleation and statistical mechanical contributions to the free energy of formation of a nucleus. It was concluded that none of these could account for the observed discrepancy in the values of A.

A possible explanation for the discrepancy may be the non-validity of the Stokes-Einstein relation between diffusion coefficient and viscosity, i.e. the assumption in the analysis that the kinetic barrier to nucleation is identical to that for viscosity may be incorrect. Another possible explanation is some error in the free energy values used in the analysis of nucleation rates. However, this seems unlikely since the discrepancy occurred even for $Li_2O.2SiO_2$ glases, where apparently accurate thermodynamic data were available from direct experimental measurements.

If the thermodynamic data are accurate and the Stokes-Einstein relation is also accepted as correct, then it seems that the classical theory and the assumptions therein are *not* valid. One assumption usually made is that the interfacial energy σ is independent of temperature. However, a temperature dependent interfacial energy, as discussed by other authors, is one possible way of accounting for the discrepancy in the pre-exponential factors.

An analysis of the induction periods for steady-state nucleation in $Li_2O.2SiO_2$ glasses, measured by several authors, yielded a *constant* value of 535 $kJ.mol^{-1}$ for the activation enthalpy for molecular diffusion. The activation enthalpy for viscous flow, on the other hand, *varied* from 555 to 1085 $kJ.mol^{-1}$ in the same temperature range (485°C to 430°C). Therefore, it is concluded that different mechanisms are responsible for the structural rearrangements involved in the two processes.

The attempt to experimentally test the Johnson-Mehl-Avrami (JMA) theory was not successful because the various assumptions of the theory were not obeyed for the glass chosen, i.e. barium disilicate. The difficulties included the irregular shape of the BS_2 spherulites, the high to low polymorphic transformation, the differing growth rates of the two crystalline forms of BS_2 and the fact that the spherulites were not 100% crystalline. For these reasons, the agreement between the calculated and measured crystallinity versus time curves was poor for this system.

Mathematical equations were derived to estimate the systematical errors involved when optical microscopy is used for the determination of nucleation rates of spherical particles. For typical cases, i.e., when a double stage heat treatment is given to glasses which have constant crystal nucleation and growth rates these equations predict *underestimates* of 3 to 14% for the nucleation rates. These predictions were verified experimentally.

Finally, the results of this work for the "simpler" binary systems have demonstrated that the idea that nucleating agents, such as TiO_2, P_2O_5, ZrO_2 etc., were primarily components to cause amorphous phase separation, which was a necessary step in the formation of fine-grained crystalline materials [1.15,6.1], is not necessarily true. Nucleating agents are much more effective than amorphous phase separation in increasing the crystal nucleation rates, although the roles of many non-metallic nucleating agents are still imperfectly understood. These findings may also apply for complex commercial glass-ceramic compositions.

6.1 Suggestions for Further Work

The SAXS study of the amorphous phase separation in $BaO-SiO_2$ glasses has shown an interesting feature, i.e. the number of droplets *decreased* from the earliest heat treatment times, while the equilibrium composition of the amorphous matrix was only reached after several hours of heat treatment. The coarsening stage, therefore, began *well before* the amorphous matrix reached the composition given by the binodal boundary. This result is at variance with a classical TEM study of phase separation in soda-lime-silica glasses [4.10]. This and other conclusions drawn from the SAXS studies, however, are subject to some uncertainty due to the corrections made for the *linear* X-ray beam. Thus, the use of a *point-like* beam, e.g. from a synchrotron source, for SAXS studies of $BaO-SiO_2$ glasses of similar compositions to those used here, could be very useful in confirming (or rejecting) the present conclusions. It would also be extremely interesting from the point of view of checking the SAXS technique for the linear beams which are normally used.

Due to the large electronic density difference between the silica-rich droplets and the baria-rich amorphous matrix, high quality thin foil TEM micrographs (and SAXS curves) can be obtained for these glasses. Therefore, a careful check of the structural parameters obtained by SAXS, e.g. number of droplets, volume fraction, specific surface area, average diameter, etc. could be made in principle by TEM using the stereo pair technique of James and McMillan [4.14]. Glasses with 28.5-29.0 mol% BaO heated at 750-800°C would be ideal for this study.

SAXS studies of phase separation in glasses with 17.7 and 31.0 mol% Li_2O, heat treated at 481°C, would be very useful for comparison with the crystal nucleation curves obtained in this work, similarly to the study of the $BaO-SiO_2$ glasses.

The measurement of the *time dependence* of the viscosity, during isothermal heat treatment of glasses undergoing phase separation, would be helpful in the interpretation of crystal nucleation and growth kinetics. The fibre extension method or a modified beam-bending technique (where very fine beams could be used) would be needed, because only very small specimens can be successfully quenched free of phase separation from high tempertures.

There is a great need for accurate thermodynamic data, i.e. enthalpy and specific heat measurements for the liquid and crystal phases from the melting point to the glass transformation range, from which the free energy ΔG can be determined. This is particularly true for "simple" glass forming systems which show internal crystal nucleation such as Li_2O-SiO_2, BaO-SiO_2, Al_2O_3-SiO_2, $Na_2O.2CaO.3SiO_2$, $2Na_2O.CaO.3SiO_2$, and possibly others. Accurate viscosities and nucleation rates in conjunction with thermodynamic data are also needed if further progress is to be made in comparing theory and experiment.

Accurate data for the self-diffusion coefficients in the transformation range and above for the various rate limiting species, e.g. oxygen and silicon, could be used to critically analyse the nucleation rate curves in terms of the classical theory. This would avoid the use of the Stokes-Einstein equation which might be in error.

If the activation energy for nucleation ΔG_D is the same as that for growth of a finite crystal $\Delta G_D'$, which may be true for non-reconstructive transformations, we can write

$$\ln\left(\frac{I}{U}\right) = \ln\left(\frac{A}{A^1}\right) - \frac{K_5 \bar{\sigma}^3 V_m^2}{kT\Delta G^2} \qquad (6.1)$$

Equation (6.1) isa combination of the nucleation and growth equations (1.20) and (1.47), when the factor $\ln[1 - \exp(-\Delta G/RT)]$ is neglected.

From a plot of $\ln\left(\frac{I}{U}\right)$ vs. $\frac{1}{T\Delta G^2}$, $\bar{\sigma}$ could be obtained and the experimental value of $\left(\frac{A}{A^1}\right)$ could be compared with that predicted by theory without requiring knowledge of the diffusion activation entropy, ΔS_D. However, the crystal growth rates at low temperatures (in the nucleation range) are generally very low and either electron microscopy techniques or a double stage heat treatment (similar to the heat treatments used here to measure the crystal growth rates in phase separating glasses) would be required for their measurement.

As emphasized by James [2.27], the fundamental problem of determining the interfacial energy σ, independently of nucleation measurements, remains unresolved. The small value of the critical nucleus size derived from experiment (for example $\approx 10\mathring{A}$ radius for LS_2 at 450°C) also questions the validity of the use of macroscopic concepts such as σ, and perhaps the assumption in the classical theory of a sharp boundary between nucleus and parent phase. There may be scope for atomistic theories which avoid the use of macroscopic concepts and the use of computer simulations of nucleation are likely to be of great importance in the future.

Already new statistical theories of phase transformations are being developed. For example, very recently one statistical theory has been shown to describe accurately the later stages of spinodal decomposition in a PbO-B_2O_3-Al_2O_3 glass [6.2]. It is hoped that the data presented in this thesis will be useful in testing any future theories of nucleation.

Finally, the Johnson-Mehl-Avrami (JMA) theory has been used for a considerable time in the analysis of phase transformations in many materials. Recently, this theory has been intensively used for predictions of the kinetics of glass formation, and for the calculation of crystal nucleation rates. However, as far as this author is aware, no experimental test of the JMA

theory has been carried out. Such a test is urgently needed, and glasses such as $Li_2O.2SiO_2$ and $Na_2O.2SiO_2.3SiO_2$ might be ideal systems for this purpose. Accurate values of crystal nucleation rates, crystal growth rates and volume fraction of crystallinity as a function of isothermal heat treatment would be needed.

APPENDIX 1

A THEORETICAL AND EXPERIMENTAL ASSESSMENT OF SYSTEMATIC ERRORS IN STEREOLOGY

Theory

According to Toshev and Gutzow [A.1] the number of circular intersections in a cross-section, N_S, through a random assembly of spherical particles is given by

$$N_S(\sigma) = \int_{\rho=0}^{\rho=1} \rho \, dN_V - \int_{\rho=\sigma}^{\rho=1} (\rho^2 - \sigma^2)^{1/2} \, dN_V \qquad (1)$$

where $\rho = D/D_M$ and $\sigma = d/D_M$; D being the diameter of a spherical particle in the assembly, d the diameter of a circular intersection and D_M the largest diameter of the distribution. dN_V, defined by $N_V(\rho)d\rho$, is the frequency distribution function (volume distribution of particles).

De Hoff and Rhines [A.2] have shown that the number of particles per unit volume, N_V, is related to the number of sectioned particles, N_S^0, by

$$N_V = \frac{2N_S^0 \, \bar{Z}}{\pi \, K(q)} \qquad (2)$$

where K(q) depends on the shape of the particles (K(q) = 1 for spheres), and

$$\bar{Z} = \frac{\sum_i \left(\frac{n_s}{d}\right)_i}{\sum_i (n_s)_i} \qquad (3)$$

where n_s is the number of circular intersections of diameter d.

If we know the functions $N_S(\sigma)$ and $\bar{Z}$ for a given system of particles it is possible to calculate the error in N_V. i.e. the fraction lost due to the resolution limit ε of the optical microscope or micrograph, normally employed in the determination of N_V.

It can be easily seen that the fraction lost, f, is

$$\frac{N_V - N_V^m}{N_V} = 1 - (1 - f_N)(1 - f_Z) \tag{4}$$

where N_V^m is the number of particles per unit volume, as determined in the micrographs, N_V is the real value and f_N is the fraction of N_S lost, given by

$$f_N = N_S(\sigma_1)/N_S^0 \tag{5}$$

where $\sigma_1 = \varepsilon/D_M$; and f_Z is the fraction of $\bar{Z}$ lost, given by

$$f_Z = 1 - \frac{\bar{Z}^m}{\bar{Z}} \tag{6}$$

where $\bar{Z}^m$ and $\bar{Z}$ are the De Hoff's factor obtained from the photographs and the real factor, respectively. They are given by the following equations:

$$\bar{Z} = \int_0^1 \frac{1}{\sigma D_M}\left[\frac{dN_S}{d\sigma}\right] d\sigma \Big/ \int_0^1 \left[\frac{dN_S}{d\sigma}\right] d\sigma \tag{7}$$

$$\bar{Z}^m = \int_{\sigma_1}^1 \frac{1}{\sigma D_M}\left[\frac{dN_S}{d\sigma}\right] d\sigma \Big/ \int_{\sigma_1}^1 \left[\frac{dN_S}{d\sigma}\right] d\sigma \tag{8}$$

Application to Some Typical Cases of Crystallization in Glasses

Case 1

Instantaneous nucleation, i.e., most of the nuclei are already formed at the temperature of study, only a linear growth occurring. A *monodispersed* system of crystals is predicted.

It can be shown that the probability that a sphere with diameter D_M upon sectioning will reveal a circle whose diameter is equal to or less than a given value d is $1 - (1 - d^2/D_M^2)^{1/2}$. Then, the fraction of circles with diameter less or equal than d, $N_S(\sigma)/N_S^0$, is given by the same expression. In terms of σ

$$N_S(\sigma) = N_S^0 \left[1 - (1 - \sigma^2)^{1/2}\right] \tag{9}$$

where N_S^0 is the total number of particles on the cross-section.

By substituting expression (9) into Equations (7) and (8)

$$\bar{Z} = \int_0^1 \frac{\sigma N_S^0}{\sigma D_M (1 - \sigma^2)^{1/2}}\, d\sigma \Big/ \int_0^1 \frac{\sigma N_S^0}{(1 - \sigma^2)^{1/2}} = \pi/2D_M$$

and

$$\bar{Z}^m = \frac{\pi/2 - \sin^{-1}\sigma_1}{D_M\,(1 - \sigma_1^2)^{1/2}}$$

According to Equations (6) and (5),

$$f_Z = 1 - \frac{\pi - 2\sin^{-1}\sigma_1}{\pi(1 - \sigma_1^2)^{1/2}} \tag{10}$$

and

$$f_N = \frac{N_S(\sigma_1)}{N_S^0} = 1 - (1 - \sigma_1^2)^{1/2} \tag{11}$$

Therefore, the total fraction lost is given by Equation (4)

$$f = \frac{2}{\pi} \sin^{-1} \sigma_1 \tag{12}$$

Case 2

Homogeneous nucleation. With constant crystal nucleation and growth fates a *uniform* size distribution of particle diameters from zero* to D_M is expected. Therefore, according to [1.1]

$$\frac{dN_v}{N_v \, d\rho} = 1$$

where N_v is the total number of crystals in the volume considered.

By substitution of dN_v into Equation (1) we obtain

$$N_S(\sigma) = N_S^0 \left[1 - (1 - \sigma^2)^{1/2} + \sigma^2 \ln\left(\frac{1 + (1 - \sigma^2)^{1/2}}{\sigma} \right) \right] \tag{13}$$

In differential form (frequency distribution)

$$\frac{dN_S}{d\sigma} = 2N_S^0 \, \sigma \ln\left[\frac{1 + (1 - \sigma^2)^{1/2}}{2} \right] \tag{14}$$

---

* In actual fact the lower limit is the critical nucleus diameter instead of zero but, for all practical purposes, this is 3-4 orders of magnitude smaller than the resolution limit, ε; and can be set to zero.

Combining Equations (7), (8) and (14)

$$\bar{Z} = \pi/D_M \tag{15}$$

and

$$\bar{Z}^m = \frac{2}{D_M}\left\{\frac{\cos\theta_1[1 - \ln(1 + \sin\theta_1)] + \theta_1 + \sigma_1 \ln \sigma_1 - \sigma_1}{1 - N_S(\sigma_1)/N_S^0}\right\} \tag{16}$$

Therefore,

$$f = 1 - \frac{2\cos\phi_1}{\pi}[1 - \ln(1 + \sin\theta_1)] + \theta_1 + \sigma_1 \ln \sigma_1 - \sigma_1 \tag{17}$$

where $\theta_1 = \sin^{-1} \sigma_1$ and $\sigma_1 = \varepsilon/D_M$.

Case 3

A uniform size distribution of particles ranging from D_m to D_M. This is the case when a glass, which behaved in the way described in Case 2, has been given a "development" heat treatment to allow observation of the growing crystals under an optical microscope. This is the commonest case in nucleation studies.

Employing a similar reasoning, it can be shown that the total fraction lost is given by [A.3]:

$$f = 1 - \frac{2\varepsilon}{\pi(D_M - D_m)}\left\{\frac{1}{\sigma_1}\cos^{-1}\sigma_1 - \frac{1}{\sigma_2}\cos^{-1}\sigma_2 + \ln\left(\frac{\tan\tfrac{1}{2}\sin^{-1}\sigma_1}{\tan\tfrac{1}{2}\sin^{-1}\sigma_2}\right)\right\} \tag{18}$$

where $\sigma_2 = \varepsilon/D_m$.

Fig. A.1. Fractional error (underestimation) in N_V as a function of the maximum diameter of the distribution (monodispersed or uniform) for resolution limits of 1, 2 and 3 μm. The experimental points indicate the measured underestimation of crystals in glasses with 29.7 and 29.9% BaO subjected to single stage heat treatments.

- ● 16x objective lens
- o 40x objective lens

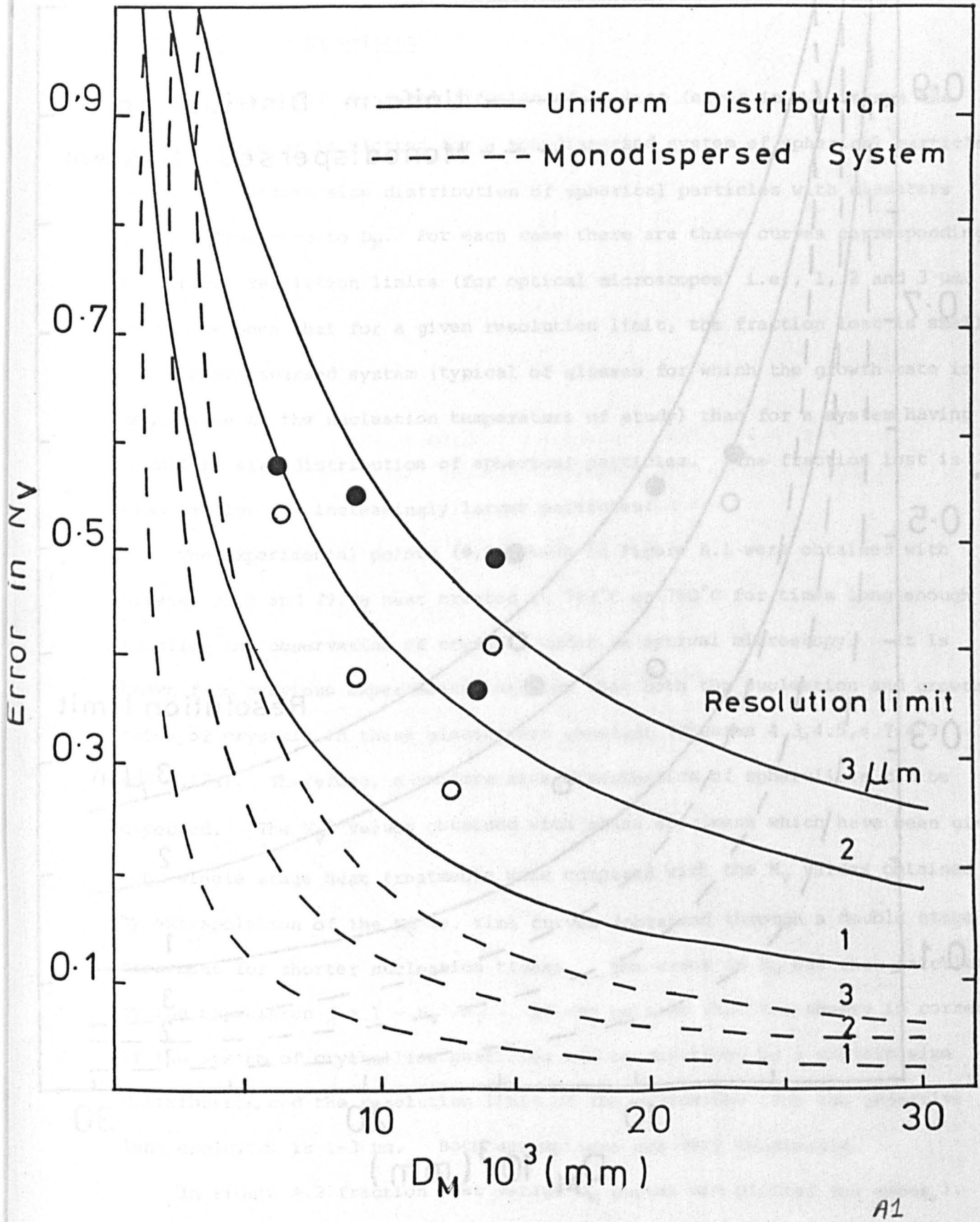
Uniform Distribution
Monodispersed System
Resolution limit
3 μm
2
1
3
2
1
0·9
0·7
0·5
0·3
0·1
Error in Ny
10
20
30
D_M 10^3 (mm)

A1

Fig A.1

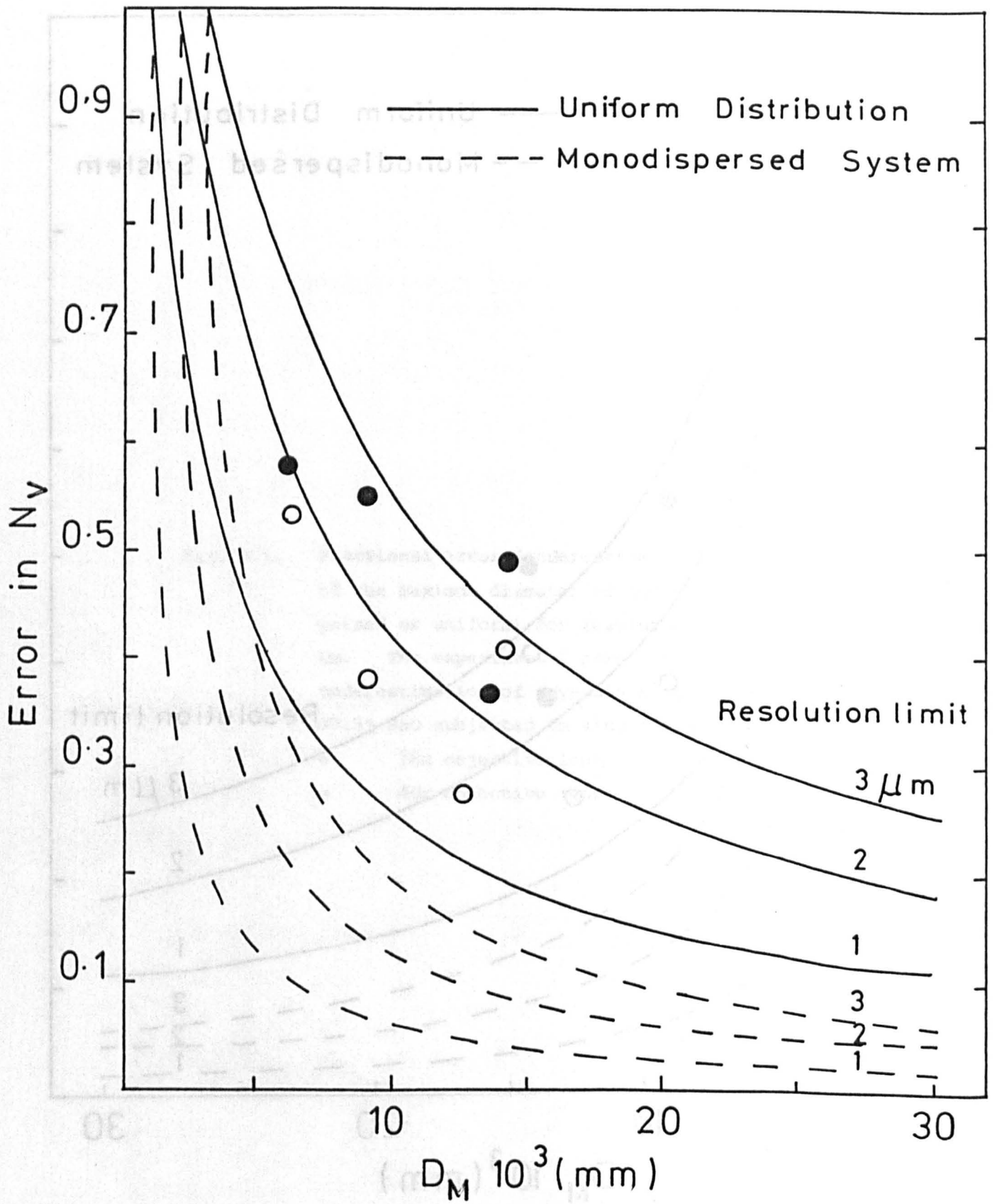
Uniform Distribution
Monodispersed System
Resolution limit
3 μm
2
1
3
2
1
0·9
0·7
0·5
0·3
0·1
Error in N_V
10
20
30
$D_M\ 10^3$ (mm)

A.1

Comparison with Experiment

In Figure A.1 the total fraction of N_V lost (error in N_V) versus the maximum diameter is plotted for a monodispersed system of spherical particles and for a uniform size distribution of spherical particles with diameters ranging from zero to D_M. For each case there are three curves corresponding to typical resolution limits (for optical microscopes) i.e., 1, 2 and 3 μm. It can be seen that for a given resolution limit, the fraction lost is smaller for a monodispersed system (typical of glasses for which the growth rate is negligible at the nucleation temperature of study) than for a system having a uniform size distribution of spherical particles. The fraction lost is also smaller for increasingly larger particles.

The experimental points (●,O) shown in Figure A.1 were obtained with glasses 29.9 and 29.7H heat treated at 743°C or 760°C for times long enough to allow the observation of crystals under an optical microscopy. It is known from previous experimental studies that both the nucleation and growth rates of crystals in these glasses are constant (Figures 4.3,4.5,4.7.4.9 and 4.12a). Therefore, a uniform size distribution of spherulites can be expected. The N_V' values obtained with glass specimens which have been given long single stage heat treatments were compared with the N_V values obtained by extrapolation of the N_V vs. time curves (obtained through a double stage treatment for shorter nucleation times). The error in N_V was then calculated by the expression $f = 1 - N_V'/N_V$. It can be seen that the theory is correct if the system of crystalline particles can be described by a uniform size distribution, and the resolution limit of the microscope (for the objective lens employed) is 1-3 μm. Both assumptions are very reasonable.

In Figure A.2 fraction lost versus D_M curves are plotted for cases 1, 2 and 3, assuming 1 μm as the resolution limit of the microscope. In the same figure there is also a family of curves for case 3, with minimum

Fig. A.2 Fractional error (underestimation) in N_v as a function of the *maximum* diameter (D_M) of the distribution for a resolution limit of 1 μm. The solid lines represent the errors for a distribution of spherical particles obtained through a double stage heat treatment, for *minimum* diameters of 2, 4, 8 and 10 μm. The dot-dash (·-·-·-) line indicates the error when the minimum diameter of the distribution is 8 μm and the resolution limit is 2 μm. The dashed curves (---) represent a uniform distribution of spheres with diameters from 0 to D_M; and a monodispersed system of spheres of diameter D_M.

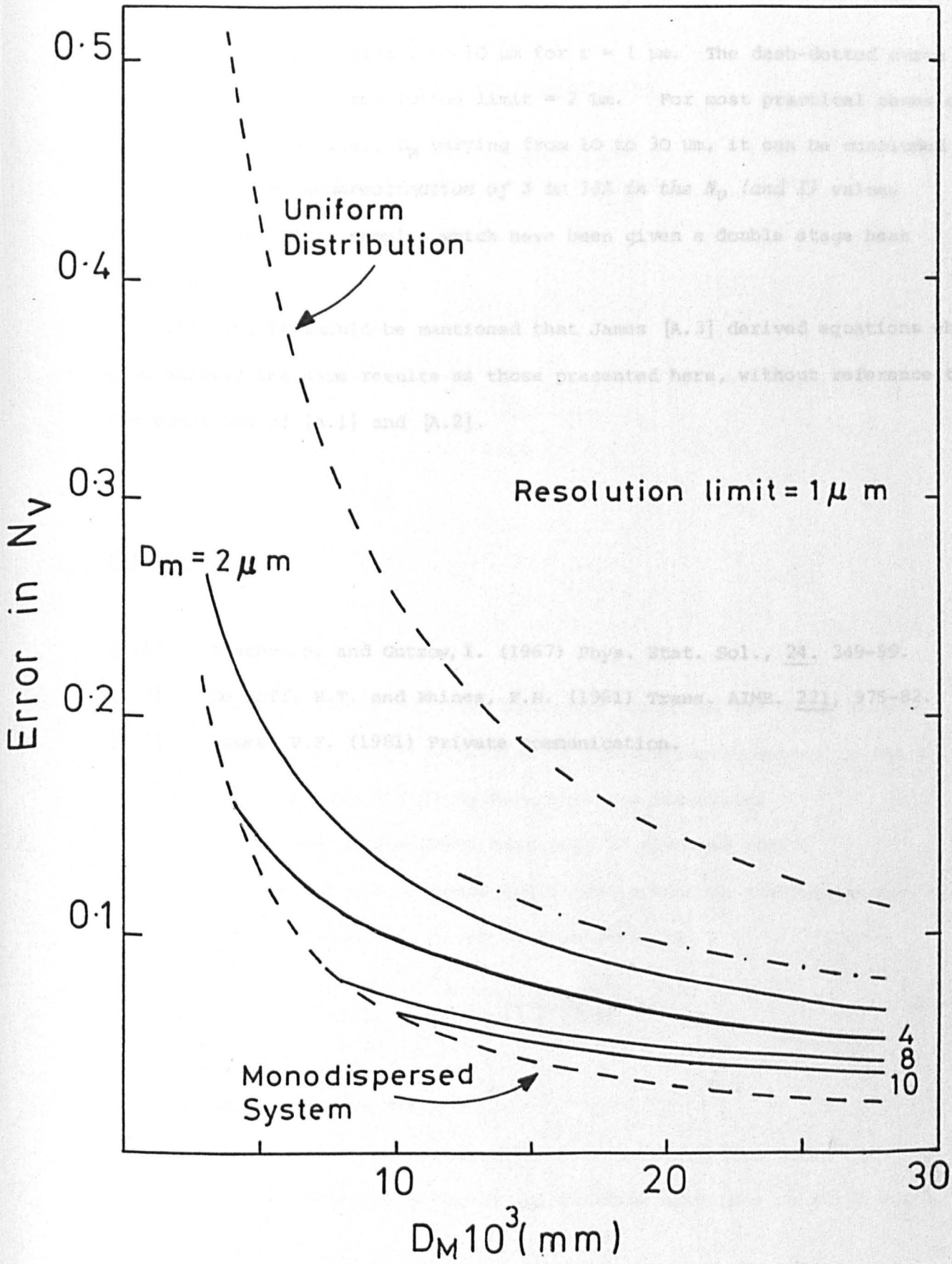
0·5
0·4
0·3
0·2
0·1
Error in N_V
Uniform
Distribution
Resolution limit = 1 μ m
D_m = 2 μ m
4
8
10
Monodispersed
System
10
20
30
$D_M 10^3$ (mm)

A2

diameters D_m varying from 2 to 10 μm for ε = 1 μm. The dash-dotted curve is for D_m = 8 μm and resolution limit = 2 μm. For most practical cases of nucleation studies i.e., D_M varying from 10 to 30 μm, it can be concluded that there is an *underestimation of 3 to 14% in the N_v (and I)* values determined for glass samples which have been given a double stage heat treatment.

Finally, it should be mentioned that James [A.3] derived equations which give exactly the same results as those presented here, without reference to the equations of [A.1] and [A.2].

References

[A.1] Toschev, S. and Gutzow, I. (1967) Phys. Stat. Sol., 24. 349-59.

[A.2] De Hoff, R.T. and Rhines, F.N. (1961) Trans. AIME. 221, 975-82.

[A.3] James, P.F. (1981) Private communication.

APPENDIX 2

Small Angle X-ray Scattering

1. Correction for the Effect of Beam Height

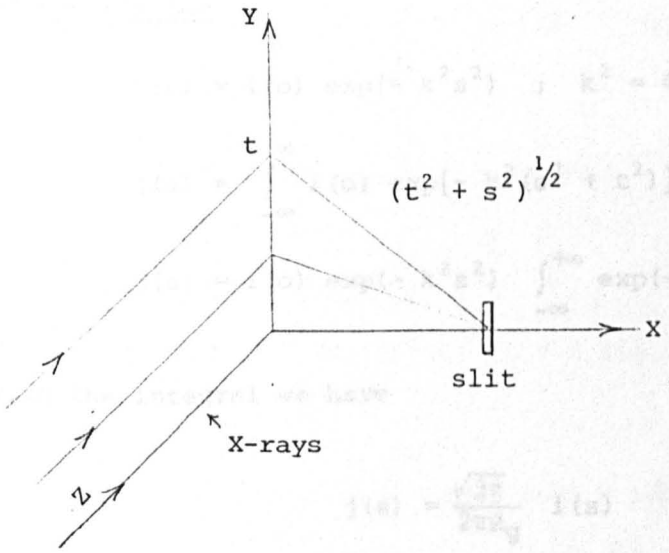

Let us define: t the coordinates along the height of the X-ray beam in the y direction, and s the modulus of the scattering vector in the x direction for an incident X-ray beam in the z direction.

i(s) = SAXS intensity of a point like beam in absolute scale

j(s) = SAXS intensity of a linear and infinite beam in absolute scale

The relationship between i(s) and j(s) is given by

$$j(s) = \int_{-\infty}^{\infty} i(\sqrt{s^2 + t^2})\,dt \qquad (1A)$$

Defining also

$I^1(s)$ = SAXS intensity of a point like beam in a relative scale

$J^1(s)$ = SAXS intensity of a linear and infinite beam in a relative scale

$$i(s) = K\, I^1(s)$$

$$j(s) = K^1 J^1(s)$$

i) Guinier's Law

$$i(s) = i(o)\, \exp(-k^2 s^2) \quad ; \quad k^2 = 4\pi^2 R_g^2/3$$

$$j(s) = \int_{-\infty}^{\infty} i(o)\, \exp[-k^2(s^2 + t^2)]\, dt$$

$$j(s) = i(o)\, \exp(-k^2 s^2) \int_{-\infty}^{+\infty} \exp(-k^2 t^2)\, dt$$

Solving the integral we have

$$j(s) = \frac{\sqrt{3\pi}}{2\pi R_g}\, i(s) \qquad (2A)$$

(ii) Porod's Law

$$i(s) = k^1 . s^{-4} \quad ; \quad k^1 = \frac{(\rho - \rho_0)^2\, S}{8\pi^3}$$

$$j(s) = \int_{-\infty}^{+\infty} \frac{k^1\, dt}{(s^2 + t^2)^2}$$

By making the substitution $t = s \tan \alpha$

$$j(s) = \frac{2k^1}{s^3} \int_0^{\pi/2} \frac{d\alpha}{(1 + \tan^2 \alpha)\, \cos^2 \alpha}$$

$$j(s) = \frac{2k^1}{s^3} \int_0^{\pi/2} \cos^2 \alpha\, d\alpha = \frac{k^1 \pi}{2s^3} \qquad (3A)$$

or

$$s^3 j(s) = \frac{\pi}{2}\, s^4\, i(s) \qquad \therefore \quad j(s) = \frac{\Delta\rho^2\, S}{16\pi^2\, s^3} \qquad (4A)$$

(iii) Integrated Intensity

In Equation (3.15) the integral $\int_0^\infty s^2\, i(s)\,ds$ appears. In terms of the observed intensities (with a linear and infinite beam) this should be replaced by the integral $\frac{1}{2}\int_0^\infty s\, j(s)\,ds$. This can be shown as follows

$$\int_0^\infty s\, j(s)\,ds = \int_0^\infty \int_{-\infty}^\infty s.i(\sqrt{s^2 + t^2})\,ds\,dt$$

By making the change of variables; $t = z \sin\alpha$ and $s = z\cos\alpha$ so that

$$t^2 + s^2 = z^2 \quad \text{and} \quad dsdt = zdzd\alpha$$

$$\int_0^\infty s\, j(s)\,ds = \int_0^\infty \int_{-\pi/2}^{+\pi/2} i(z)z^2 \cos\alpha\, dzd\alpha$$

$$\int_0^\infty s\, j(s)\,ds = 2\int_0^\infty z^2\, i(z)\,dz \qquad (5A)$$

In the same way it can be seen that

$$\int_0^\infty j(s)\,ds = \pi \int_0^\infty s\, i(s)\,ds \qquad (6A)$$

2. Determination of SAXS Parameters as a Function of the Experimental Intensities

Let us define

$J(\varepsilon)$ = SAXS intensity of a linear and infinite beam, in a relative scale, as a function of the scattering angle ε (degrees).

$$J(\varepsilon) = \frac{1}{K} \int_{-\infty}^{+\infty} i(\sqrt{\varepsilon_s^2 + \varepsilon_t^2}) \frac{d\varepsilon_t}{dt} \cdot dt$$

$$J(\varepsilon) = \frac{d\varepsilon_t}{dt} \frac{1}{K} \int_{-\infty}^{+\infty} i(\sqrt{\varepsilon_s^2 + \varepsilon_t^2})\, dt$$

$$J(\varepsilon) = \frac{d\varepsilon_t}{dt} J^1(s)$$

At low angles; $s = \pi\varepsilon/180\lambda$; ε (degrees)

$$J(\varepsilon) = \frac{180\lambda}{\pi} J(s) \qquad (7A)$$

a) Diameter of the Scattering Particles (D)

Equation (3.13) can be written for the scattering produced by a linear beam, in a relative scale, as

$$J^1(s) = J^1(o) \exp(-4\pi^2 R_g^2 s^2/3)$$

Substituting s by $\pi\varepsilon/180\lambda$; ε (degrees) and taking logarithm

$$\log J = \log J(o) - \frac{0.4343 \times 4\pi^4}{3 \times 180^2 \lambda^2} \varepsilon^2$$

Thus if log J is plotted as a function of ε^2, the curve tends to a straight line of slope α for small values of ε. This slope gives the radius of gyration of the particles. For $\lambda = 1.54$ Å

$$R_g = 36.91 \sqrt{-\alpha}$$

For spherical particles of diameter D; $R_g = (3/20)^{\frac{1}{2}} D$ and

$$D = 95.3 \sqrt{-\alpha} \quad (\text{Å}) \tag{8A}$$

b) Volume of Particles (v)

According to Equations (2A) and (7A)

$$i(0) = K \frac{2\pi^2 R_g}{180\sqrt{3\pi\lambda}} J(0) \tag{b1}$$

According to Equation (5A)

$$\int_0^\infty 2\pi s \, j(s) ds = \int_0^\infty 4\pi s^2 \, i(s) ds$$

$$\int_0^\infty 2\pi s \, j(s) ds = 2\pi K \int_0^\infty s \, J^1(s) ds$$

$$\int_0^\infty 2\pi s \, j(s) ds = \frac{2\pi^4 K}{180^3 \lambda^3} \int_0^\infty \varepsilon \, J(\varepsilon) d\varepsilon \tag{b2}$$

Referring to Equation (3.17) and combining (b1) and (b2)

$$\frac{i(0)}{4\pi \int_0^\infty s^2 \, i(s) ds} = v = \frac{180^2 \lambda^3 \, R_g \, J(0)}{\sqrt{3\pi^5} \int_0^\infty \varepsilon J(\varepsilon) d\varepsilon} .$$

$$v = \frac{180^2 \lambda^2 D J(0)}{\sqrt{20\pi^5} \int_0^\infty \varepsilon J(\varepsilon) d\varepsilon} \tag{9A}$$

c) Specific Surface of the Particles (S_V)

The combination of Equations (4A), (3.17) and (5A) gives

$$\frac{s^3\, j(s)}{2\pi \int_0^\infty s\, j(s)\, ds} = \frac{S}{16\pi\phi_1 V} \qquad (c1)$$

where ϕ_1 is the volume fraction of dispersed phase and V the total volume irradiated; $\phi_1 V = N.v$

At the beginning j(s) was defined as $K^1 J^1(s)$. If the scattering angle, ε, is expressed in degrees:

$$s^3\, J^1(s) = \pi^4 \varepsilon^3 J(\varepsilon)/180^4 \lambda^4 \qquad (c2)$$

and

$$\int_0^\infty 2\pi s\, j(s)\, ds = \frac{2\pi K \pi^3}{180^3 \lambda^3} \int_0^\infty \varepsilon J(\varepsilon)\, d\varepsilon \qquad (c3)$$

From (c1), (c2) and (c3)

$$S_V = \frac{S}{V} = \frac{8\pi^2 \phi_1}{180\lambda} \cdot \frac{\varepsilon^3 J(^3)}{\int_0^\infty \varepsilon J(\varepsilon)\, d\varepsilon} \qquad (10A)$$

In this equation, $\varepsilon^3 J(\varepsilon)$ is the constant of Porod (valid for the wings of the scattering curve) and $\int_0^\infty \varepsilon J(\varepsilon)\, d\varepsilon$ is the integrated intensity in reciprocal space.

d) Number of Scattering Particles (N)

According to Equation (3.14)

$$i(0) = i_e(0)\ N\Delta\rho^2 v^2 \qquad (d1)$$

Referring to Equation (b1)

$$j(0) = \frac{1}{K}\frac{180\sqrt{3\pi\lambda}}{2\pi^2 R_g}\, i(0) \qquad (b1)$$

Combining (d1) and (b1) and introducing $v^2 = KD^6$

$$J(0) = \text{Constant} \cdot N\Delta\rho^2 D^5$$

$$N = \text{Constant}\ J(0)/\Delta\rho^2 D^5 \qquad (11A)$$

It is not possible to obtain the true number of particles if the scattering curve is in a relative (arbitrary) intensity scale. However, it is possible to follow the relation variation of the number of droplets with time of heat treatment if the electronic density difference between phases is constant (valid for the final stage of APS).

3. Normalization and Correction of the Experimental SAXS Curves

The true scattered intensity J is proportional to the thickness of the sample x, and to the intensity of the X-ray source IVC, and is inversely proportional to its attenuation coefficient, $A = I_o/I$. So, J d x.IVC/A.

Also $\ln I_o/I = \ln A = \mu\rho x$

then $x = \ln A/\mu\rho$

where μ is the mass absorption coefficient and ρ the density of the glass.

Therefore

$$J = K \cdot \ln A \cdot IVC/\mu\rho A \qquad (a)$$

The experimental air scattering (IA) has to be taken into account, and the experimental intensity scattered by the specimen (IS) corrected by means of the expression

$$J = (IS-BK)/A - (IA-BK) \qquad (b)$$

where BK is the background scattering (electronic noise and cosmic rays) and J is the corrected intensity.

The normalized intensity, $J(\varepsilon)$, for different glass compositions and thicknesses, and variations in the X-ray source intensity, is achieved by combining Equations (a) and (b) to give, at a scattering angle ε

$$J(\varepsilon) = \frac{\mu\rho}{IVC.\ln A}\left[IS(\varepsilon).A - IA(\varepsilon) - BK(A-1)\right] \qquad (12A)$$

The product $\mu\rho$ depends only on the chemical composition of the glass, and it was introduced in the calculation of the binodal boundary at 743°C because, in this case, the relation Q(27.0)/Q(28.3B) was used. The actual normalization expression used is given by Equation (3.35).

7. References

1.1 Stookey S.D. (1956) Brit. Patent 752,243.

1.2 McMillan P.W. (1979) "Glass Ceramics" 2nd ed., Academic Press, London.

1.3 Hood H.P. and Nordberg M.E. (1938) U.S. Patent 2,106,744; (1940) U.S. Patent 2,215,039.

1.4 Moriya T. (1955) Bull. Tokio Inst. Tech., Ser. B2,47.

1.5 Porai-Koshits E.A. (1958) "The Structure of Glass" Vol. 1, p.112, Consultants Bureau, New York.

1.6 Rawson H. (1967) "Inorganic Glass Forming Systems", Academic Press, London.

1.7 Porai-Koshits E.A. ed. (1973) "The Structure of Glass" vol. 8 Consultants Bureau, New York.

1.8 Charles R.J. (1973) Am. Ceram. Soc. Bull. 52, 673.

1.9 Doremus R.H. (1973) "Glass Science" J. Wiley and Sons, New York.

1.10 James P.F. (1975) J. Mater. Sci. 10, 1802.

1.11 Uhlmann D.R. and Kolbeck A.G. (1976) Phys. Chem. Glasses, 17, 146.

1.12 Pye L.D. (1977) in "Treatise on Materials Science and Technology" Vol. 11, p. 151, Academic Press, New York.

1.13 Vogel W. (1977) J. Non-Cryst. Solids 25/26, 170.

1.14 Craievich A.F. (1977) Ceram. Crist. 16, 32.

1.15 Tomozawa M. (1979) in "Treatise on Materials Science and Technology" Vol. 17, p.71, Academic Press, New York.

1.16 Zener C. (1949) J. Appl. Phys. 20, 950.

1.17 Frank R.C. (1950) Proc. R. Soc. London Ser. A201, 586.

1.18 Carslaw H.S. and Jaeger J.C. (1959) "Conduction of Heat in Solids", Oxford University Press.

1.19 Wert C. and Zener C. (1950) J. Appl. Phys. 21, 5.

1.20 Ham F.H. (1958) J. Phys. Chem. Solids 6, 335; (1959) J. Appl. Math. 17, 137.

1.21 Zarzycki J. and Naudin F. (1969) J. Non-Cryst. Solids 1, 215.

1.22 Greenwood G.W. (1956) Acta Met. 4, 243.

1.23 Lifshitz I.M. and Slyozov V.V. (1961) J. Phys, Chem. Solids 19, 35.

1.24 Wagner C. (1961) Z. Electrochem. 65, 581.

1.25 Haller W. (1965) J. Chem. Phys. 42, 686.

1.26 Jain S.C. and Hughes, H.E. (1978) J. Mat.Science 13, 1611.

1.27 Hillert M. (1961) Acta Metall. 9, 525.

1.28 Cahn J.W. (1961) Acta Metall. 9, 795.

1.29 Cook H.E. (1970) Acta Metall. 18, 297.

1.30 Cahn J.W. (1965) J. Chem. Phys. 42, 93.

1.31 Hammel J.J.(1965) Proc. XII ICG, Brussels, p. 3.

1.32 Haller W. and Macedo P.B. (1968) Phys. Chem. Glasses 9, 153.

1.33 Hopper R.W. and Uhlmann D.R. (1970) Disc. Faraday Soc. 50, 166.

1.34 Rundman K.B. and Hilliard J.E. (1967) Acta Metall. 15, 1025.

1.35 Zarzycki J. and Naudin F. (1967) C.R. Acad. Sci., Ser. B256, 1456.

1.36 Tomozawa M., Herman H. and MacCrone R.K. (1969) Proc. Int. Symp. Mech. Phase Trans. Cryst. Solids, Br. Inst. Met. Monogr. No. 33.

1.37 idem (1970) Phys. Chem. Glasses 11, 136.

1.38 Neilson G.F. (1969) Phys. Chem. Glasses 10, 54.

1.39 De Fontaine D. (1967) Ph.D. Thesis, Northwestern Univ., Evanston, Illinois.

1.40 Srinivasan G.R., Sarkar A., Gupta P.K. and Macedo P.B. (1976) J. Non-Cryst. Solids 20, 141.

1.41 Tomozawa M. (1978) J. Am. Ceram. Soc. 51, 444.

1.42 Fine M.E. (1964) "Introduction to Phase Transformations in Condensed Systems" MacMillan, New York.

1.43 Burke J. (1965) "The Kinetics of Phase Transformations in Metals" Pergamon Press, London.

1.44 Christian J.W. (1969) "The Theory of Transformations in Metals and Alloys,Pergamon Press, London.

1.45 Zettlemoyer A.C.,ed. (1969) "Nucleation" M. Dekker, New York.

1.46 Russell K.C. (1975) in "Nucleation III" ed. A.C. Zettlemoyer, M. Dekker, New York.

1.47 Rowlands E.G. (1976) "Nucleation and Crystal Growth in the Li_2O-BaO-SiO_2 System" Ph.D. Thesis, Sheffield University, UK.

1.48 Volmer M. and Weber A. (1926) Z. Physikchem. 119, 227.

1.49 Becker R. and Doering W. (1935) Ann. Phys. 24, 719.

1.50 Turnbull D. and Fisher J.C. (1949) J. Chem. Phys. 17, 71.

1.51 JANAF Thermochemical Tables, 2nd Ed. (1971) U.S. Dept. Commerce, NBS, Washington, D.C.

1.52 Hoffman J.D. (1958) J. Chem. Phys. 29, 1192.

1.53 Gonzalez-Oliver C.J.R. (1979) "Crystal Nucleation and Growth in Na_2O-CaO-SiO_2 Glasses" Ph.D. Thesis, Sheffield University.

1.54 BensonG.C. and Shuttleworth R. (1951) J. Chem. Phys. 19, 130.

1.55 Cahn J.W. and Hilliard J.E. (1958) J. Chem. Phys. 28, 258.

1.56 Cahn J.W. and Hilliard J.E. (1959) J. Chem. Phys. 31, 688.

1.57 Turnbull D. (1950) J. Appl. Phys. 21, 1022.

1.58 Skapski A.S. (1956) Acta Mettal. 4, 576.

1.59 Turnbull D. and Cohen M.H. (1958) J. Chem. Phys. 29, 1049.

1.60 Gutzow I. (1980) Contemp. Phys. 21, 121(I); 21, 243(II).

1.61 Kashchiev D. (1969) Surface Sci. 14, 209.

1.62 James P.F. (1974) Phys. Chem. Glasses 15, 95.

1.63 Berkes J.S. and White W.B. (1969) J. Amer. Ceram. Soc. 52, 231.

1.64 Hammel J.J. (1971) in "Advances in Nucleation and Crystallization in Glasses" ed. L.L. Hench and S.W. Freiman, Am. Ceram. Soc. Columbus, Ohio, p. 1.

1.65 Hinz W. (1977) Proc. XI ICG, p. 215, Prague.

1.66 James P.F., Scott B. and Armstrong P. (1978) Phys. Chem. Glasses, 19, 24.

1.67 Burnett D.G. and Douglas R.W. (1971) Phys. Chem. Glasses 12, 117.

1.68 Filipovich V.N. and Kalinina A.M. (1971) Neorg. Mater. 7, 1844.

1.69 Matusita K. and Tashiro M. (1973) J. Non-Cryst. Solids 11, 471.

1,70 Kalinina A.M., Fokin V.M. and Filipovich V.M. (1976) Transl. Fiz. Khim. Stekla 2, 298.

1.71 Klein L.C.,Handwerker C.A. and Uhlman D.R. (1977) J. Crystal Growth 42, 47.

1.72 Rowlands E.G. and James P.F. (1979) Phys. Chem. Glasses 20, 1; 20, 9.

1.73 Takahashi K. and Yoshio T. (1973) J. Ceram. Soc. Japan 81, 524 (in Jap.).

1.74 Neilson G.F. and Weinberg M.C. (1979) J. Non-Cryst. Solids 34, 137.

1.75 James P.F. and Rowlands E.G. (1979) in "Phase Transformations" The Institution of Metallurgists 2, III-27.

1.76 Gonzalez-Oliver C.J.R. and James P.F. (1980) J. Non-Cryst. Solids 38/39, 699.

1.77 Cranmer D., Salomaa R., Yinnon H. and Uhlmann D.R. (1981) J. Non-Cryst. Solids 45, 127.

1.78 Lumsden J. (1952) "Thermodynamics of Alloys" Inst. of Metals, London.

1.79 Heady R.B. and Cahn J.W. (1973) J. Chem. Phys. 58, 896.

1.80 Sundquist B.E. and Oriani R.A. (1967) Trans. Faraday Soc., 63, 561.

1.81 Huang J.S., Vernon S. and Wong N.C. (1974) Phys. Rev. Letters 33, 140.

1.82 Sarkies K.W. and Frenkel N.E. (1971) J. Chem. Phys. 54, 433.

1.83 Turnbull D. (1952) J. Chem. Phys. 20, 411.

1.84 Jones D.R.H. (1974) J. Mater. Sci. 9, 1.

1.85 Servi I.S. and Turnbull D. (1966) Acta Mettal. 14, 161.

1.86 Lothe J. and Pound G.M. (1962) J. Chem. Phys. 36, 2080, ibid (1968) 48, 1849; in "Nucleation" (1969) p. 109, ed. A.C. Zettlemoyer, M. Dekker, New York.

1.87 Kirkwood D.H. (1970) Acta Metal. 18, 563.

1.88 Miyazawa Y. and Pound G.M. (1974) J. Crystal Growth, 23, 45.

1.89 West A.W. (1974) "Nucleation in Ni-Al alloys" Ph.D. Thesis, Sheffield University, UK.

1.90 Uhlmann D.R. (1971) ibid 1.64, p. 91.

1.91 Kirkpatrick R.J. (1975) Am. Miner. 60, 798.

1.92 Gutzow I. (1977) "Crystal Growth and Materials" ed. E. Kaldis and H.J. Scheel, North-Holland, Amsterdam, p. 379.

1.93 Gutzow I. (1977) J. Crystal Growth 42, 15.

1.94 Christiansen N.J., Cooper A.R. and Rawal B.S. (1973) J. Am. Ceram.Soc. 56, 557.

1.95 Hopper R.W.and Uhlmann D.R. (1973) J. Crystal Growth 19, 177.

1.96 Kirkpatrick R.J. (1974) Am. J. Sci 273, 215.

1.97 Meiling G.S. and Uhlmann D.R. (1967) Phys. Chem. Glasses 8, 62.

1.98 Volmer M. and Marder M. (1931) Z. Phys. Chem. (Leipzig) 154, 97.

1.99 Turnbull D. and Cohen M.H. (1960) in "Modern Aspects of the Vitreous State" Vol. 1,ed. J.D. Mackenzie, Butterworths, London.

1.100 Jackson K.A., Uhlmann D.R. and Hunt J.D. (1967) J. Crystal Growth 1, 1.

1.101 Wilson H.A. (1900) Phil. Mag. 50, 238.

1.102 Frenkel, J. (1932) Phys. Z. Sowjet Union 1, 498.

1.103 Hillig W.B. (1966) Acta Mettal. 14, 1868.

1.104 Calvert P.D. and Uhlmann D.R. (1972) J. Crystal Growth 12, 291.

1.105 Hillig W.B. and Turnbull D. (1956) J. Phys. Chem. 24, 914.

1.106 Jackson K.A. (1958) in "Growth and Perfection of Crystals" ed. R.H. Doremus, B.H. Roberts and D. Turnbull, J. Wiley and Sons, New York.

1.107 Shkol'nikov E.V. (1979) Sov. J. Glass Phys. Chem. 6, 153.

1.108 Hammel J.J. (1967) J. Chem. Phys. 46, 2234.

2.1 Roth R.S. and Levin E.M. (1959) J. Res. Nat. Bur. Standards 62, 193.

2.2 Douglass R.M. (1958) Am. Miner. 43, 517.

2.3 Katscher H., Rissert G. and Liebau F. (1973) Zeut. für Krist. 137, 146.

2.4 Oshlslegal G. (1975) J. Am. Ceram. Soc. 58, 148.

2.5 Charles R.J. (1967) Phys. Chem. Glasses 8, 185.

2.6 Seward III T.P., Uhlmann D.R. and Turnbull D. (1968) J. Am. Ceram. Soc. 51, 278 and 634.

2.7 Haller W., Blackburn D.H. and Simmons J.H. (1974) J. Am. Ceram. Soc. 57, 120.

2.8 MacDowell J.F. (1965) Proc. Brit. Ceram. Soc., No. 3, 101.

2.9 Freiman S.W., Onoda G.Y. and Pincus A.G. (1972) J. Am. Ceram. Soc. 55, 354; (1971) ibid 102, p. 141.

2.10 Lewis M.H. and Smith G. (1976) J. Mat. Science 11, 2015.

2.11 Kracek F.C. (1930) J. Phys. Chem. 34, 2645; (1939) J. Am. Chem. Soc. 61, 2870.

2.12 Andreev N.S., Goganov D.A. and Porai-Koshits E.A. (1964) in "Structure of Glass" Vol. 3, Consultants Bureau, New York.

2.13 Moriya Y., Warrington D.H. and Douglas R.W. (1967) Phys. Chem. Glasses 8, 19.

2.14 James P.F. and Keown S.R. (1974) Phylos. Mag. 30, 789.

2.15 Lewis M.H., Metcalf-Johansen J. and Bell P.S. (1979) J. Am. Ceram. Soc. 62, 278.

2.16 Doremus R.H. and Turkalo A.M. (1972) Phys. Chem. Glasses 13, 14.

2.17 Kinser D.L. and Hench L.L. (1968) J. Am. Ceram. Soc. 51, 445; (1970) J. Mat.Science 5, 369.

2.18 Hench L.L., Frieman S.W. and Kinser D.L. (1971) Phys. Chem. Glasses 12, 58.

2.19 Kalinina A.M. (1970) Neorg. Mat. 6, 907; Engl. Transl. p. 796.

2.20 Liebau F. (1961) Acta Cryst. 14, 389.

2.21 West A.R. and Glasser F.P. (1971) ibid 1.64,p. 151; (1967) Phys. Chem. Glasses 8, 224.

2.22 Tashiro M. (1968) Proc. VIII ICG, p. 133, London.

2.23 Hammel J.J. (1969) in "Nucleation" ed. A.C. Zettlemoyer, M. Dekker, New York.

2.24 Scholes S. (1970) Disc. Faraday Soc. 50, 222.

2.25 Uhlmann D.R. (1970) Disc. Faraday Soc. 50, 233.

2.26 Zarzycki J. (1970) Disc. Faraday Soc. 50, 122.

2.27 James P.F. (1982) Proc. Symposium on Nucleation and Crystallization in Glasses, Washington D.C.

2.28 Tomozawa M. (1972) Phys. Chem. Glasses 13, 161.

2.29 Stookey S.D. (1959) Glast. Ber. 32K, (V,ICG), p. 1.

2.30 Vogel W. and Gerth K. (1962) Proc. of the Symposium on Nucleation and Crystallization in Glasses and Melts, p. 11. Amer. Ceram. Soc., Columbus.

2.31 Vogel W. (1965) Proc. VII ICG, paper 33, Brussels.

2.32 Vogel W. (1966) Glass Tech. 7, 15.

2.33 Vogel W. (1971) "Structure and Crystallization of Glasses" Pergamon Press, Oxford.

2.34 Ohlberg S.M., Golob H.R. and Strickler, D.W. (1962) ibid 2.30, p. 55.

2.35 Maurer R.D. (1962) J. Appl. Phys. 33, 2132.

2.36 Maurer R.D. (1962) ibid 2.30, p. 5.

2.37 Kalinina A.M., Filipovich V.N., Kolesova V.A. and Bondar' I.A. (1964) "The Structure of Glass" vol. 3, p. 53, ed. E.A. Porai-Koshits, Consultants Bureau, New York.

2.38 Buzhinskii I.M., Sabaeva E.I. and Khomyakov A.N. (1964) ibid 2.37, p. 133.

2.39 Doherty P.E., Lee P.W. and Davies R.S. (1967) J. Am. Ceram. Soc. 50, 77.

2.40 Burnett D.G. and Douglas R.W. (1970) Disc. Faraday Soc. 50, 200.

2.41 Bayer G. and Hoffman W. (1966) Glass Tech. 7, 94.

2.42 Takusagawa N. and Saito H. (1970) J. Ceram. Soc. Japan 78, 411 (in Jap.)

2.43 Leger L. and Bray J. (1968) Silicate Industriels XXIII, 257.

2.44 Kanazawa T., Nakai A. and Kawazoe H. (1972) J. Ceram. Soc. Japan 80, 456 (in Jap.).

2.45 Phillips S.V. and McMillan P.W. (1965) Glass Tech. 6, 46.

2.46 Harper H., James P.F. and McMillan P.W. (1970) Disc. Faraday Soc. 50, 206.

2.47 Harper H. and McMillan P.W. (1972) Phys. Chem. Glasses 13, 97.

2.48 McMillan P.W. (1974) Proc. X ICG 14, 1.

2.49 Nakagawa K. and Izumitani T. (1969) Phys. Chem. Glasses 10, 179.

2.50 Zanotto E.D. and Craievich A.F. (1981) J. Mat. Science 16, 973.

2.51 Matusita K. and Tashiro M. (1973) Phys. Chem. Glasses 14, 77.

2.52 Matusita K., Maki T. and Tashiro M. (1974) Phys. Chem. Glasses 15, 106.

2.53 Hautojärvi P., Vehanen A., Komppa V. and Pajanne E. (1978) J. Non-Cryst. Solids 29, 365.

2.54 Ramsden A.H. (1977) "Crystal Nucleation and Growth in $BaO-SiO_2$ Glasses", Ph.D. Thesis, University of Sheffield.

2.55 Ogura T., Hayami R. and Kadota M. (1968) J. Ceram. Soc. Japan 76, 277 (in Jap.).

2.56 Tomozawa M. (1973) Phys. Chem. Glasses 14, 112.

2.57 Komppa V. (1981) Proc. Symposium on Phase Transformations in Vitreous Systems, Warwick, UK. Pub. Soc. Glass Tech.

2.58 Scherer G.W. and Uhlmann D.R. (1976) J. Non-Cryst. Solids 21, 199.

3.1 Vogel A.I. (1961) "Quantitative Inorganic Analysis" 3rd Ed., Green and Co. Ltd., London.

3.2 Price W.J. (1978) "Analytical Atomic Absorption Spectroscopy" Heyden and Sons Limited, London.

3.3 Wise W.M., Burdo R.A. and Sterlace J.S. (1978) Prog. Analyt. Atom. Spect. 1, 201; Corning Research (1978) p. 162.

3.4 Sweatman T.R. and Long V.P. (1969) Journal Petrol. 10, Part 2, 332.

3.5 Matveev M.A. and Velya V.V. (1959) Glass Ceram. 16, 543.

3.6 Scholze H. (1959) Glast. Ber. 32, 81-88; 142-152; 278-281; 314-320; 381-386; 421-426.

3.7 Scholze H. (1966) Glass Ind., Oct. 546; Nov. 622; Dec. 670.

3.8 Boulos E.N. and Kreidl N.J. (1972) J. Can. Ceram. Soc. 41, 83.

3.9 Gonzalez-Oliver C.J.R., Johnson P.S. and James P.F. (1979) J. Mater. Sci. 14, 1159.

3.10 Shelbi J.E. (1979) J. Appl. Phys. 50, 8010.

3.11 James P.F. (1982) Proc. Symposium on Nucleation and Crystallization in Glasses, Washington D.C.

3.12 DeHoff R.T. and Rhines F. (1961) Trans. AIME 221, 975.

3.13 Nemilov S.V. (1977) Soviet J. Glass Phys. Chem., p. 137, transl. from Fiz. Khim, Stekla 3, 148.

3.14 De Bast J. and Gilard P. (1965) Compt. Rend. Rech. No. 32, 26.

3.15 Streicher F. (1926) "Zurtheorie des Baugrundes", Baruin Genieur 48, 48; 49, 949.

3.16 Timoshenko S. and Goodier J.N. (1951) "Theory of Elasticity" p. 372 McGraw-Hill, London.

3.17 Goodier J.N. (1936) Phil. Mag. 22, 678.

3.18 Douglas, R.W., Armstrong W.L., Edward J.P. and Hall D. (1965) Glass Tech. 6, 52.

3.19 Bruckner R. and Demharter G. (1975) Glast Ber. 48, 12.

3.20 Ohlberg S.M. and Strickler D.W. (1962) J. Am. Ceram. Soc. 45, 170.

3.21 Cervinka L. and Dusil J. (1976) J. Non-Cryst. Solids 21, 125.

3.22 Hilliard J.E. and Cahn J.W. (1961) Trans. AIME 221, 344.

3.23 Guinier A. and Fournet G. (1955) "Small Angle Scattering of X-rays" J. Wiley and Sons, New York.

3.24 Porod G. (1951) Kolloid Z. 124, 83; (1952) 125, 51; (1953), 133. 16.

3.25 Ruland W. (1971) J. Appl. Cryst. 4, 70; (1974) 7, 383.

3.26 Schmidt P.W. (1960) Acta Cryst. 13, 480; (1965) 19, 938; J. Appl. Cryst. (1970) 3, 137; (1974) 7, 439.

3.27 Vonk, C.G. (1971) J. Appl. Cryst. 4, 340.

3.28 ibid 3.23, p. 114.

3.29 Debye P., Anderson H.R. and Brumberger H. (1957) J. Appl. Phys. 28, 679.

3.30 Brown D.S. and Wetton R.E. (1978) "Developments in Polymer Characterisation" chap. 6, ed. J.V. Dawkins, Applied Science Publishers Limited, London.

3.31 Brown D.S., Warner F.P. and Wetton R.E. (1972) Polymer 13, 575.

3.32 Longman G.W., Wignall G.D., Hemming M. and Dawkins J.V. (1974) Colloid and Pol. Sci. 252, 298.

3.33 Guinier A. (1963) "X-ray Diffraction" chap. 10,W.H. Freeman and Company, London.

3.34 ibid 3.23, p. 48.

3.35 Fournet G. (1951) Bull. Soc. Franc. Minéral. et Crist. 74, 39.

3.36 Verwey E.J.W. and Overbeck J.T.G. (1945) "Theory of Stability of Lyophobic Colloids" Elsevier, Amsterdam.

3.37 Rothwell W.S. (1968) J. Appl. Phys. 39, 1840.

3.38 ibid 3.23, p. 68.

3.39 Luzatti W. (1960) Acta Cryst. 13, 939.

3.40 Cullity B.D. (1978) "Elements of X-ray Diffraction" 2nd ed., Addison-Wesley Pub., Reading, Massachusetts.

4.1 Johnson W.A. and Mehl R.F. (1939) Trans. AIME 135, 416.

4.2 Avrami M. (1939) J. Phys. Chem. 7, 1103; (1940) 8, 212; (1941) 9, 177.

4.3 Uhlmann D.R. (1972) J. Non-Cryst. Solids 7, 337.

4.4 Hopper R.W., Scherer G. and Uhlmann D.R. (1974) J. Non-Cryst. Solids 15, 45.

4.5 Onorato P.I.K. and Uhlmann D.R. (1976) J. Non-Cryst. Solids 22, 367.

4.6 Onorato P.I.K. and Uhlmann D.R. (1980) J. Non-Cryst. Solids 41, 189.

4.7 YinnonH. and Uhlmann D.R. (1981) J. Non-Cryst. Solids 44, 37.

4.8 Mandelkern L. (1964) "Crystallization of Polymers" chap. 8, McGraw-Hill, New York.

4.9 Sharples A. (1966) "Introduction to Polymer Crystallization" chap. 4,5, Edward Arnold Limited, London.

4.10 Burnett D.G. and Douglas R.W. (1970) Phys. Chem. Glasses 11, 125.

4.11 Neilson G.F. (1970) Disc. Faraday Soc. 50, 145.

4.12 Gerold V. (1967) " Small Angle X-ray Scattering" p. 277, ed. H. Brumberger, Gordon and Breach, New York.

4.13 McCurrie R.A. and Douglas R.W. (1967) Phys. Chem. Glasses 8, 132.

4.14 James P.F. and McMillan P.W. (1970) Phys. Chem. Glasses 11, 59.

4.15 Zarzycki J. and Naudin F. (1967) Phys. Chem. Glasses 8, 11.

4.16 Neilson G.F. (1972) Phys. Chem. Glasses 13, 70.

4.17 Craievich A.F. (1975) "Mecanismos de Separação de Fases em Sólidos Vitreos" Livre Docente Thesis, IFQSC, Universidade de S. Paulo, S. Carlos, Brazil.

4.18 Zanotto E.D. (1978) "Separação de Fases Amorfas e Nucleação de Cristais em Vidros do Sistema Li_2O-SiO_2" M.Sc. Thesis, IFQSC, Universidade de S. Paulo, S. Carlos, Brazil.

4.19 Williams J.A., Rindone G.E. and McKinstry H.A. (1969) Proc. of the Conference on SAXS in Glass and High Temperature Materials, University of Missouri.

4.20 Visser T.J.M. and Stevels J.M. (1972) J. Non-Cryst. Solids 7, 365.

4.21 Lillie H.R. (1933) J. Am. Ceram. Soc. 16, 619.

4.22 Taylor N.W. and Doran R.F. (1941) J. Am. Ceram. Soc. 24, 103.

4.23 Bockris J.O'M., Mackenzie J.D. and Kitchener J.A. (1955) Trans. Faraday Soc. LI, 1734.

4.24 Aver'yanov V.I. and Porai-Koshits E.A. (1965) "The Structure of Glass" vol. 5, p. 63 Consultants Bureau, New York.

4.25 Korelova A.I., Degen M.G. and Alekseeva O.S. (1964) "The Structure of Glass" vol. 3, p. 65, Consultants Bureau, New York.

4.26 Porai-Koshits E.A. and Goganov D.A. (1965) ibit 4.24, p. 82.

4.27 Shartsis L., Spinner S. and Capps W. (1952) J. Amer. Ceram. Soc. 35, 155.

4.28 Schultz J.M. (1974) "Polymer Materials Science" chap. 9, Prentice-Hall, Inc., New Jersey.

4.29 Lam A.H.T. "ASTM X-ray Powder Diffraction Data File" No. 15-637.

4.30 Roy R. and Osborn E.F. (1949) J. Am. Chem. Soc. 71, 2086.

4.31 Rindone G.E. (1962) J. Am. Ceram. Soc. 45, 7.

4.32 Gruner K., Kolterman M, and Müller K.P. (1967) Glastech. Ber. 40, 185.

4.33 Noshiro M. and Jitsugiri Y. (1968) J. Ceram. Soc. Japan, p. 59.

5.1 Filipovich V.N. and Kalinina A.M. (1971) Neorg. Mat. 7, 1844.

5.2 Tuzzeo J.J. (1976) "Effects of Pressure on Kinetics of Crystal Nucleation in Lithium Disilicate Glass", Ph.D. Thesis, The Ohio State University, USA.

5.3 Fokin V.M., Filipovich V.N. and Kalinina A.M. (1977) Transl. Fiz. Khim. Stekla 3, 129.

5.4 Ito M., Sakaino T. and Moriya T. (1968) Bull. Tokio Inst. Tech. No. 88, 127.

5.5 Oishi Y., Terai R. and Ueda H. (1975) in "Mass Transport Phenomena in Ceramics" ed. A.R. Cooper and A.H. Heuer 9, p. 297, Plenum Press, New York.

5.6 Kirkwood J.G. and Buff F.P. (1949) J. Chem. Phys. 17, 338.

5.7 Robertson D. and Pound G.M. (1973) J. Crystal Growth 19, 269.

5.8 Reiss H. (1976) in "Precipitation" Faraday Disc. Chem. Soc. No. 61, p. 213.

5.9 Kalinina A.M., Filipovoch V.N. and Fokin V.M. (1980) J. Non-Cryst. Solids 38/39, 723.

6.1 Vogel W. (1981) Friedrich Schiller University in Jena, personal communication.

6.2 Craievich A.F. and Sanchez M.J. (1981) Phys. Rev. Letters, 47, 1308.